Experimental and theoretical techniques for quantum-enhanced metrology and optical quantum information processing

Peter C. Humphreys
Worcester College, Oxford

Submitted for the degree of Doctor of Philosophy
Hilary Term 2015

Supervised by
Prof. Ian A. Walmsley

Clarendon Laboratory
University of Oxford
United Kingdom

Experimental and theoretical techniques for quantum-enhanced metrology and optical quantum information processing

Peter C. Humphreys
Worcester College, Oxford

Submitted for the degree of Doctor of Philosophy
Hilary Term 2015

Abstract

Over the last few decades, quantised excitations of the electromagnetic field have proven to be an ideal system with which to investigate and harness quantum optical phenomena. The techniques developed have enabled fundamental tests of quantum mechanics as well as practical applications in quantum metrology and quantum information processing. Advancing to larger-scale entangled quantum systems will open up new regimes of quantum many-body physics, allowing us to probe the limits of quantum mechanics and enabling truly quantum-enhanced technologies. However, moving towards this goal will require further experimental and theoretical innovations. The work described in this thesis focuses on several different aspects of optical quantum information, but are ultimately all linked by this long-term aim. The first part of this thesis describes a novel method for strain-based active control of quantum optical circuits and a new method for the characterisation of high efficiency detectors. Building on this, I discuss in detail two different fields of quantum optics that stand to benefit from these techniques. I initially consider quantum-enhanced metrology, including work aimed towards demonstrating a truly better-than-classical phase measurement, and a theoretical exploration of multiple-phase estimation. Finally, I focus on linear-optical quantum information processing, exploring in detail the use of time-frequency encodings for quantum computing.

To my parents

Acknowledgements

There are few very groups in which I could have gotten away with doing this degree in the way that I did! I mean this in the best possible way - the combination of being part of an epic team while also being allowed the freedom to pursue my random interests is unique, and I wouldn't trade my experience for anything.

Ian - thank you for creating such a supportive group (our attitude definitely follows your lead), and of course for providing so much guidance along the way. Ben - you have literally been my walking encyclopedia; I am always amazed at how much you know about everything that matters. I like to think that my bodging and your methodical approach were complementary, but I suspect that progress was mostly made by you picking up the pieces after me! Steve - you somehow managed to keep us moving in approximately the right direction, while always being more than happy (I suspect in fact happiest) to dive in at the deep end in discussing random technical details. I already miss having you in the same office for easy access with distractions. Justin - I may have stolen your desk, but I could never replace you; a year later and I think Ben still hasn't recovered! You are obviously a badass physicist, but (clearly more importantly), your football, beer and brisket sessions were the delicious bedrock that our team was built on. Animesh - you tolerated my feeble attempts at theory, whilst politely avoiding mentioning that perhaps I should stick with experiments. I learned a lot from you, and enjoyed your unique brand of humour! Marco - thanks for sharing your knowledge on every aspect of quantum optics. I remain convinced that you are a member of the Italian quantum mafia. At the very least, I always know where to go to get the inside information on any group on the planet!

There are of course many other amazing people I worked with, including (but not limited to!) Josh, Merritt and Thomas. Thanks to all of you, and to everyone else in the group! In addition, I would like to thank the Southampton crew, in particular Paolo and James. You guys seem to be almost singlehandedly running a fabrication effort that rivals that of major commercial companies!

Thanks to all of my family and extended family, and in particular my parents, for always being there, guiding me and helping me whenever I have needed you. We have had pretty amazing childhoods, and I wouldn't be who I am today without that. Anna and Alex, you are fantastic siblings, and I have really loved being able to escape from Oxford to come and hang with you at the weekends - that will definitely be one of the things I will miss most on leaving here.

Finally I want to thank Liselotte. More than anything else, you have defined my time in Oxford. You have been there for me during the ups and the downs, and have never wavered in all that time. I have never met anyone as caring or unconditionally supportive as you, and just importantly, we've had a lot of fun along the way. I hope this is just the start of our adventures together.

Author's publications

Journal publications

1) P. C. Humphreys, B. J. Metcalf, T. Gerrits, T. Hiemstra, A. E. Lita, J. Nunn, S. W. Nam, A. Datta, W. S. Kolthammer, and I. A. Walmsley, "Tomography of photon-number resolving continuous-output detectors," *New Journal of Physics*, vol. 17, p. 103044, 2015.

2) P. C. Humphreys, W. S. Kolthammer, J. Nunn, M. Barbieri, A. Datta, and I. A. Walmsley, "Continuous-variable quantum computing in optical time-frequency modes using quantum memories," *Physical Review Letters*, vol. 113, p. 130502, 2014.

3) P. C. Humphreys, B. J. Metcalf, J. B. Spring, M. Moore, P. S. Salter, M. J. Booth, W. S. Kolthammer, and I. A. Walmsley, "Strain-optic active control for quantum integrated photonics," *Optics Express*, vol. 22, no. 18, p. 21719, 2014.

4) B. J. Metcalf, J. B. Spring, P. C. Humphreys, N. Thomas-Peter, M. Barbieri, W. S. Kolthammer, X.-M. Jin, N. K. Langford, D. Kundys, J. C. Gates, *et al.*, "Quantum teleportation on a photonic chip," *Nature Photonics*, vol. 8, no. 10, pp. 770–774, 2014.

5) P. C. Humphreys, M. Barbieri, A. Datta, and I. A. Walmsley, "Quantum enhanced multiple phase estimation," *Physical Review Letters*, vol. 111, p. 070403, 2013.

6) P. C. Humphreys, B. J. Metcalf, J. B. Spring, M. Moore, X.-M. Jin, M. Barbieri, W. S. Kolthammer, and I. A. Walmsley, "Linear optical quantum computing in a single spatial mode," *Physical Review Letters (selected for a Physics Viewpoint)*, vol. 111, no. 15, p. 150501, 2013.

7) B. J. Metcalf, N. Thomas-Peter, J. B. Spring, D. Kundys, M. A. Broome, P. C. Humphreys, X.-M. Jin, M. Barbieri, W. S. Kolthammer, J. C. Gates, *et al.*, "Multiphoton quantum interference in a multiport integrated photonic device," *Nature Communications*, vol. 4, p. 1356, 2013.

8) B. Calkins, P. L. Mennea, A. E. Lita, B. J. Metcalf, W. S. Kolthammer, A. Lamas-Linares, J. B. Spring, P. C. Humphreys, R. P. Mirin, J. C. Gates, *et al.*, "High quantum-efficiency photon-number-resolving detector for photonic on-chip information processing," *Optics Express*, vol. 21, no. 19, pp. 22657–22670, 2013.

9) J. B. Spring, P. S. Salter, B. J. Metcalf, P. C. Humphreys, M. Moore, N. Thomas-Peter, M. Barbieri, X.-M. Jin, N. K. Langford, W. S. Kolthammer, *et al.*, "On-chip low loss

heralded source of pure single photons," *Optics Express*, vol. 21, no. 11, pp. 13522–13532, 2013.

10) J. B. Spring, B. J. Metcalf, P. C. Humphreys, W. S. Kolthammer, X.-M. Jin, M. Barbieri, A. Datta, N. Thomas-Peter, N. K. Langford, D. Kundys, *et al.*, "Boson sampling on a photonic chip," *Science*, 2012.

Contents

List of Figures

List of Tables

Chapter 1

Introduction

Quantum mechanics allows for behaviours that have no classical analogue, including superposition states[1], entanglement[2] and non-local correlations[3,4]. However, as shown by our resolutely classical everyday experiences, controllably accessing this quantum world is experimentally challenging. Over the last few decades, quantised excitations of the electromagnetic field have been shown to be an ideal system with which to investigate and harness these phenomena. This is primarily due to their ease of manipulation and since they do not interact easily with one another, minimising unwanted decoherence. These advantages have motivated the development of the field of quantum optics, which is concerned with the investigation and manipulation of non-classical states of light. The techniques developed have enabled fundamental tests of quantum mechanics[5] as well as practical applications in quantum metrology[6,7] and quantum information processing[8,9].

The currently achievable levels of few-photon entanglement have constrained many applications of quantum mechanics to proof-of-principle demonstrations. Taking the field forward to larger-scale entangled quantum systems will open up new regimes of quantum many-body physics, allowing us to probe the limits of quantum mechanics and enabling truly quantum-enhanced technologies. However, moving towards this goal will require further experimental and theoretical innovations. The work described in this thesis focuses on several different aspects of optical quantum information, but are ultimately all linked by this long-term aim.

1.1 Thesis outline

After first introducing the necessary background and mathematical framework in this Chapter, in Part I of this thesis I will discuss two experimental tools under development by our group. In Chapter 2, I will initially focus on a novel method for low-loss and rapid phase control using the strain-optic effect. Strain-optic phase shifting is three orders of magnitude faster than thermo-optic phase shifting, the current workhorse of integrated optical experiments; this increase in bandwidth allows for switching over time scales in which pulses can be easily stored in a fibre-optical loop. Our approach could therefore enable near-term demonstrations of the feed-forward protocols necessary in many areas of quantum computation.

I will then move on to a discussion of our work on high efficiency superconducting transition-edge sensor detectors in Chapter 3. These cryogenic detectors have demonstrated quantum efficiencies of up to 98%[10] and true photon-number resolution. With these advantages come additional challenges in detector characterisation; motivated by this, I have explored how to effectively carry out detector tomography on such detectors.

Part II of this thesis will focus on quantum-enhanced metrology, one of the primary fields that stands to benefit from high-efficiency detectors and low-loss phase elements. I will begin by introducing the theoretical framework for metrology in Chapter 4. I will then move to a discussion of planned experiments for a truly quantum-enhanced phase measurement in Chapter 5, showing that our recent experimental advances should be sufficient to enable us to beat the so-called standard quantum limit in the near future. Finally, I will shift to a more fundamental perspective, considering theoretically the problem of quantum-enhanced multiple-phase estimation in Chapter 6.

Part III of the thesis will be concerned with the related field of linear-optical quantum information processing. The challenge of building a universal quantum computer is formidable no matter which physical platform is considered, and optics is no exception. However, the huge potential benefits of such a device are sufficient motivation to continue to develop the building blocks for quantum information processing. Additionally, there are many intermediate goals of interest, from probing the behaviour of large entangled systems [2] to the problem of Boson Sampling [11,12]. I will begin this part of the thesis by briefly introducing the central ideas of quantum computer in Chapter 7. After this introduction, I will discuss in detail the use of time-frequency encodings for linear-optical quantum computing. These encodings have the potential to significantly increase the size of Hilbert space available for the encoding of quantum information in electromagnetic fields; a necessary innovation given the number of modes likely to be necessary for fault-tolerant quantum computing. In Chapter 8 I will focus on a scheme for linear-optical quantum computing using single photons encoded in time bins. This includes the first experimental demonstration of a time-bin encoded two qubit gate. Finally, in Chapter 9, I will discuss a theoretical proposal for extending these ideas to more general time-frequency encodings, finding that Raman quantum memories can act as versatile elements for time-frequency-mode based optical quantum information processing.

1.2 Quantisation of the electromagnetic field

A quantum treatment of the electromagnetic field can be formulated in terms of the four-vector potential $\hat{\boldsymbol{A}}$[13]. In the Lorentz gauge, this potential must satisfy the wave equation of motion

$$\nabla^2 \hat{\boldsymbol{A}} = \frac{1}{c^2} \frac{\partial^2 \hat{\boldsymbol{A}}}{\partial t^2}. \tag{1.1}$$

This wave equation can be solved by decomposing the potential into terms corresponding to a set of orthogonal modes (here labelled by k), such that $\hat{\boldsymbol{A}} = \hat{\boldsymbol{A}}^{+} + \hat{\boldsymbol{A}}^{-}$, where $\hat{\boldsymbol{A}}^{+} = \sum_k A_k \boldsymbol{u}_k(\boldsymbol{r}) \hat{\alpha}_k(t)$, $\hat{\boldsymbol{A}}^{-} = (\hat{\boldsymbol{A}}^{+})^\dagger$ and $A_k = \sqrt{\frac{\hbar}{2\omega_k \epsilon_0}}$ is a dimensional factor. With this decomposition, the wave equation can be separated into Helmholtz equations for the spatially-dependent components $\boldsymbol{u}_k(\boldsymbol{r})$ of each mode and quantum harmonic oscillator equations for the time-varying components $\hat{\alpha}_k(t)$[14]. These time-varying components therefore have the form $\hat{\alpha}_k(t) = \hat{a}_k e^{-\mathrm{i}\omega_k t}$, $\hat{\alpha}_k^\dagger(t) = \hat{a}_k^\dagger e^{\mathrm{i}\omega_k t}$, where $\hat{a}$ and $\hat{a}^\dagger$ represent conventional annihilation and creation operators respectively. These are endowed with the commutation relations $[\hat{a}_j, \hat{a}_k] = 0$, $\left[\hat{a}_j, \hat{a}_k^\dagger\right] = \delta_{jk}$. Combining these components gives the overall solution for the vector potential

$$\hat{\boldsymbol{A}} = \sum_k \sqrt{\frac{\hbar}{2\omega_k \epsilon_0}} \left[\hat{a}_k \boldsymbol{u}_k(\boldsymbol{r}) e^{-\mathrm{i}\omega_k t} + \hat{a}_k^\dagger \boldsymbol{u}_k^*(\boldsymbol{r}) e^{\mathrm{i}\omega_k t}\right]. \tag{1.2}$$

In the eigenbasis of the field (which depends on the specific boundary conditions of the problem considered), this solution for the vector potential allows the field Hamiltonian to be expressed as[14]

$$\hat{H} = \sum_k \hbar\omega_k(\hat{a}_k^\dagger \hat{a}_k + \frac{1}{2}). \tag{1.3}$$

This Hamiltonian has no coupling term between different modes, which means that the Hilbert space is spanned by product states of the eigenstates for each mode. Therefore, without loss of generality, we can temporarily focus on a single mode k.

The eigenstates for a given mode of the electromagnetic field are *Fock states* (each labelled by a different value of n_k)

$$|n_k\rangle = \frac{1}{\sqrt{n_k!}}(\hat{a}_k^\dagger)^{n_k} |0\rangle , \tag{1.4}$$

with associated energies

$$E_k(n_k) = \hbar\omega_k(n_k + \frac{1}{2}). \tag{1.5}$$

Fock states have the usual properties that

$$\hat{a}_k^\dagger |n_k\rangle = \sqrt{n+1}\, |(n+1)_k\rangle , \tag{1.6}$$

$$\hat{a}_k |n_k\rangle = \sqrt{n}\, |(n-1)_k\rangle . \tag{1.7}$$

The vacuum state $|0\rangle$ is defined as the state for which $\hat{a}_k |0\rangle = 0$. Successive eigenstates of the field then correspond to the addition of a discrete quanta of energy to the previous eigenstate. These quanta are typically thought of as photons - bosonic particles occupying the field. The number operator $\hat{n}_k = \hat{a}_k^\dagger \hat{a}_k$ therefore gives the photon number for mode k.

1.2.1 Superpositions

The quantised electric field supports quantum behaviours with no classical analogue. At the basis of many of these quantum phenomena is one of the most fundamental aspects of quantum mechanics, which is the existence of *superpositions* of quantum states.

Due to the linearity of quantum mechanics, any normalised linear combination of eigenstates will also be a valid solution to the equations of motion. This allows for superpositions of different field mode excitations. For example, one can consider a superposition of photons distributed across the modes a, b and c

$$|\psi\rangle = \alpha_1 |n_{1a}\rangle \otimes |n_{1b}\rangle \otimes |n_{1c}\rangle + \alpha_2 |n_{2a}\rangle \otimes |n_{2b}\rangle \otimes |n_{2c}\rangle + \alpha_3 |n_{3a}\rangle \otimes |n_{3b}\rangle \otimes |n_{3c}\rangle , \qquad (1.8)$$

where α_j are the complex valued weights of each term in the superposition, constrained by $\sum_j |\alpha_j|^2 = 1$. A condensed notation is often employed for product states of photons in multiple modes, using a single state vector $|n_a, n_b, n_c\rangle$ to represent the occupation state of all the modes. In this notation, the above state would be written

$$|\psi\rangle = \alpha_1 |n_{1a}, n_{1b}, n_{1c}\rangle + \alpha_2 |n_{2a}, n_{2b}, n_{2c}\rangle + \alpha_3 |n_{3a}, n_{3b}, n_{3c}\rangle . \qquad (1.9)$$

An insight into the challenges of simulating quantum mechanical systems, but also the potential of quantum information processing, can be gained by considering the wavefunction of N different photonic excitations, each distributed across d modes. At its most general, this wavefunction requires d^N terms to fully describe its state. This exponential scaling presents challenges for the classical simulation of quantum phenomena, since all of these complex numbers must be kept track of at every stage in the evolution of the quantum state.[1] However, these superposition states also seem to be an important part of the power of quantum mechanics, with the potential to enable quantum technologies ranging from quantum key distribution[16] to quantum enhanced metrology[17], and the ultimate goal of universal quantum computing[8].

1.3 Continuous-variable quantum optics

So far we have considered the electromagnetic field from a *discrete-variable* (DV) perspective, emphasising the quantisation of the field into discrete Fock states. While this representation can provide many insights into the quantum behaviour of light, it will also be helpful to introduce the alternative *continuous-variable* (CV) picture of an electromagnetic field mode. This picture is formally equivalent to the photon-number representation, but provides a different perspective that often reveals features that are less evident in the Fock basis. It therefore lends itself to new ways of thinking about metrology and quantum information processing, as I will explore in Chapters 5 & 9. Here I will initially give a brief introduction to the CV quantum optics formalism, aiming to give a pedagogical overview of the field. For further details, the interested reader is directed to the review papers by Braunstein and van Loock [18] and Weedbrook et al. [19] along with the comprehensive introduction to Gaussian states by Ferraro et al. [20].

I will start by returning to the initial electromagnetic mode Hamiltonian given in Eqn. 1.3,

$$\hat{H} = \sum_k \hbar\omega_k(\hat{a}_k^\dagger \hat{a}_k + \frac{1}{2}).$$

---

[1] Although this is a significant challenge, continuing progress is being made in improving the efficiency of classical simulations of quantum systems. For example, for many systems it is possible to use alternative representations to dramatically reduce the number of terms that must be kept track of[15].

Introducing the dimensionless *position* and *momentum* operators [2]

$$\hat{x}_k = \frac{1}{2}(\hat{a}_k + \hat{a}_k^\dagger), \tag{1.10}$$

$$\hat{p}_k = -\frac{\mathrm{i}}{2}(\hat{a}_k - \hat{a}_k^\dagger), \tag{1.11}$$

the field Hamiltonian can be rewritten as

$$\hat{H} = \sum_k \hbar\omega_k(\hat{x}_k^2 + \hat{p}_k^2). \tag{1.12}$$

These operators have the commutation relations $[\hat{x}_j, \hat{x}_k] = 0$, $[\hat{p}_j, \hat{p}_k] = 0$, $[\hat{x}_j, \hat{p}_k] = \frac{i}{2}\delta_{j,k}$.

Here I will again initially focus on a single mode, and will therefore temporarily drop the mode index k. I first note that, unlike the creation and annihilation operators, the position and momentum operators are Hermitian operators, and therefore are observables of the field. In fact, they are the observables for the electromagnetic field quadratures, as can be seen by calculating the electric field associated with the vector potential (Eqn. 1.2) [13] at a given location [3]

$$\boldsymbol{E}(t) = \frac{1}{2}\boldsymbol{E}_0\,(\hat{a}\,e^{-\mathrm{i}\omega t} + \hat{a}^\dagger\,e^{\mathrm{i}\omega t}) \tag{1.13}$$

$$= \boldsymbol{E}_0\,(\hat{x}\cos(\omega t) + \hat{p}\sin(\omega t)). \tag{1.14}$$

---

[2] The position and momentum operators get their names from the quantisation of a quantum harmonic oscillator, in which case they actually represent the position and momentum of a particle. As will be discussed below, here they simply represent orthogonal components of the electromagnetic field.

[3] The electric field form given here requires one to assume that $\boldsymbol{u}_k$ is real, without loss of generality.

1.3.1 Quadrature operators

It is possible to generalise $\hat{x}$ and $\hat{p}$ to define *quadrature operators* of the field

$$\hat{x}_\phi = \frac{1}{2}(\hat{a}e^{-\mathrm{i}\phi} + \hat{a}^\dagger e^{\mathrm{i}\phi}), \tag{1.15}$$

$$\hat{p}_\phi = -\frac{\mathrm{i}}{2}(\hat{a}e^{-\mathrm{i}\phi} - \hat{a}^\dagger e^{\mathrm{i}\phi}). \tag{1.16}$$

Notice that ϕ parametrises a continuous rotation of the quadrature basis

$$\begin{pmatrix} \hat{x}_\phi \\ \hat{p}_\phi \end{pmatrix} = \begin{pmatrix} \cos(\phi) & \sin(\phi) \\ -\sin(\phi) & \cos(\phi) \end{pmatrix} \begin{pmatrix} \hat{x}_0 \\ \hat{p}_0 \end{pmatrix}, \tag{1.17}$$

and therefore that $\hat{x}_{\pi/2} = \hat{p}_0$.

The quadrature operators have associated eigenstates $\hat{x}_\phi \left|x_\phi\right\rangle = x_\phi \left|x_\phi\right\rangle$ and $\hat{p}_\phi \left|p_\phi\right\rangle = \left|p_\phi\right\rangle$. These eigenstates are orthogonal, $\left\langle x_\phi \middle| x'_\phi \right\rangle = \delta(x_\phi - x'_\phi)$, $\left\langle p_\phi \middle| p'_\phi \right\rangle = \delta(p_\phi - p'_\phi)$ and complete

$$\int_{-\infty}^{\infty} \left|x_\phi\right\rangle \left\langle x_\phi\right| = \mathbb{1}, \tag{1.18}$$

$$\int_{-\infty}^{\infty} \left|p_\phi\right\rangle \left\langle p_\phi\right| = \mathbb{1}, \tag{1.19}$$

where $\mathbb{1}$ represents the identity operator.

Since $\hat{x}_\phi$ and $\hat{p}_\phi$ are conjugate operators, $\left|x_\phi\right\rangle$ and $\left|p_\phi\right\rangle$ are related by a Fourier transformation

$$\left|p_\phi\right\rangle = 1/\sqrt{\pi} \int_{-\infty}^{\infty} e^{2\mathrm{i}p_\phi x_\phi} \left|x_\phi\right\rangle \mathrm{d}x_\phi. \tag{1.20}$$

These expressions highlight the continuous nature of these observables; unlike for photon number, a field can take any value of x_ϕ or p_ϕ. However, in contrast to classical variables, $\hat{x}_\phi$ and $\hat{p}_\phi$ are non-commuting observables, and it is therefore fundamentally impossible to simultaneously assign values to x_ϕ and p_ϕ for a field mode with arbitrary precision due to the uncertainty relation

$$\left\langle \delta x_\phi^2 \right\rangle \left\langle \delta p_\phi^2 \right\rangle \geq \frac{1}{4} \left| \langle [\hat{x}_\phi, \hat{p}_\phi] \rangle \right|^2 = \frac{1}{16}. \tag{1.21}$$

Finally, I note that quadrature eigenstates can also be expressed in the photon number basis as

$$|x_\phi\rangle = e^{-x_\phi^2} \left(\frac{2}{\pi} \right)^{1/4} \sum_{n=0}^{\infty} \frac{H_n(\sqrt{2}x)}{2^{n/2}\sqrt{n!}} e^{-\mathrm{i}n\phi} |n\rangle , \tag{1.22}$$

where $H_n(x)$ is the n-th Hermite polynomial[20].

1.3.2 Notation for multiple modes

In order to compactly manipulate expressions involving the quadratures of n modes, I will employ the vector notation $\hat{\boldsymbol{R}} = (\hat{x}_1, \hat{p}_1, \hat{x}_2, \hat{p}_2, \ldots, \hat{x}_n, \hat{p}_n)$ and $\boldsymbol{\alpha} = (x_1, p_1, x_2, p_2, \ldots, x_n, p_n)$. Note that $\hat{\boldsymbol{R}}$ is a vector of quadrature operators, while $\boldsymbol{\alpha}$ is a vector of real numbers. I further define the *covariance matrix* $\boldsymbol{\Gamma}$ for a state, with elements given by

$$\Gamma_{jk} = \frac{1}{2} \langle R_j R_k + R_k R_j \rangle - \langle R_j \rangle \langle R_k \rangle . \tag{1.23}$$

Using this notation, the Heisenberg uncertainty relation translates to an inequality on

$\mathbf{\Gamma}$[18,20]

$$\mathbf{\Gamma} + \frac{\mathrm{i}}{4}\mathbf{\Omega} \geq 0, \tag{1.24}$$

where $\mathbf{\Omega}$ is the skew symmetric matrix

$$\mathbf{\Omega} = \bigoplus^{n} \boldsymbol{\omega}, \quad \boldsymbol{\omega} = \begin{pmatrix} 0 & 1 \\ -1 & 0 \end{pmatrix}. \tag{1.25}$$

This inequality requires that the matrix sum on the left hand side has only positive eigenvalues, and expresses in a compact form the positivity of the density matrix for a system[20].

1.3.3 The Wigner function

As a complete basis, it is possible to express any wavefunction directly in terms of the eigenstates of a quadrature operator. However, a useful alternative representation is in terms of the *Wigner* function[18,20]. This is a "quasi-probability distribution" in the phase space of x and p for each mode.

The Wigner function for a single mode with density operator $\hat{\rho}$ is given by[18]

$$W[\hat{\rho}](x,p) = \frac{2}{\pi}\int \mathrm{d}y\, e^{4\,\mathrm{i}yp} \left\langle x-y\right| \hat{\rho} \left|x+y\right\rangle. \tag{1.26}$$

For completeness, I will also give the most general form of the Wigner function for n modes,

$$W[\hat{\rho}](\boldsymbol{\alpha}) = \int_{\mathbb{R}^{2n}} \frac{\mathrm{d}^{2n}\mathbf{\Lambda}}{(2\pi)^{2n}}\, e^{\mathrm{i}\mathbf{\Lambda}^T\boldsymbol{\alpha}}\, \mathrm{Tr}[\hat{\rho}\, e^{\mathrm{i}\boldsymbol{R}^T\mathbf{\Omega}\mathbf{\Lambda}}], \tag{1.27}$$

where $\hat{\boldsymbol{R}}$, $\boldsymbol{\Omega}$ and $\boldsymbol{\alpha}$ are the same as defined in Section 1.3.2.

The Wigner function is called a quasi-probability distribution because it shares many features with a classical probability distribution. Specifically, it is normalised

$$\int \mathrm{d}^{2n}\boldsymbol{\alpha}\, W[\hat{\rho}](\boldsymbol{\alpha}) = 1, \tag{1.28}$$

and gives the expected form for the quadrature marginal probability distributions

$$\int \mathrm{d}^{2n}\boldsymbol{\alpha}\, \delta(x_k - x_k')\, W[\hat{\rho}](\boldsymbol{\alpha}) = \left\langle x_k' \right| \hat{\rho} \left| x_k' \right\rangle . \tag{1.29}$$

The Wigner function also satisfies a trace rule for the expectation value of operators [4]

$$\mathrm{Tr}[\hat{\rho}\, \hat{O}] = \pi^n \int \mathrm{d}\boldsymbol{\alpha}^{2n}\, W[\hat{\rho}](\boldsymbol{\alpha})\, W[\hat{O}](\boldsymbol{\alpha}). \tag{1.30}$$

The utility of the Wigner function arises from this final property since, once the Wigner function of a state is known, it is straightforward to calculate the expectation values and variances of many observables of interest, such as the quadratures or the photon number.

An interesting aspect of the Wigner function is that, unlike a classical probability distribution, it can take negative values. Although this may initially seem unphysical, this is because the Wigner function is not a joint probability distribution, even though its marginals are proper probability distributions[20]. Example Wigner functions for one-photon and two-photon Fock states are plotted in Fig. 1.1.

---

[4] $W[\hat{O}](\boldsymbol{\alpha})$ formally exists for any operator. However, it has a particularly simple form for symmetrically ordered moments of the creation and annihilation operators, which include the quadrature operators[18,21]. This explains the particular utility of the Wigner function in continuous variables, as compared to other equivalent distributions[18,20].

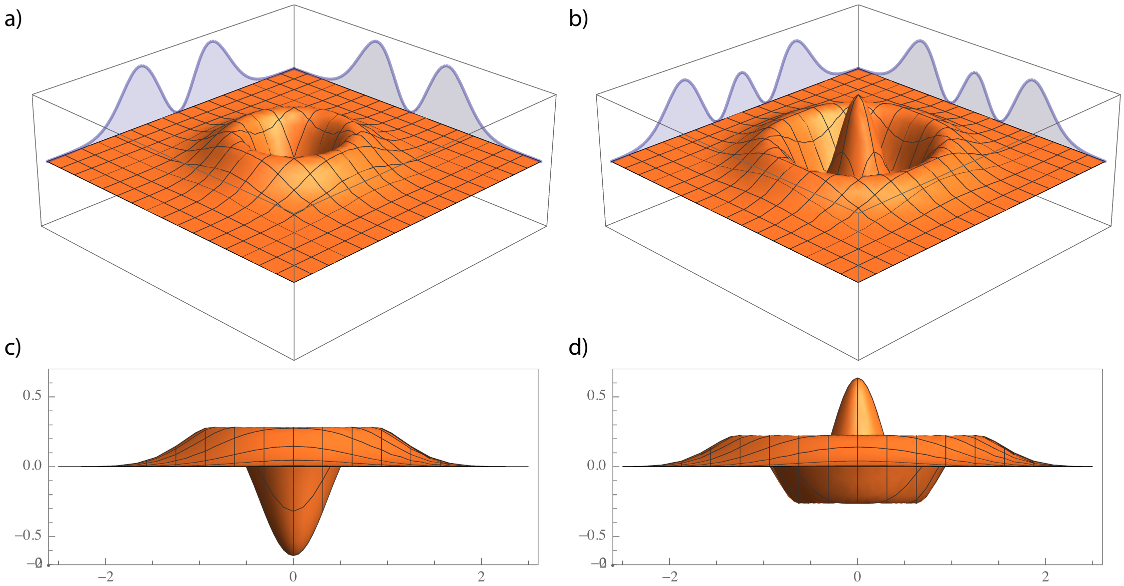

Figure 1.1: Example Wigner functions for a) a one-photon Fock state and b) a two-photon Fock state. Also plotted in blue are the marginal quadrature distributions for each state. Side views are plotted in c) and d) to highlight the occurrence of negative values of the Wigner function for these states. As an aside, it is interesting to note that the value of the Wigner function at the origin for n photon Fock states is given by $\frac{2}{\pi}(-1)^n$. This is related to the useful observation that, for single mode states, the Wigner function at the origin can be directly measured through photon-counting measurements[22].

1.3.4 Gaussian states

Gaussian states are an important class of quantum states with Gaussian Wigner functions, i.e. Wigner functions of the form

$$W[\hat{\rho}](\boldsymbol{\alpha}) = \frac{\mathrm{Exp}\left[-\frac{1}{2}(\boldsymbol{\alpha}-\bar{\boldsymbol{\alpha}})^T\boldsymbol{\Gamma}^{-1}(\boldsymbol{\alpha}-\bar{\boldsymbol{\alpha}})\right]}{(2\pi)^n\sqrt{\mathrm{Det}[\boldsymbol{\Gamma}]}}. \tag{1.31}$$

Here, $\bar{\boldsymbol{\alpha}} = \mathrm{Tr}[\rho\,\hat{\boldsymbol{R}}]$ gives the expectation value of the quadratures $\hat{\boldsymbol{R}}$ of the state, and $\boldsymbol{\Gamma}$ is the covariance matrix defined by Eqn. 1.23.

Gaussian states are therefore completely determined by the first and second moments of the quadrature operators. They are particularly important experimentally since, as will be further discussed below, they are the only states that can be generated solely by the linear-optical interaction Hamiltonian (Eqn. 1.34). Note that Gaussian states always have completely positive Wigner functions.

The vacuum state $|0\rangle$ introduced in Section 1.2 is a Gaussian state with zero first order moment $\bar{\boldsymbol{\alpha}} = (0, 0)$ and the balanced covariance matrix

$$\boldsymbol{\Gamma}_{\text{vac}} = \begin{pmatrix} \frac{1}{4} & 0 \\ 0 & \frac{1}{4} \end{pmatrix}. \tag{1.32}$$

This covariance matrix saturates the inequality in Eqn. 1.24, showing that the vacuum is a minimum uncertainty state.

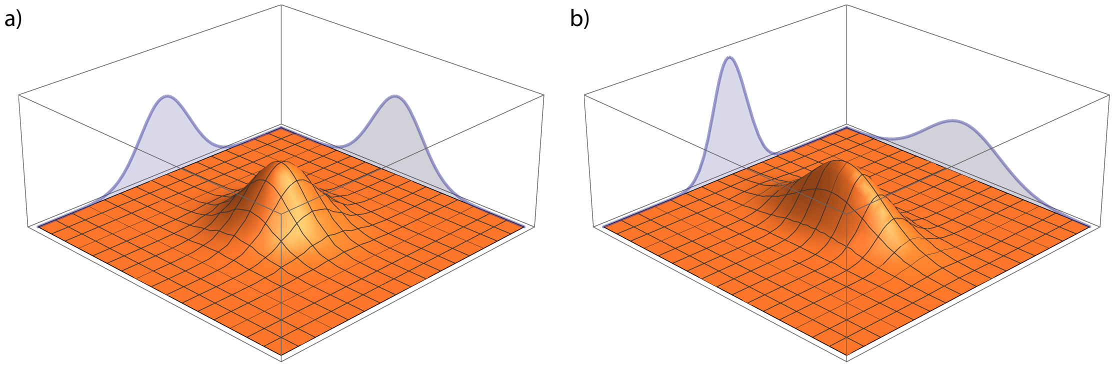

Figure 1.2: Wigner functions for a) the vacuum state and b) a representative Gaussian state with different variances in the $\hat{x}$ and $\hat{p}$ quadratures. Also plotted in blue are the marginal quadrature distributions for each state.

Coherent states

Coherent states are Gaussian states that are eigenstates of the annihilation operator, $\hat{a}\,|\alpha\rangle = \alpha\,|\alpha\rangle$, where $\alpha \in \mathcal{C}$. In the Fock state basis, coherent states are given by

$$|\alpha\rangle = e^{-|\alpha|^2/2} \sum_n \frac{\alpha^n}{\sqrt{n!}} |n\rangle \,. \tag{1.33}$$

Like the vacuum state, coherent states are minimum uncertainty states with balanced covariance matrices (as given in Eqn. 1.32). The importance of these states in quantum optics stems from the fact that many classical light sources, including lasers, are well described as coherent states, or as statistical mixtures of coherent states[23]. I will discuss these states further in Section 1.4.2, when I introduce the displacement operation.

1.4 Modal interactions

I have now introduced the two main formalisms for the state of the electromagnetic field. However, we have so far only considered the Hamiltonian for the electromagnetic field in isolation. Any physical system will also consist of matter fields that will unavoidably couple to the electromagnetic field. At its most general, this coupling can lead to extremely complex light-matter dynamics requiring the full framework of quantum electrodynamics. Fortunately, in quantum photonics we mostly work far off-resonance with any direct atomic transition. Therefore, to a good approximation, our interactions do not lead to any change in the quantum state of the medium and can be treated as effective modal interactions. By understanding these effective interactions, we can develop techniques for the controllable manipulation of quantum information encoded in the field modes.

Guided by the interactions that are experimentally accessible in a quantum-optics lab, in this thesis I will only consider bi-linear Hamiltonians of the form[20]

$$\hat{H} = \sum_{k} g_{k}^{(1)} \hat{a}_{k}^{\dagger} + \sum_{k,j} g_{kj}^{(2)} \hat{a}_{k}^{\dagger} a_{j} + \sum_{k,j} g_{kj}^{(3)} \hat{a}_{k}^{\dagger} a_{j}^{\dagger} + \text{h.c.} \tag{1.34}$$

It is helpful to consider the effects of this interaction Hamiltonian in the Heisenberg picture, in which it is the operators, as opposed to the state eigenvectors, that undergo unitary evolution. This allows us to consider the effect of each term in a more transparent input-state independent fashion. When working in the Heisenberg picture, and whenever considering the unitary evolution corresponding to a given Hamiltonian, I will set $\hbar = 1$ and will, without loss of generality, incorporate the time over which the Hamiltonian is applied into the effective interaction strength.

In the Heisenberg picture, the interaction Hamiltonian (Eqn. 1.34) can produce arbitrary Bogoliubov transformations (plus linear displacements), the most general linear transformation of creation and annihilation operators,

$$\hat{a}_k \rightarrow \sum_j A_{jk}\hat{a}_j + \sum_j B_{jk}\hat{a}_j^\dagger + w_k. \tag{1.35}$$

Directly implementing such a transformation can be experimentally challenging, since it can be a function of an arbitrary number of modes. I will therefore focus in this thesis on pair-wise modal interactions. However, I will then show in Section 1.4.3 that these pair-wise interactions are in fact sufficient to implement any Bogoliubov transformation with a number of operations that is only quadratic in the number of modes.

1.4.1 Photon-number conserving interactions

Interaction Hamiltonians with only terms of the form $\hat{H}_{\text{LO}} = \sum_{k,j} g_{kj}^{(2)}\hat{a}_k^\dagger\hat{a}_j + g_{kj}^{(2)*}\hat{a}_j^\dagger\hat{a}_k$ preserve photon number and are the easiest to generate experimentally. I will first consider cases in which $j = k$, before considering those in which $j \neq k$.

Phase shifts

Evolution under the interaction Hamiltonian

$$\hat{H}_{PS} = \phi\, \hat{a}_k^\dagger \hat{a}_k \tag{1.36}$$

$$\equiv \phi \left(\hat{x}_k^2 + \hat{p}_k^2 - \frac{1}{2} \right) \tag{1.37}$$

has the same form as free evolution under the free space Hamiltonian (Eqn. 1.3), and accordingly in the Schrödinger picture simply leads to phase evolution of the Fock states. In the Heisenberg picture, the unitary *phase shift* operator $\hat{P}(\phi) = e^{-\mathrm{i}\hat{H}_{\mathrm{PS}}}$ (also known as the *rotation* operator) induces the operator transformation

$$\hat{a}_k^\dagger \to \hat{P}^\dagger(\phi) \hat{a}_k^\dagger \hat{P}(\phi) = e^{\mathrm{i}\phi} \hat{a}_k^\dagger. \tag{1.38}$$

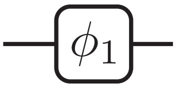

Figure 1.3: Symbol for a phase shifter

Physically, this corresponds to a modification of the optical path length for a mode, for example due to the addition of a material with a different index of refraction into the mode. The symbol for a phase shifter is shown in Fig. 1.3.

The action of the rotation operator upon the quadrature operators is trivially equivalent to a rotation of the quadrature basis such that $\hat{x}_\chi \to \hat{x}_{\chi+\phi}$ (Eqn. 1.17). An example of the effect of this rotation on a state's Wigner function is plotted in Fig. 1.4.

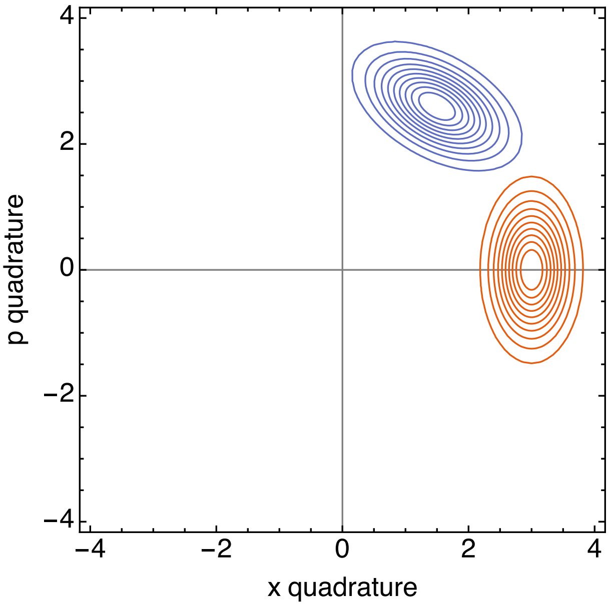

Figure 1.4: Contour plot of the Wigner functions for a Gaussian state before (red) and after (blue) a $\pi/3$ phase shift. As can be seen, a phase shifter acts to rotate a state in phase space.

Beam splitters

The interaction Hamiltonian

$$\hat{H}_{\mathrm{BS}} = \mathrm{i}\,\theta\, e^{\mathrm{i}\chi}\, \hat{a}_j^\dagger \hat{a}_k - \mathrm{i}\,\theta\, e^{-\mathrm{i}\chi}\, \hat{a}_k^\dagger \hat{a}_j \tag{1.39}$$

$$\equiv -2\,\theta\,\left((\hat{x}_j \hat{x}_k + \hat{p}_j \hat{p}_k) \sin\chi + (\hat{x}_j \hat{p}_k - \hat{x}_k \hat{p}_j) \cos\chi \right) \tag{1.40}$$

couples two electromagnetic modes. The simplest example of an element that creates this interaction is a partially reflective mirror; the incoming light can either be transmitted through the mirror, or reflected by its surface. Elements that act to couple different electromagnetic modes are often called *beam splitters*.

The evolution of the creation operators $\hat{a}_j^\dagger$ and $\hat{a}_k^\dagger$ under this transformation is

$$\begin{pmatrix} \hat{a}_j^\dagger \\ \hat{a}_k^\dagger \end{pmatrix} \to e^{\mathrm{i}\hat{H}_{\mathrm{BS}}} \begin{pmatrix} \hat{a}_j^\dagger \\ \hat{a}_k^\dagger \end{pmatrix} e^{-\mathrm{i}\hat{H}_{\mathrm{BS}}} = \begin{pmatrix} \cos\theta & e^{-\mathrm{i}\chi}\sin\theta \\ -e^{\mathrm{i}\chi}\sin\theta & \cos\theta \end{pmatrix} \begin{pmatrix} \hat{a}_j^\dagger \\ \hat{a}_k^\dagger \end{pmatrix}. \tag{1.41}$$

The typical convention in quantum optics is to set $\chi = 0$ (as other values of χ simply correspond to the addition of a relative phase shift on one mode before and after the beam splitter). This gives

$$\begin{pmatrix} \hat{a}_j^\dagger \\ \hat{a}_k^\dagger \end{pmatrix} \to \begin{pmatrix} \cos\theta & \sin\theta \\ -\sin\theta & \cos\theta \end{pmatrix} \begin{pmatrix} \hat{a}_j^\dagger \\ \hat{a}_k^\dagger \end{pmatrix}. \tag{1.42}$$

In rest of this thesis, beam splitter operations will always follow this convention, unless otherwise noted. I will denote the operator associated with this conventional interaction $\hat{U}_{\mathrm{BS}}(\theta) = e^{-\mathrm{i}\hat{H}_{\mathrm{BS}}}$. An equivalent notation is given by parameterising a beam splitter in terms of the transmissivity $\eta = \cos^2\theta$; these will be used interchangeably. The symbol for a beam splitter is shown in Fig. 1.5.

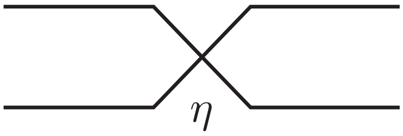

Figure 1.5: Symbol for a beam splitter

The action of this conventional BS interaction on the quadrature operators is given by

$$\begin{pmatrix} \hat{x}_j \\ \hat{p}_j \\ \hat{x}_k \\ \hat{p}_k \end{pmatrix} \rightarrow \begin{pmatrix} \cos\theta & 0 & \sin\theta & 0 \\ 0 & \cos\theta & 0 & \sin\theta \\ -\sin\theta & 0 & \cos\theta & 0 \\ 0 & -\sin\theta & 0 & \cos\theta \end{pmatrix} \begin{pmatrix} \hat{x}_j \\ \hat{p}_j \\ \hat{x}_k \\ \hat{p}_k \end{pmatrix}. \tag{1.43}$$

Homodyne measurement

Beam splitters enable the measurement of the quadrature observables using *homodyne* detection, in which a given field mode, with annihilation operator $\hat{a}_j$, is interfered at a balanced beam splitter with an intense *local oscillator* (LO) field mode with annihilation operator $\hat{a}_{\mathrm{LO}}$. This local oscillator establishes a shared reference frame (i.e. a phase reference).

For clarity, I will label the output modes of the beam splitter with indices 1 and 2. After this beam splitter, the annihilation operators for the two output modes are given by

$$\hat{a}_1 = \frac{1}{\sqrt{2}}(\hat{a}_j + \hat{a}_{\mathrm{LO}}), \tag{1.44}$$

$$\hat{a}_2 = \frac{1}{\sqrt{2}}(-\hat{a}_j + \hat{a}_{\mathrm{LO}}). \tag{1.45}$$

We assume that the local oscillator is sufficiently intense that $\hat{a}_{\mathrm{LO}}$ can be well approximated by a classical amplitude α_{LO}. Using photodiodes to measure the intensity observables $\hat{I}_i = \kappa\, \hat{a}_i^\dagger \hat{a}_i$ (where κ is a constant) therefore gives

$$\hat{I}_1 = \kappa\, (\hat{a}_j^\dagger \hat{a}_j + \alpha_{\mathrm{LO}}\, \hat{a}_j^\dagger + \alpha_{\mathrm{LO}}^*\, \hat{a}_j + |\alpha_{\mathrm{LO}}|^2)/2, \tag{1.46}$$

$$\hat{I}_2 = \kappa\, (\hat{a}_j^\dagger \hat{a}_j - \alpha_{\mathrm{LO}}\, \hat{a}_j^\dagger - \alpha_{\mathrm{LO}}^*\, \hat{a}_j + |\alpha_{\mathrm{LO}}|^2)/2. \tag{1.47}$$

The difference photocurrent is therefore

$$\Delta\hat{I} = \hat{I}_1 - \hat{I}_2 = \kappa(\alpha_{\mathrm{LO}}\,\hat{a}_j^\dagger + \alpha_{\mathrm{LO}}^*\,\hat{a}_j). \tag{1.48}$$

The complex amplitude of the LO can be expressed as $|\alpha_{\mathrm{LO}}|\,e^{i\theta}$, giving

$$\Delta\hat{I} = \kappa\,|\alpha_{\mathrm{LO}}|\,(e^{i\theta}\hat{a}_j^\dagger + e^{-i\theta}\hat{a}_j). \tag{1.49}$$

This is simply the quadrature observable scaled by the amplitude of the LO. This allows different quadratures to be measured based on the choice of θ. By systematically measuring the quadrature amplitude as a function of θ, the complete phase space distribution of the state can be determined[24].

N-mode U(N) transformations

The two optical components I have introduced so far, phase shifters and beam splitters, act on one and two modes respectively. In combination they can generate any two mode transformation from the group SU(2)[8]. This can be achieved through the sequential application of a phase shifter, followed by a beam splitter, and a second phase shifter, as shown in Fig. 1.6[25].

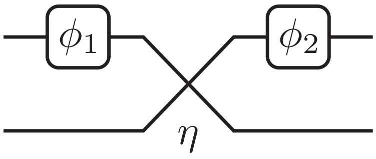

Figure 1.6: Arbitrary single qubit operations can be implemented using two phase shifters and a beam splitter.

However, it is desirable to be able to build more complex optical circuits that transform a set of input modes $\hat{a}_k^\dagger$ based on any N-mode unitary mapping $\hat{a}_k^\dagger \rightarrow \sum_j^N u_{jk}\hat{a}_j$ (i.e. any transformation from the group $\mathrm{U}(N)$). This more general device is typically called an *N-port interferometer*. Directly implementing such an $N \times N$ transformation between optical modes can be experimentally challenging[26], which might seem to limit the complexity of optical experiments. Fortunately, Reck et al.[27] showed that it is possible to decompose any N-port interferometer into a network of only $N(N-1)/2$ beam splitters and phase shifters. This decomposition underlies most approaches to generating such transformations in quantum optics experiments to date[28].

1.4.2 Non-photon-number conserving interactions

While beam splitters and phase shifters are fundamentally important optical components, with only these photon-number conserving interactions it is impossible to generate non-classical states of light.[5] Quantum-optical experiments must therefore exploit the non-photon-number conserving terms in the interaction Hamiltonian given in Eqn. 1.34.

Here I will consider the effect of each of these additional terms in turn. I will primarily focus on the effects of these terms without considering in detail their experimental implementations, while noting that they can be generated using several different methods[30]. However, I will return to this issue in Chapter 9, discussing a novel approach to generating several of these interactions using Raman quantum memories.

---

[5] The most generally accepted definition of a non-classical quantum harmonic oscillator state is that it cannot be expressed as a proper distribution of coherent states[29].

Displacements

The *displacement* Hamiltonian is given by

$$\hat{H}_{\mathrm{D}} = \mathrm{i}(\lambda\,\hat{a}_k^\dagger - \lambda^*\,\hat{a}_k) \tag{1.50}$$

$$\equiv -\Im(\lambda)\,\hat{x} + \Re(\lambda)\,\hat{p}, \tag{1.51}$$

where $\Re(\lambda)$ and $\Im(\lambda)$ represent the real and imaginary parts of λ respectively. The associated displacement operator is given by $\hat{D}(\lambda) = e^{-\mathrm{i}\hat{H}_{\mathrm{D}}}$.

In the Heisenberg picture, this Hamiltonian acts to displace the creation and annihilation operators

$$\hat{a}_k \to \hat{a}_k + \lambda, \tag{1.52}$$

$$\hat{a}_k^\dagger \to \hat{a}_k^\dagger + \lambda^*. \tag{1.53}$$

For quadrature operators, the equivalent transformation is

$$\begin{pmatrix} \hat{x}_k \\ \hat{p}_k \end{pmatrix} \to \begin{pmatrix} \hat{x}_k \\ \hat{p}_k \end{pmatrix} + \begin{pmatrix} \Re(\lambda) \\ \Im(\lambda) \end{pmatrix}. \tag{1.54}$$

The effect of the displacement operation in phase space is shown in Fig. 1.7. As can be seen, this operation only affects the first-order moments of the quadratures, displacing a state without otherwise changing its Wigner function.

Since the vacuum state is an eigenstate of $\hat{a}_k$, any displaced vacuum state will also be an eigenstate of $\hat{a}_k$. This can easily be seen using $\hat{D}^\dagger(\lambda)\hat{a}_k\hat{D}(\lambda) = \hat{a}_k + \lambda$ (equivalent to

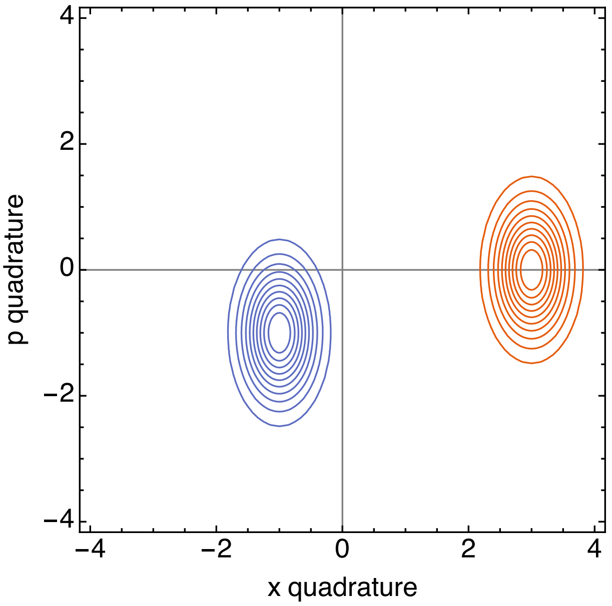

Figure 1.7: Contour plot of the Wigner functions for a Gaussian state before (red) and after (blue) a displacement operation. As can be seen, the displacement operator $\hat{D}(\lambda)$ acts to displace a state in phase space.

Eqn. 1.52),

$$\hat{a}_k \hat{D}(\lambda) |0\rangle = \hat{D}(\lambda)(\hat{a}_k + \lambda) |0\rangle \tag{1.55}$$

$$= \lambda \hat{D}(\lambda) |0\rangle . \tag{1.56}$$

As discussed in Section 1.3.4, coherent states are defined as eigenstates of the annihilation operator $\hat{a}_k$. Therefore displaced vacuum states must be coherent states, and any coherent state can be expressed as a displaced vacuum state. Eqn. 1.52 further shows that the displacement operation leaves a state's covariance matrix $\mathbf{\Gamma}$ unchanged. This shows that coherent states have the same covariance matrix as the vacuum state, and so are also minimum uncertainty states with balanced covariance matrices, as was previously asserted without proof.

A common approach to implementing displacement operations is to mix the target state on an highly unbalanced beam splitter with an ancillary coherent state. If the beam splitter is sufficiently unbalanced, to a good approximation the state is displaced in the direction of the first order moment of the coherent state[31].

Single-mode squeezing

Single-mode squeezing (SMS) of the mode k is induced by the Hamiltonian

$$\hat{H}_{\mathrm{SMS}} = \mathrm{i}\, e^{\mathrm{i}\chi}\, \frac{r}{2}\, (\hat{a}_k^\dagger)^2 - \mathrm{i}\, e^{-\mathrm{i}\chi}\, \frac{r}{2}\, (\hat{a}_k)^2 \tag{1.57}$$

$$\equiv r\cos\chi(\hat{x}_k\hat{p}_k + \hat{p}_k\hat{x}_k) - r\sin\chi(\hat{x}_k^2 - \hat{p}_k^2). \tag{1.58}$$

In the Heisenberg picture, the associated squeezing operator $\hat{S}(r,\chi) = e^{-\mathrm{i}\hat{H}_{\mathrm{SMS}}}$ leads to the transformation

$$\hat{a}_k \to \mu\, \hat{a}_k + \nu\, \hat{a}_k^\dagger, \tag{1.59}$$

where $\mu = \cosh r$ and $\nu = e^{\mathrm{i}\chi}\sinh r$.

For the quadrature operators, the transformation is given by

$$\begin{pmatrix} \hat{x}_k \\ \hat{p}_k \end{pmatrix} \to (\mu\, \mathbb{1}_2 + \boldsymbol{N}) \begin{pmatrix} \hat{x}_k \\ \hat{p}_k \end{pmatrix}, \tag{1.60}$$

where

$$\boldsymbol{N} = \begin{pmatrix} \Re(\nu) & \Im(\nu) \\ \Im(\nu) & -\Re(\nu) \end{pmatrix}. \tag{1.61}$$

If $\chi = 0$, this simplifies to

$$\begin{pmatrix} \hat{x}_k \\ \hat{p}_k \end{pmatrix} \rightarrow \begin{pmatrix} e^r & 0 \\ 0 & e^{-r} \end{pmatrix} \begin{pmatrix} \hat{x}_k \\ \hat{p}_k \end{pmatrix}. \tag{1.62}$$

In this case, it is easy to see that $\langle \delta \hat{x}_k^2 \rangle \rightarrow e^{2r} \langle \delta \hat{x}_k^2 \rangle$ and $\langle \delta \hat{p}_k^2 \rangle \rightarrow e^{-2r} \langle \delta \hat{p}_k^2 \rangle$. The single mode squeezing operator acts to *squeeze* the mode in one quadrature, reducing its variance, and *anti-squeeze* the mode in the other quadrature, increasing its variance proportionately (Fig. 1.8). This allows the variance of one quadrature to be suppressed below the coherent state uncertainty of $\langle \delta x^2 \rangle = \frac{1}{4}$ while still satisfying the Heisenberg uncertainty relation (Eqn. 1.21). This suppression of the uncertainty in one quadrature is at the root of several continuous-variable quantum technological applications, including quantum-enhanced phase estimation[32] (as will be discussed further in Chapter 5).

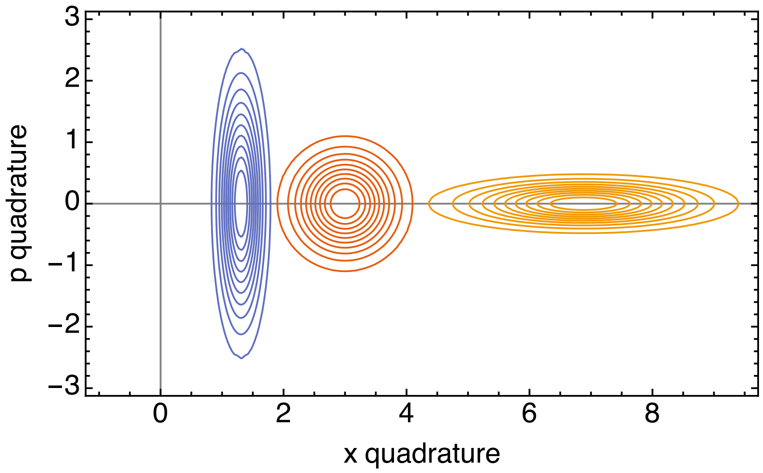

Figure 1.8: Contour plot of the Wigner functions for Gaussian states before and after single-mode squeezing. The red initial state is a minimum-uncertainty coherent state (equivalent to displaced vacuum). The blue state is squeezed in the x quadrature and anti-squeezed in the p quadrature, while the orange state is squeezed in the opposite direction. Notice that, along with modifying the covariance of a state, squeezing also correspondingly rescales the first-order moments of the state quadratures (i.e. also acts to displace states with non-zero first order moments).

In the photon number basis, single-mode squeezed vacuum (SMSV) states have the form[20]

$$|\psi\rangle = \frac{1}{\sqrt{\mu}} \sum_{N=0}^{\infty} (\frac{\nu}{2\mu})^N \frac{\sqrt{(2N)!}}{N!} |2N\rangle \tag{1.63}$$

$$= \frac{1}{\sqrt{\cosh r}} \sum_{N=0}^{\infty} e^{\mathrm{i}N\chi} \frac{\tanh^N r}{2^N} \frac{\sqrt{(2N)!}}{N!} |2N\rangle \,, \tag{1.64}$$

and have average photon number $n = \left\langle \hat{a}_k^\dagger \hat{a}_k \right\rangle = \sinh^2 r$.

As can be seen, SMSV states only consist of even photon number terms. This would be expected from the form of the interaction Hamiltonian, as it can only create and annihilate photons in pairs.

Two-mode squeezing

Two-mode squeezing (TMS) operations are associated with the interaction Hamiltonian

$$\hat{H}_{\mathrm{TMS}} = \mathrm{i}e^{\mathrm{i}\chi} r \hat{a}_j^\dagger \hat{a}_k^\dagger - \mathrm{i}e^{-\mathrm{i}\chi} r \hat{a}_j \hat{a}_k \tag{1.65}$$

$$\equiv 2r\cos\chi(\hat{x}_j\hat{p}_k + \hat{p}_j\hat{x}_k) - 2r\sin\chi(\hat{x}_j\hat{x}_k - \hat{p}_j\hat{p}_k). \tag{1.66}$$

In the Heisenberg picture, this operation induces the mode transformation

$$\begin{pmatrix} \hat{a}_j \\ \hat{a}_k \end{pmatrix} \to \begin{pmatrix} \mu & 0 \\ 0 & \mu \end{pmatrix} \begin{pmatrix} \hat{a}_j \\ \hat{a}_k \end{pmatrix} + \begin{pmatrix} 0 & \nu \\ \nu & 0 \end{pmatrix} \begin{pmatrix} \hat{a}_j^\dagger \\ \hat{a}_k^\dagger \end{pmatrix}. \tag{1.67}$$

Again, this can be re-expressed in terms of quadrature operators

$$\begin{pmatrix} \hat{x}_j \\ \hat{p}_j \\ \hat{x}_k \\ \hat{p}_k \end{pmatrix} \to \begin{pmatrix} \mu\,\mathbb{1}_2 & \boldsymbol{N} \\ \boldsymbol{N} & \mu\,\mathbb{1}_2 \end{pmatrix} \begin{pmatrix} \hat{x}_j \\ \hat{p}_j \\ \hat{x}_k \\ \hat{p}_k \end{pmatrix}, \tag{1.68}$$

where μ and $\boldsymbol{N}$ are as defined in Section 1.4.2.

If we again set $\chi = 0$, it is possible to gain an insight into how two-mode squeezing affects the quadratures. By calculating the difference between the quadrature operators for the two modes, we find that $(\hat{x}_j - \hat{x}_k) \to e^{-r}(\hat{x}_j - \hat{x}_k)$, and also that $(\hat{p}_j - \hat{p}_k) \to e^{r}(\hat{p}_j - \hat{p}_k)$. It is easily shown that $\langle \delta(\hat{x}_j - \hat{x}_k)^2 \rangle \to e^{-2r} \langle \delta(\hat{x}_j - \hat{x}_k)^2 \rangle$ and $\langle \delta(\hat{p}_j - \hat{p}_k)^2 \rangle \to e^{-2r} \langle \delta(\hat{p}_j - \hat{p}_k)^2 \rangle$. The quadratures of the two modes therefore become correlated under two-mode squeezing.

An experimentally important state is the two-mode squeezed vacuum (TMSV) state. In the photon number basis, TMSV is given by[20]

$$|\psi\rangle = \frac{1}{\sqrt{\mu}} \sum_{N=0}^{\infty} (\frac{\nu}{\mu})^N |N, N\rangle \tag{1.69}$$

$$= \frac{1}{\sqrt{\cosh r}} \sum_{N=0}^{\infty} e^{\mathrm{i}N\chi} \tanh r^N |N, N\rangle, \tag{1.70}$$

and has average photon number $n = \left\langle \hat{a}_j^\dagger \hat{a}_j + \hat{a}_k^\dagger \hat{a}_k \right\rangle = 2\sinh^2 r$. Two-mode squeezed vacuum states are closely related to single-mode squeezed vacuum states. In fact, it can be shown that mixing the two modes of a TMSV state on a balanced beam splitter gives two uncorrelated, equally squeezed SMSV states at its output[20].

As can be seen from Eqn. 1.70, the two modes are exactly correlated in the photon number basis. Therefore, by measuring the number of photons in one mode, it is possible to exactly determine (in the lossless case) the number of photons in the other mode without disturbing it. This correlation underlies the workhorse sources of single photons in quantum-optics labs, so-called spontaneous-parametric downconversion (SPDC) sources, in which the detection of a single photon in one mode is used to herald the existence of a single photon in the other mode.

Two-mode squeezed vacuum states are also highly entangled in the quadrature basis, with a Wigner function given by[33]

$$W_{\mathrm{TMSV}} = \frac{4}{\pi^2} \exp\left\{-e^{-2r}\left[(x_j + x_k)^2 + (p_j - p_k)^2\right] - e^{2r}\left[(x_j - x_k)^2 + (p_j + p_k)^2\right]\right\}. \tag{1.71}$$

In the limit of $r \to \infty$, the quadratures of the two states become perfectly correlated, giving the maximally entangled EPR state[33,34]. This state has infinite energy and is therefore unphysical, however TMSV states with finite squeezing represent a valuable source of entanglement for many continuous-variable protocols[18], including quantum-enhanced metrology. I will discuss two applications of two-mode squeezed vacuum states for quantum-enhanced phase estimation in detail in Chapter 5.

Both single-mode and two-mode squeezing interactions are commonly induced by using a suitable nonlinear material and a strong ancillary electromagnetic field, for example in an optical-parametric oscillator[30]. As I will consider further in Chapter 9, interactions in these materials are typically governed by Hamiltonians of the form

$$\hat{H} = K\, \hat{a}_i^\dagger\, \hat{a}_j^\dagger\, \hat{a}_k + K^*\, \hat{a}_k^\dagger\, \hat{a}_i\, \hat{a}_j, \tag{1.72}$$

where i,j and k label three different optical modes, and K is a material dependent parameter. If we take the strong field limit of mode k, again replacing $\hat{a}_k$ with the complex amplitude α_k, this is approximately

$$\hat{H} \approx K\alpha_k \, \hat{a}_i^\dagger \, \hat{a}_j^\dagger + K^* \alpha_k^* \, \hat{a}_i \, \hat{a}_j, \tag{1.73}$$

which is the two-mode squeezing Hamiltonian we desire. If modes j and k are instead the same mode, this then corresponds to the single-mode squeezing Hamiltonian.

As a final practical note on squeezed states, I note that in experiments levels of squeezing are often reported in the form t dB (decibels) as opposed to the interaction strength r. Both quantities are best understood in terms of the reduction achieved in the variance of the squeezed quadrature (with the other quadrature made correspondingly noisier). As I have discussed, for SMSV states, the variance after squeezing is given by $\left\langle \delta\hat{p}_k^2 \right\rangle \rightarrow e^{-2r} \left\langle \delta\hat{p}_k^2 \right\rangle$, while for TMSV states, it is the difference between the quadratures of the two modes that is squeezed, such that $\left\langle \delta(\hat{p}_j - \hat{p}_k)^2 \right\rangle \rightarrow e^{-2r} \left\langle \delta(\hat{p}_j - \hat{p}_k)^2 \right\rangle$. For both SMSV and TMSV the fractional reduction is given by e^{-2r}. Expressed in decibels, the equivalent reduction for t dB of squeezing is $10^{-t/10}$. These two quantities are therefore connected by the formula

$$r = \log_e(10)/20 \, t \tag{1.74}$$

$$r \approx 0.115 \, t. \tag{1.75}$$

1.4.3 Arbitrary Bogoliubov transformations

In this Chapter, I have only considered pair-wise Gaussian interactions. However, in general we would like to be able to implement any arbitrary Bogoliubov transformation of the form (reproduced from the start of this section)

$$\hat{a}_k \to \sum_j A_{jk}\hat{a}_j + \sum_j B_{jk}\hat{a}_j^\dagger. \tag{1.76}$$

Braunstein observed[35] that the matrices A and B can be decomposed via the Bloch-Messiah reduction into

$$A = UA_DV^\dagger, \qquad B = UB_DV^T, \tag{1.77}$$

where U and V are unitary matrices and A_D and B_D are a pair of non-negative diagonal matrices such that $A_D^2 - B_D^2 = \mathbb{1}$, with $\mathbb{1}$ the identity matrix.

The corollary of this observation is that any such Bogoliubov transformation can be implemented with the combination of: a linear $\mathrm{U}(N)$ transformation, followed by a set of parallel single-mode squeezing operations in each mode, and finally another linear $\mathrm{U}(N)$ transformation. As I discussed in Section 1.4.1, these $\mathrm{U}(N)$ transformations can be efficiently decomposed into beam splitter operations and phase shifting operations, requiring only $N(N-1)/2$ beam splitter and phase shifter elements each. It therefore immediately follows that any Bogoliubov transformation can be implemented using $N(N-1)$ beam splitters and phase shifters, along with N single-mode squeezing operations.

Part I

Developing experimental tools

Chapter 2

Strain-optic active control for quantum integrated photonics

Most quantum optics experiments are composed of a combination of non-classical light sources, modal interactions, and measurements of the resulting fields. The construction of higher-complexity quantum optics experiments therefore rests on the further development of these three technologies. In this part of the thesis I will discuss two separate projects that I have been involved in to further the state-of-the-art in these areas. In this chapter I will introduce a novel method for active control of quantum circuits based on the strain-optic effect. Then, in the following chapter, I will discuss our efforts to set up a new laboratory to run cryogenic single-photon-sensitive detectors. This will include recent work on detector tomography of photon-number-resolving detectors.

2.1 Integrated photonics

Historically, quantum optical experiments have used bulk optical components to couple different spatial and polarisation modes. This approach was favoured as these optical components are comparatively low loss, and can be re-used in many different experiments. However, as these experiments have become more complex, this approach has become less feasible. Bulk optics must be carefully manually aligned and are prone to drifting over time, leading to imperfect modal overlap between modes (i.e. coupling to other unwanted modes). Additionally, bulk optical interferometers must be actively phase stabilised, typically using a reference laser and control electronics. As each two mode interferometer making up an N-mode unitary must be individually stabilised, this quickly becomes challenging experimentally.

Integrated optical waveguide circuits present a promising alternative to bulk quantum optics[12,36–39]. Waveguides within a bulk substrate can be engineered to support only a single spatial-mode[36,40] and are intrinsically phase stable, ensuring high fidelity quantum interference. They require no alignment, and are much more compact than their bulk equivalents, with optical components on the millimetre scale.

Our group has been heavily involved in furthering the state-of-the-art in integrated quantum optical devices. This has been pursued in collaboration with our fabrication partners at the University of Southampton and the Engineering Department at the University of Oxford, with a focus on silica-based integrated waveguide circuits. For quantum optical applications, two crucial requirements are total device efficiency and, for proof-of-concept work in particular, ease of fabrication. These issues have put silica-based devices at the forefront of integrated QIP experiments. Silica photonic chips provide low propagation losses, efficient coupling to silica fibre - providing a robust and convenient ultra-low loss delay line, and fabrication by direct laser writing[41].

Silica waveguides have been used as quantum light sources[42,43], quantum channels connecting remote nodes[44] and integrated optical circuits as a means to generate the interference needed for computational protocols[12,45]. Using a silica waveguide chip, we recently demonstrated both the first three-photon quantum interference[28], and the first quantum teleportation on an integrated device[39]. We are currently working with our partners to extend this technology to larger numbers of modes and more complex circuits.

The primary drawbacks of silica as a quantum optics platform are its comparative lack of optical non-linearity as compared to materials such as lithium niobate[46] or potassium titanyl phosphate (KTP)[47], and the low refractive index contrast achievable between the waveguide core and the surrounding bulk material. This low refractive index contrast limits the minimum bend radius of waveguides, and therefore constrains the minimum feature sizes to around the millimeter level[48]. Silicon waveguides can achieve much smaller feature sizes, but suffer from poor mode matching to fibre[49], unavoidable two-photon loss processes[50] and typically require less flexible lithographic fabrication techniques.

2.2 Strain-optic phase control

An outstanding technical requirement for integrated optical quantum information processing is low-loss, rapid active control of spatial and polarisation modes. Such active control is necessary for a host of essential applications including multiplexing heralded light sources[51–53], feed-forward control for linear-optical quantum computing[8] and quantum communication[44]. Fast spatial and polarisation control with quantum light has been shown using the electro-optic effect in lithium niobate[54]. Unfortunately, relatively inefficient coupling to silica fibres[55,56] and the complexity of fabrication processes currently present roadblocks to near-term quantum application. For standard silica devices the electro-optic effect is non-existent, and instead, experiments to date have relied on thermo-optic control[57]. This approach, however, offers no polarisation sensitivity, is inherently slow (on the ms timescale), and is fundamentally incompatible with cryogenic detectors due to the associated heat load. It is also incompatible with typical femtosecond-laser written devices[41] as typical substrates are too thick, leaving these devices with no mechanism for active control. Another approach recently demonstrated in silicon nitride uses nano-electromechanical structures[58] to achieve sub-μs switching speeds. However, this requires relatively sophisticated fabrication and has not been implemented in silica.

In this chapter I will introduce a technique for the active reconfiguration of quantum photonic circuits using the strain-optic effect. In this approach, a stress is applied to the region in which light propagates, creating a local change in the refractive index and an corresponding phase shift for the guided waves. This effect has previously been employed to create polarisation independent phase shifters on silica-on-silicon telecommunications devices[59]. We have extended this idea, capitalising on the fact that strain generally causes anisotropic changes in refractive index, and thus results in birefringence aligned to the strain field[60]. The prototype unit uses a millimetre-scale actuator to achieve a polarisation-sensitive effect that may be readily applied to common platforms, including direct laser-written waveguides in silica. Operation is shown on the microsecond timescale, sufficient to implement feed-forward control entirely within silica guided-wave devices. Our switching method introduces no excess loss beyond the propagation loss associated with the silica substrate, allowing the realisation of low-loss polarisation switches. This approach is a promising near-term route to achieving scalable reconfigurable quantum information processing channels, based on a combination of polarisation, spatial and temporal encoding[61].

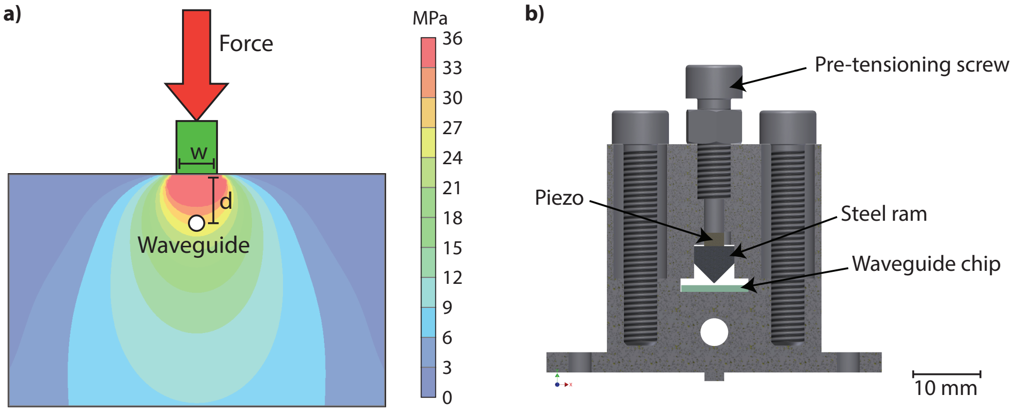

Figure 2.1: a) Schematic of the strain-optic phase shifter. A force (red arrow) applied to a steel ram (green box) by a charged piezoelectric element modifies the stress (theoretical contours shown) at the location of a waveguide (white circle). b) Cross-section through the prototype stressing rig. A piezo-electric element applies force to a steel ram positioned over a waveguide. A pre-tensioning screw is used to place the piezo under initial tension.

The device, illustrated in Fig. 2.1, is described by a simple model using the well-known photo-elastic effect. An external pressure is applied over a region of the chip's surface, resulting in an elastic stress, and corresponding strain, throughout the chip. At the location of a buried waveguide, the change in the refractive index n along direction i, where $i \in \{x, y, z\}$, is given by $\delta n_i = \sum_j -\frac{1}{2} n^3 \rho_{ij} \sigma_j / E$, where E is the Young's modulus, σ_j is the stress along direction j, and ρ is the (polarisation dependent) strain-optic coefficient tensor. By assuming that the ram is centred over the waveguide, and that the stress is therefore vertically aligned (direction z), this can be simplified to $\delta n_i = -\frac{1}{2} n^3 \rho_{iz} \sigma_z / E$. The result is a change in the propagation constant of a guided mode compared to an unstrained guide. For silica, $\rho_{xz} = \rho_{yz} = 0.12$ and $\rho_{zz} = 0.26$[62]; it is this difference that creates a birefringent effect.

The stress required to induce a given phase shift θ is a function of the length l of the stressed region, and is approximated by

$$\sigma_z = \frac{E\theta\lambda}{\pi l n^3 \rho_{iz}}. \tag{2.1}$$

For example, in order to induce a phase shift of 2π for vertically polarised 830 nm light in a silica waveguide with a stressed region of length 1 mm, a change in refractive index of $\delta n = 8.3 \times 10^{-5}$ must be induced (much smaller than the waveguide index contrast of $\delta n \approx 5 \times 10^{-3}$). This corresponds to a stress of 14 MPa, roughly two orders of magnitude less than the compressive strength of silica.

Strain-optic phase shifting was demonstrated using direct-written waveguides in a fused-silica photonic chip (Lithosil Q1). These waveguides were fabricated using a regeneratively amplified Ti:Sapphire source delivering 100 fs pulses at a repetition rate of 1 kHz. The beam was focused with a 0.5 NA, 20× objective, and the fused silica substrate translated through the focus at 25 μm/s perpendicular to the optic axis. Slit beam shaping was applied to control the structural cross-section of the waveguide[40]. The fabricated waveguides displayed typical values for propagation loss <0.5 dB/cm, coupling loss to single mode fibre <0.5 dB and birefringence $<2\times10^{-5}$[63].

An external pressure is generated by pressing a steel ram with a contact surface 1 mm long by 0.1 mm wide onto the surface of the silica above a waveguide. The force on the ram is generated either by turning a screw in contact with its upper surface or by charging a piezoelectric element positioned between the screw and ram. A force of only 20 N is needed to create a stress of 14 MPa under the ram; this is readily generated by a 3x3x2 mm piezoelectric element (Physik Instrumente PICMA Chip Actuator). As shown in Fig. 2.1, the stress at the location of a waveguide depends on its depth. Unless specified otherwise, experiments were carried out on waveguides located 100 μm from the silica surface, resulting in a stress approximately 80% of that immediately under the ram.

2.2.1 Classical operation

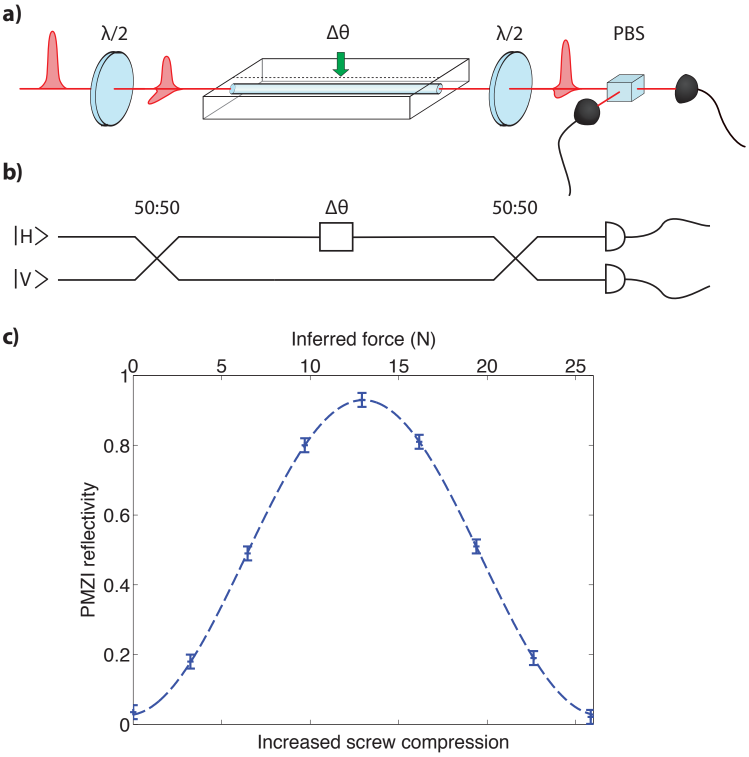

Figure 2.2: a) Schematic of the polarisation Mach-Zehnder interferometer built using the strain-optic device sandwiched by two half-wave plates. Applying stress to the waveguide induces a birefringence, leading to a relative phase shift between two polarisation components in the guide. b) Equivalent mode representation where each polarisation is depicted as a spatial mode. c) The normalised intensity of one polarisation output from the PMZI as a function of increased screw compression. The inferred force was estimated from the birefringence that would be required to produce the measured change in PMZI reflectivity. Sinusoidal modulation is observed, with a fringe visibility of 97 ± 3%.

To construct a polarisation switch, we embedded the manipulated waveguide between static waveplates, used to rotate the polarisation axes of the light by $\pi/4$. This was achieved with waveplates external to the chip, but these elements may alternatively be built directly in guiding structures using static stresses[64–66]. The two waveplates create a polarisation Mach-Zehnder interferometer (PMZI), as shown in Fig. 2.2a & b. A strain-induced modification to the waveguide, such that a phase shift of π radians is created in one polarisation relative to the other, will switch the polarisation of the modes at the output of the PMZI. The relative birefringent phase shift, and therefore the change in the PMZI output intensity I induced by a stress σ_z, can be determined from

$$I = \cos^2(\Delta\theta/2), \text{ where } \Delta\theta = \pi n^3(\rho_{zz} - \rho_{xz})\,\sigma_z l/(E\lambda). \tag{2.2}$$

Control of the polarisation of classical light with a PMZI is shown in Fig. 2.2c. The power at the output ports was recorded at certain screw positions as the screw compression was increased by hand. The interference visibility was determined by manually positioning the screw to maximise and minimise the reflectivities. A visibility of $97 \pm 3\%$ was recorded, with the deviation from unit visibility likely primarily resulting from leakage through the chip in non-guided modes and scatter from the guided mode into non-guided modes.

While absolute calibration of the reflectivity determined by a given screw position is not feasible due to trial-to-trial variation in mechanical alignment, the estimated force on the ram shown was calculated from the observed reflectivity and Eqn. 2.2. With the piezoelectric element added between the screw and ram, as described above, 60 V corresponded to a π phase shift, and arbitrary reflectivities were reproducible within 1%. With both drive methods, reflectivity drifts of maximally 10% occur over a few hours of constant application. It is suspected that this can be rectified through improvements to the mechanical rigidity

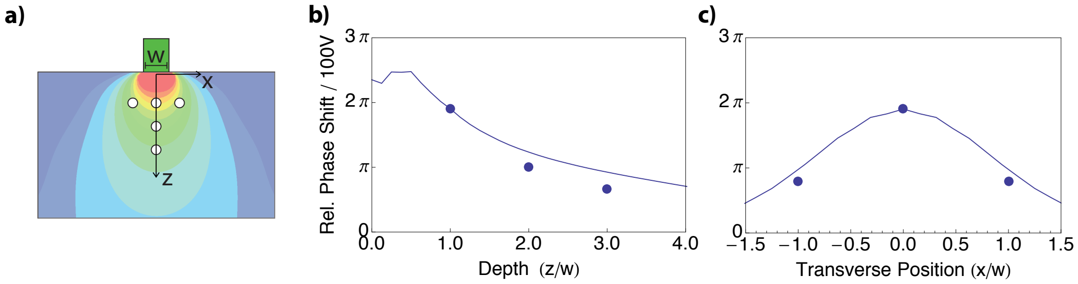

Figure 2.3: a) An array of waveguides (white) was used to map out the relative phase shift induced between vertical and horizontal polarisations in the region of the stressor. Shown are relative phase shifts as a function of b) depth and c) transverse position, in units of the ram width $w = 100\mu m$. The transverse measurements are from waveguides at depth w. The solid line shows data from a finite-element calculation, scaled to match the data point at depth w and zero transverse position.

in the mounting of the piezoelectric above the waveguide. Further development will be required to optimise the overall reliability and lifetime of active devices based on the strain-optic effect. Commercially available thermo-optic and electro-optic switching devices can have lifetimes measured in the billions of switching operations [67,68]. This level of reliability is not required for initial quantum optics experiments, however, it is the level that would be needed for strain-optic devices to become a commercially appealing technology.

The profile and extent of the stress field (Fig. 2.1) determines the effect of a strain-optic controller on neighbouring waveguides, an important issue for multi-path integrated architectures. To test the theoretical model, we measured the induced relative phase shift for an array of guides written at different depths and horizontal positions relative to the stressing element, as illustrated in Fig. 2.3a. The resulting relative phase shifts are shown in Fig. 2.3b and Fig. 2.3c. As can be seen, the strain field transverse decay length (to 10% of its initial value) is $2\,w$, where w is the ram width, suggesting that the effect can be readily localised.

2.2.2 Non-classical Hong-Ou-Mandel interference

Importantly, for our stressor design the refractive index contrast $\delta n \ll n$, so there is no scattering due to the induced strain. Therefore the overall transmission of the device is unaffected by including the switching element. This is borne out by our experiments, in which a variation in transmission of less than 1% is seen. This low loss makes the strain-optic control method particularly well suited to quantum applications. We demonstrated this by inputting heralded single photons from two spontaneous parametric down-conversion (SPDC) sources (introduced in Section 1.4.2) to the PMZI, with one photon in each polarisation. At a fixed stress level, scanning the temporal delay between the photons produced a non-classical Hong-Ou-Mandel (HOM) interference dip[69] in the photon detection coincidences, as shown in Fig. 2.4a. I will discuss this effect further in Section 7.2.2, however, in this context I simply note that HOM interference is a quantum interference effect that manifests itself in the correlations between the light in the output modes of a beam splitter when individual single photons are coupled into the two input modes. For a balanced beam splitter, and indistinguishable single photon inputs, the two photons are always found in the same output mode.

Setting the temporal delay between the photons to zero maximises the photon indistinguishability and therefore the HOM interference. At this setting, applying stress modulates the visibility of the HOM interference with a period half that of the classical fringes (Fig. 2.4b). The maximum recorded HOM dip visibility is 0.90 ± 0.04; the deviation from unity results from residual distinguishability between the two single photons. A visibility of greater than 0.5 for HOMI dips in which the single photon rate is unaffected by delay (as in this case) is an indication of non-classical interference[70].

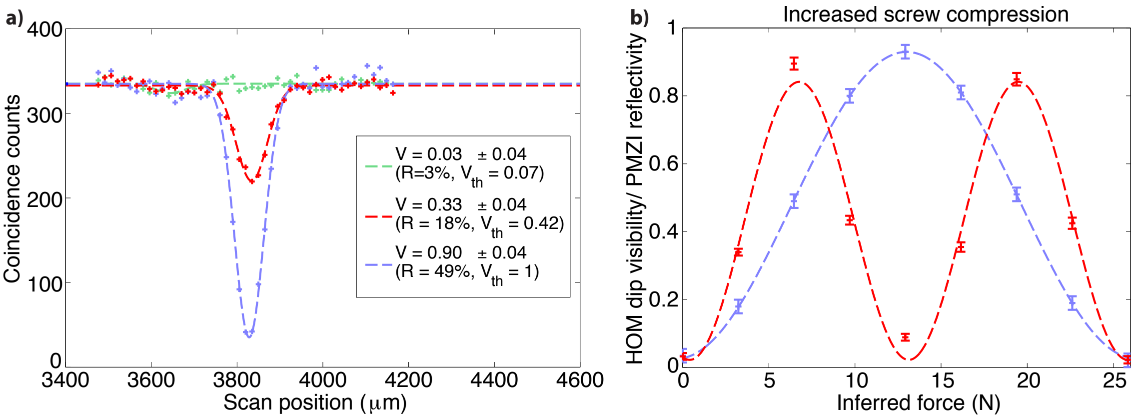

Figure 2.4: a) Quantum Hong-Ou-Mandel interference as a function of the relative temporal delay between two single photons input to the PMZI. Three dips are shown for different PMZI reflectivities R. Also given are the theoretical dip visibilities V_{th} assuming perfect quantum interference. b) A modulation in the interference visibility (red) is seen as a function of the screw compression. For reference the classical interference (Fig. 2.2) is also shown (blue).

2.2.3 Switching time

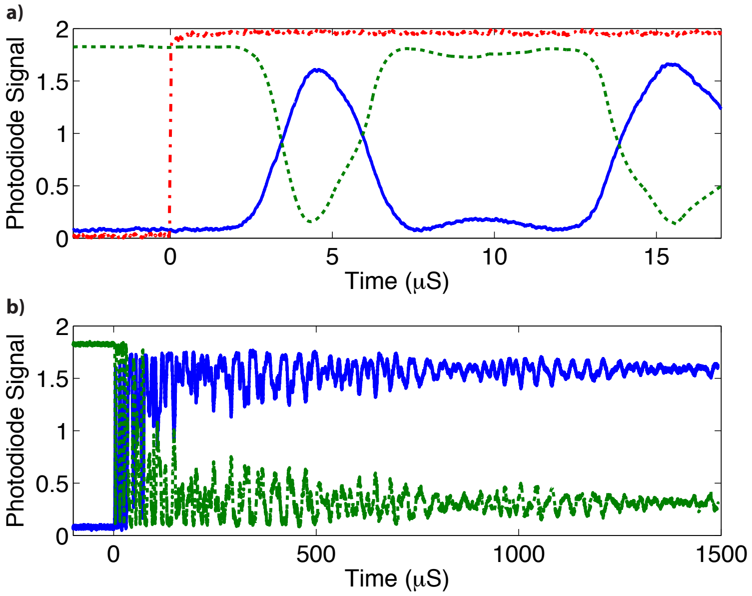

Figure 2.5: Demonstration of the switching time. A control signal (red dot-dashed line) initiates the switch operation, leading to the discharge of a piezoelectric actuator. The transmission of each polarisation component (blue solid line and green dashed line) through the PMZI shows a) a rise time of 1.7 μs (with subsequent mechanical ringing) and b) a reset time of 1.5 ms due to this ringing.

To investigate switching time, we applied a current pulse to the piezoelectric actuator clamped above the ram. A single field-effect-transistor switch was gated by a low-voltage square wave from a waveform generator to apply up to 70 V across the actuator. An example of the PMZI output response is shown in Fig. 2.5. The switch response comprises a trigger-to-switch delay time of 2 μs and rise time (10% to 90%) of 1.7 μs. The observed switch time is limited by the fundamental resonance of the coupled piezoelectric-silica system, due to undesired mechanical oscillations. In this simple configuration, the reset time for the switch was approximately 1 ms because of the reflection of the acoustic wave induced by the pulsed strain at the chip surface. This can be mitigated by appropriate impedance matching into a damping material, such as aluminium[71]. The practical consequence of a non-negligible reset time is a reduction in the repetition rate for a quantum optics experiment or the effective clock rate of an optical information processor.

Even with our un-optimised design, the observed switch time is sufficient for immediate use in proof-of-concept quantum information applications involving feed-forward control. A few-microsecond optical delay can be achieved with a sub-km fibre path, which introduces less than 0.2 dB loss (in addition to the pre-existing <0.5 dB coupling loss). The ultimate limit to the switch rise time is determined by the velocity of sound, v, in the material. A simple estimate is given by the time taken for a strain wave to propagate across the guided mode; for $v = 3000$ m/s and a mode diameter of 10 μm, this is 5 ns. This limit could in principle be achieved with an impulse ram that strikes the chip surface, which is not the case for our setup, in which the ram and chip begin in contact.

2.3 Conclusions

In conclusion, we have demonstrated a method for polarisation-dependent active phase control in silica waveguide photonic chips based on the strain-optic effect. This approach is inherently low-loss, making it ideally suited to the stringent requirements of quantum optical applications. This was shown by using stain-optic switching to control the on-chip quantum interference of two single photons. Further, we demonstrated that the technique allows rapid switching, which opens the door to new applications in feed-forward optical quantum control.

Chapter 3

Transition-edge sensors

3.1 Single-photon sensitive detectors

Single-photon sensitive detectors are fundamentally important components of almost all discrete-variable experiments, required for optical quantum information tasks ranging from the heralding of photons from SPDC sources (Section 1.4.2) and other non-Gaussian state creation protocols[72] to implementing the measurements required at every stage of many optical quantum computing schemes[8].

For all of these applications, the system detection efficiency of the detectors is a critical parameter. As the number of photons that need to be detected in a given protocol increases, the likelihood of successfully detecting all of the photons is an exponentially decreasing function of this quantum efficiency. Therefore small improvements in efficiency can have a significant impact on experimental success rates.

Historically, high-quantum efficiency detectors have not been available for the telecommunications band around 1500 nm, at which losses in integrated silica devices are at their lowest. This has forced quantum-optics experiments to be carried out in the 800 nm near-IR region, which has significantly higher associated losses. However, recently transition edge sensor (TES) superconducting detectors have become available with unparalleled quantum efficiencies of up to 98% [10,73], telecommunications wavelength compatibility and true photon number sensitivity [73].

This step change in performance over traditional avalanche photodiode detectors [74] will enable new regimes of complexity to be attained in quantum optical experiments. However, this improvement comes at a cost; these detectors must run at cryogenic temperatures, typically requiring a dilution refrigerator to cool them to tens of mK. During my PhD, I have been involved in setting up these TES detectors in collaboration with Sae Woo Nam's group at NIST Boulder [73]. This involved commissioning an Oxford Instruments Kelvinox dilution refrigerator, installing experimental wiring, and developing software to interface with the detectors. Now that these detectors have been successfully brought online, it is anticipated that this will enable higher photon number quantum optics experiments, along with experiments that rely on the intrinsic photon number sensitivity of TES detectors [75–77]. In particular, these detectors should allow us to demonstrate a truly quantum enhanced phase measurement in the near future, as will be discussed further in Chapter 5.

However, in order to be able to employ these detectors in experiments, it is first necessary to be able to characterise their operation. Unlike other commonly used approaches to pseudo-number-resolution based on linear-optical circuits and 'click' detectors (such as time-multiplexed detectors [78]), the output of a TES detector is a time-dependent voltage, with a non-linear dependence on the photon number. This signal must be deciphered with minimal reliance on the inner workings of the detector. Efficiently extracting information from a photon number resolving detector is therefore a problem of significant interest and challenge to the community[79–81]. In this chapter I will discuss a novel approach to detector characterisation that we have developed for TES detectors. The methods developed should also be widely applicable to other detectors with continuous outputs.

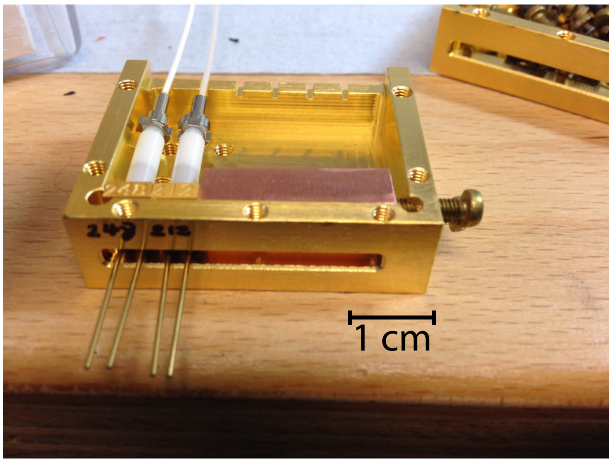

Figure 3.1: Transition edge sensor detectors mounted for installation in a dilution fridge.

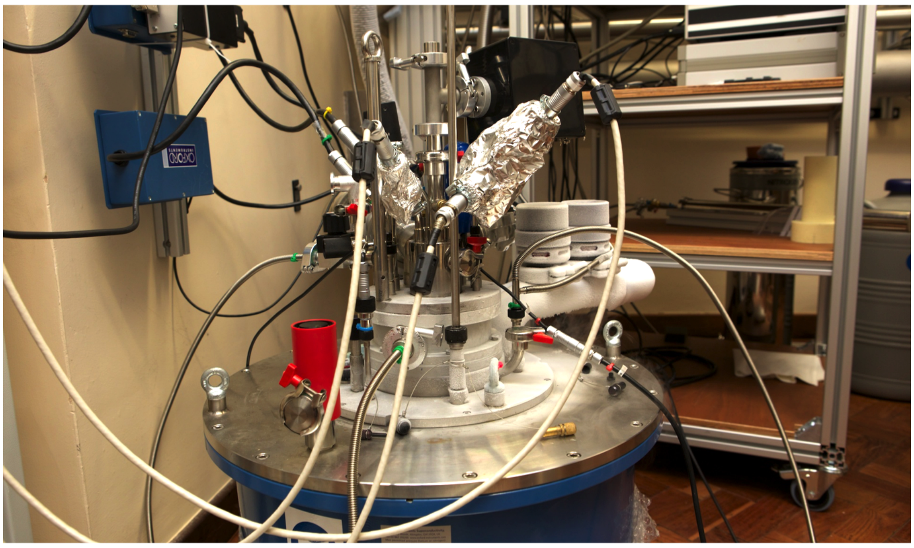

Figure 3.2: Oxford instruments Kelvinox dilution refrigerator, fully wired up to run TES detectors.

3.2 Tomography of photon-number resolving continuous-output detectors

The signal produced by a continuous-output detector is typically a time-dependent voltage with some dependence on photon number which may in general be nonlinear, as shown in Fig. 3.3a. A set of such output signals $\mathbf{V} = \{v_i(t)\}$, arising from a set of input states of the incident light beam, can be represented using a set of basis functions $\{w_j(t)\}$, such that

$$v_i(t) = \sum_j^n s_{ij} w_j(t). \tag{3.1}$$

where s_{ij} represent the weighting components for each signal $v_i(t)$. These s_{ij} are each drawn from their respective associated sample spaces S_j. In general, this implies that, in order to capture the full output of the detector, it is necessary to determine the weighting components s_{ij} for all of the n basis functions for each signal to be measured. For a truly continuous signal, n is in principle infinite, but of course for any real experiment the upper limit to n is set by the sampling record length of the detector. This is set by the ratio of the sampling time window to the temporal resolution of the electronics. However, this finite signal still spans a space of high dimension; in our work a single trace from a TES detector consists of 1024 16-bit numbers. Directly analysing this signal is therefore impractical. This is particularly the case for detector tomography, which is necessary to rigorously characterise the relationship between input states and output signals[82,83]. Detector tomography requires a sufficiently small space of outputs that the probability of a given outcome can be estimated precisely from the measured data. For the full output space of our detector signal, I estimate the probability of the same trace occurring twice (to within the resolution of the analogue-todigital converter) in a data set of 10^5 traces, the maximum that can be recorded in one second, to be on the order of 10^{-4}. This renders tomography in this full space infeasible. This motivates the development of an approach to the characterization of continous-output detectors that enables accurate and precise signal analysis and detector tomography.

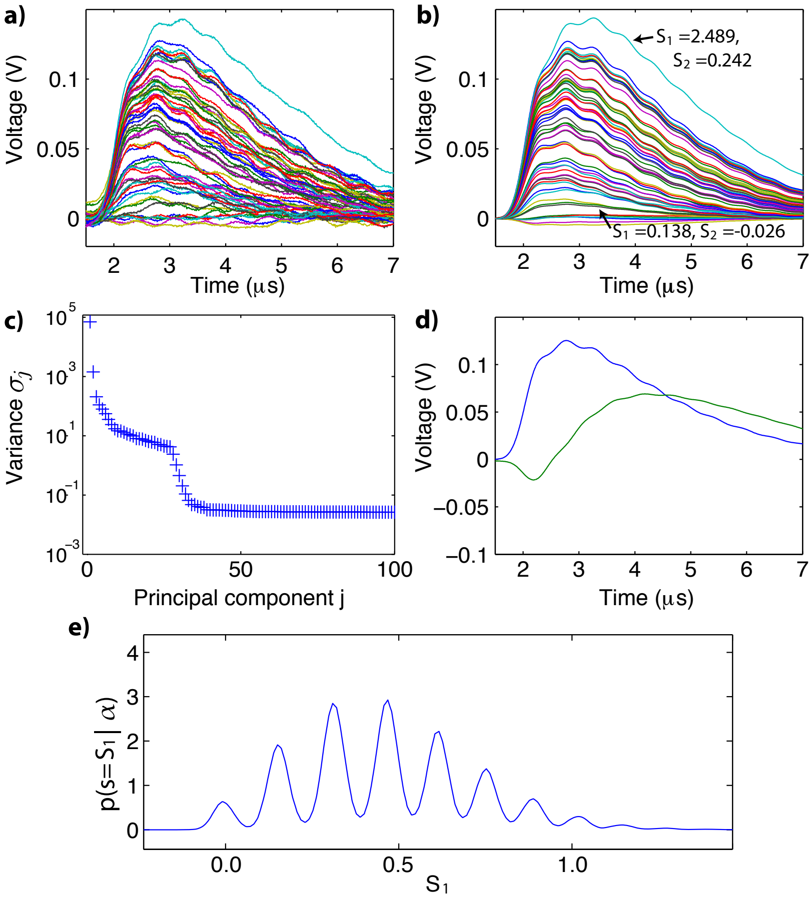

Figure 3.3: a) Representative TES traces $v_i(t)$ from a data set of 180,000 total signals. b) Truncated representation of the same traces using only the first two principal components $w_1(t)$ and $w_2(t)$. c) Variance σ_j of the set of principal component scores $\{s_{ij}\}$ as a function of the principal component number j. d) Principal components $w_1(t)$ (blue) and $w_2(t)$ (green). e) Probability density function $p(s = S_1 | \, |\alpha|^2 = 3.1)$ for outcomes s in the space of S_1, given a coherent-state input $|\alpha\rangle\langle\alpha|$ with a mean of 3.1 photons per pulse.

Detector tomography has been previously carried out for continuous-output PNRDs with 5% quantum efficiencies[80], in which the continuous-output problem was circumvented by 'binning' the detector output based on the maximum amplitude of the signal. This approach does not make optimal use of the information available. Furthermore, as I will discuss, the numerical techniques for detector tomography used in the study are not effective in the high detection-efficiency regime, which is now accessible with TES detectors. Another recent work has explored algorithmic methods of interpreting the response of high detection-efficiency PNRDs based on cluster analysis[81]. Although this may prove useful for rapid characterisation of a detector, it is not a tomographic technique and is therefore unable to provide a rigorous characterisation of the detector response.

3.2.1 Principal component analysis

I first consider the problem of efficiently extracting information from a high-dimensional detector signal data set. This is achieved by employing a standard technique from multi-variate statistics, namely principal component analysis[84]. For a given data set, this approach determines the optimal set of 'principal component' basis functions $\{w_j(t)\}$ such that each successive basis function captures the maximum amount of information possible from the data set (as measured by the variance of the 'principal component scores' $\{s_{ij}\}$, given by $\sigma_j = \left\langle s_{ij}^2 \right\rangle - \left\langle s_{ij} \right\rangle^2$), while maintaining orthogonality with the previous components. Crucially, this implies that if the principal component basis is truncated to compress the data, the maximum amount of the variance of the original data set will still be captured. In other words, the truncated principal component basis will provide the most faithful reconstruction of the data for a given number of components.

In an actual experiment, the signals $v_i(t)$ and therefore the basis functions $w_j(t)$ are necessarily discretised due to the finite temporal resolution of the detector. In this case the set of signals $\mathbf{V}$ can be expressed as a matrix. It can be shown that the problem of determining $\{w_j(t)\}$ for $\mathbf{V}$ is equivalent to finding the eigenvectors of the matrix $\tilde{\mathbf{V}}^T\tilde{\mathbf{V}}$, where $\tilde{\mathbf{V}}$ is the data set with the mean signal subtracted[84]. These eigenvectors can be efficiently determined using singular value decomposition. Once $w_i(t)$ are known, s_{ij} can be calculated from the detector signals $v_j(t)$ by $s_{ij} = \int v_j(t)w_i(t)\mathrm{d}t$.

We applied principal component analysis to a data set of 180,000 TES traces, taken with a range of 300 different coherent state inputs with average photon numbers spanning from 0 to approximately 15 photons per pulse. We found that this size of data set was a reasonable balance between ensuring that enough traces were sampled while minimising the time required to acquire and process the signals. In Fig. 3.3a & b, example TES traces from this data set are plotted both in their original form, and in a reduced form using only the first two principal components $w_1(t)$ and $w_2(t)$. As can be seen, with just these two components, most of the structure of the traces has been reproduced. This can be shown more formally by comparing the variance σ_j of $\{s_{ij}\}$ for different principal component numbers j, as plotted in Fig. 3.3c. A larger variance shows that a given component is capturing more distinguishing information between the traces in the data set. The variance σ_1 is two orders of magnitude greater than σ_2, and this trend continues, with σ_j rapidly decreasing as a function of j.

Interestingly, as Fig. 3.3d shows, $w_1(t)$ is very close to the mean shape of the TES traces. This would be expected theoretically in the small-signal limit, in which the TES trace height simply scales linearly with the photon number[85]. This confirms that projecting onto the mean trace shape, as used by Ref. [81], is a useful approach for distinguishing TES signals in the few-photon limit using only a single parameter. Beyond providing a justification for this choice of processing method, the higher order principal components that are revealed by our analysis can provide additional data with which to characterise the response of a detector, particularly for higher photon numbers. For example, $w_2(t)$ captures the increase in the pulse length with photon number (due to an increase in thermal recovery time), as will be further discussed below.

3.2.2 Detector tomography

Detector tomography is necessary to determine the correspondence between the reduced detector signals and the input number of photons [82]. The goal of detector tomography is to determine the positive-operator-valued measure (POVM) $\{\hat{\pi}(s) = \sum_{n,m=0}^{\infty} \theta_{n,m}(s) \, |n\rangle\langle m|\}$ (written here in the Fock state basis) that fully characterises the detector response; this is parameterised by the outcome s in the space of $(S_1, S_2, \dots S_n)$. Once the POVM is known, the probability density for detector outcome s, given input state ρ, is determined by the Born rule

$$p(s|\rho) = \mathrm{Tr}\left[\rho \, \hat{\pi}(s)\right]. \tag{3.2}$$

The standard approach to tomography consists of experimentally estimating the outcome probability densities $p(s|\rho_k)$ for a set of known probe basis states $\{\rho_k\}$. Using these estimated probabilities, Eqn. 3.2 can then, in principle, be inverted to find $\hat{\pi}(s)$.

The set of probe states $\{\rho_k\}$ must provide a sufficient basis for the operator space of the POVM $\{\hat{\pi}(s)\}$; in other words, it must be tomographically complete. This constraint is satisfied by using a well established method [82] for tomography of PNRDs based on coherent state probes $|\alpha\rangle\langle\alpha|$. It is well known that coherent states form an over-complete basis for an optical mode. Coherent states are also straightforward to generate in the lab and retain Poissonian photon number statistics and the same functional form of Wigner distribution despite experimental losses during preparation, making them ideal probe states. Additionally, as TES detectors are phase insensitive, their response depends only on the magnitude of the coherent state parameter α, and not its phase. This significantly reduces the number of probe states needed to form a tomographically complete set of basis operators and removes the need for any phase reference in the experiment.

Calibrated light source

It is necessary to use a calibrated light source in order to produce coherent-state probes with known energies for detector tomography. Since we do not have access to a source calibrated to a radiometric standard, we built a calibrated source based on a Newport 918D-IG-OD3R power meter, which provides a specified calibration accuracy of 2% of absolute power and a linearity of better than 0.5%. This power meter was used to calibrate a series of fixed attenuators to reduce the output from a pulsed laser to the single-photon level with a known mean-photon number per pulse[86].

Our method uses a fibre beam splitter with a fixed fibre attenuator connected on one of the output ports, as shown in Fig. 3.4a. As long as this attenuation is well within the linear dynamic range of the power meter, we can obtain a calibration curve for the combined splitter-attenuator device relating the power measured at port $1A$ to the power at port $1B$. In our case, the attenuation required to reach the single photon level is much greater than the dynamic range of the power meter. This forces us to use a second, calibrated splitter-attenuator device in series with the first Fig. 3.4b. A weighted total least-squares algorithm[87] was used to find the total attenuation taking account of the absolute power errors in both variables. The total attenuation is given by the product of the two attenuators,

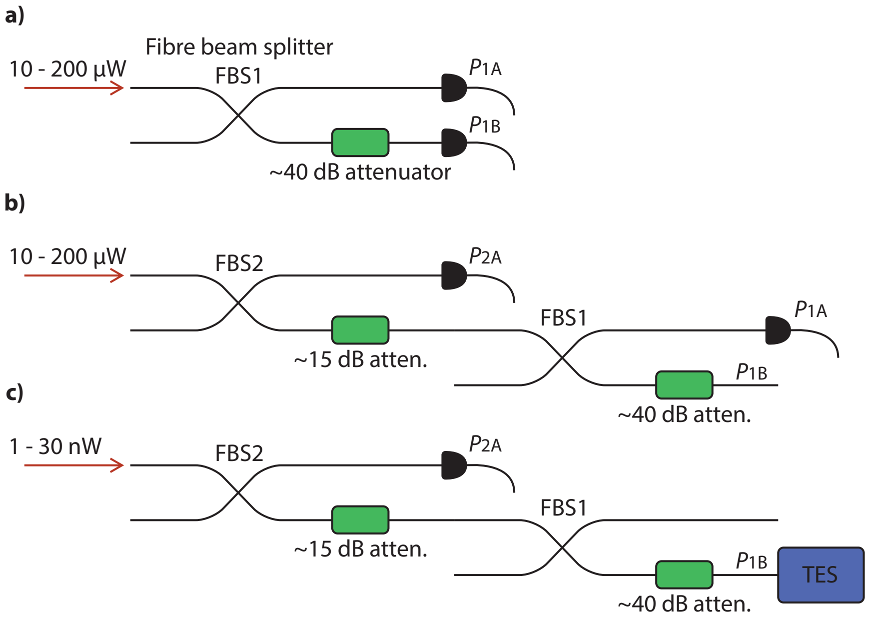

Figure 3.4: Calibrated light source. Because the dynamic range of our power meter is insufficient to span the attenuation required to reduce the coherent-state energy to the single-photon level, we perform the calibration in two steps at the expense of increased error. We use the laser diode running in CW mode to calibrate the attenuators, since the power meter is most accurate in this mode. a) We first take a series of measurement of the output powers P_{1A} and P_{1B} for a range of input powers to the fibre beam splitter. This allows the output power at port $1B$ to be determined from the power at port $1A$. b) A second fibre beam splitter is connected to the first one, along with an additional attenuation. A series of measurements of P_{2A} and P_{1A} are made for a range of input powers. By combining these results with those from the first step, we can calculate the output power at port $1B$ for a given power at $2A$. c) For the detector characterisation we switch the laser to pulsed operation and attenuate the input light to the nanowatt level.

but the errors in the measurements add linearly since they are not independent. Thus our final calibrated attenuation was found to be

$$\eta_{\text{att}} = (2.10 \pm 0.16) \times 10^{-6}. \tag{3.3}$$

This relates the power measured at the monitor port $2A$ to the power at port $1B$, such that $P_{2B} = \eta P_{1B}$ (Fig. 3.4c). A variable attenuator is used to set the input power level before the calibrated attenuator so that we can probe our detector with a variety of coherent state amplitudes. We monitor the input power to the attenuator using port $2A$ and calculate the average photon number per pulse in port $1B$ which is coupled to the TES. The value of η_{att} also includes a correction to account for the Fresnel reflection from the unterminated fibre when plugged into the monitor power meter, which leads us to underestimate the total power that will be input when this fibre is instead directly coupled to the fibre leading to the TES. Fibre specifications give this loss at about 3.3% but there is a 1% uncertainty in this figure[88].

Detector tomography experiment

As for the principle component analysis, we measured the detector response to a set of 300 different probe energies equally spaced between 0 and 15 photons on average per pulse. However, in this case, we acquired a larger data set of 49152 traces for each probe energy, since the tomography procedure is more sensitive to statistical noise than principle component analysis. These measured signals were used to estimate the probability density functions $\{p(s|\alpha_k)\}$.[1] Fig. 3.3e shows an example measured probability density function for outcomes s in the space of S_1 given a probe state with a mean of 3.1 photons per pulse. In Fig. 3.5 this is extended to plot example probability density functions for outcomes in the two-dimensional output space of S_1 and S_2 given different coherent-state inputs. Additional structure along S_2 is visible, and could be incorporated into signal analysis to further distinguish input states. However, since the dominant contribution to the data variance is from $w_1(t)$, particularly for the low photon numbers considered here, we choose to solely focus on S_1 for the remainder of the analysis. This slightly reduces the information available, but significantly reduces the computational demands of our numerical methods. It is anticipated

---

[1] The probability density functions were calculated using Gaussian-kernel density estimation[89]. This technique is better suited to this problem than using histograms, as it is not necessary to choose an arbitrary binning of the data. Instead, this approach directly gives continuous-valued estimates of the functions.

that this technical shortcoming can be overcome in future extensions of this work.

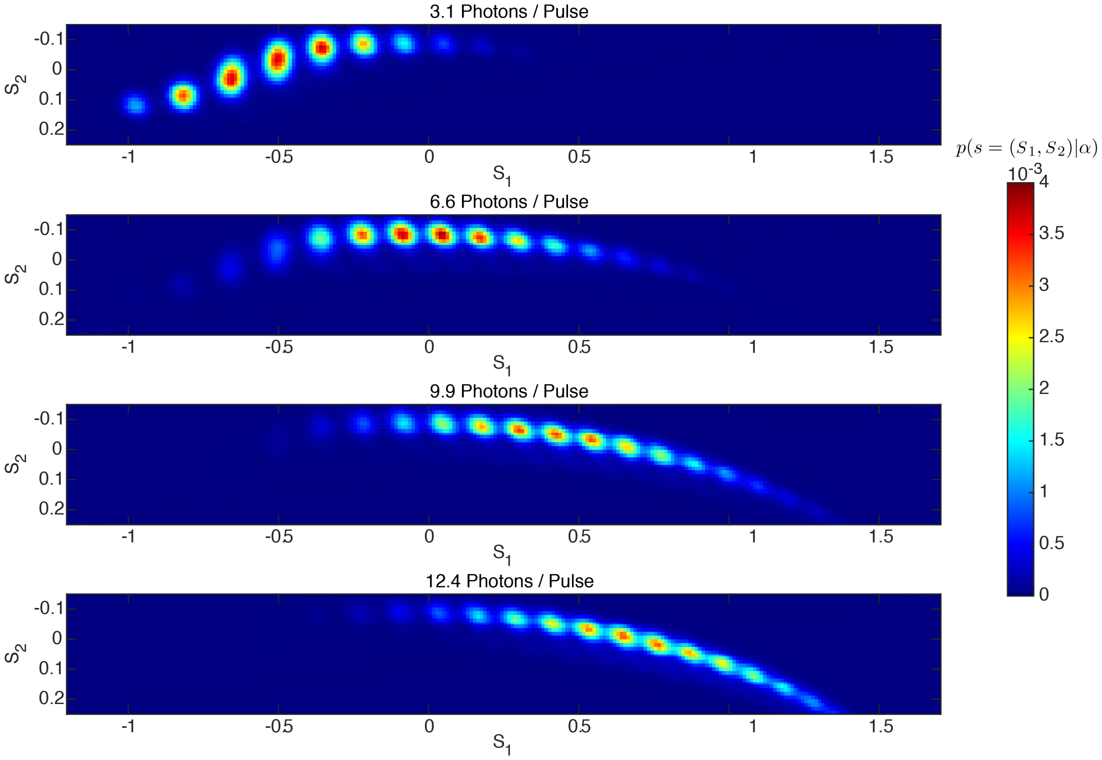

Figure 3.5: Example probability density functions for outcomes s in the space of S_1 and S_2 given coherent-state probes with varying average photon numbers.

These probability density functions $p(s|\alpha_k)$ are in fact a direct estimate of the Husimi Q function for a given $|\alpha_k|$, and are therefore sufficient to fully characterise the operation of the detector [82,90]. Although these measurements are sufficient, for many quantum optics applications it is of interest to determine the response of the detector in the photon number basis, for example, when heralding states produced in SPDC [91].

A phase insensitive detector will have POVM elements diagonal in the photon-number basis; these can therefore be expressed as

$$\hat{\pi}(s) = \sum_{n=0}^{\infty} \theta_n(s) \left|n\right\rangle\!\left\langle n\right| . \tag{3.4}$$

Coherent-state probes are given in this basis by [2]

$$|\alpha\rangle = \exp(-|\alpha|^2/2)\sum_{n=0}^{\infty}\frac{\alpha^n}{\sqrt{n!}}|n\rangle . \tag{3.5}$$

Inserting Eqns. 3.4 & 3.5 into the Born rule (Eqn. 3.2), we find that the probability density for a given outcome is

$$p(s|\alpha) = \sum_{n=0}^{\infty} F_{\alpha,n}\,\theta_n(s). \tag{3.6}$$

where $F_{\alpha,n} = |\alpha|^{2n}\frac{\exp(-|\alpha|^2)}{n!}$.

Using the set of probability density functions $p(s|\alpha_k)$ associated with the input probe states $\{|\alpha_k\rangle\}$, this relation can be numerically inverted to find the best solution for $\theta_n(s)$ consistent with the physicality constraints

$$\theta_n(s) \geq 0, \qquad \text{and} \qquad \int \theta_n(s)\,\mathrm{d}s \leq 1. \tag{3.7}$$

It is well known that the problem of inverting Eqn. 3.2 to obtain $\hat{\pi}(s)$ is ill-conditioned[82]. We found that published methods of performing this numerical inversion based on constrained least squares techniques[80] did not give satisfactory results. This may be in part due to the reduced overlap between the POVM elements for different photon numbers as compared to previous studies, because of our much higher system detection efficiency. This means that regularisation techniques designed to promote this overlap[82,83] do not work as effectively.

---

[2] This assumes that the input state is a pure state, however this can easily be extended to mixed state inputs[82] (for example, as resulting from classical uncertainties in α).

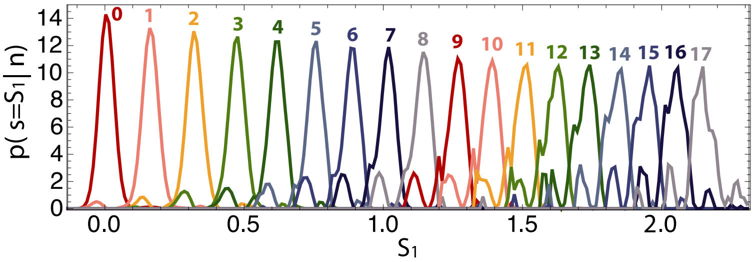

Figure 3.6: Constrained least squares solutions for the Fock state POVM elements showing the responses to vacuum and up to 17 photons. The solution shows discontinuous jumps in probability density, particularly for higher photon numbers, that are inconsistent with our knowledge of the detector operation

3.2.3 Maximum likelihood detector tomography routine

We used insights from the collected data to develop a novel detector tomography routine that is effective for high quantum efficiencies. We adopted a model in which the detector response to photon number n (in the space of S_1) is given by the sum of $n+1$ Gaussians, with widths, heights, and positions as free variables. This Gaussian-mixture model[92] is consistent with detectors for which several different sources of noise contribute to the response of the detector to a given photon number, leading to an overall Gaussian error as might be expected from the central limit theorem. Our approach is readily extendable to higher order components $(S_2, S_3 \dots)$, however, as previously discussed, we chose to focus on S_1.

The Gaussian-mixture model gives the following expression for the POVM coefficients for photon number n

$$\theta_{n,s} = \sum_{j=1}^{n+1} \beta_{n,j} \mathcal{N}(s|\mu_{n,j}, \sigma_{n,j}). \tag{3.8}$$

where $\beta_{n,j}$ is a weighting factor for the Gaussian probability distribution $\mathcal{N}(s|\mu_{n,j}, \sigma_{n,j})$ in the outcome space s, with mean $\mu_{n,j}$, and standard deviation $\sigma_{n,j}$.

We imposed the constraint that $\mu_{n,j} = \mu_{n+1,j}$, i.e. that the Gaussians from different photon numbers should be aligned. This is physically motivated by the fact that the detector cannot distinguish between cases where n photons were input and cases where $n+1$ photons were input and one photon was lost. Removing this constraint does not alter the solution significantly, beyond leading to a slight jitter in the location of the peaks for each photon number. However, this jitter complicates the additional analysis that we carried out, particularly with regard to compensating for the uncertainty in the probe state energies (as will be discussed in the next section). No constraint is placed on $\sigma_{n,j}$.

Substituting Eqn 3.8 into Eqn 3.6 gives

$$p(s|\alpha,\chi) = \sum_{n,j} F_{\alpha,n}\beta_{n,j}\mathcal{N}(s|\mu_{n,j},\sigma_{n,j}), \tag{3.9}$$

where χ is used a shorthand to denote the set of all the parameters $\beta_{n,j}, \mu_{n,j}, \sigma_{n,j}$, in order to make the dependence on the model explicit.

This expression gives the posterior probability density for the TES detector producing an outcome s in our model, given an input coherent-state probe $|\alpha\rangle\langle\alpha|$. This posterior probability should be maximised for the measured data. Typically, maximum likelihood estimation[92] is carried out based on a set of observed outcomes $\{s_{i1}\}$. In this case, the quantity to be maximised is the log-likelihood

$$\begin{aligned} \mathcal{L} &= \log\left(\prod_i p(s_{i1}|\alpha_i,\chi)\right) \\ &= \sum_i \log\left(\, p(s_{i1}|\alpha_i,\chi)\,\right). \end{aligned} \tag{3.10}$$

However, due to the large number of data points that we sample, evaluation of this sum becomes impractical. Instead, we used our data set $\{s_{i1}\}$ to estimate the outcome probability density $q(s|\alpha_k)$ for each $|\alpha_k\rangle\langle\alpha_k|$. We can use this distribution to rewrite Eqn. 3.10 as

$$\mathcal{L} = \sum_k \int N_k\, q(s|\alpha_k) \log\left(p(s|\alpha_k, \chi) \right) \mathrm{d}s, \tag{3.11}$$

where N_k is the total number of samples measured at each value of α_k. Since we measured the same number of samples per coherent state value, we neglect this constant factor that has no impact on the maximum likelihood estimation.

The full expression for the log-likelihood therefore becomes

$$\mathcal{L} = \sum_k \int \mathrm{d}s\, q(s|\alpha_k) \log\left(\sum_{n,j} F_{\alpha_k,n}\, \beta_{n,j}\, \mathcal{N}(s|\mu_{n,j}, \sigma_{n,j}) \right). \tag{3.12}$$

In order to maximise this log-likelihood, we follow the standard approach[92] of taking derivatives with respect to each parameter in the model. For example, differentiating with respect to $\mu_{n,j}$ gives

$$\frac{\partial \mathcal{L}}{\partial \mu_{n,j}} = \sum_k \int q(s|\alpha_k)\, \gamma_{s,k,n,j} \sigma_{n,j} (s - \mu_{n,j})\, \mathrm{d}s, \tag{3.13}$$

in which

$$\gamma_{s,k,n,j} = \frac{F_{\alpha_k,n}\, \beta_{n,j}\, \mathcal{N}(s|\mu_{n,j}, \sigma_{n,j})}{\sum_{n,j} F_{\alpha_k,n}\, \beta_{n,j}\, \mathcal{N}(s|\mu_{n,j}, \sigma_{n,j})}. \tag{3.14}$$

Rearranging leads to the following expression for $\mu_{n,j}$

$$\mu_{n,j} = \frac{1}{N_{n,j}} \sum_k \int q(s|\alpha_k)\, \gamma_{s,k,n,j}\, s\, \mathrm{d}s, \quad \text{where } N_{n,j} = \sum_k \int q(s|\alpha_k)\, \gamma_{s,k,n,j}\, \mathrm{d}s. \tag{3.15}$$

Similarly we find that

$$\sigma_{n,j} = \frac{1}{N_{n,j}} \int q(s|\alpha_k)\, \gamma_{s,k,n,j}\, (s - \mu_{n,j})^2 \, \mathrm{d}s, \tag{3.16}$$

$$\beta_{n,j} = \frac{N_{n,j}}{N_n}, \quad \text{where } N_n = \sum_j N_{n,j}. \tag{3.17}$$

Note that these expressions for the parameters are dependent on $\gamma_{s,k,n,j}$, and therefore do not form a closed-form solution. This means that the optimal solution cannot be found analytically. However, it can be shown that a simple routine consisting of the repeated application of two steps will converge to a solution[92]. In the first step, the current values of the parameters are used to calculate $\gamma_{s,k,n,j}$. This is then used in the second step to re-estimate the optimal values of the parameters using Eqns. 3.15, 3.16 & 3.17.

The results of this inversion are shown in Fig. 3.7a. The efficacy of this model-based routine can be estimated by using the calculated POVM to reconstruct the original data set. The L_1 difference between this reconstruction and the original data (normalised by the L_1 norm of the original data set) is 0.054 as compared to 0.047 for the unphysical reconstruction given by a least-squares approach. This shows that this model equally effectively captures the detector response (with only 0.7% lower overlap than the least squares approach) while providing a fit that is more consistent with our knowledge of the detector operation.

Incorporating calibration uncertainty

As a final step, it is necessary to incorporate the uncertainty in the coherent-state probe energies η_{att} used to determine the coherent state probe energies. The POVM element coefficient $\theta_n(s)$ gives the probability density $p(s|n)$ that one will measure outcome s given n

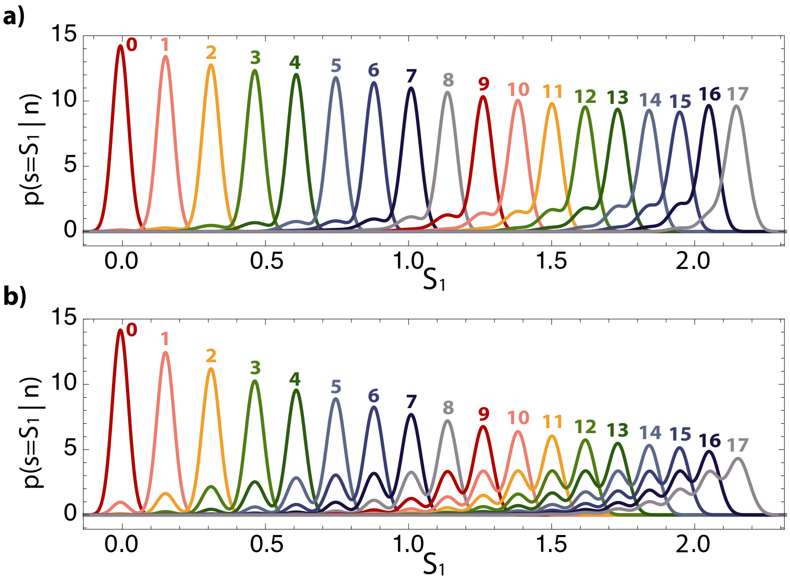

Figure 3.7: a) Fock state POVM elements $\theta_n(s) = p(s|n)$ determined from our parameterised detector tomography routine. Note that these solutions are continuous functions in the space of S_1, and have not been arbitrarily binned into different 'photon-number' outcomes. b) Fock state POVM elements after incorporating the uncertainty in the probe state energies.

input photons. This probability is actually $p(s|n, \eta_{\text{att}})$ since η_{att} is a variable in our tomography calculations. Our uncertainty in η_{att} must therefore be accounted for. Based on our error analysis (and assuming normally distributed errors), we can estimate the probability density $p(\eta_{\text{att}})$ for η_{att}. Additionally, we can calculate $p(s|n, \eta_{\text{att}})$ for different η_{att}. Combining these, we can incorporate this statistical uncertainty into our POVM using

$$p(s|n) = \int p(s|n, \eta_{\text{att}}) p(\eta_{\text{att}}) \mathrm{d}\eta_{\text{att}}. \tag{3.18}$$

The results of this analysis are shown in Fig. 3.7b. The higher photon-number POVM elements are particularly sensitive to this uncertainty, and show correspondingly large deviations from their ideal values. This highlights the crucial importance of an accurately calibrated probe state source for detector tomography. Our setup has a high calibration uncertainty of 8%, however, calibration uncertainties of less than 1% are achievable[86,93]. Since this shortcoming is not intrinsic to our detector, in the following analysis I will assume such a 1% calibration uncertainty, as this better demonstrates the information that our protocol can provide.

Detector quantum efficiency

The POVM elements that we calculate using detector tomography completely characterise the detector response. Model-free detector tomography is obtained by treating the detector as a black box, and so in principle does not contain information on the system detection efficiency, i.e. the loss that occurs between the input and the detector.

However, the less general, but physically motivated model-based detector tomography approach that we have adopted can allow us to make an estimate of this efficiency. As noted above, we assume that the response of the detector to each photon number is composed of several Gaussian elements. We can make the further assumption that these different Gaussian elements occur due to the action of loss on an initial Fock state, leading to a statistical mixture of photon numbers at the detector, with one Gaussian element per photon number state detected. Therefore the heights of these elements should follow a binomial distribution within each of the Fock state POVM elements. For a given system detection efficiency, it is then possible to calculate the expected height of these Gaussian elements and compare them to the actual tomography results. We used a numerical routine to find the loss level that minimised the L2 norm between this predicted output and the tomography data.

This analysis suggests that our system detection efficiency is 0.98 (+0.02/−0.08). [3] The

---

[3] The system detection efficiency is defined as the efficiency with which a photon in the fiber connected

asymmetric uncertainty arises as the efficiency is upper bounded at 1.0. Additionally, we find a strong agreement between the predicted photon number distribution and the tomography data, as shown in Fig. 3.8, suggesting that our initial assumption is correct.

3.2.4 Application of tomography data

The above tomography procedure gives the probability density $p(s|n)$ for a specific outcome s given an n-photon input to the detector. However, in typical experiments, one is actually interested in the complementary probability density $p(n|s)$ that the input contained n photons given that the detector measured outcome s.

Calculating this requires Bayes' theorem $p(n|s) = p(s|n)p(n)/p(s)$ and thus depends on the prior probability $p(n)$ of an n-photon input. Here, as an example I consider two distinct priors which might arise in applications. First, I consider a Poisson distribution $p(n|\alpha) = e^{-|\alpha|^2} |\alpha|^{2n} /n!$ which would result from a coherent state input. I also consider a thermal distribution $p(n|\lambda) = (1 - \lambda^2)\lambda^{2n}$ which describes a thermal state input and, importantly, the single-mode marginal statistics of a spontaneous parametric down-conversion source. If one mode of such a source is sent to a detector, $p(n|s, \lambda)$ represents the statistical mixture of photon numbers onto which the other mode is projected. Such information is extremely important for quantum information and metrology applications.

Two example probability distributions $p(n|s, \alpha)$ and $p(n|s, \lambda)$ are plotted in Fig. 3.9a & b. As can be seen, the two priors lead to significant differences in the distributions. For the thermal distribution, the thermal prior suppresses the overlap between the outcomes associated with neighbouring photon numbers. This is because, for small λ, $n + 1$ input photons will occur much less frequently than n photons. Therefore the predominant overlap

---

to the detector is detected[94].

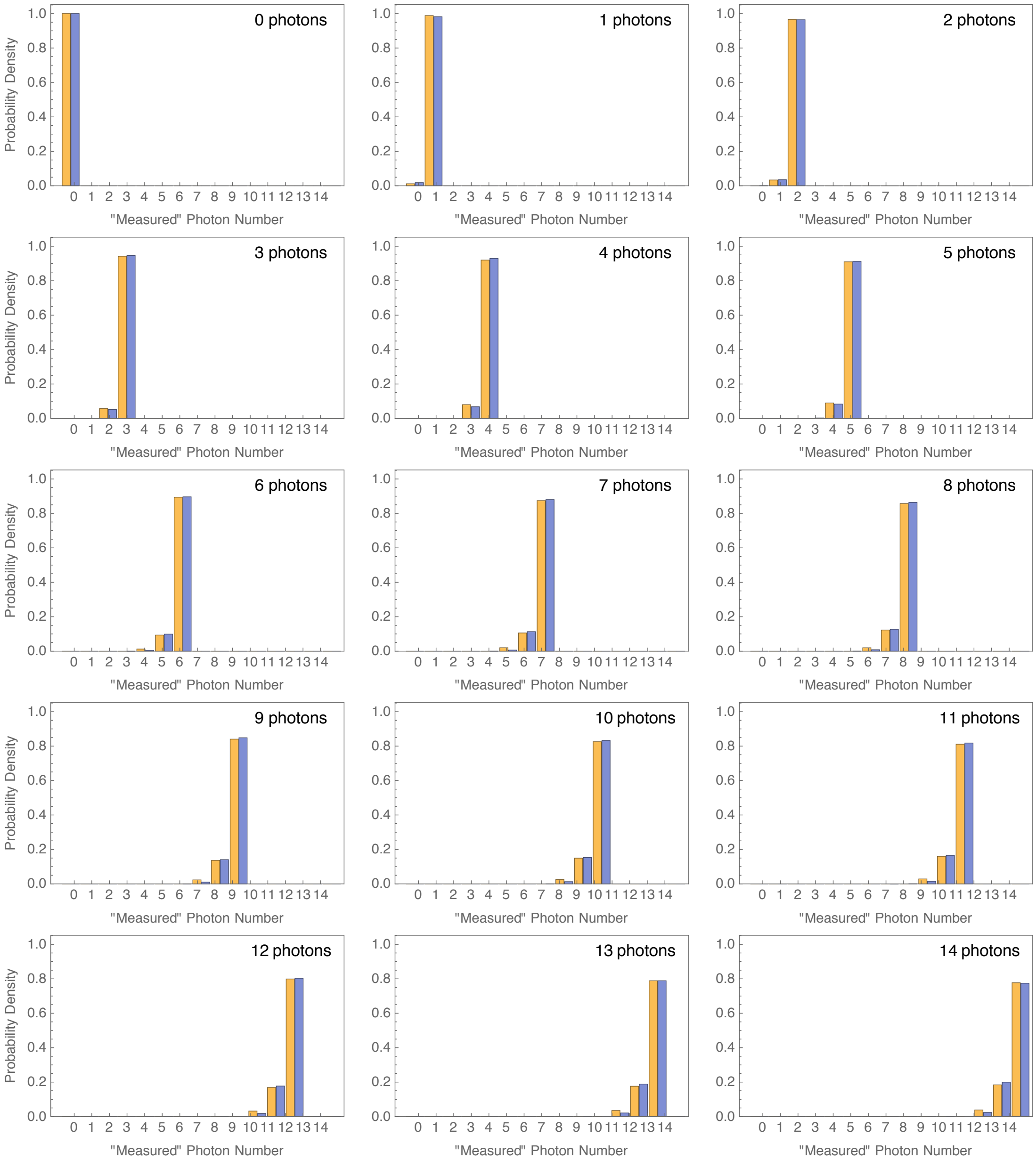

Figure 3.8: Estimating the system detection efficiency. One can assume that the different Gaussian elements that make up the detector response to a given photon number are due to losses between the input and the detection, leading to a reduced number of photons actually being detected. This loss therefore leads to a binomial distribution of Gaussian response elements when an initial Fock state is input to the detector. The relative weights of each of these Gaussian elements, as inferred from our maximum likelihood estimation protocol, are plotted here in gold. From this data, we can carry out a numerical routine to determine the detection efficiency most consistent with our data. The predicted photon (and therefore Gaussian element) distribution resulting from this estimated detection efficiency is shown in blue for comparison.

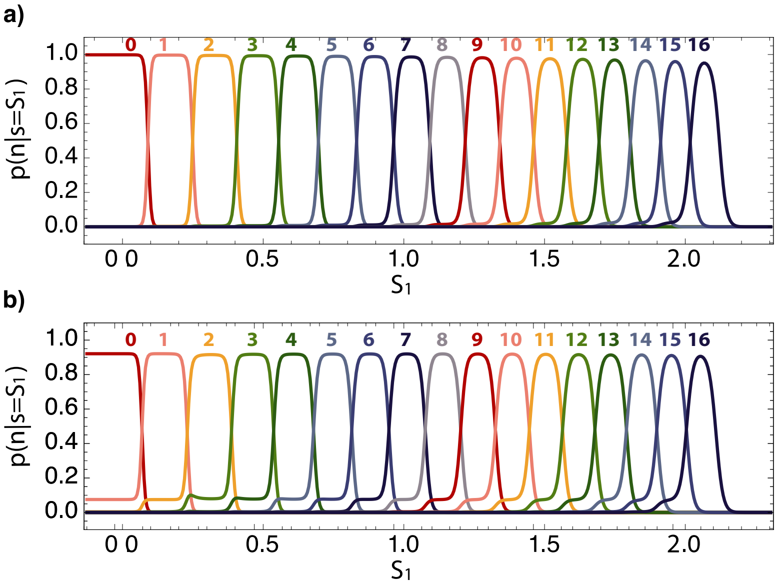

Figure 3.9: Example distributions $p(n|s)$ from our tomography data, which give the probability that the input contained n photons given that the detector measured outcome s. The effect of the prior input photon number probabilities can be seen in the difference between a) a thermal distribution with $\lambda^2 = 0.1$, and b) a Poisson distribution with $|\alpha|^2 = 5$.

contribution, due to an $n + 1$-photon input being detected in the space of outcomes most associated with n input photons, occurs correspondingly less frequently than genuine n-photon inputs.

The Poissonian prior plotted in Fig. 3.9b has the opposite effect as the thermal prior, since for n less than the mean photon number, an input of $n + 1$ photons is more probable than an input of n photons, and therefore the overlap is promoted. It should be noted that in both cases, due to the truncation of our detector tomography at 17 input photons, the distributions $p(n|s)$ become inaccurate in regions in which significant contributions would be expected from photon numbers greater than this. In practice, this simply translates to an operational requirement that detector tomography must be extended to include all photon numbers that are expected to contribute in any given experiment.

Characterising photon number resolution

Closely linked to determining $p(n|s)$ is the problem of finding a quantitative measure of the 'photon-number resolution' of the detector. Since $p(n|s)$ only gives information on the confidence with which a specific outcome s can determine the photon-number input, we propose a measure that represents an average of this confidence, weighted by the probability density for s given n input photons,

$$\begin{aligned} C_n &= \int_{-\infty}^{\infty} p(n|s)p(s|n)\,\mathrm{d}s = \int_{-\infty}^{\infty} \frac{p(s|n)^2 p(n)}{p(s)}\,\mathrm{d}s \\ &= \int_{-\infty}^{\infty} \frac{p(s|n)^2 p(n)}{\sum_k p(s|k)p(k)}\,\mathrm{d}s. \end{aligned} \tag{3.19}$$

Given an input of n photons, this confidence C_n represents the average probability ascribed to the n photon component of the inferred state $\rho(s) = \sum_n p(n|s)\,|n\rangle\langle n|$. More loosely, it represents the probability that the detector gives the correct photon number. Additionally, C_n is given by $\int \langle n|\,\rho(s)\,|n\rangle\, p(s|n)\mathrm{d}s$, the average squared fidelity between the inferred detected state and an n photon number state $|n\rangle$, weighted by the probability $p(s|n)$. For the detection of a heralding state from a spontaneous parametric down-conversion (SPDC) source[91], this will therefore also be the fidelity of the heralded state with $|n\rangle$. Note that the detector does not have information on the specific input photon-number n; however, a prior distribution must be specified. This confidence is therefore a function of the distribution chosen. Fig. 3.10a shows the confidence for different photon numbers as a function of the SPDC source thermal prior distribution parameter λ^2, where $p(|n,n\rangle\,|\,\lambda) = (1-\lambda^2)\lambda^{2n}$.

In order to facilitate comparison between different detectors, it may be useful to determ-

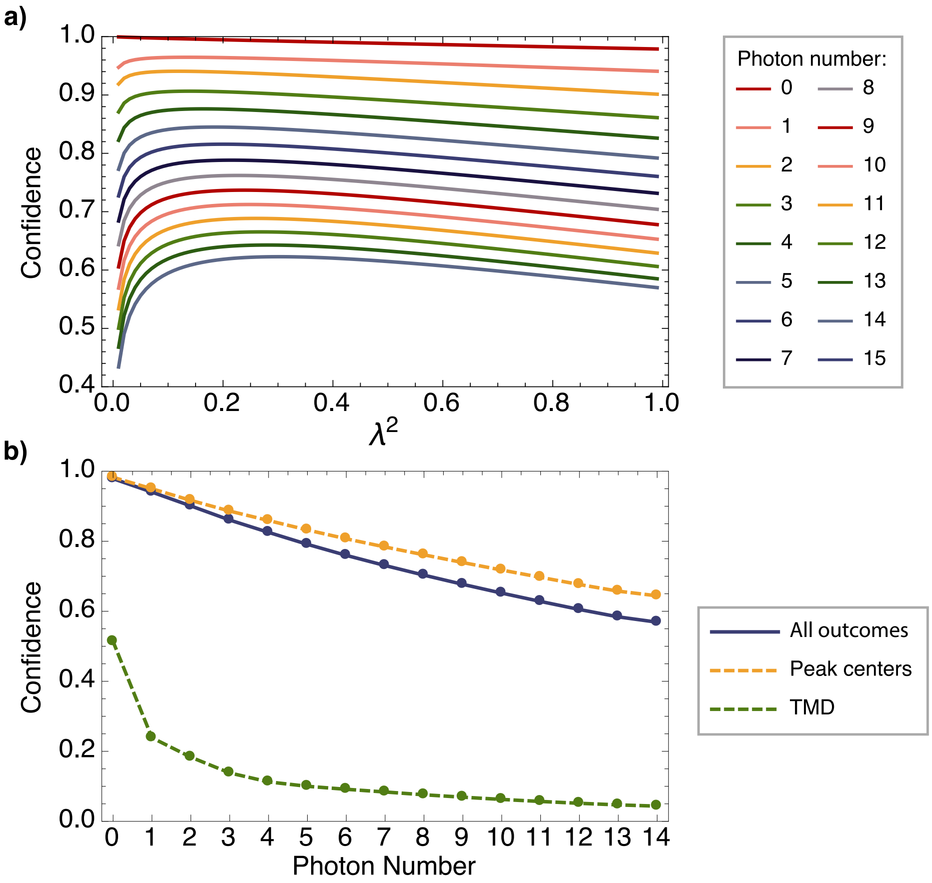

Figure 3.10: a) Calculated confidence C_n for different photon numbers as a function of the thermal prior distribution parameter λ^2. b) Calculated confidence for our detector given a flat prior, as a function of photon number n (blue). Confidence for outcomes at the centres of the peaks in $p(s|n)$ (dashed yellow). Confidence for a time-multiplexed pseudo-number-resolving detector (dashed green).

ine this confidence given a bounded flat prior for the photon number,

$$C_n = \int_{-\infty}^{\infty} \frac{p(s|n)^2}{\sum_k p(s|k)} \, \mathrm{d}s. \tag{3.20}$$

This is plotted in Fig. 3.10b. As would be expected, our detector is extremely effective at resolving vacuum and lower photon numbers, while for higher photon numbers, the increasing effect of the detection inefficiency and gradual saturation of the detector leads to a reduced confidence in the outcomes. To demonstrate that this measure is widely applicable to different PNRDs, the confidence for the time-multiplexed pseudo-number-resolving detector with 8 time bins presented in [82] is also shown.

For certain applications [76], it is important to maximise the fidelity of the inferred detected state with a photon number state (C_n). In these cases, the fidelity can be improved using post-selection strategies in which only a subset of outcomes are accepted. This is possible to explore using our detector tomography data since our treatment has explicitly avoided any binning of outcomes.

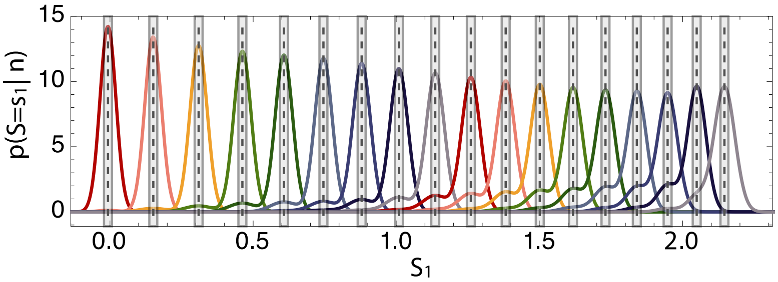

Figure 3.11: Post-selecting on outcomes within windows centred on the peak maxima can be employed to boost the confidence of detected photon states.

One strategy is to only consider outcomes within windows centred on the peak maxima (Fig. 3.11). As would be expected, the highest confidence is obtained in the limit of the window width tending to zero, in which case the number of accepted outcomes would also tend to zero. This limit therefore upper bounds the performance of this strategy, and is plotted in Fig. 3.7. For our detector, the increase in confidence as compared to using the full space of outcomes is comparatively modest, since the overlap between different photon number POVM elements is dominated by the detection efficiency. However, as the detection efficiency of detectors improves, the intrinsic overlap between neighbouring Gaussian peaks is expected to become increasingly important. In this case, this post-selection strategy should become more effective.

3.3 Conclusions

We have demonstrated a novel approach to detector characterisation. This has allowed us to confirm the high quantum efficiency of our TES detectors, putting us in a position to be able to employ these detectors for quantum optical experiments with higher photon numbers than was previously achievable. In particular, we anticipate being able to apply these detectors for quantum metrology experiments in the near future. I will discuss this further in the next part of this thesis, which is focused on experimental and theoretical aspects of quantum metrology.

Part II

Quantum Metrology

Chapter 4

Introduction to quantum metrology

Metrology is an extraordinarily wide ranging discipline, encompassing all forms of measurement of quantities and phenomena. This breadth is reflected in its crucial importance to the scientific process, since measurement forms the basis of all scientific investigations. Surprisingly, despite this wide applicability, a strong theoretical basis for the fundamental process of measurement has been developed that unifies the diverse branches of this field. Based on these tools, it is possible to rigorously quantify the information that can be gained through a given measurement process.

Any physical measurement process will unavoidably suffer from experimental imperfections. These will lead to statistical uncertainties in the results of the measurement. Often these errors occur due to unwanted coupling to other systems, and can therefore in principle be avoided through improved experimental design. However, there are also more fundamental uncertainties in the state of the probe and the system due to their quantum mechanical nature. These uncertainties imply that it is impossible, even theoretically, to make a measurement with arbitrary precision.

This is an important result in and of itself, however, it also motivates an even more interesting question: Given these fundamental limits, is it possible to design non-classical probe states and measurement schemes that can provide higher precision measurements than their purely classical counterparts could ever, even theoretically, allow? This question immediately leads to several others, including: a) what do we mean by non-classical?, and b) how can we compare the precisions allowed by different measurement processes? These questions underlie the nascent field of quantum metrology. In order to delve further into this field, it will be helpful to briefly introduce some of the most commonly used theoretical framework.

4.1 Single parameter estimation theory

For pedagogical clarity, I will initially consider the estimation of a single parameter (loosely following the treatment in Ref. [17]), before extending the formalism to multiple parameter estimation in Chapter 6. Developing further the initial notion of a measurement, one can more precisely define the measurement process (Fig. 4.1a) as consisting of:

- Preparation of a probe state with density matrix $\hat{\rho}_0$.
- Evolution (not necessarily unitary) of the probe state under the action of a quantum channel $\Phi_\theta(\hat{\rho}_0) = \hat{\rho}_\theta$.
- Measurement of the state, as described by a positive-operator valued measure (POVM) consisting of a set of operators $\{\hat{\Pi}_k\}$, each associated with a different possible outcome k.

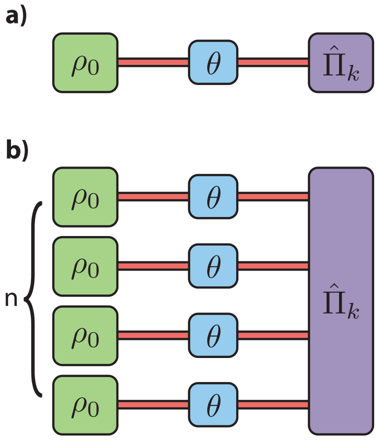

Figure 4.1: a) A measurement process consists of the preparation of a probe state ρ, followed by evolution under a quantum channel parametrised by θ and finally measurement, as described the set of operators $\{\hat{\Pi}_k\}$. b) Measurements are typically repeated multiple times using n probe states. In this case the most general measurements could consist of joint measurements of the output states.

A measurement is typically repeated multiple times using n probe states, in which case it is useful to consider the overall evolution of the full set of probe states $\hat{\rho}_0^{\otimes n}$ (Fig. 4.1b). This allows us to consider any possible measurement scheme for the n probes, including those employing joint measurements of the probes. For a given measurement scheme, the probability of obtaining the set of results $\mathbf{k} = (k_0, k_1, k_2 \ldots)$ is determined by the Born rule:

$$p_n(\mathbf{k}|\theta) = \mathrm{Tr}[\hat{\rho}_\theta^{\otimes n}\, \hat{\Pi}_{\mathbf{k}}^{(n)}]. \tag{4.1}$$

With suitable numerical techniques[17], $\mathbf{k}$ can be used to make an estimate φ of the value of θ. However, there will generally be some uncertainty associated with the estimate φ, which is captured by the distribution

$$p(\varphi|\theta) = \sum_{\mathbf{k}} p_{\mathrm{est}}(\varphi|\mathbf{k})\, p_n(\mathbf{k}|\theta), \tag{4.2}$$

where $p_{\text{est}}(\varphi|\mathbf{k})$ gives the probability density ascribed to φ given the results $\mathbf{k}$.

A root mean square error (RMSE) for the estimate of θ can be calculated based on this distribution

$$\delta\theta = \sqrt{\sum_{\varphi}(\varphi - \theta)^2 \, p(\varphi|\theta)}. \tag{4.3}$$

It can be shown that this error is constrained by the Cramér-Rao bound (CRB) [95]:

$$\delta\theta \geq 1/\sqrt{\mathcal{F}_n(\theta)} \tag{4.4}$$

where the Fisher information, $\mathcal{F}_n(\theta)$, is defined as

$$\mathcal{F}_n(\theta) = \sum_{k} \frac{[\partial_\theta p_n(\mathbf{k}|\theta)]^2}{p_n(\mathbf{k}|\theta)}. \tag{4.5}$$

This bound holds in the case of asymptotically locally unbiased estimators (estimators for which $\varphi \to \theta$ in the limit of $n \to \infty$, which includes all non-pathological cases). The Fisher information captures the amount by which the probability distribution over the measurement outcomes changes as a function of the parameter θ to be measured. Intuitively, the more sensitive the distribution is to θ, the lower the error will be on its estimated value.

The CRB provides a lower bound on the error achievable for a given measurement scheme (as embodied by a particular choice of POVM). However, in order to compare different strategies, we would ideally find the minimum error achievable with any possible physical measurement. It can be shown mathematically that it is possible to maximise the Cramér-Rao bound over all POVMs to give the quantum Cramér-Rao bound (QCRB) [17,95], which therefore bounds all CRBs from below

$$\delta\theta \geq 1/\sqrt{\mathcal{F}_n(\theta)} \geq 1/\sqrt{\mathcal{I}_n(\theta)}. \tag{4.6}$$

The quantum Fisher information $\mathcal{I}(\theta)$ is solely a function of the probe state $\hat{\rho}_\theta^{\otimes n}$, and is most generally given by

$$\mathcal{I}(\theta) = \mathrm{Tr}[\hat{L}_\theta((\partial\hat{\rho}_\theta/\partial\theta)^{\otimes n})\,\hat{\rho}_\theta^{\otimes n}\,\hat{L}_\theta((\partial\hat{\rho}_\theta/\partial\theta)^{\otimes n})]. \tag{4.7}$$

In this expression, the symmetric logarithmic derivative (SLD) for an operator is

$$\hat{L}_\theta(\hat{O}) = \sum_{j,k:\lambda_j+\lambda_k\neq 0} \left(\frac{2\,O_{j,k}\,|j\rangle\,\langle k|}{(\lambda_j+\lambda_k)} \right) \tag{4.8}$$

where $O_{j,k}$ are the elements of $\hat{O}$ expressed in the basis that diagonalises $\hat{\rho}_\theta^{\otimes n}$ (and therefore $\hat{\rho}_\theta$), such that $\hat{\rho}_\theta = \sum_j \lambda_j\,|j\rangle\,\langle j|$.

Several important characteristics of the QFI deserve emphasis at this point. First, I note that the quantum Fisher information is additive for product states, so that $\mathcal{I}(\hat{\rho}_\theta^{\otimes n}) = n\mathcal{I}(\hat{\rho}_\theta)$. This additivity directly leads to an $n^{-1/2}$ scaling in the QCRB, since therefore

$$\delta\theta \geq 1/\sqrt{n\,\mathcal{I}(\theta)}. \tag{4.9}$$

Remembering that the QCRB gives the maximal information available using any conceivable POVM in the full space of $\hat{\rho}^{\otimes n}$, this implies that unentangled (product state) probes are bound to produce at best such an $n^{-1/2}$ scaling in the precision of a measurement. This fundamental constraint is termed the standard quantum limit (SQL). Another ramification of this additivity is that it must therefore be possible to saturate this bound using local measurements of each probe and adaptive estimators. This implies that measurement schemes based on entanglement of the probes (Fig. 4.2a) are not necessary to saturate this bound[96]. Finally, it can be shown that $\mathcal{I}(\theta)$ is convex, and therefore the minimum error is always achieved by a pure state[97].

As an aside, I note that for such pure states $\hat{\rho}_\theta = |\psi_\theta\rangle\langle\psi_\theta|$, the SLD and QFI simplify significantly to

$$\hat{L}_\theta^{\text{pure}} = 2\left(|\psi'_\theta\rangle\langle\psi_\theta| + |\psi_\theta\rangle\langle\psi'_\theta|\right), \tag{4.10}$$

$$\mathcal{I}(\theta) = 4\left(\langle\psi'_\theta|\,\psi'_\theta\rangle - \left|\langle\psi_\theta|\,\psi'_\theta\rangle\right|^2\right), \tag{4.11}$$

where $|\psi'_\theta\rangle = \partial|\psi_\theta\rangle/\partial\theta$.

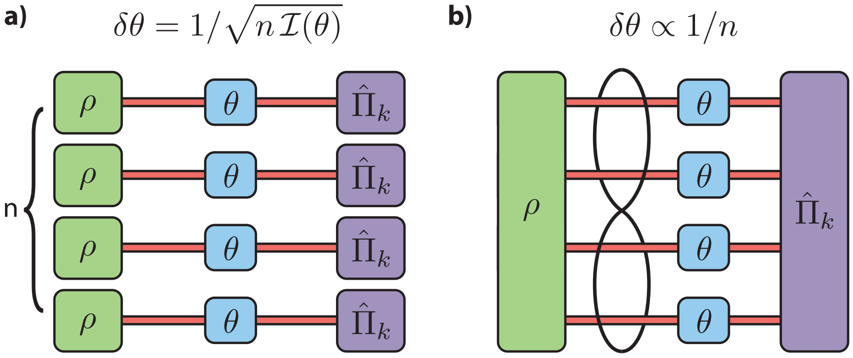

Figure 4.2: a) Local measurements are sufficient to saturate the quantum Cramér-Rao bound given unentangled probe states, giving a measurement error that scales with $n^{-1/2}$ in the number of probes n. b) However, entangling the probes before they interact with the system can lead to a measurement advantage in some cases, potentially allowing a Heisenberg (n^{-1}) scaling in the measurement error.

The standard quantum limit gives the fundamental bound to the precision of measurements using unentangled probe product states. However, if the probes are entangled before interacting with the system to be measured (Fig. 4.2b), it is possible to surpass this scaling and therefore achieve a higher measurement precision. As an example, I will consider one of the most fundamental problems in quantum metrology, interferometric phase estimation. I model this by assuming that a probe state input to the two modes a and b of an interferometer, with annihilation operators $\hat{a}$ and $\hat{b}$ respectively, undergoes the unitary evolution $e^{\mathrm{i}(\hat{a}^\dagger\hat{a}-\hat{b}^\dagger\hat{b})\theta/2}$.

Given n total probes, one can consider strategies based on entangling a fixed number N of these probe states into the state $|\psi\rangle_N$ before the interferometer, so that the total resource is $|\psi\rangle_N^{\otimes M}$, where $n = MN$. Given this constraint, it can be shown[98] that the optimal strategy is to use N00N states, which are maximally entangled states of the form

$$|\mathrm{N00N}\rangle = 1/\sqrt{2}(|N,0\rangle + |0,N\rangle), \tag{4.12}$$

where I have employed the notation $|N_a, N_b\rangle$ to denote a state with N_a photons in mode a and N_b photons in mode b. Calculation of the QCRB for N00N states gives

$$\delta\theta \geq \frac{1}{N\sqrt{M}}, \tag{4.13}$$

as opposed to

$$\delta\theta \geq \frac{1}{\sqrt{NM}} \tag{4.14}$$

for the same number of unentangled probe states. Employing these entangled probe states therefore allows for an $N^{-1/2}$ enhancement in estimation error as compared to “classical” strategies. This overall N^{-1} scaling of the error with increased entangled probe state size is known as the Heisenberg bound.[1] Although this scaling can be achieved in the lossless limit, it has been shown that, under lossy conditions, it is in general no longer possible to maintain this scaling in the asymptotic limit of $N \to \infty$[100]. In fact, N00N states are particularly sensitive to losses, since the loss of even a single photon is sufficient to remove all phase information from the state. This has motivated the development of more robust quantum-enhanced phase estimation strategies, as we will discuss further in the next chapter.

These results have motivated the development of the field of quantum metrology. Single parameter estimation has been explored both theoretically[98,101,102] and experimentally, with photonic systems as the leading platform[7,103–107]. The dominance of photonics stems to the relative simplicity of experimental quantum optics implementations and the low decoherence rate of photons as carriers of quantum information. Additionally metrology is a particularly important problem in optics, since many sensing experiments, including strain measurement, range finding and gravitational wave detection[32,107] can be performed by optical phase estimation. Producing a quantum advantage in these measurements may therefore have significant real-world applications.

In the following chapters I shall discuss two projects that I have pursued in quantum metrology. In Chapter 5, I will introduce two proposed schemes for optical phase estimation under realistic experimental conditions. This will show that our recent experimental efforts should enable us to demonstrate a sub-SQL quantum enhanced measurement in the near future. Following this, I will discuss a theoretical investigation on the simultaneous estimation of multiple phases in Chapter 6.

---

[1] The Heisenberg bound is guaranteed to be asymptotically attainable as $M \to \infty$[17]. For finite M, attainability of this bound is more complex. However, recent work[99] suggests that although N00N states are not able to obtain this bound asymptotically for large N and $M = 1$, a modified state is able to do so.

Chapter 5

Experimental quantum-enhanced metrology

The primary goal of experimental quantum metrology is to design experiments that can beat the *standard quantum limit* (SQL) in measurement precision. However, the exact meaning of 'beating the standard quantum limit' has often been ambiguous in the quantum metrology literature. In particular, many studies have not properly accounted for the resources used in a quantum protocol, often post-selecting on favourable outcomes[104,108,109].

To clarify the issue of quantum-enhancement in metrology, I propose the following test: given that I send n probes per trial through my sample (or, depending on the experiment, an average of n photons per trial), do I acquire more information on a given parameter of interest than would *ever be possible* using n uncorrelated probe states? This is a subtly different (and stronger) claim than beating the *standard interferometric limit* (SIL), in which case more information is acquired than would be possible using n uncorrelated photons and the same measurement apparatus. Importantly, given these definitions, post-selection (i.e.

choosing not to analyse some trials) cannot improve quantum enhancement. To date, very few experiments have shown quantum enhancement according to this criteria.

Squeezed light has been used to improve the sensitivity of both the GEO600 and LIGO gravitational wave detectors, allowing sub-SIL measurements[107,110–112].[1] Additionally, there has been at least one experiment in which a proper accounting of resources suggests that sub-SQL quantum enhancement has been achieved[7]. In this experiment, a single-mode squeezed state was used to probe an optical phase, and was then measured using homodyne detection. However, this requires a local oscillator to act as a phase reference, which must be stabilised relative to the probe path - in effect, the local oscillator path is the second arm of an interferometer with the probe state. This local oscillator was excluded from the resource count in this experiment. Although there are some practical applications in which this might not be a problem, there are many situations in which one might consider the light in both arms of the interferometer to constitute a resource, for example, when probing the relative phase induced by different regions of a delicate sample. Such cases would not be compatible with a local-oscillator-based measurement.

5.1 Phase estimation using Holland-Burnett states

Alternative approaches based on photon-counting measurements can be shown to provide sub-SQL precision without a local oscillator. For states with a definite number of photons N, the N00N states introduced in Section 4.1 provide the optimal precision for phase estimation

---

[1] In the case of the GEO600 detector experiment, careful analysis shows that the enhancements achieved were on the order necessary to surpass the SQL[111]. However, without additional details on the exact losses in the experiment it is not possible to definitively confirm this.

in the lossless case[113], with a quantum Fisher information (QFI)

$$\mathcal{I}_{\text{N00N}}(\theta) = N^2. \tag{5.1}$$

Unfortunately, these states are exponentially difficult to generate using linear optics and are extremely sensitive to the losses present in any realistic experiment.[2] Given a total transmission efficiency of η, the QFI for N00N states is reduced to

$$\mathcal{I}_{\text{N00N}}(\theta) = N^2\eta^N. \tag{5.2}$$

This reduction occurs because the loss of even a single photon from a N00N state removes all phase information. The probability that no photons are lost during transmission is given by the factor η^N appearing in the QFI[37].

Holland-Burnett states, denoted HB(K)[101], are more robust to loss, and can provide near optimal precision for phase estimation[114]. These states are also comparatively straightforward to generate experimentally, by simply combining two K-photon Fock states on a balanced beam splitter. This results in the state

$$\begin{aligned} |\text{HB}(K)\rangle &= \hat{U}^{\text{BS}}(1/2)\,|K,K\rangle \qquad (5.3)\\ &= \sum_{n=0}^{K} A_n\,|2n, 2K-2n\rangle\,, \qquad (5.4)\\ \text{where } A_n &= \frac{\sqrt{(2n)!(2K-2n)!}}{2^K n!(K-n)!}. \end{aligned}$$

The relative weights of these terms, as are shown for $K = 10$ in Fig. 5.1, can give an

---

[2] Although exact N00N states are experimentally challenging to generate, a promising approach to generating approximate N00N states is by mixing Fock states and coherent states on a beam splitter[105].

intuition for the source of the quantum enhancement from using HB(K) states, as well as their comparative robustness. As with N00N states, HB(K) states have terms with a large difference in photon number between each mode, which will acquire large phase differences in the interferometer. However, unlike for a N00N state, losing photons from HB(K) states still leaves some of the initial superposition intact. This is because almost all of the terms have at least one photon in both of the modes, and therefore less information is lost when the missing photons are traced over.

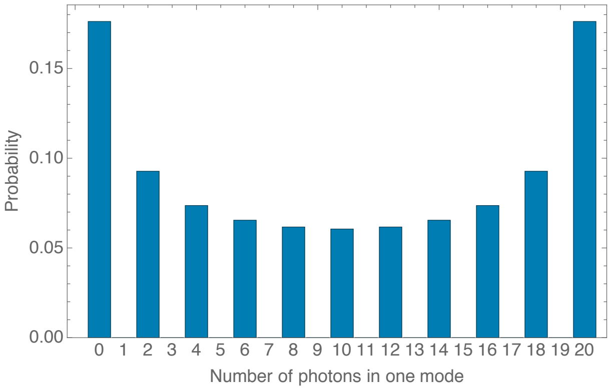

Figure 5.1: Probabilities $|\langle n, 2k-n|\ \mathrm{HB}(K)\rangle|^2$ associated with each superposition term in the Holland Burnett HB(10) state, labelled by the photon number n in the first mode. As can be seen, quantum interference encourages terms with a large difference in photon number between the two modes (small and large n values).

In the lossless case, the QFI for phase estimation using HB(K) states (which consist of $N = 2K$ photons) is given by

$$\mathcal{I}_{\mathrm{HB}} = N(N/2+1). \tag{5.5}$$

As can be seen, this gives the same scaling with N as the N00N states, although with a constant pre-factor that is half the size. Unfortunately, it is not possible to give an analytic expression for the QFI in the presence of loss in both arms of the interferometer[76,115].

Instead, here I will calculate the classical Fisher information for phase estimation using HB states and photon-number resolving detection. I will show that this measurement scheme can saturate the QCRB under lossless conditions.

In the Heisenberg picture, a balanced Mach-Zehnder interferometer (Fig. 5.2) implements the modal transformations

$$\begin{pmatrix} \hat{a}_j^\dagger \\ \hat{a}_k^\dagger \end{pmatrix} \rightarrow e^{\mathrm{i}\frac{\theta}{2}} \begin{pmatrix} \cos\frac{\theta}{2} & \mathrm{i}\sin\frac{\theta}{2} \\ \mathrm{i}\sin\frac{\theta}{2} & \cos\frac{\theta}{2} \end{pmatrix} \begin{pmatrix} \hat{a}_j^\dagger \\ \hat{a}_k^\dagger \end{pmatrix}. \tag{5.6}$$

Using this relation, one can determine the evolution of initial Fock state inputs

$$|K,K\rangle \rightarrow \frac{1}{K!}\left(\cos\frac{\theta}{2}\hat{a}_j^\dagger + \mathrm{i}\sin\frac{\theta}{2}\hat{a}_k^\dagger\right)^K \left(\mathrm{i}\sin\frac{\theta}{2}\hat{a}_j^\dagger + \cos\frac{\theta}{2}\hat{a}_k^\dagger\right)^K |0\rangle \tag{5.7}$$

$$= \frac{(\mathrm{i}\cos\frac{\theta}{2}\sin\frac{\theta}{2})^K}{K!}\sum_x^K\sum_y^K \binom{K}{x}\binom{K}{y}(\mathrm{i}\tan\frac{\theta}{2})^{y-x}(\hat{a}_j^\dagger)^{x+y}(\hat{a}_k^\dagger)^{2K-x-y}|0\rangle \tag{5.8}$$

This sum can be evaluated to find that

$$|K,K\rangle \rightarrow \sum_x^{2K} \begin{cases} (-\mathrm{i})^{K-x}\sqrt{\frac{x!}{(2K-x)!}}P_K^{K-x}(\cos\theta)\,|x,2K-x\rangle & : x \leq K \\ (-\mathrm{i})^{x-K}\sqrt{\frac{(2K-x)!}{x!}}P_K^{x-K}(\cos\theta)\,|x,2K-x\rangle & : x \geq K \end{cases} \tag{5.9}$$

where $P_K^{K-x}(\cos\theta)$ represent the associated Legendre polynomials.

I now show that the QCRB is saturated for $\theta = 0$, noting that it can further be shown that it is also saturated for all other values of θ[76]. In this case, it is only necessary to consider the outcome corresponding to detecting K photons in each mode, with completeness of the set of outcomes enforced by simply grouping all other outcomes together into one. The probability of detecting K photons in each mode is simply given by $p(K,K|\theta) = P_K(\cos\theta)^2$.

Therefore the total Fisher information for these two outcomes is given by (Eqn. 4.5)

$$\mathcal{F}_{\mathrm{PNRD}}(\theta) = \frac{[\partial_\theta p(K,K|\theta)]^2}{p(K,K|\theta)} + \frac{[\partial_\theta 1 - p(K,K|\theta)]^2}{1 - p(K,K|\theta)} \tag{5.10}$$

$$= \frac{4(K+1)^2(\cot\theta P_K(\cos\theta) - \csc\theta P_{K+1}(\cos\theta))^2}{P_K(\cos\theta)^2 - 1} \tag{5.11}$$

In the limit of $\theta \to 0$, this gives $\mathcal{F}(0) = 2K(K+1)$, proving equality with $\mathcal{I}_{\mathrm{HB}}$ (Eqn. 5.5).

5.1.1 Phase estimation under lossy conditions

Previous works have examined experimental phase estimation using HB(K) states under lossy conditions[37,76,116]. Here I adopt a slightly different approach to these papers, focusing on the effects of imperfect preparation efficiency η_p and detection efficiency η_d. I model the effects of these efficiencies by inserting beam splitters to loss modes at appropriate points in the protocol (Fig. 5.2). Notice that since these efficiencies are the same for each arm, it is in fact possible to commute the losses through the phases and simply consider mathematically one loss stage that combines the effect of all of the losses. However, I make a distinction between the preparation efficiency and detection efficiency, since they contribute differently to the classical limits.

In the proposed definition of quantum enhancement, we care about the number of photons that interact with the sample. In the model, given N input photons, this will be $\eta_p N$, and so it is fair to compare quantum strategies to the best classical strategies that also send $\eta_p N$ photons through the sample. In contrast, losses due to the detection efficiency lead to a reduction in the information gained from the photons that interacted with the sample, and so it is not fair to also add this inefficiency to the equivalent classical

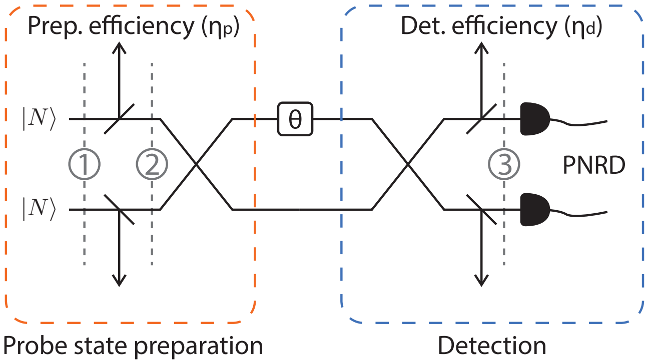

Figure 5.2: Model for phase estimation using HB(N) states, including losses due to finite preparation efficiencies η_p and detector efficiencies η_d. Numbers in circles are used in the main text to refer to the probe state at these points in the model.

strategy when calculating the SQL. In contrast, the related SIL is a weaker bound that gives the lowest achievable error possible using classical probes and the same experimental setup. Therefore, in this case it is possible to include the detection efficiency when calculating the information that can be gained from a classical protocol.

Borrowing from Ref. [76], I will use the abbreviation

$$\hat{X} \circ \hat{Y} \equiv \hat{X}\hat{Y}\hat{X}^{\dagger}. \tag{5.12}$$

I will also employ $\hat{U}_{ij}^{\mathrm{BS}}(\eta)$ (as introduced in Section 1.4.1) to denote a beam splitter unitary with transmissivity η between modes i and j.

The model starts (at point 1 in Fig. 5.2) with an initial state $\hat{\sigma}_1 = \hat{\rho}_a \otimes \hat{\rho}_b$, where $\hat{\rho}_{a,b} = |K\rangle\langle K|_{a,b}$ are pure Fock states. Loss is incorporated by mixing each mode with vacuum loss modes $\hat{\vartheta}$, labelled c and d respectively, and tracing over these modes. Note that I incorporate both η_p and η_d at once for simplicity. This gives (at point 2 in Fig. 5.2)

$$\hat{\sigma}_2 = \mathrm{Tr}_{cd}\left[\hat{U}^{\mathrm{BS}}_{ac}(\eta_p\eta_d) \circ \hat{U}^{\mathrm{BS}}_{bd}(\eta_p\eta_d) \circ (\hat{\sigma}_1 \otimes \hat{\vartheta}_c \otimes \hat{\vartheta}_d)\right]. \tag{5.13}$$

Next, the modes a and b are mixed on a balanced beam splitter, a phase is applied to mode a with the rotation operator $\hat{P}_a(\theta)$ (along with the identity operation $\mathbb{1}$ to mode b), and the modes a and b are mixed again. The final state is therefore (at point 3 in Fig. 5.2)

$$\hat{\sigma}_3 = \hat{U}^{\mathrm{BS}}_{ab}(1/2) \circ (\hat{P}_a(\theta) \otimes \mathbb{1}_b) \circ \hat{U}^{\mathrm{BS}}_{ab}(1/2) \circ \hat{\sigma}_2. \tag{5.14}$$

The probability of detecting m and n photons in modes a and b is then given by

$$\langle m, n| \, \hat{\sigma}_3 \, |m, n\rangle \, . \tag{5.15}$$

These measurement probabilities can be used to calculate the classical Fisher information using Eqn. 4.5. This is a complicated function of $\eta_p\eta_d$, however, it is lower bounded by its value at $\theta = 0$,

$$\mathcal{F}_{\mathrm{HB}} = N(N/2+1)(\eta_p\eta_d)^{N/2+1}. \tag{5.16}$$

As can be seen, this gives the same scaling with N as the N00N states, but with a square root improvement in the rate of degradation due to losses. Using this relation, I calculated the precision achievable using HB(1) and HB(2) states, and compared this to the SIL and the SQL (Fig. 5.3).

As can be seen, the threshold efficiencies for a sub-SQL measurement are close to the

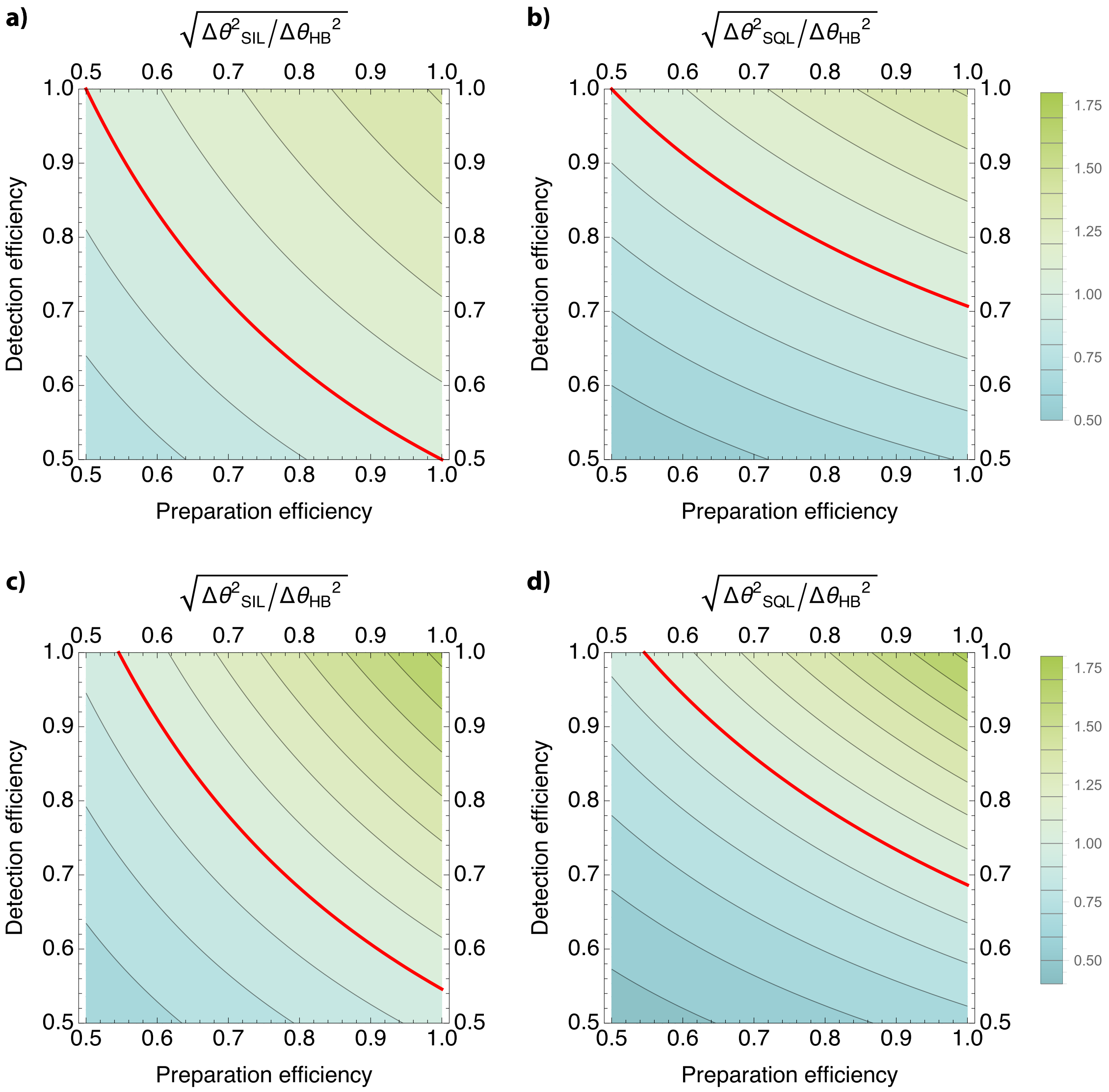

Figure 5.3: Ratio between the achievable error using HB(1) states and a) the SIL and b) the SQL, as a function of preparation efficiency η_p and detector efficiency η_d. The red line shows the contour at which equality is achieved. Similar plots for HB(2) states are shown in c) and d).

current state-of-the-art. We have been working to develop the experimental tools necessary to achieve this, including the high quantum efficiency TES detectors discussed in Chapter 3, and high preparation efficiency sources[42]. It is anticipated that this will soon allow us to demonstrate a HB(1) experiment with sub-SQL precision.

5.2 Phase estimation using two-mode squeezed vacuum

Experimental phase estimation with HB(K) states requires two Fock-state sources and two photon counting detectors. The most advanced approach for this achieving this would use two SPDC sources in a heralded configuration, and four TES detectors in all - two for heralding Fock states and two for the measurement. We do not as-of-yet have this capability; however, I have recently developed an alternative experimental proposal for demonstrating a sub-SQL phase measurement using only a single SPDC source and two photon-number-resolving detectors. A theoretical model for this scheme is shown in Fig. 5.4.

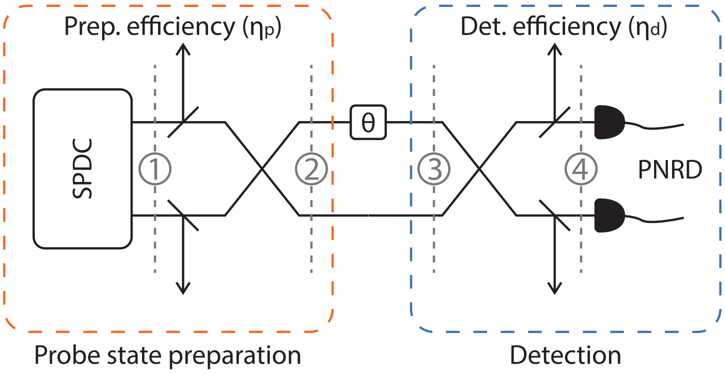

Figure 5.4: Model for phase estimation using SPDC to generate two-mode squeezed vacuum. Photon-number-resolving detectors (PNRD) are employed to measure the squeezed modes after the phase. Numbers in circles are used in the main text to refer to the probe state at these points in the model.

It is well known that it is possible to beat the SQL for phase estimation using the two-mode squeezed vacuum (TMSV) states that were introduced in Section 1.4.2. These are directly produced by SPDC sources. For Gaussian states such as TMSV, with first order moments $\bar{\boldsymbol{\alpha}}$ covariance matrix $\boldsymbol{\Gamma}$ and $\boldsymbol{\Omega}$ as defined in Section 1.3.2, it can be shown that the quantum Fisher information is given by[117]

$$\mathcal{I}(\theta) = 8\,\partial_\theta \tilde{\mathbf{\Gamma}}^T (16\,\mathbf{\Gamma} \otimes \mathbf{\Gamma} - \mathbf{\Omega} \otimes \mathbf{\Omega})^{-1} \partial_\theta \tilde{\mathbf{\Gamma}} + \frac{1}{2} \partial_\theta \bar{\boldsymbol{\alpha}}^T \mathbf{\Gamma}^{-1} \partial_\theta \bar{\boldsymbol{\alpha}}, \tag{5.17}$$

where $\tilde{\mathbf{\Gamma}}$ gives $\mathbf{\Gamma}$ reshaped into the form of a vector.[3]

This expression gives the QFI for Gaussian states with non-singular $\hat{\rho}$. However, many states of interest are singular, including all pure states. Although a general solution cannot be found for these states, a solution can be found for states that satisfy the relation

$$16\,(\mathbf{\Gamma}\,\mathbf{\Omega})^2 = -\nu^2 \mathbb{1}, \tag{5.18}$$

where $\mathbb{1}$ gives the identity matrix. This class of states (termed *isothermal* states by Monras[117]) conveniently includes pure states, and all of the states that I will consider here. For these states, the QFI is given by

$$\mathcal{I}(\theta) = \frac{1}{2} \frac{\nu^2}{1+\nu^2} \mathrm{Tr}\left[\partial_\theta \mathbf{\Gamma} \mathbf{\Gamma}^{-1} \partial_\theta \mathbf{\Gamma} \mathbf{\Gamma}^{-1}\right] + \frac{1}{2} \partial_\theta \bar{\boldsymbol{\alpha}}^T \mathbf{\Gamma}^{-1} \partial_\theta \bar{\boldsymbol{\alpha}} \tag{5.19}$$

In order to use the formulae, I need to determine the covariance matrix $\mathbf{\Gamma}$ and first order moments $\bar{\boldsymbol{\alpha}}$ for the state after application of the phase (and losses). The covariance matrix

---

[3] The differences between the expressions here and in previous work by Monras[117] are due to a difference in the definition of the quadratures.

for the initial TMSV state (at point 1 in Fig. 5.4) is given by

$$\boldsymbol{\Gamma}_1 = \begin{pmatrix} \frac{1}{4}\cosh(2r) & 0 & \frac{1}{2}\cosh(r)\sinh(r) & 0 \\ 0 & \frac{1}{4}\cosh(2r) & 0 & -\frac{1}{2}\cosh(r)\sinh(r) \\ \frac{1}{2}\cosh(r)\sinh(r) & 0 & \frac{1}{4}\cosh(2r) & 0 \\ 0 & -\frac{1}{2}\cosh(r)\sinh(r) & 0 & \frac{1}{4}\cosh(2r) \end{pmatrix}, \tag{5.20}$$

while the elements of $\bar{\boldsymbol{\alpha}}$ are all zero.

Interestingly, after the first balanced beam splitter (at point 2 in Fig. 5.4, but neglecting loss for the moment), the TMSV state is converted into two uncorrelated single-mode squeezed vacuum states, with

$$\boldsymbol{\Gamma}_2 = \begin{pmatrix} \frac{e^{-2r}}{4} & 0 & 0 & 0 \\ 0 & \frac{e^{2r}}{4} & 0 & 0 \\ 0 & 0 & \frac{e^{2r}}{4} & 0 \\ 0 & 0 & 0 & \frac{e^{-2r}}{4} \end{pmatrix}. \tag{5.21}$$

It may be initially surprising that this unentangled state is useful for quantum metrology. However, this result is in agreement with Ref. [118] and closely mirrors a recent work by Lang et al.[119], in which it was shown that the government state for phase measurement given two fixed mean photon-number input states is also made up of two unentangled single mode squeezed states.

Finally, I add in the phase evolution and the coupling to loss modes. Since the losses commute through the phase and beam splitters, I again incorporate the preparation and detection efficiencies at the same time. Additionally, instead of applying the phase θ to only one mode, as depicted in Fig. 5.4, I apply the phase θ_a to the first mode, and θ_b

to the second mode. I then calculate the QFI for the relative phase $\theta = \theta_a - \theta_b$. This is physically equivalent to the situation shown in Fig. 5.4 (due to global phase freedom), however, it ensures that the calculated QFI is for the relative phase between the modes. If I instead calculate the QFI for θ_a, I find that it is double the QFI for θ. This is because the QFI does not discriminate between measurements with and without an external phase reference[120]. It would be possible to obtain this extra information on θ_a by measuring using an external phase reference, while completely ignoring the second mode. Calculating the QFI for $\theta = \theta_a - \theta_b$ therefore ensures that I am considering the measurement of the relative phase of the two modes. Note that this is not an issue for fixed photon number states, as they do not carry a phase. Therefore an external phase reference cannot provide any information on the phase evolution, and it is only through the relative phase evolution of the different components of a superposition state that phases are observable.

The covariance matrix for the probe state (at point 3 in Fig. 5.4) is now given by

$$\mathbf{\Gamma}_3 = \begin{pmatrix} A_-(\theta_a) & B(\theta_a) & 0 & 0 \\ B(\theta_a) & A_+(\theta_a) & 0 & 0 \\ 0 & 0 & A_+(\theta_b) & B(\theta_b) \\ 0 & 0 & B(\theta_b) & A_-(\theta_b) \end{pmatrix} \tag{5.22}$$

where

$$A_\pm(\theta) = \frac{1}{4}\left(\eta_p\eta_d\left(\cosh(2r) \pm \cos(2\theta)\sinh(2r)\right) + (1-\eta_p\eta_d)\right), \tag{5.23}$$

$$B(\theta) = -\frac{1}{4}\eta_p\eta_d\sin(2\theta)\sinh(2r). \tag{5.24}$$

Using Eqn. 5.19 and the expression for $\mathbf{\Gamma}_3$, I can calculate the QFI for θ[121],

$$\mathcal{I}_{\mathrm{TMSV}}(\theta) = \frac{N(N+2)(\eta_p\eta_d)^2}{1+N(1-\eta_p\eta_d)\eta_p\eta_d}. \tag{5.25}$$

The results of this calculation show that TMSV can in principle beat the standard quantum limit ($\mathcal{I} = N$). However, it is of course necessary to show that a feasible measurement can saturate this bound, or at least still provide better-than-SQL performance. In the lossless limit, it has been shown that parity detection can saturate the QCRB[122]. Unfortunately, this approach is extremely sensitive to loss, and cannot beat the SQL for total system efficiencies of less than 90%[121]. Additionally, there is currently no simple experimental scheme for parity detection (i.e. a scheme that just gives parity information).

I note that in the lossless limit, homodyne detection can also saturate the QCRB for phase estimation[117]. However, as discussed previously, this requires a phase-stable local oscillator, which must be counted as a resource for many metrological problems of interest. In addition, an interesting observation for general metrological problems is that, under lossy conditions, homodyne detection can no longer in general saturate the QCRB for parameter estimation using Gaussian states[117]. For isothermal states with zero first order moments, it can be shown that the maximum achievable classical Fisher information for any measurement scheme consisting of a set of arbitrary Gaussian operations followed by homodyne detection is given by

$$\mathcal{F}_{\mathrm{Hom}}(\theta) = \frac{1+\nu^2}{2\nu^2}\mathcal{I}(\theta). \tag{5.26}$$

For phase estimation using TMSV under lossy conditions, this gives

$$\mathcal{F}_{\text{Hom}}(\theta) = \frac{N(N+2)(\eta_p \eta_d)^2}{1 + 2N(1 - \eta_p \eta_d)\eta_p \eta_d}. \tag{5.27}$$

Our proposed scheme for phase estimation with TMSV employs photon-counting detection. I have analysed this scheme using a similar model experimental setup as for HB(K) states (Fig. 5.4), in which losses in both preparation and detection are considered. This scheme is not dissimilar to that considered by Ref. [123], although there the authors post-selected on only a single detection outcome and neglected the effects of loss. In this more general analysis, I consider all possible detection outcomes, and find that it should be possible to achieve a sub-SQL precision given a realistic loss budget, assuming the experimental state of the art.

I start (at point 1 in Fig. 5.4) with the initial two-mode state (equivalent to Eqn. 1.70 with $\lambda = \tanh(r)$)

$$|\psi\rangle_1 = \sqrt{1-\lambda^2} \sum_{N=0}^{\infty} \lambda^N |N\rangle_a |N\rangle_b . \tag{5.28}$$

The corresponding density matrix is given by $\hat{\sigma}_1 = |\psi\rangle_1 \langle\psi|$. I now follow the same procedure as for HB states in Section 5.1.1. Loss is incorporated by mixing each mode with vacuum loss modes $\hat{\vartheta}$, labelled c and d respectively, and tracing over these modes. This gives (at point 2 in Fig. 5.4)

$$\hat{\sigma}_2 = \hat{U}^{\text{BS}}_{ab}(1/2) \circ \text{Tr}_{cd} \left[\hat{U}^{\text{BS}}_{ac}(\eta_p \eta_d) \circ \hat{U}^{\text{BS}}_{bd}(\eta_p \eta_d) \circ (\hat{\sigma}_1 \otimes \hat{\vartheta}_c \otimes \hat{\vartheta}_d) \right]. \tag{5.29}$$

Finally, adding the phase θ and the second beam splitter gives (at point 4 in Fig. 5.4) the output state

$$\hat{\sigma}_4 = \hat{U}_{ab}^{\mathrm{BS}}(1/2) \circ (\hat{P}_a(\theta) \otimes \mathbb{1}) \circ \hat{\sigma}_2. \tag{5.30}$$

The probability of detecting m and n photons in modes a and b is then given by

$$\langle m, n| \, \hat{\sigma}_4 \, |m, n\rangle \, . \tag{5.31}$$

Fig. 5.5 shows the achievable error for the PNRD measurement scheme, given specified preparation efficiencies η_p and detection efficiencies η_d (simple analytic expressions for the classical Fisher information were not obtained). As shown in Chapter 3, our transition-edge detectors have estimated quantum efficiencies of 98% (+2%/−8%). Additionally, SPDC source preparation efficiencies above 80% have been demonstrated[42,47,91]. We are currently working to integrate such a high-preparation-efficiency source based on Eckstein et al.'s design[47] with our detectors. Comparing these efficiencies to the results of these calculations therefore suggests that we may soon be in a position to be able to carry out a sub-SQL phase estimation experiment using this scheme.

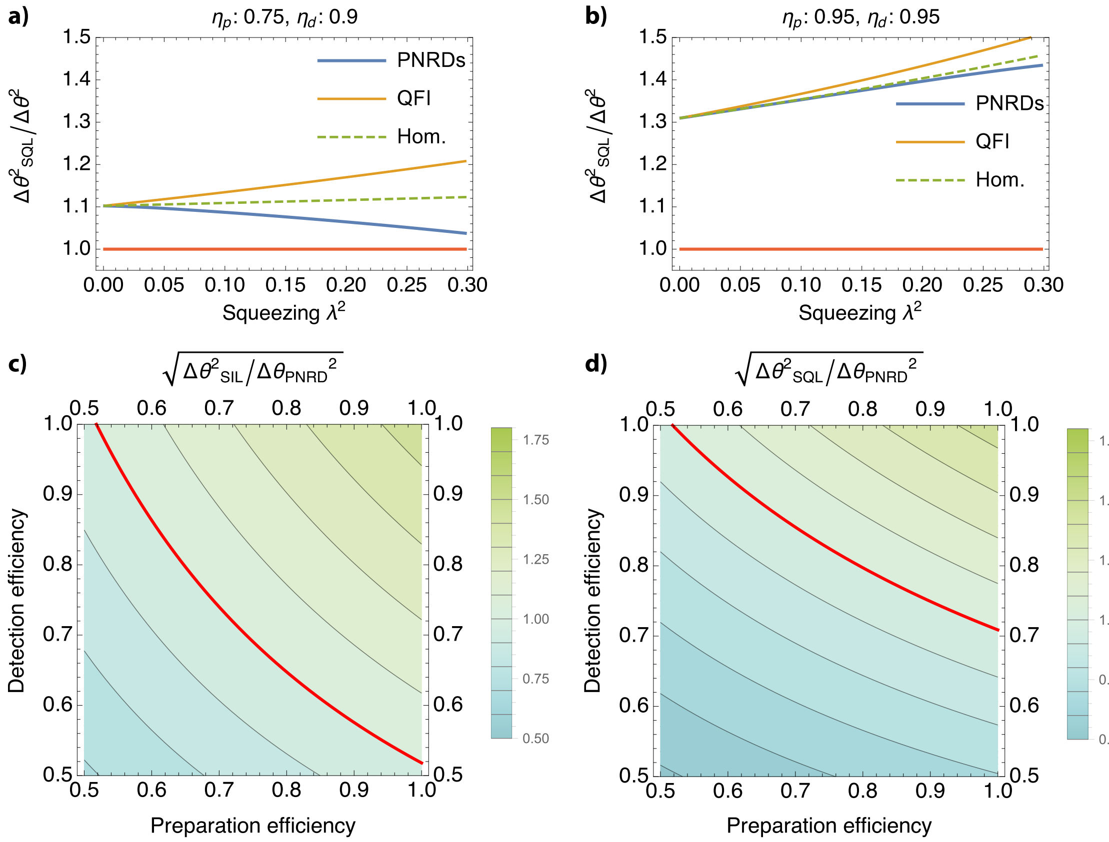

Figure 5.5: a), b) Ratio of the achievable error for the PNRD measurement scheme to the SQL for specified preparation efficiencies η_p and detection efficiencies η_d, plotted for different levels of squeezing of the SPDC source (blue). The ratio is given such that such that a bigger ratio implies a greater advantage. Also plotted are the ratios of the QFI to the SQL (orange), and for reference, the FI for homodyne detection to the SQL (green dashed). As can be seen, under anticipated experimental conditions, the quantum enhancement is largest for small squeezing levels. In c) and d) the squeezing level is fixed at $\lambda^2 = 0.05$. Plotted are the ratios between the achievable errors for our scheme and a) the SIL and b) the SQL, as a function of the preparation efficiency η_p and detector efficiency η_d. The red line shows the contour at which equality is achieved.

Chapter 6

Multi-parameter quantum metrology

Chapter 4 introduced the central framework of quantum enhanced metrology. For simplicity, this initial discussion was restricted to the estimation of a single parameter. However, almost all real world systems are characterised by many different variables, and it is often of importance to be able to measure these parameters simultaneously. This is not a trivial extension to single parameter estimation, and is more involved theoretically[124].

Several works have explored aspects of multiple parameter estimation from a quantum information perspective. In the case of the estimation of parameters characterising a set of non-commuting unitary operations, it was shown that entangled states and measurements can attain the Heisenberg limit in the number of photons used in each probe state[125–127]. In the commuting case, the problem of estimating d phases with an ensemble of single-photon probe states has been considered. A Bayesian approach showed that the cost of estimation increases with the number of parameters involved[128], and a Fisher information based approach showed that entangling two multi-level systems provides no advantage over using a single multi-level system[129]. More recently, the error associated with estimating two phases using three and four mode interferometers (and three and four photons respectively) has been investigated[130]. Finally, the simultaneous measurement of phase and loss[124], and separately, phase and phase diffusion[131] have been studied.

6.1 Quantum imaging

One of the most important metrology problems to the wider research community is that of microscopy and imaging. Producing a quantum advantage in imaging would be of significant benefit in fields such as biology, particularly for the imaging of samples that are sensitive to the total illumination. Various approaches to quantum imaging have been proposed, typically exploring methods for increasing the diffraction limited resolution of optical imaging systems[132–138]. A recent classical investigation of quantum enhanced imaging made use of point estimation theory, quantifying differences between images by means of a single parameter[139]. However, imaging is inherently a multi-parameter estimation problem, and deeper insights can be gained by studying it as such.

As an initial exploration of quantum imaging, we have considered a simple discretised model for phase imaging based on this approach. Phase imaging is a cornerstone of optical microscopy (Fig. 6.1a), typically realised using the related techniques of phase contrast and differential interference contrast imaging[140], that allows differences in refractive index to be detected in otherwise transparent media. So far, the potential for quantum enhancements to these techniques has yet to be explored. Our approach maps phase imaging onto the problem of multiple simultaneous phase estimation (Fig. 6.1b).

As I will show, our results provide a strategy for the estimation of multiple phases using correlated quantum states, in which the multi-parameter nature of the problem leads

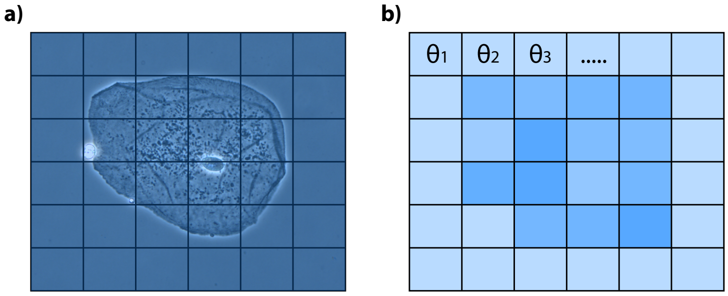

Figure 6.1: a) A phase contrast image (courtesy of wikipedia) b) A discretised model for phase imaging consists of estimating a series of phases simultaneously.

to an intrinsic benefit when exploiting quantum resources. A surprising outcome of our analysis is that our quantum strategy provides an $\mathcal{O}(d)$ advantage, where d is the number of phases, over the optimal quantum individual estimation scheme of using N00N states[113]. We further show that a resource advantage can be provided over the best classical phase estimation schemes.

6.1.1 Framework for multi-parameter metrology

In order to tackle this problem, an extension of the formalism developed in Section 4.1 is required to incorporate multiple parameters. In this case, the precision with which it is possible to measure the vector of parameters $\boldsymbol{\theta}$ is governed by the covariance matrix $\mathrm{Cov}(\boldsymbol{\theta})$, defined as

$$[\mathrm{Cov}(\boldsymbol{\theta})]_{l,m} = \sum_{\boldsymbol{\varphi}} (\varphi_l - \theta_l)(\varphi_m - \theta_m)\, p(\boldsymbol{\varphi}|\boldsymbol{\theta}), \tag{6.1}$$

where $\boldsymbol{\varphi}$ represents the estimated value of $\boldsymbol{\theta}$.

The associated multi-parameter quantum Cramér-Rao bound [141] is then given by

$$\mathrm{Cov}(\boldsymbol{\theta}) \geq (M\mathcal{I}_{\boldsymbol{\theta}})^{-1}. \tag{6.2}$$

$\mathcal{I}_{\boldsymbol{\theta}}$ is now the quantum Fisher information *matrix* while M remains as the classical contribution from repeating the experiment M times.[1] This is a $d \times d$ sized matrix inequality which is satisfied when $\mathrm{Cov}(\boldsymbol{\theta}) - (M\mathcal{I}_{\boldsymbol{\theta}})^{-1}$ is a positive matrix.

We choose to restrict ourselves to pure states, since, as discussed previously, it is known that pure states maximise the quantum Fisher information. The QFI matrix is therefore given by [141,142]

$$[\mathcal{I}_{\boldsymbol{\theta}}]_{l,m} = \frac{1}{2} \langle\psi_{\boldsymbol{\theta}}| (\hat{L}_l\hat{L}_m + \hat{L}_m\hat{L}_l) |\psi_{\boldsymbol{\theta}}\rangle . \tag{6.3}$$

where the operator $\hat{L}_m$ is the symmetric logarithmic derivative for the parameter θ_m as defined for pure states in Eqn. 4.10.

Unlike in the single parameter case, saturation of the QCRB for all parameters simultaneously is not guaranteed. For pure states probes, in order for this bound to be saturated the condition $\mathrm{Im}\left[\langle\psi_{\boldsymbol{\theta}}|\, \hat{L}_l\, \hat{L}_m\, |\psi_{\boldsymbol{\theta}}\rangle\right] = 0$ must be satisfied [143]. This is not always the case in multi-parameter estimation problems [124].

6.2 Multiple-phase estimation

We aim to address the question of how to estimate d independent phases most efficiently with N photons. In order to do this, we adopt a model consisting of a $d+1$-mode interferometer with a preparation, an interaction, and a measurement stage as in Fig. (6.2). The

---

[1] In this multi-parameter scenario, a single trial has to necessarily consist of an estimate of all d phases.

preparation stage creates an arbitrary pure input state of the form

$$|\psi\rangle = \sum_{k=1}^{D} \alpha_k \, |N_{k,0}, N_{k,1}, ..N_{k,d}\rangle \equiv \sum_{k=1}^{D} \alpha_k \, |\mathbf{N}_k\rangle \, . \tag{6.4}$$

The distribution of photons in a given configuration k is expressed compactly by a vector $\mathbf{N}_k$, composed of individual components $N_{k,m}$ that give the number of photons in mode m, such that $\sum_{m=0}^{d} N_{k,m} = N$. $D = (N+d)!/N!d!$ is the number of distinct configurations of distributing N photons across $d+1$ modes. Exploiting the global phase freedom of the problem, we choose the mode labelled 0 as our reference mode and therefore the modes registering the phases are labelled $\{1, \cdots, d\}$. To each of these configurations, we associate a complex amplitude α_k. The state is normalised by requiring that $\sum_{k=1}^{D} |\alpha_k|^2 = 1$.

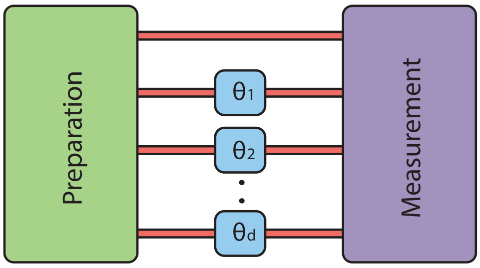

Figure 6.2: We consider the simultaneous estimation of d phases using a setup consisting of state preparation (green), independent phase application in each mode (blue) and state measurement (purple).

The input state acquires a phase through the unitary transformation $\hat{U}_{\boldsymbol{\theta}} = e^{i\sum_{m=1}^{d} \hat{N}_m \theta_m}$, where θ_m is the phase accrued and $\hat{N}_m$ the number operator for mode m. Denoting $\boldsymbol{\theta} = \{\theta_1, \cdots, \theta_d\}$, the evolved state is given by

$$|\psi_{\boldsymbol{\theta}}\rangle = \hat{U}_{\boldsymbol{\theta}} \, |\psi\rangle = \sum_{k=1}^{D} \alpha_k e^{\mathrm{i}\mathbf{N}_k \cdot \boldsymbol{\theta}} \, |\mathbf{N}_k\rangle \, . \tag{6.5}$$

6.2.1 Bounds for multiple-phase estimation

Given our expression for the probe state after application of the phases (Eqn. 6.5), we find

$$\hat{L}_{\theta_l} = 2\sum_{i,j} i(N_{i,l} - N_{j,l})\, e^{i\,(\mathbf{N}_i - \mathbf{N}_j).\boldsymbol{\theta}} \alpha_i\, \alpha_j^* \left|\mathbf{N}_i\right\rangle \left\langle \mathbf{N}_j\right| \tag{6.6}$$

and

$$\hat{L}_{\theta_l}\hat{L}_{\theta_m} = -4\sum_{i,j,k}(N_{i,l} - N_{j,l})(N_{j,m} - N_{k,m}) e^{i\,(\mathbf{N}_i - \mathbf{N}_k).\boldsymbol{\theta}} \alpha_i \left|\alpha_j\right|^2\, \alpha_k^* \,\left|\mathbf{N}_i\right\rangle \left\langle \mathbf{N}_k\right|. \tag{6.7}$$

We can use these expressions to calculate the QFI

$$\begin{aligned} \left[\mathcal{I}_{\boldsymbol{\theta}}\right]_{l,m} &= 4\sum_{i,j}(N_{i,l}N_{i,m} - N_{i,l}N_{j,m}) \left|\alpha_i\right|^2\, \left|\alpha_j\right|^2 \\ &= 4\sum_{i} N_{i,l}N_{i,m} \left|\alpha_i\right|^2 - 4\sum_{i,j} N_{i,l}N_{j,m} \left|\alpha_i\right|^2\, \left|\alpha_j\right|^2. \end{aligned} \tag{6.8}$$

This is more neatly expressed as

$$\mathcal{I}_{\boldsymbol{\theta}} = 4\sum_{i} \left|\alpha_i\right|^2 \mathbf{N}_i\mathbf{N}_i^T - 4\sum_{i,j} \left|\alpha_i\right|^2 \left|\alpha_j\right|^2 \mathbf{N}_i\mathbf{N}_j^T. \tag{6.9}$$

Since we are interested in purely quantum enhancements, we henceforth set $M = 1$ in Eqn. (6.2). Then taking the trace of both sides gives a lower bound on the total variance of all the phases estimated

$$\left|\Delta\boldsymbol{\theta}\right|^2 \equiv \sum_{m=1}^{d} \delta\theta_m^2 \equiv \mathrm{Tr}\left[\mathrm{Cov}(\boldsymbol{\theta})\right] \geq \mathrm{Tr}\left[\mathcal{I}_{\boldsymbol{\theta}}^{-1}\right]. \tag{6.10}$$

Additionally, in order to determine whether it is possible to saturate this bound, we calculate

$$\langle\psi_{\boldsymbol{\theta}}|\, \hat{L}_{\theta_l}\hat{L}_{\theta_m}\, |\psi_{\boldsymbol{\theta}}\rangle = 4\sum_{i,j}(N_{i,l}N_{i,m} - N_{i,l}N_{j,m})\, |\alpha_i|^2\ |\alpha_j|^2\, . \tag{6.11}$$

It is clear that this is real for all l, m and $\boldsymbol{\theta}$ and thus the QCRB can be saturated for the estimation of multiple phases simultaneously.

6.2.2 Optimal probe states

Here we consider three different scenarios in turn. We start with the case of simultaneous multiple-phase estimation, before considering the estimation of each phase simultaneously. Finally we consider the case of phase estimation using only classical resources.

Simultaneous quantum multiple-phase estimation

It is interesting to note that the diagonal elements $[\mathcal{I}_{\boldsymbol{\theta}}]_{\,l,l}$ reduce to the variance in the occupation of mode l:

$$[\mathcal{I}_{\boldsymbol{\theta}}]_{\,l,l} = 4\sum_i\ N_{i,l}^2\, |\alpha_i|^2 - 4\,(\sum_i N_{i,l}\, |\alpha_i|^2)^{\,2} \tag{6.12}$$

$$= 4(\langle N_l^2\rangle - \langle N_l\rangle^2). \tag{6.13}$$

In the single-parameter case, this is the origin of the enhanced precision of N00N states, since for these states this variance scales as N^2. This suggests that states with a large photon number variance in each mode should also be optimal for multiple phase estimation. Based on this intuition, we consider a generalisation in which our quantum probe is a coherent superposition of N photons in one of the modes and none in any of the other d modes.

Due to the symmetry of our problem over the d modes in which we choose to estimate the phases, we specifically consider the quantum probe

$$|\psi\rangle \quad = \alpha\left(|0,N,0,..,0\rangle + |0,0,N,..,0\rangle\,..+|0,0,..,N\rangle\right) + \beta\,|N,0,0,..,0\rangle \tag{6.14}$$

with the constraint that $d\alpha^2 + \beta^2 = 1$. For these states, the QFI matrix can be found using Eqn. (6.9). As the QFI only depends on the amplitude of α and β, we assume that they are real without loss of generality. Under this assumption, β is uniquely determined by the normalisation condition and is therefore no longer an independent variable. We therefore find that

$$[\mathcal{I}_{\boldsymbol{\theta}}]_{\,l,m} = 4N^2\,(\delta_{l,m}\,\alpha^2 - \alpha^4). \tag{6.15}$$

The minimum total variance in Eqn. (6.10) can be found by minimising Tr $\left[\mathcal{I}_{\boldsymbol{\theta}}^{-1}\right]$ via differentiation with respect to α, giving

$$|\Delta\boldsymbol{\theta}_s|^2 = \frac{(1+\sqrt{d})^2\,d/4}{N^2} \tag{6.16}$$

for $\alpha = 1/\sqrt{d+\sqrt{d}}$. We label the corresponding probe state as $|\psi_s\rangle$, which has the form

$$\begin{aligned} |\psi_s\rangle \quad &= \tfrac{1}{\sqrt{d+\sqrt{d}}}\left(|0,N,0..,0\rangle + |0,0,N,..,0\rangle\,..+|0,0,..,0,N\rangle\right) \\ &\qquad + \tfrac{1}{\sqrt{1+\sqrt{d}}}\,|N,0,0,..,0\rangle\,. \end{aligned} \tag{6.17}$$

Independent quantum multiple-phase estimation

This bound should now be compared to the variance of estimating the d phases $\boldsymbol{\theta}$ using d separate interferometers independently using optimal N00N states.

We first determine the best strategy for the estimation of two phases with an even total number of photons $2n$, using $n-x$ and $n+x$ photons for each phase to be estimated respectively. Since, for a N00N state, the variance for estimating a single phase using m photons is $1/m^2$, we find that the total variance for estimating the two independent phases is

$$|\Delta\boldsymbol{\theta}|^2 = \frac{1}{(n+x)^2} + \frac{1}{(n-x)^2}. \tag{6.18}$$

This has a minimum when

$$\begin{aligned} \partial_x |\Delta\boldsymbol{\theta}|^2 &= -2\left(\frac{1}{(n+x)^3} - \frac{1}{(n-x)^3}\right) = 0 \\ &\Rightarrow 3xn^2 + x^3 = 0. \end{aligned} \tag{6.19}$$

The only real root occurs when $x=0$. Therefore the minimum error is achieved when the number of photons used to estimate each phase is the same (n).

For an odd number $2n+1$ of photons, using $n-x$ and $n+x+1$ photons for each mode respectively, we find

$$|\Delta\boldsymbol{\theta}|^2 = \frac{1}{(n+x+1)^2} + \frac{1}{(n-x)^2}. \tag{6.20}$$

This has a minimum when

$$\begin{aligned}\partial_x \left|\Delta\boldsymbol{\theta}\right|^2 = -2\left(\frac{1}{(n+x+1)^3} - \frac{1}{(n-x)^3}\right) = 0 \\ \Rightarrow (1+2x)(x^2+x+3n^2+3n+1) = 0.\end{aligned} \tag{6.21}$$

This only has a real root for $x=-1/2$. Therefore the minimum realisable error is achieved when using n and $n+1$ photons or symmetrically, $n+1$ and n photons to estimate the respective phases.

Since this is the case for the estimation of two phases, it can be seen that a similar pairwise comparison could be carried out for different phases in a $d>2$ phase estimation problem. In each case, if there is an imbalance of more than 1 photon between the resources employed to estimate each phase, a smaller error can be achieved by re-balancing the resources between the phases. This will eventually lead to the optimal phase estimation strategy in which the photons are divided as evenly as possible between all of the phases. More specifically, if N photons are used, we define n as the quotient of N/d and r as the remainder. The best strategy employs $n+1$ photons to estimate each of r phases, and n photons to estimate each of the other $d-r$ phases. Therefore

$$\left|\Delta\boldsymbol{\theta}\right|^2 = \frac{d-r}{n^2} + \frac{r}{(n+1)^2}. \tag{6.22}$$

Here we show that the approximate expression given by assuming that N is divisible by d, denoted here as $\left|\Delta\boldsymbol{\theta}_{\text{approx}}\right|^2$, always gives a better than (or equal to) estimate of the error achievable using N00N states as the exact derivation.

$$|\Delta\boldsymbol{\theta}_{\text{approx}}|^2 = d\left(\frac{d}{N}\right)^2 = d\left(\frac{d}{nd+r}\right)^2 \tag{6.23}$$

$$(|\Delta\boldsymbol{\theta}_{\text{approx}}|^2 - |\Delta\boldsymbol{\theta}|^2) \propto d^3n^2(n+1)^2 - (nd+r)^2((n+1)^2(d-r)+rn^2)$$

$$= (r-d)(r+2nr+2nd+3n^2d) \tag{6.24}$$

$$\therefore (|\Delta\boldsymbol{\theta}_{\text{approx}}|^2 - |\Delta\boldsymbol{\theta}|^2) < 0, \tag{6.25}$$

since $r < d$. Thus the approximate expression gives a better error than is actually achievable, with equality if and only if N is exactly divisible by d. This lower bounds the total variance for independent quantum multiple-phase estimation as

$$|\Delta\boldsymbol{\theta}_{\text{ind}}|^2 = d^3/N^2. \tag{6.26}$$

Classical multiple-phase estimation

In a classical strategy where the probe is restricted to uncorrelated coherent states of the form $\otimes_{i=1}^{d} |\alpha_i\rangle$, such that $\sum_{i=1}^{d} \langle\alpha_i| \hat{N}_i |\alpha_i\rangle = N$, a similar argument shows that the total variance is bounded by

$$|\Delta\boldsymbol{\theta}_{\text{clas}}|^2 = d^2/N. \tag{6.27}$$

Comparing simultaneous and individual strategies

As expected, both the quantum strategies follow the Heisenberg scaling in the total number of photons for the total variance. However, the quantum simultaneous strategy has an

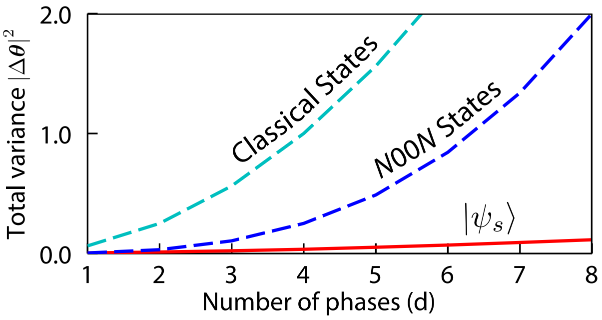

Figure 6.3: Strategies for multiple phase estimation using $N = 16$ photons. The red line gives the total variance $|\Delta\boldsymbol{\theta}_s|^2$ for the quantum simultaneous strategy using the states $|\psi_s\rangle$, the blue dashed line gives the variance $|\Delta\boldsymbol{\theta}_{\text{ind}}|^2$ achievable using N00N states, and the cyan dashed line gives the variance $|\Delta\boldsymbol{\theta}_{\text{clas}}|^2$ for an equivalent classical state.

additional advantage over the others. Comparing the three bounds, we find

$$|\Delta\boldsymbol{\theta}_s|^2 \leq |\Delta\boldsymbol{\theta}_{\text{ind}}|^2 \leq |\Delta\boldsymbol{\theta}_{\text{clas}}|^2 , \tag{6.28}$$

where the first inequality is strict for $d > 1$, and the second for $d < N$. As typical instances would consist of many more photons than the number of parameters to be estimated, we are guaranteed that our strategy of simultaneous quantum estimation is better than individual estimation. Furthermore, the advantage, shown in Fig. (6.3), over the best quantum strategy of independent estimation improves linearly with the number of phases, scaling as $1/4d$. This is our main result.

The advantage of simultaneous quantum phase estimation using $|\psi_s\rangle$ (Eqn. 6.17) is $\mathcal{O}(d)$. However, this linear advantage is not unique. For example, setting $\alpha = \beta = 1/\sqrt{d+1}$ in Eqn. (6.14) provides a slightly different probe state $|\psi_w\rangle$ that has a total variance of $|\Delta\boldsymbol{\theta}|^2 = d(d+1)/2N^2$, providing a scaling enhancement of $1/2d$.

$$|\psi_w\rangle \;\; = \tfrac{1}{\sqrt{d+1}} \left(|N, 0, 0.., 0\rangle + |0, N, 0, .., 0\rangle .. + |0, 0, .., 0, N\rangle\right) \tag{6.29}$$

This state therefore preserves the $\mathcal{O}(d)$ scaling improvement over individual phase estimation, and provides a total variance within a factor of 2 of that of the optimal state for large d. In an actual experiment, it may be easier to produce this balanced probe state, in which the phase and reference mode amplitudes are the same.

One might further wonder if $|\psi_s\rangle$ provides the maximum possible advantage that can be obtained by quantum probes of the form Eqn. (6.4). We do not have an analytic proof that this is the case, and numerical searches are hampered by the unfavourable scaling in the number of state configurations D, since in the limit of large N, d, this is $D \sim 2^{(N+d)S}$, where S is the binary Shannon entropy of $d/(N+d)$. We have, however, performed a numerical optimisation to find the states with the minimal total variance in the parameter ranges $d = 1:6, n = 1:6$ and found that the optimal states are always $|\psi_s\rangle$.

The definition of a trial is central for a proper accounting of resources and therefore for identifying any quantum advantages. We have defined a trial to consist of a complete characterisation of all d phases using N photons. Alternative definitions can be considered, such as when a trial simply consists of a single illumination of the sample with N photons, with freedom to use these photons differently in each trial. In the latter case, an alternative strategy of using all N photons to estimate a single phase in a given trial, switching through the phases to be estimated in each trial, can also produce an $\mathcal{O}(d^2)$ scaling in the variance. Now, however, Nd photons are required in order to provide one set of estimates for the phases, this will lead to d fewer trials per phase, and therefore a factor $1/d$ slower convergence to the Cramér-Rao bound.

6.2.3 Optimal measurements to saturate the QCRB

We now turn to the problem of identifying measurements that can realise quantum advantages in multi-phase estimation. Although we know that the QRCB can be saturated in principle, it is important to identify the measurements that allow us to do so in practise. As in the single-parameter case (Eqn. 4.5), it is possible to evaluate the performance of different measurement strategies through the calculation of the Fisher Information (FI) matrix[95]

$$[F_{\boldsymbol{\theta}}]_{l,m} = \sum_k \frac{\partial_{\theta_l} p(k|\boldsymbol{\theta})\, \partial_{\theta_m} p(k|\boldsymbol{\theta})}{p(k|\boldsymbol{\theta})}. \tag{6.30}$$

It is known that the single parameter QCRB, and the multi-parameter QCRB in a pure-state model can always be saturated[95,143]. In the former case, the optimal measurements are given by the SLDs, while in the latter case, Matsumoto[143] presented a POVM with $d+2$ projectors that attains the QCRB. Here we present another method for finding a set of POVM elements that saturates the QCRB at a specific point in the space of $\boldsymbol{\theta}$. This requires a complete POVM $\{\hat{\Pi}_k\}$ in which one element is a projector onto the output state $|\psi_{\boldsymbol{\theta}_s}\rangle$ (Eqn. 6.5) associated with *the arbitrarily chosen, but specific* $\boldsymbol{\theta}_s$ at which we want the QCRB to be saturated.

To distinguish the initial POVM element associated with the probe eigenstate from the others, we label it as the $k=1$ element $\hat{\Pi}_1 = |\psi_{\boldsymbol{\theta}_s}\rangle\langle\psi_{\boldsymbol{\theta}_s}|$. Our POVM is in fact a PVM (projection-valued measure), and so the other elements $\hat{\Pi}_k$ are also projectors, such that $\hat{\Pi}_k = |\beta_k\rangle\langle\beta_k|$. Therefore $\sum_k \hat{\Pi}_k = \sum_{k\neq 1} |\beta_k\rangle\langle\beta_k| + |\psi_{\boldsymbol{\theta}_s}\rangle\langle\psi_{\boldsymbol{\theta}_s}| \equiv \mathbb{1}$ where $\mathbb{1}$ is the identity matrix. We further note that our proof will require that, for all of these $k \neq 1$ POVM elements, $\hat{\Pi}_k |\psi_{\boldsymbol{\theta}_s}\rangle = 0$, i.e. $\hat{\Pi}_0$ is orthogonal to all of the other $\hat{\Pi}_k$.

We first note that, for a pure state, the quantum Fisher information (Eqn. 6.3) can also be expressed as

$$[\mathcal{I}_{\boldsymbol{\theta}}]_{\,l,m} = 4\,\mathrm{Re}\,[\langle \partial_{\theta_l}\psi |\, \partial_{\theta_m}\psi\rangle - \langle \partial_{\theta_l} |\, \psi\rangle \, \langle\psi |\, \partial_{\theta_m}\rangle]. \tag{6.31}$$

For a measurement using a given set of POVM elements $\{\hat{\Pi}_k\}$, the corresponding classical Fisher information is given by

$$[F_{\boldsymbol{\theta}}]_{\,l,m} = \sum_k \frac{\partial_{\theta_l} p(k|\boldsymbol{\theta})\, \partial_{\theta_m} p(k|\boldsymbol{\theta})}{p(k|\boldsymbol{\theta})} \tag{6.32}$$

$$= \sum_k \frac{\partial_{\theta_l} \langle\psi|\, \hat{\Pi}_k \,|\psi\rangle \;\partial_{\theta_m} \langle\psi|\, \hat{\Pi}_k \,|\psi\rangle}{\langle\psi|\, \hat{\Pi}_k \,|\psi\rangle} \tag{6.33}$$

$$= \sum_k \frac{(\langle\partial_{\theta_l}\psi|\, \hat{\Pi}_k \,|\psi\rangle + \langle\psi|\, \hat{\Pi}_k \,|\partial_{\theta_l}\psi\rangle)(\langle\partial_{\theta_m}\psi|\, \hat{\Pi}_k \,|\psi\rangle + \langle\psi|\, \hat{\Pi}_k \,|\partial_{\theta_m}\psi\rangle)}{\langle\psi|\, \hat{\Pi}_k \,|\psi\rangle}. \tag{6.34}$$

Since $\{\hat{\Pi}_k\}$ are Hermitian, this can be simplified to

$$[F_{\boldsymbol{\theta}}]_{\,l,m} = \sum_k \frac{4\mathrm{Re}[\langle\partial_{\theta_l}\psi|\, \hat{\Pi}_k \,|\psi\rangle]\,\mathrm{Re}[\langle\psi|\, \hat{\Pi}_k \,|\partial_{\theta_m}\psi\rangle]}{\langle\psi|\, \hat{\Pi}_k \,|\psi\rangle}. \tag{6.35}$$

In order to calculate $[F_{\boldsymbol{\theta}_s}]_{\,l,m}$, we need to evaluate this expression at $\boldsymbol{\theta}_s$. We first consider the component contributed by the element $\hat{\Pi}_1 = |\psi_{\boldsymbol{\theta}_s}\rangle\langle\psi_{\boldsymbol{\theta}_s}|$. This is simply given by

$$\frac{4\,\mathrm{Re}[\langle\partial_{\theta_l}\psi_{\boldsymbol{\theta}_s}|\, \psi_{\boldsymbol{\theta}_s}\rangle]\,\mathrm{Re}[\langle\psi_{\boldsymbol{\theta}_s}|\, \partial_{\theta_m}\psi_{\boldsymbol{\theta}_s}\rangle]}{1}. \tag{6.36}$$

It is easy to show that $\mathrm{Re}[\langle\partial_{\theta_m}\psi|\, \psi\rangle] = 0$ for any parameter θ_l [144], which implies that the above expression also equals zero.

To evaluate the contributions of the other POVM elements as the phase tends to $\boldsymbol{\theta}_s$, we are forced to consider their limiting values, since the denominator of the components tends to zero at $\boldsymbol{\theta}_s$. We therefore evaluate $[F_{\boldsymbol{\theta}}]_{\,l,m}$ for our probe state when the system phases are displaced from $\boldsymbol{\theta}_s$ by a small change in the phase $\delta\theta_j$ in an arbitrarily chosen mode j. This allow us to express our state to first order as $|\psi\rangle = |\psi_{\boldsymbol{\theta}_s}\rangle + \delta\theta_j \left|\partial_{\theta_j}\psi_{\boldsymbol{\theta}_s}\right\rangle$. We again note that, for these $k \neq 1$ POVM elements, we require $\hat{\Pi}_k |\psi_{\boldsymbol{\theta}_s}\rangle = 0$. Expanding our expression for the FI, we find

$$[F_{\boldsymbol{\theta_s}}]_{\,l,m} = 4 \lim_{\delta\boldsymbol{\theta}\to 0} \sum_{k\neq 1} \frac{4\,\delta\theta_i\delta\theta_j \operatorname{Re}[\langle\partial_{\theta_l}\psi_{\boldsymbol{\theta}_s}|\,\hat{\Pi}_k\,|\partial_{\theta_i}\psi_{\boldsymbol{\theta}_s}\rangle]\operatorname{Re}[\langle\partial_{\theta_m}\psi_{\boldsymbol{\theta}_s}|\,\hat{\Pi}_k\,\left|\partial_{\theta_j}\psi_{\boldsymbol{\theta}_s}\right\rangle]}{\delta\theta_i\delta\theta_j\,\langle\partial_{\theta_i}\psi_{\boldsymbol{\theta}_s}|\,\hat{\Pi}_k\,\left|\partial_{\theta_j}\psi_{\boldsymbol{\theta}_s}\right\rangle}. \tag{6.37}$$

Expanding $\hat{\Pi}_k$ as $|\beta_k\rangle\langle\beta_k|$, a sufficient condition to saturate the bound is that for each k, $\langle\partial_{\theta_m}\psi_{\boldsymbol{\theta}_s}|\,\beta_k\rangle$ is *either* real for all m *or* imaginary for all m. We will demonstrate below that this can always be satisfied. For the moment assuming that this is the case, the Fisher information can be expressed as

$$[F_{\boldsymbol{\theta_s}}]_{\,l,m} = \lim_{\delta\boldsymbol{\theta}\to 0} \sum_{k\neq 1} \frac{4\,\delta\theta_i\delta\theta_j\ \langle\partial_{\theta_i}\psi_{\boldsymbol{\theta}_s}|\,\beta_k\rangle\langle\beta_k|\,\partial_{\theta_l}\psi_{\boldsymbol{\theta}_s}\rangle\ \langle\partial_{\theta_m}\psi_{\boldsymbol{\theta}_s}|\,\beta_k\rangle\left\langle\beta_k\right|\left.\partial_{\theta_j}\psi_{\boldsymbol{\theta}_s}\right\rangle}{\delta\theta_i\delta\theta_j\,\langle\partial_{\theta_i}\psi_{\boldsymbol{\theta}_s}|\,\beta_k\rangle\left\langle\beta_k\right|\left.\partial_{\theta_j}\psi_{\boldsymbol{\theta}_s}\right\rangle}. \tag{6.38}$$

This can be trivially rearranged to

$$[F_{\boldsymbol{\theta_s}}]_{\,l,m} = \lim_{\delta\boldsymbol{\theta}\to 0} \sum_{k\neq 1} \frac{4\,\delta\theta_i\delta\theta_j\ \langle\partial_{\theta_m}\psi_{\boldsymbol{\theta}_s}|\,\beta_k\rangle\langle\beta_k|\,\partial_{\theta_l}\psi_{\boldsymbol{\theta}_s}\rangle\ \langle\partial_{\theta_i}\psi_{\boldsymbol{\theta}_s}|\,\beta_k\rangle\left\langle\beta_k\right|\left.\partial_{\theta_j}\psi_{\boldsymbol{\theta}_s}\right\rangle}{\delta\theta_i\delta\theta_j\,\langle\partial_{\theta_i}\psi_{\boldsymbol{\theta}_s}|\,\beta_k\rangle\left\langle\beta_k\right|\left.\partial_{\theta_j}\psi_{\boldsymbol{\theta}_s}\right\rangle}. \tag{6.39}$$

Therefore

$$[F_{\boldsymbol{\theta_s}}]_{\,l,m} = 4\sum_{k\neq 1}\langle\partial_{\theta_m}\psi_{\boldsymbol{\theta}_s}|\,\beta_k\rangle\langle\beta_k|\,\partial_{\theta_l}\psi_{\boldsymbol{\theta_s}}\rangle\,. \tag{6.40}$$

Using $\sum_{k\neq 1} |\beta_k\rangle\langle\beta_k| = \mathbb{1} - |\psi_{\boldsymbol{\theta}_s}\rangle\langle\psi_{\boldsymbol{\theta}_s}|$, this gives

$$[F_{\boldsymbol{\theta_s}}]_{\,l,m} = 4\,\mathrm{Re}[\langle\partial_{\theta_l}\psi_{\boldsymbol{\theta}_s}|\,\partial_{\theta_m}\psi_{\boldsymbol{\theta}_s}\rangle - \langle\partial_{\theta_l}\psi_{\boldsymbol{\theta}_s}|\,\psi_{\boldsymbol{\theta}_s}\rangle\,\langle\psi_{\boldsymbol{\theta}_s}|\,\partial_{\theta_m}\psi_{\boldsymbol{\theta}_s}\rangle]. \tag{6.41}$$

Comparing this with Eqn. 6.31, we find that the expressions for the quantum and classical Fisher information matrices for the specific set of phases $\boldsymbol{\theta}_s$ are the same. Since this is the case, as long as the condition on the commutativity of the SLDs is also satisfied, these elements must be capable of saturating the QCRB at this point.

It is of course necessary to determine whether the constraint on $\langle\partial_{\theta_m}\psi_{\boldsymbol{\theta}_s}|\,\beta_k\rangle$ can be satisfied. Noting again that $\mathrm{Re}[\langle\partial_{\theta_m}\psi|\,\psi\rangle] = 0$ for any parameter θ_m [144], $|\partial_{\theta_m}\psi_{\boldsymbol{\theta}_s}\rangle$ can be expressed as $\sum_{x=1}^{D} \mathrm{i}\,\gamma_{m,x}\,\alpha_{x,\boldsymbol{\theta}_s}\,|\mathbf{N}_x\rangle$ where, as in Eqn. 6.4, $|\psi_{\boldsymbol{\theta}_s}\rangle$ is expanded in the number state basis such that $|\psi_{\boldsymbol{\theta}_s}\rangle = \sum_{x=1}^{D} \alpha_{x,\boldsymbol{\theta}_s}\,|\mathbf{N}_x\rangle$, and where $\gamma_{m,x}$ are real parameters.[2]

It is therefore straightforward to construct a suitable POVM set such that $\langle\partial_{\theta_m}\psi_{\boldsymbol{\theta}_s}|\,\beta_k\rangle$ are either real or imaginary for all θ_m. This can be achieved by ensuring that $|\beta_k\rangle = \sum_{x=1}^{D} \beta_{k,x}\,e^{-\arg(\alpha_{x,\boldsymbol{\theta}_s})}\,|\mathbf{N}_x\rangle$, where $\beta_{k,x}$ are also real (or imaginary, if real $\langle\partial_{\theta_m}\psi_{\boldsymbol{\theta}_s}|\,\beta_k\rangle$ are desired). The constraint that $\beta_{k,x}$ are real (or imaginary) can be satisfied for POVM sets constructed through, for example, a Gram-Schmidt process.

One such construction, for the probe $|\psi_w\rangle$ (Eqn. 6.29) and $\boldsymbol{\theta}_s = \mathbf{0}$, is given by $\{\hat{\Pi}_k\} = \{|\beta_k\rangle\langle\beta_k|\}$ where $|\beta_k\rangle = \sum_m \beta_{k,x}\,|\mathbf{N}'_m\rangle$ and $|\mathbf{N}'_m\rangle$ is the configuration with N photons in

---

[2] $\mathrm{Re}[\langle\partial_{\theta_m}\psi|\,\psi\rangle] = 0$ must hold for any choice of initial state $\psi = \alpha_x\,|\mathbf{N}_x\rangle$. This can only be the case if each number state basis element in $|\psi_{\boldsymbol{\theta}_s}\rangle$ (after phase evolution), $\alpha_{x,\boldsymbol{\theta}_s}\,|\mathbf{N}_x\rangle$, has only imaginary overlap with the corresponding element in $|\partial_{\theta_m}\psi_{\boldsymbol{\theta}_s}\rangle$.

mode x and no photons in any other mode. The component amplitudes are given by

$$\beta_{k,x} = \begin{cases} \sqrt{\frac{(k-2)!}{(k)!}}, & x \leq k-1; \\ -\sqrt{\frac{k-1}{k}}, & x = k; \\ 0, & x > k, \end{cases} \tag{6.42}$$

for $k = 2, \cdots, d+1$ and $x = 1, \cdots, d+1$. The additional $k = 1$ state is given by $\beta_{1,x} = 1/\sqrt{d+1}$. An explicit construction for $d = 3$ is given in Table 6.1. A similar set of projectors can also be obtained for $|\psi_s\rangle$ (Eqn. 6.17), this is shown in Table 6.2.

Table 6.1: Phase measurement projectors $|\beta_k\rangle$ onto the $d+1$ basis state components of the balanced $|\psi_w\rangle$, with $\beta_{k,x}$ as defined in the main text. The first mode is the reference mode. Shown here are the projectors for measuring $d = 3$ phases, constructed so that the measurements saturate the QCRB when $\boldsymbol{\theta} = [0, 0, \ldots, 0]$.

k	$\beta_{k,1}$	$\beta_{k,2}$	$\beta_{k,3}$	$\beta_{k,4}$
1	$\frac{1}{2}$	$\frac{1}{2}$	$\frac{1}{2}$	$\frac{1}{2}$
2	$-\frac{1}{\sqrt{2}}$	$\frac{1}{\sqrt{2}}$	0	0
3	$-\frac{1}{\sqrt{6}}$	$-\frac{1}{\sqrt{6}}$	$\sqrt{\frac{2}{3}}$	0
4	$-\frac{1}{2\sqrt{3}}$	$-\frac{1}{2\sqrt{3}}$	$-\frac{1}{2\sqrt{3}}$	$\frac{\sqrt{3}}{2}$

Table 6.2: Equivalent optimal phase measurement projectors for the optimal state $|\psi_s\rangle$.

k	$\beta_{k,1}$	$\beta_{k,2}$	$\beta_{k,3}$	$\beta_{k,4}$
1	$\frac{1}{\sqrt{1+\sqrt{3}}}$	$\frac{1}{\sqrt{3+\sqrt{3}}}$	$\frac{1}{\sqrt{3+\sqrt{3}}}$	$\frac{1}{\sqrt{3+\sqrt{3}}}$
2	$-\sqrt{\frac{\sqrt{3}-1}{2}}$	$\sqrt{\frac{3-\sqrt{3}}{2}}$	0	0
3	$-\frac{3^{3/4}\sqrt{\sqrt{3}-1}}{3+\sqrt{3}}$	$-\frac{\sqrt{3(\sqrt{3}-1)}}{3+\sqrt{3}}$	$\sqrt{\sqrt{3}-1}$	0
4	$\sqrt{\frac{1}{2}\left(3\sqrt{3}-5\right)}$	$\sqrt{\frac{1}{6}\left(9-5\sqrt{3}\right)}$	$\sqrt{\frac{1}{6}\left(9-5\sqrt{3}\right)}$	$-\sqrt{\frac{1}{6}\left(3+\sqrt{3}\right)}$

As can be seen, the probability $p_k(\boldsymbol{\theta}) = \left|\langle\psi_w|\, \hat{U}_{\boldsymbol{\theta}}\, |\beta_k\rangle\right|^2$ associated with each outcome is transparently related to the phases, with p_2 involving only θ_1, p_3 only θ_1, θ_2 and so on. This suggests that an estimator could be easily created that would allow one to determine the probability distribution for the phases given a set of experimental outcomes.

For these POVM sets, the saturation of the QFI stems from the strong contribution to the Fisher information of outcomes with low probabilities, since the *relative change* in the frequency of these outcomes can be much larger than for outcomes with high probability. As $\boldsymbol{\theta}$ tends to $\boldsymbol{\theta}_s$, the $|\psi_s\rangle \langle\psi_s|$ element has an outcome probability that tends to unity, while the other POVM elements give vanishing probabilities associated with their measurement outcomes. This makes the outcome distribution especially sensitive to small displacements from $\boldsymbol{\theta}_s$. There is however a caveat to this: although the proof only requires the POVM set to consist of a minimum of two elements, one expects that d linearly independent measurement outcomes are needed to estimate d parameters. For sets with fewer elements than this, there is not enough information available to uniquely determine the values of each phase. Instead, a hyper-surface is defined within the parameter space upon which each point is consistent with the measured set of outcomes. The position of this hyper-surface can be known very accurately (due to the high precision implied by the QFI), but it will be impossible to determine where on the hyper-surface the system is. With sufficient POVM elements, this degeneracy can be lifted so that this hyper-surface is reduced to a unique point in the parameter space.

6.2.4 Realistic probes and measurements

The optimal probe states and measurements involve quantum correlated states that may be challenging to implement in practise. In this section, we present examples of probe states that may be relatively easier to prepare, and show that the enhancements predicted earlier are achievable using realistic measurements.

For single parameter estimation, it was shown that the Holland-Burnett (HB) state [76,101], generated by interfering two pure N photon states on a 50/50 beam splitter, can also lead to a $1/N^2$ Heisenberg scaling in estimation. This state is significantly easier to generate than the ideal N00N state since it does not rely on the use of optical non-linear interactions or quantum gates. Further, these states are also known to be close to optimal with respect to losses in the quantum sensor.

We consider a multi-mode generalisation of these states, generated by means of Fourier multi-port devices that implement a ($d+1$ dimensional) quantum Fourier transform (QFT) [106,130,145]

$$\hat{a}_k \to (d+1)^{-1/2} \sum_m \omega^{mk}\, \hat{a}_m, \text{where } \omega = \exp\left(\mathrm{i}\frac{2\pi}{(d+1)}\right). \tag{6.43}$$

For two modes a QFT is equivalent to a 50/50 beam-splitter. As in the creation of HB states, n photons are input into each mode of the QFT device, leading to an $N = n(d+1)$ photon state output, that we denote HB(n, d). This state is then used for phase estimation. Our results include as a special case recent work by Spagnolo *et al.* [130] which explored the QFI associated with this device for the specific case of $d = 2, 3$ with $n = 1$.

Fig. (6.4) shows numerical calculations of the expected variance of estimation for these states, calculated from the QCRB (Eqn. (6.10)). Our calculations suggest that the HB$(1, d)$ states give the closest performance to the probe $|\psi_s\rangle$ previously considered. As the number of photons input into each mode is increased, the variance of estimation moves away from that achievable using $|\psi_s\rangle$, and approaches the error for simultaneous phase estimation using N00N states. The observed decrease in performance of the HB(n, d) state is because the probability amplitude associated with the terms in which the photons are highly bunched in one mode decreases significantly with n and d[146], and it is these terms that are most sensitive to the phases in the interferometer. It is also this property, however, that ensures that these states are robust against loss in the single phase case[76], something that is not a property of the NOON states. The degree to which multi-phase estimation can be loss-tolerant is not yet known.

Although HB(n, d) states do not perform as well as comparable $|\psi_s\rangle$ probe states, they do at least as well as N00N states, which are just as challenging to prepare as $|\psi_s\rangle$ states. The ease of experimental generation of multi-mode HB states may make them an attractive candidate for multiple phase estimation protocols. This is particularly the case for $n = 1$ states, which could be produced using heralded single photons, and demonstrate the best comparative performance over N00N states of the same photon number.

In addition to the challenges of optimal state preparation, the optimal measurements involve projections onto complex multi-photon states, and thus they may not be experimentally feasible. It is therefore important to show that an experimentally realistic measurement scheme exists that can achieve or approach the QCRB. We calculated numerically the variance of the phase estimation given by the classical Fisher information for HB(n, d) states using a detection scheme in which the different modes are combined using a balanced Fourier multi-port device, followed by ideal photon-number-resolving detectors (PNRD). Since the probability of different combinations of detector outcomes depends on the phases, a maximum likelihood scheme could in principle be used to estimate the phases given a set

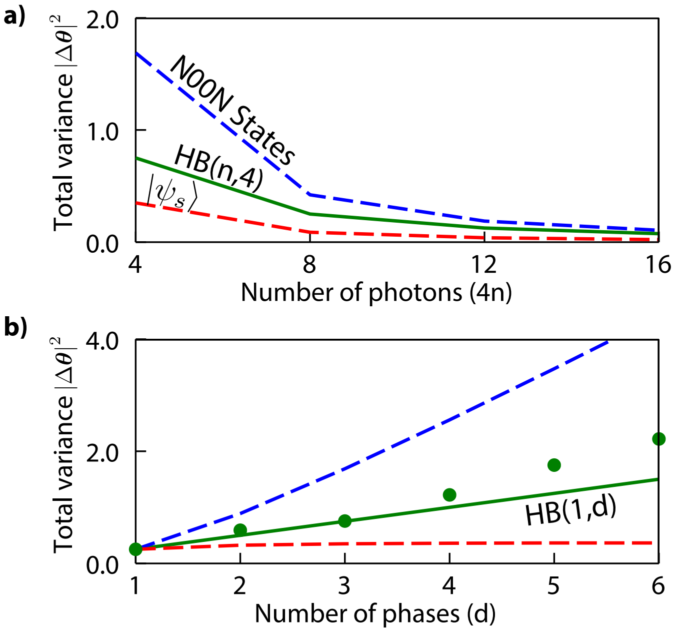

Figure 6.4: a) *Realistic probes:* The green line gives numerical calculations of the total variance from the QCRB for the simultaneous estimation of 4 phases using HB$(n, 4)$ states as a function of n. For comparison, the blue and red dashed lines give the QCRB for equivalent N00N and $|\psi_s\rangle$ states respectively. b) *Realistic measurements:* The green dots show the total variance for the simultaneous estimation of d phases using a HB$(1, d)$ state and a measurement apparatus consisting of a Fourier multi-port followed by PNRDs. The green line gives the QCRB variance error for the same HB$(1, d)$ state, while the blue and red dashed lines again give the QCRB for equivalent N00N and $|\psi_s\rangle$ states respectively.

of measured detector outcomes. As the accuracy of estimation is dependent on the value of $\boldsymbol{\theta}$, numerical optimisation over the phases was used determine the minimum possible error. Calculations were carried out for the multi-mode HB$(1, d)$ states (the class of HB(n, d) states that exhibited the best performance), and are shown in Fig. (6.4b). The calculated variance is comparable to the QFI, and below that achievable using N00N states.

6.3 Conclusions

Our analysis of imaging as a multi-parameter estimation problem presents an alternative approach to the typical methods based on enhancing diffraction limits, and may be of interest for other quantum enhanced imaging problems. In addition, our results should be of wide interest as many problems, such as strain sensing, range finding and gravitational wave detection can be recast as optical phase estimation[17].

Part III

Quantum Information

Chapter 7

Linear-optical quantum computing

The development of increasingly sophisticated techniques for coherent quantum control of quantum systems has become synonymous with the tantalising prospect of building a universal quantum computer. This goal is a long term one, and it is still not clear which of several potential systems will prove to be capable of realising universal quantum computation[147]. This motivates the continued development of different approaches in parallel, with each standing to gain from the advances in techniques and understanding developed in the others. In this chapter, I will briefly introduce the key ideas in quantum computing and discuss different potential models for so-called *linear-optical quantum computing*, (LOQC) which uses only electromagnetic fields and the interaction Hamiltonian introduced in Section 1.4. This will lay the foundations for a more comprehensive discussion of LOQC using time-frequency modes.

7.1 The quantum circuit model

As is the case with classical computing, quantum computing is often framed in terms of a *circuit model*. In this picture, specific controlled unitary interactions (*quantum gates*) are applied to a specific set of input quantum states in order to implement a desired protocol. After the full set of quantum gates has been applied, the results of the computation are determined by measuring the output quantum states. Any realistic model for a quantum computer will also require additional measurements to be made throughout the computation process in order to correct errors that will inevitably arise due to imperfect operations.

In the quantum circuit model, information is most commonly encoded using the smallest possible units of quantum information, quantum bits or qubits[25]. Qubits are a superposition of two logical states $|\mathbf{0}\rangle$ and $|\mathbf{1}\rangle$ (where I have used a bold font to distinguish the notation for logical states and photon number states)

$$|\psi\rangle_{\text{qubit}} = \alpha\,|\mathbf{0}\rangle + \beta\,|\mathbf{1}\rangle\,. \tag{7.1}$$

As a quantum state, the qubit has a global phase that cannot be measured; I can exploit this phase freedom to make α real. With this convention, a useful method of visualising the state of single qubits is as a vector on the *Bloch sphere*. This can be seen by parameterising $|\psi\rangle$ as

$$|\psi\rangle_{\text{qubit}} = \cos(\theta)\,|\mathbf{0}\rangle + e^{\mathrm{i}\phi}\sin(\theta)\,|\mathbf{1}\rangle\,. \tag{7.2}$$

With this parametrisation, θ and ϕ give the spherical polar coordinates of the state on the Bloch sphere, as shown in Fig. 7.1.[1] Arbitrary single qubit operations therefore correspond to rotations around this sphere.

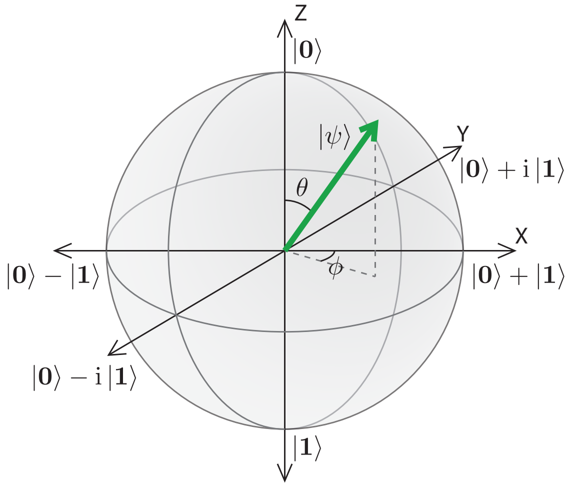

Figure 7.1: A single qubit can be represented as a point on the Bloch sphere

Vector notation

In addition to the Bloch sphere representation, it is often helpful to represent the state of the (pure) qubit in Eqn. 7.1 as a vector

$$\begin{pmatrix} \alpha \\ \beta \end{pmatrix}. \tag{7.3}$$

---

[1] For pure states, the radial coordinate for the qubit is always one.

This vector notation can be easily extended to multiple qubit states $|\psi\rangle^{\otimes n}$. For example, the two-qubit state $\alpha_{00}\,|\mathbf{00}\rangle + \alpha_{01}\,|\mathbf{01}\rangle + \alpha_{10}\,|\mathbf{10}\rangle + \alpha_{11}\,|\mathbf{11}\rangle$ is given by the state vector

$$\begin{pmatrix} \alpha_{00} \\ \alpha_{01} \\ \alpha_{10} \\ \alpha_{11} \end{pmatrix}. \tag{7.4}$$

In this notation, unitary operations between logical states can be represented as matrices operating on state vectors. I will employ this representation in the following chapters.

Single qubit operations

The *Pauli* matrices (together with the identity matrix) span the full vector space of 2 × 2 Hermitian matrices, and therefore often provide a useful basis in which to express single qubit operations. Here I give these matrices, along with the conventional symbol used to denote the operation in the quantum circuit notation, in which each qubit is denoted by a different wire.

$$\begin{array}{lcc} X: & -\boxed{X}- & \begin{pmatrix} 0 & 1 \\ 1 & 0 \end{pmatrix} \\ \\ Y: & -\boxed{Y}- & \begin{pmatrix} 0 & -\mathrm{i} \\ \mathrm{i} & 0 \end{pmatrix} \\ \\ Z: & -\boxed{Z}- & \begin{pmatrix} 1 & 0 \\ 0 & -1 \end{pmatrix} \end{array} \tag{7.5}$$

Exponentiating these matrices (directly equivalent to exponentiating a Hamiltonian operator $\hat{H}$ to give a unitary evolution operator $e^{-\mathrm{i}\hat{H}t}$) gives the *rotation operators*, defined as

$$X(\theta) \equiv e^{-\mathrm{i}\theta X/2} = \begin{pmatrix} \cos(\frac{\theta}{2}) & -\mathrm{i}\sin(\frac{\theta}{2}) \\ -\mathrm{i}\sin(\frac{\theta}{2}) & \cos(\frac{\theta}{2}) \end{pmatrix} \tag{7.6}$$

$$Y(\theta) \equiv e^{-\mathrm{i}\theta Y/2} = \begin{pmatrix} \cos(\frac{\theta}{2}) & -\sin(\frac{\theta}{2}) \\ \sin(\frac{\theta}{2}) & \cos(\frac{\theta}{2}) \end{pmatrix} \tag{7.7}$$

$$Z(\theta) \equiv e^{-\mathrm{i}\theta Z/2} = \begin{pmatrix} e^{-\mathrm{i}\frac{\theta}{2}} & 0 \\ 0 & e^{\mathrm{i}\frac{\theta}{2}} \end{pmatrix} \tag{7.8}$$

These operators correspond to rotations around the X, Y and Z axes of the Bloch sphere respectively.

7.1.1 Universality

Several questions naturally arise when considering any computational model. The first is whether the quantum circuit model is *universal*. Universality is most generally defined as being able to implement any unitary operation within a d-dimensional Hilbert space. For the quantum circuit model, the input states are typically qubits; in this case an equivalent statement of universality is being able to implement any unitary operation on n qubits.

It can be shown that the qubit quantum circuit model is universal with an appropriate choice of quantum gates. In particular, the quantum circuit model is universal with arbitrary single-qubit operations and an appropriate single choice of two-qubit gate[148]. The set of arbitrary single-qubit operations consists of all operations in the $SU(2)$ group of rotations, and can be decomposed in terms of the Pauli matrices as

$$U = Z(\alpha)Y(\beta)Z(\gamma). \tag{7.9}$$

Any such single qubit operation therefore also corresponds to a rotation around the Bloch sphere.

Although it is possible to directly implement arbitrary single-qubit operations in many quantum systems, arbitrary operations are incompatible with known quantum computing error-correcting codes[25]. For fault tolerant quantum computing, it is therefore necessary to restrict the allowed single-qubit gates to a discrete set. One possible set consists of the *Hadamard* gate, the *phase* gate, and the $\pi/8$ gate.

$$\begin{array}{ccc}
\text{Hadamard :} & -\boxed{H}- & \frac{1}{\sqrt{2}}\begin{pmatrix} 1 & 1 \\ 1 & -1 \end{pmatrix} \\[2em]
\text{Phase :} & -\boxed{S}- & \begin{pmatrix} 1 & 0 \\ 0 & \mathrm{i} \end{pmatrix} \\[2em]
\pi/8 : & -\boxed{T}- & \begin{pmatrix} 1 & 0 \\ 0 & e^{\mathrm{i}\pi/4} \end{pmatrix}
\end{array} \tag{7.10}$$

Note that the phase gate corresponds to two sequential $\pi/8$ gates, and is therefore not required to implement arbitrary single-qubit operations. However, it is typically included in the gate set, since it is needed in order to carry out fault-tolerant quantum computing based on the stabilizer formalism[25].

With this discrete set of gates, it is no longer possible to exactly implement any n qubit unitary. Although this is the case, it can be shown that it is still possible to approximately implement any unitary operation to an arbitrary accuracy. In this sense, this restricted set of the Hadamard, phase, $\pi/8$ and a two-qubit gate are considered to be universal for quantum computation.

It can be shown that almost any two-qubit gate allows for universal quantum computation[149]. However, a common choice of two-qubit gate is the *controlled-not* (CNOT) gate. This gate is the quantum equivalent of the classical controlled-not gate, and simply acts to flip the state of a target qubit if the control qubit is in the state $|\mathbf{1}\rangle$, but leaves the target qubit untouched if the control qubit is in the state $|\mathbf{0}\rangle$. In the computational basis this corresponds to the unitary matrix

$$U_{\mathrm{CNOT}} = \begin{pmatrix} 1 & 0 & 0 & 0 \\ 0 & 1 & 0 & 0 \\ 0 & 0 & 0 & 1 \\ 0 & 0 & 1 & 0 \end{pmatrix}. \tag{7.11}$$

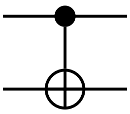

Figure 7.2: The symbol for a CNOT gate in the circuit representation. The top line is the control qubit. If this qubit is in the state $|\mathbf{1}\rangle$, the state of the target qubit in the bottom rail is flipped.

A CNOT gate is equivalent to another important two-qubit gate, the controlled-Z gate (CZ), with the addition of a Hadamard gate on one of the qubits before and after the CZ gate. The unitary matrix for the CZ gate in the computational basis is

$$U_{\mathrm{CZ}} = \begin{pmatrix} 1 & 0 & 0 & 0 \\ 0 & 1 & 0 & 0 \\ 0 & 0 & 1 & 0 \\ 0 & 0 & 0 & -1 \end{pmatrix}. \tag{7.12}$$

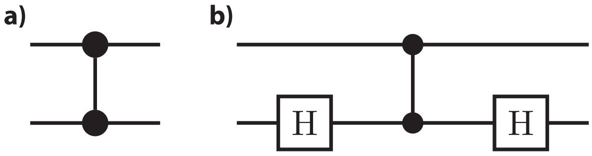

Figure 7.3: a) The symbol for a CZ gate in the circuit representation. b) A CZ gate between two Hadamard gates is equivalent to a CNOT gate.

7.1.2 Efficiency

Although this set of gates is universal, and therefore any unitary can be implemented to arbitrary accuracy, there exist unitaries that cannot be implemented *efficiently* - these unitaries require a number of gates that is exponential in the number of qubits n to approximate to a given accuracy[25]. As with classical information theory, this implies the existence of different complexity classes for quantum information protocols. A corollary of this result is that there therefore exist Hamiltonians that cannot be efficiently simulated by a quantum computer. An interesting open question is whether these Hamiltonians exist in nature, since if they did, they could then in principle be used to perform computation beyond the quantum circuit model[25].

7.1.3 The DiVincenzo criteria

Any physical implementation of a quantum computer must provide the means to encode, manipulate and measure quantum information. For the circuit model, these requirements have been formalised into the DiVincenzo criteria[150], which state that any quantum computer must provide: [2]

i) A scalable physical system with well-characterised qubits;

ii) the ability to initialise the state of the qubits to a simple fiducial state, such as $|0000\ldots\rangle$;

iii) long relevant decoherence times, much longer than the gate operation time;

iv) a universal set of quantum gates;

v) a qubit-specific measurement capability.

Different potential physical implementations of a quantum computer each naturally excel at some of these criteria; however, so far no system has been found that performs significantly better than others in all of these respects. Quantum computers based on ions and atoms allow for ready implementation of controlled particle interactions through electromagnetic effects. The flip side of this is that, due to these strong mutual interactions, and through interactions with their environment, they have historically suffered from decoherence and problems in scalability[147]. In contrast, optical systems are appealing due to their comparative resistance to dephasing, and due to the relative ease with which quantum information can be encoded in different degrees of freedom of the electromagnetic field. Along with these advantages comes a significant disadvantage: the resistance to dephasing from inter-

---

[2] The condensed wording of the criteria presented here is borrowed verbatim from Ref [151].

actions with other field modes also means that it is challenging to implement the non-linear interactions between modes that are necessary for universal quantum computation.

7.2 Discrete-variable linear-optical quantum computing

A single photon in a superposition across two modes will have the state vector

$$|\psi\rangle = \alpha\,|1,0\rangle + \beta\,|0,1\rangle\,. \tag{7.13}$$

A qubit can be encoded in a single photon by associating the physical state $|1,0\rangle$ with the logical state $|\mathbf{0}\rangle$, and the physical state $|0,1\rangle$ with the logical state $|\mathbf{1}\rangle$. This is termed a *dual-rail* encoding for quantum information, since the logical state of the qubit is determined by which mode the single photon occupies. Here I will discuss linear-optical quantum computing based on this encoding.[3] I will consider an abstract set of electromagnetic field modes, assuming the ability to implement phase shifter and beam splitter interactions without concerning ourselves with the particular details of any given optical scheme. For this discussion, I will also assume the ability to generate single photons as required, while noting that this is a significant technical challenge in its own right [74].

7.2.1 Single qubit gates

In the dual-rail encoding, arbitrary single qubit operations can be implemented using two phase shifters and a beam splitter (Section 1.4.1). Now that we have developed the appropriate notation, it can be seen that this is because phase shifters correspond to $Z(\theta)$ rotations,

---

[3] It is also in principle possible to implement linear-optical quantum computing using a *single-rail* encoding, in which vacuum represents $|\mathbf{0}\rangle$ and 1 photon represents $|\mathbf{1}\rangle$. In this case, two-qubit gates are trivial and deterministic but single qubit gates require non-linear operations [8].

while beam splitters correspond to $Y(\theta)$ rotations (up to global phase factors). It is therefore possible to implement arbitrary rotations using the decomposition $Z(\alpha)Y(\beta)Z(\gamma)$. This enables straightforward application of all of the gates in the universal gate set introduced in Section 7.1.1, bar the two-qubit gate. It might seem inefficient to restrict ourselves to these operations when it is possible to implement arbitrary single-qubit operations. However, as I previously discussed, it is necessary to restrict the gates used in order to employ known fault-tolerant quantum computing schemes.

7.2.2 Two-qubit gates

Although single-qubit operations are easily implemented in this dual-rail encoding, two-qubit operations are significantly more challenging since photons do not directly interact with each other. It is, in principle, possible to induce effective two-qubit interactions through the matter mediated nonlinear cross-Kerr effect (which induces the interaction Hamiltonian $H_{CK} = (\hat{a}^\dagger)^2\hat{a}^2$). However, creating a sufficiently strong nonlinear two-photon interaction in a scalable, low-loss fashion has not proven possible to date. This is an area of active research[152]. As an example of the state-of-the-art, Firstenberg et al.[153] used rubidium atoms in highly excited Rydberg states as a non-linear medium, inducing a non-linear phase shift between two single photons that exceeded one radian. However, this phase shift was accompanied by significant absorption (of order 50%) and required a magneto-optical trap to cool the rubidium vapour. Further work is therefore needed to extend this to transmission levels at which quantum non-linear optics will become feasible.

For some time, the lack of a usable two-photon interaction seemed to be an insurmountable difficulty for universal photonic quantum computers. However, in 2001, Knill, Laflamme and Milburn (KLM) showed that it was in principle possible to create a two-photon gate using only linear-optical elements and extra *ancilla* photons[154]. This is possible due to quantum interference between indistinguishable photons that only manifests itself in their correlation functions. The prototypical example of this effect is Hong-Ou-Mandel (HOM) interference[69].

Hong-Ou-Mandel interference

I briefly introduced Hong-Ou-Mandel interference between single photons when discussing the integrated strain-optic stressor in Section 2.2.2. Here I will explain this effect in more detail.

Consider two field modes j and k coupled by a balanced beam splitter. As introduced in Section 1.4.1, in the Heisenberg picture this leads to evolution of the annihilation operators

$$\begin{pmatrix} \hat{a}_j \\ \hat{a}_k \end{pmatrix} \to \frac{1}{\sqrt{2}} \begin{pmatrix} 1 & 1 \\ -1 & 1 \end{pmatrix} \begin{pmatrix} \hat{a}_j \\ \hat{a}_k \end{pmatrix}. \tag{7.14}$$

Consider a single photon input in mode j (using the state notation $|n_j, n_k\rangle$)

$$\begin{aligned} |1,0\rangle &= \hat{a}_j^\dagger |0,0\rangle & (7.15)\\ &\to \frac{1}{\sqrt{2}}(\hat{a}_j^\dagger + \hat{a}_k^\dagger) |0,0\rangle & (7.16)\\ &= \frac{1}{\sqrt{2}}(|1,0\rangle + |0,1\rangle). & (7.17) \end{aligned}$$

As would be expected, the photon exits the beam splitter in a superposition of the two output modes. Similarly, a single photon in mode k will also exit in a superposition of the two modes

$$|0,1\rangle \rightarrow \frac{1}{\sqrt{2}}(|0,1\rangle - |1,0\rangle). \tag{7.18}$$

Now instead consider a single photon input in each mode of the beam splitter at the same time. Classically, and if the photos are distinguishable in any of their degrees of freedom, one would expect the output statistics to simply be the product of the output statistics for the single input cases. However, quantum mechanically, one finds that

$$\begin{aligned} |1,1\rangle &= \hat{a}_j^\dagger \hat{a}_k^\dagger |0,0\rangle & (7.19)\\ &\rightarrow \frac{1}{2}(\hat{a}_j^\dagger + \hat{a}_k^\dagger)(-\hat{a}_j^\dagger + \hat{a}_k^\dagger)|0,0\rangle & (7.20)\\ &= \frac{1}{2}(\hat{a}_j^\dagger \hat{a}_k^\dagger + \hat{a}_k^{\dagger 2} - \hat{a}_j^{\dagger 2} - \hat{a}_k^\dagger \hat{a}_j^\dagger)|0,0\rangle & (7.21)\\ &= \frac{1}{2}(\hat{a}_k^{\dagger 2} - \hat{a}_j^{\dagger 2})|0,0\rangle & (7.22)\\ &= \frac{1}{\sqrt{2}}(|0,2\rangle - |2,0\rangle). & (7.23) \end{aligned}$$

The photons always emerge from the beam splitter in the same output mode. This counter-intuitive “interference without interaction” is due to quantum interference between the amplitudes for the case in which both photons are reflected, and the case in which both photons are transmitted. These two terms exactly cancel, leaving only the correlated output terms. This is possible because of the fundamental indistinguishability of the photons; no matter how I choose to measure the photon in the output mode, I can gain no information on which input mode it came from, and therefore I have no way of distinguishing between both being transmitted, and both being reflected.[4] Notice that this effect is only apparent

---

[4] In a real experiment, it is necessary to ensure that the input modes couple only to each other, and that

in the correlations between the photons: the first-order moments of the photon-number are the same, and there is therefore the same expectation in the number of photons emitted into each mode as in the distinguishable case.

Linear-optical two-qubit gates

These quantum interference effects can be harnessed to make a two-qubit gate. A useful pedagogical example is the decomposition of a CZ operation using two *non-linear sign shift* (NS) gates, as shown in Fig. 7.4. The NS gate acts on the photon number occupation of a single mode. Its action, expressed in this photon number basis, is to map [5]

$$\alpha\,|0\rangle + \beta\,|1\rangle + \gamma\,|2\rangle \rightarrow \alpha\,|0\rangle + \beta\,|1\rangle - \gamma\,|2\rangle\,. \tag{7.24}$$

Under this operation, vacuum and single photon inputs remain unchanged, while a two photon input acquires a π phase shift.

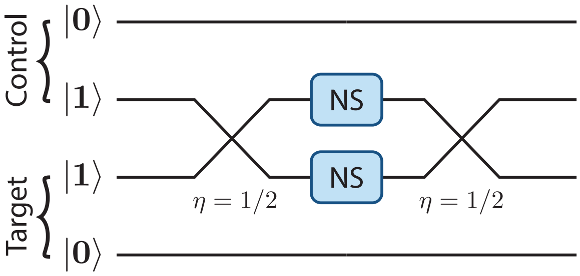

Figure 7.4: A CZ gate can be decomposed in the dual rail encoding using a pair of beam splitters and two nonlinear sign shift (NS) gates.

---

they therefore do not differ in polarisation, spatial-mode profile or spectral-temporal characteristics[155]. Alternatively, it can be sufficient to simply ensure that the 'paths' that the photons took to the detectors are indistinguishable, for example by spectral filtering after the beam splitter, or by using a sufficiently fast detector: this can even allow for HOM interference between photons with different central frequencies[156].

[5] Note that I neglect higher photon numbers as they do not arise in the circuit that we are considering.

With this definition of a NS gate, one can now consider the action of the CZ circuit on the different qubit input states:

- $|\mathbf{0},\mathbf{0}\rangle$ - Clearly, if both photons are input in the $|\mathbf{0}\rangle$ state, the state is trivially left unchanged.

- $|\mathbf{1},\mathbf{0}\rangle$ & $|\mathbf{0},\mathbf{1}\rangle$ - If one photon is in the $|\mathbf{1}\rangle$ state, after the first beam splitter this photon will be in a superposition across the two inner rails. Both terms of this superposition will be left unchanged by the NS gates. Since two successive balanced beam splitters leave a state unchanged, i.e. $U_{BS}(\pi/4)\,U_{BS}(\pi/4) = \mathbb{1}$, the photon will exit the second beam splitter in the same rail as it started in. These input states therefore also remains unchanged.

- $|\mathbf{1},\mathbf{1}\rangle$ - If both qubits are in the state $|\mathbf{1}\rangle$, two photons will be input into the first beam splitter. Hong-Ou-Mandel interference will ensure that these photons exit the beam splitter in the state $|2,0\rangle + |0,2\rangle$. Both of these terms will acquire a π phase shift due to the NS gates. This phase will not change the action of the final beam splitter, and so the initial state will be output by the circuit, but with a π phase shift.

Comparing each of these possibilities with U_{CZ} (Eqn. 7.12) shows that this circuit does indeed implement the CZ operation for dual-rail encoded qubits.

Probabilistic NS gates

This decomposition provides a convenient remapping of the problem of implementing a CZ operation into the problem of building non-linear sign shift gates. Unfortunately, this by itself is not sufficient to allow for optical quantum computing, as it is not possible to build a deterministic NS gate with only linear-optical components. However, it is possible to build a probabilistic NS gate based on post-selection.

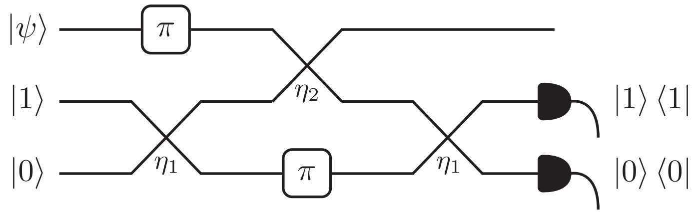

Figure 7.5: Implementation of a probabilistic nonlinear sign shift (NS) gate using linear optics.

Consider the circuit shown in Fig. 7.5. The initial input state $(\alpha|0\rangle+\beta|1\rangle+\gamma|2\rangle)\otimes|1\rangle\otimes|0\rangle$ evolves under the action of the beam splitter elements to a complex entangled output state. Upon the detection of a single photon in rail 2 and the detection of vacuum in rail 3, it can be shown that the (unnormalised) output state in rail 3 is given by

$$\begin{aligned}&(1-\eta_1+\eta_1\sqrt{\eta_2})\,\alpha|0\rangle+(-2\eta_1\eta_2+\eta_1\sqrt{\eta_2}+\eta_1-\sqrt{\eta_2})\,\beta|1\rangle\\&+\sqrt{2}\left(\sqrt{2}\eta_1\eta_2^{3/2}+\frac{\eta_1\eta_2^{3/2}}{\sqrt{2}}-\frac{\eta_1\eta_2}{\sqrt{2}}-\sqrt{2}\eta_1\sqrt{\eta_2}+\frac{\eta_2}{\sqrt{2}}\right)\gamma|2\rangle\,.\end{aligned} \tag{7.25}$$

Setting $\eta_1=1/(4-2\sqrt{2})$ and $\eta_2=(3-2\sqrt{2})$, this simplifies to

$$\frac{1}{2}(\alpha|0\rangle+\beta|1\rangle-\gamma|2\rangle), \tag{7.26}$$

which exactly corresponds to the input state after transformation by a NS gate.

As with all other linear-optical non-linear gates, this probabilistic-NS gate relies on Hong-Ou-Mandel interference to entangle the state of the input photons. Since this HOM interference is only apparent in the higher-order correlation functions of the photons, it cannot change the marginal output statistics of $|\psi\rangle$. However, measuring the other photon gives access to this correlation information, which can be used to herald the probabilistic non-linearity.

As can be seen, successful NS gate operation necessarily only occurs with probability 1/4. Therefore the CZ gate decomposition introduced in Fig. 7.4 will only succeed 1/16 of the time! Additionally, each NS gate requires an extra ancillary single photon resource. This again seems at face value to be an insurmountable problem, since the probability of a series of CZ gates succeeding will decrease exponentially as the number of gates increases.

The KLM scheme

The insight of Knill, Laflamme and Milburn [154] was to develop a method through which two-qubit gates could be applied to comparatively cheap additional ancilla photons, and then, upon success, near-deterministically mapped onto the photons encoding the computational results. In this way, these precious photons could be protected from this probabilistic process. By attempting the two-qubit gates upon a sufficiently large number of extra photons, the probability of the gate succeeding on at least one pair could be brought arbitrarily close to unity for only a polynomial increase in the number of photons needed. Therefore, in principle, the probability of the entire computational protocol succeeding could also be made near unity with a number of photons polynomial in the size of the problem. This proved for the first time that efficient universal quantum computation with linear optics was theoretically possible.

The KLM scheme still requires an extremely large overhead of photons for computation, with hundreds of thousands of single photons needed to implement a single CZ gate with 95% probability even in completely idealised conditions [9]. Fortunately, this original proposal has inspired others to develop significantly more efficient protocols for LOQC. These protocols require fewer resources, and can in principle provide full fault tolerance to both computational errors and (crucially) photon loss. A full treatment of these different protocols is beyond the scope of this thesis; for more information, the interested reader is directed to a few of the review papers on this subject [8,9]. However, we will briefly introduce an important class of protocols generally termed measurement-based quantum computing (MBQC), and also often known as one-way quantum computing.

7.2.3 Measurement-based quantum computing

In the standard circuit model of quantum computing, an initial state is encoded on a set of carriers of quantum information. Gates are then directly enacted upon these carriers in an appropriate sequence, and the final state of the carriers is measured to determine the results. As discussed above, this requires the ability to near-deterministically implement two-qubit gates in order to ensure that the protocol succeeds with reasonable probability.

A promising alternative approach is *measurement-based quantum computing* [157,158]. In order to understand how measurement-based quantum computing works, it is helpful to consider two single qubits, the first in the arbitrary state $|\psi\rangle = \alpha\,|\mathbf{0}\rangle + \beta\,|\mathbf{1}\rangle$, and the second in the state $|\mathbf{0}\rangle$. These states are first entangled with a CNOT operation, giving the state

$$\alpha\,|\mathbf{0},\mathbf{0}\rangle + \beta\,|\mathbf{1},\mathbf{1}\rangle\,. \tag{7.27}$$

If a Hadamard operation is applied to the first qubit, this is transformed to

$$\frac{1}{\sqrt{2}}\left(\alpha(|\mathbf{0},\mathbf{0}\rangle + |1,\mathbf{0}\rangle) + \beta(|\mathbf{0},\mathbf{1}\rangle - |\mathbf{1},\mathbf{1}\rangle)\right) \tag{7.28}$$

$$= \frac{1}{\sqrt{2}}\left((\alpha\,|\mathbf{0},\mathbf{0}\rangle + \beta\,|\mathbf{0},\mathbf{1}\rangle) + (\alpha\,|\mathbf{1},\mathbf{0}\rangle - \beta\,|\mathbf{1},\mathbf{1}\rangle)\right). \tag{7.29}$$

Finally, the state of the first qubit is measured. Dependent on the outcome m (0 or 1) of this measurement, the state of the second qubit will be projected onto

$$= Z^m(\alpha\,|\mathbf{0}\rangle + \beta\,|\mathbf{1}\rangle). \tag{7.30}$$

The unknown state of the first qubit has therefore been mapped onto the state of the second qubit, modulo a known Z operation. For obvious reasons, this is often referred to as a *teleportation* operation. It can be expressed as a quantum circuit:

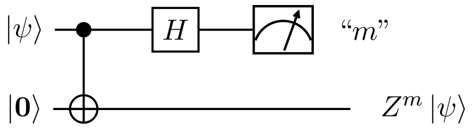

It is useful to be able to re-express this circuit using the CZ gate, as this is diagonal in the computational basis. To do this, we can use the identity in Fig 7.3b, along with $HZ = XH$. This allows us to rewrite the quantum circuit as

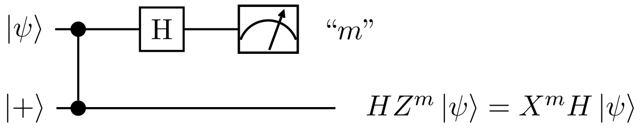

To see how this circuit is useful, consider the input state $Z(\alpha)\,|\psi\rangle$

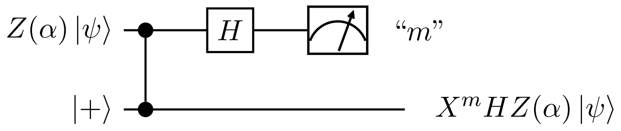

Since the CZ operation is diagonal in the computational basis, we can commute the $Z(\alpha)$ operation through to give the equivalent circuit

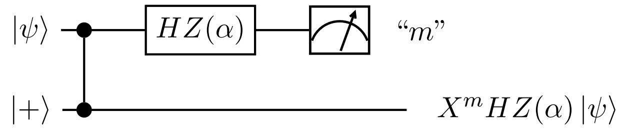

When written in this way, it becomes clear that we can reinterpret this circuit to show that, by changing the basis in which we measure (as given by $HZ(\alpha)$), we can implement an arbitrary $Z(\alpha)$ operation on ψ. This is the concept underlying so-called measurement-based quantum computing.

By adding additional entanglement links to further ancilla photons, it is possible to extend this to encompass arbitrary single-qubit operations.

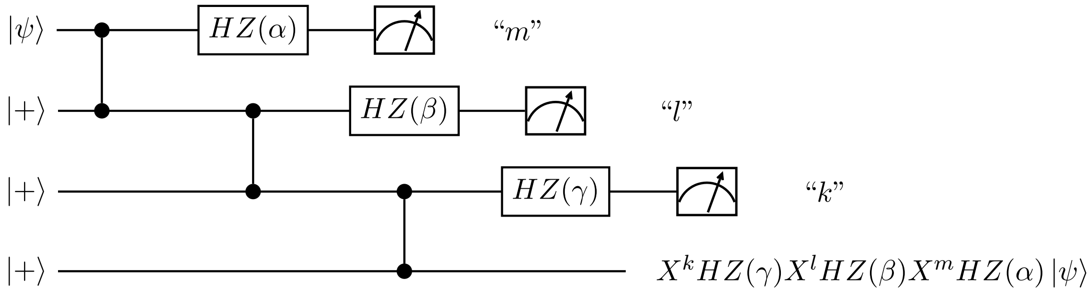

Using $Z(\alpha)X = XZ(-\alpha)$, along with our previous identities, we can manipulate the output of this circuit to give

$$\begin{aligned}
&= X^k H X^l Z((-1)^l \gamma) H X^m Z((-1)^m \beta) H Z(\alpha) \left|\psi\right\rangle \\
&= X^k Z^l H Z((-1)^l \gamma) Z^m H Z((-1)^m \beta) H Z(\alpha) \left|\psi\right\rangle \\
&= X^k Z^l X^m H Z((-1)^l \gamma) H Z((-1)^m \beta) H Z(\alpha) \left|\psi\right\rangle \\
&= X^k Z^l X^m H Z((-1)^l \gamma) X((-1)^m \beta) Z(\alpha) \left|\psi\right\rangle . \qquad (7.31)
\end{aligned}$$

This is equivalent to the single qubit transformation

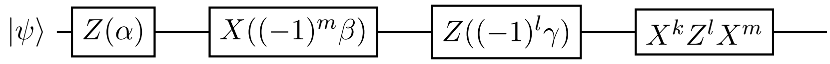

Note that the transformation induced by each measurement changes depending on the previous measurement outcome. It is therefore not enough to simply keep track of all the measurement results. Instead, each measurement basis must be adapted to compensate for the previous results. This protocol therefore requires feed-forward control and defines a definite direction for the quantum computation, hence it is often called one-way quantum computing. This is very different from the standard quantum circuit model, in which each operation is unitary and therefore reversible.

These circuits demonstrate that a chain of teleportation operations can implement arbitrary single-qubit operations. By adding in entanglement links between these chains, it is additionally possible to implement two-qubit gates. This follows trivially from the fact that the entanglement links are equivalent to a CZ operation between two qubits. Therefore any quantum circuit can be mapped into an appropriate series of measurements on a two-dimensional grid of entangled qubits. This resource state is typically called a *cluster state*.[6]

---

[6] Sometimes the term cluster state is reserved for graphs with a regular structure, while the more general

Cluster states are often represented as a graph, with qubits as nodes, and edges representing entanglement between qubits (e.g. as shown in Fig. 7.6).

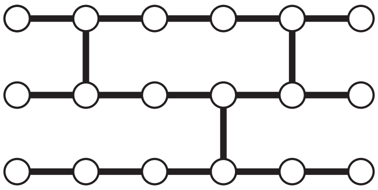

Figure 7.6: A 2D cluster-state of entangled qubits is universal for quantum computing.

Cluster-state quantum computing provides an appealing approach to LOQC, as the burden is shifted from the near-deterministic implementation of gates to the preparation of a large entangled resource state. It can be shown that this is significantly more resource efficient than the KLM scheme[159]. Additionally, cluster states are naturally compatible with highly efficient error-correcting schemes based on surface codes[160].

7.3 Continuous-variable quantum computing

So far, I have only discussed linear-optical quantum computing using discrete variable encodings. However, the continuous nature of the quadrature observables introduced in Section 1.3 suggests an alternative paradigm for optical quantum information processing. In continuous-variable quantum computing, instead of encoding quantum information in the discrete occupation number of a field mode, it is instead encoded directly in the field quadratures[18,19,161]. Anticipating the use of this approach in Chapter 9, here I will briefly introduce the central concepts of CV quantum computing, loosely following the treatment given in Ref. [18].

---

term *graph state* is used for any network topology. Here I choose to refer to any of these states as cluster states.

The continuous nature of the field quadratures allows for the encoding of ‘qumodes’, which are a generalisation of the discrete-valued qubit to this infinite-dimensional Hilbert space[18,20]

$$|\psi_{\text{qumode}}\rangle = \int_{-\infty}^{\infty} \mathrm{d}x_k \, \psi(x_k) \, |x_k\rangle \, . \tag{7.32}$$

This continuum of states poses a challenge when trying to define what is meant by universality for a CV quantum computer. In the discrete-variable case (Section 7.1.1), universality was defined as being able to approximate, to arbitrary accuracy, any unitary operation in a given d-dimensional space with a finite number of operations. However, as d tends to infinity, an infinite number of parameters are required to even specify a particular unitary. For the continuous-variable case, we therefore restrict ourselves to a subclass of operations for which we can define such a notion of universality. Motivated by the forms of experimentally realisable operations, a common choice is the set of all unitary operations that are a polynomial function of the quadrature operators[18]. A continuous-variable quantum computer is then universal if it can implement any unitary of this form with a finite number of operations.

From Section 1.4.3, we know that it is experimentally feasible to implement arbitrary unitary transformations that are quadratic in the quadrature operators using only displacement operations, phase-shifting operations, single-mode squeezing operations and beam splitter operations. However, with only these quadratic operations, it is not possible to construct any higher order polynomials. This set is therefore not sufficient for universal continuous-variable quantum computing.

Fortunately, the addition of any operator which is at least cubic in the quadrature operators, i.e. any non-Gaussian operation, allows us to create arbitrary orders of polynomial in the quadrature operators. I will not reproduce a general proof of this here, however an insight can be gained by considering the commutation relations for operations that are cubic in the quadrature operators:

$$[\hat{x}^3, \hat{x}^n \hat{p}^m] = \frac{3m\mathrm{i}}{2} \hat{x}^{n+2} \hat{p}^{m-1} + \text{additional lower order terms}, \tag{7.33}$$

$$[\hat{p}^3, \hat{x}^n \hat{p}^m] = \frac{-3n\mathrm{i}}{2} \hat{x}^{n-1} \hat{p}^{m+2} + \text{additional lower order terms}. \tag{7.34}$$

Therefore, if one can implement the operation $[\hat{x}^3, \hat{x}^n \hat{p}^m]$ or $[\hat{x}^3, \hat{x}^n \hat{p}^m]$, one can raise a transformation from order $n + m$ in the quadrature operators to order $n + m + 1$. This can be achieved by using the approximate identities for the application of two Hamiltonians $\hat{A}$ and $\hat{B}$ for periods of duration $\delta t \ll 1$ (where as previously I have set $\hbar = 1$),[149,162]

$$e^{-\mathrm{i}\hat{A}\delta t} e^{-\mathrm{i}\hat{B}\delta t} e^{\mathrm{i}\hat{A}\delta t} e^{\mathrm{i}\hat{B}\delta t} = e^{[\hat{A},\hat{B}]\delta t^2} + O(\delta t^3), \tag{7.35}$$

$$e^{\mathrm{i}\hat{A}\delta t} e^{\mathrm{i}\hat{B}\delta t} e^{\mathrm{i}\hat{B}\delta t} e^{\mathrm{i}\hat{A}\delta t} = e^{\mathrm{i}(\hat{A}+\hat{B})\delta t} + O(\delta t^3). \tag{7.36}$$

With these approximate identities, it can be seen that a polynomial of any desired order in $\hat{x}$ and $\hat{p}$ can be constructed by repeated application of a cubic quadrature operation. This can be extended to show that similar commutation relations exist for any operation that is at least cubic in the quadrature operators, and hence any non-Gaussian operation is sufficient for universal quantum computing[18,163]. This is analogous to the discrete-variable case, in which it is sufficient to be able to implement only one form of two-qubit gate for universal quantum computing (Section 7.1.1). A closely linked result was given in Ref. [164], in which it was shown that quantum circuits consisting only of Gaussian initial states and Gaussian operations can be efficiently classically simulated.[7]

An alternative definition of universality follows from schemes in which a discrete-variable system is embedded within a continuous-variable space. For example, in Ref. [161], a qubit is encoded as a superposition of two continuous-variable states. In this case, it was found that a set consisting of Gaussian operations along with the cubic phase gate $e^{\mathrm{i}\gamma\hat{x}^3}$ allows for universal discrete-variable quantum computing.

As with any approach to linear-optical quantum computing, continuous-variable quantum computing has its strengths and weaknesses. One significant advantage as compared to discrete-variable optical implementations is that Gaussian states can be created on-demand, and entanglement can be generated deterministically using beam splitters and squeezing operations[18,20]. Additionally, all of the gates required to build a universal quantum computer can in principle be implemented deterministically without requiring single photon level nonlinear interactions[161]. A substantial obstacle is that, in practice, it is challenging to implement the non-Gaussian operations, although there are some promising approaches based on using the non-linearity of photon-number resolving detection[72,161,166–168]. An additional drawback is that continuous-variable quantum computing is somewhat less developed theoretically than its discrete-variable counterpart, particularly with regard to error correction and loss tolerance[169–171]. Even the question of how to implement a given Hamiltonian, given a specific non-Gaussian operation, is an area of active research[163,172].

---

[7] More specifically, Ref. [164] proves that circuits in which both the initial states and operations can be represented by positive Wigner functions can be efficiently classically simulated. For pure states, this corresponds exactly to Gaussian states, while for mixed states, non-Gaussian states can also have positive Wigner functions[165].

7.3.1 Measurement-based continuous-variable quantum computing

As with DV quantum computing, a promising approach to CV quantum information processing is through measurement-based quantum computing using cluster states[173–175] (Section 7.2.3). The canonical model of continuous-variable cluster-state computing is a straightforward remapping of the discrete-variable approach to the CV regime. In this approach, $|\mathbf{0}\rangle$ and $|+\rangle$ states are replaced with qumodes in the $x_k = 0$ eigenstate $|0_{x_k}\rangle = 1/\sqrt{\pi}\int_{-\infty}^{\infty}|p_k\rangle\,\mathrm{d}p_k$ and the $p_k = 0$ eigenstate $|0_{p_k}\rangle = 1/\sqrt{\pi}\int_{-\infty}^{\infty}|x_k\rangle\,\mathrm{d}x_k$ respectively. As with the DV case, these states are therefore related by a basis rotation. Note that these quadrature eigenstates are the infinitely-squeezed limit of a single-mode squeezed vacuum state, and therefore can only be prepared approximately. This leads to errors that accumulate during protocols, however, it has been shown that these can in principle be corrected for[171]. Continuing the remapping, the DV CZ gate is replaced with its CV equivalent, which implements the unitary operation $\hat{U}_{\mathrm{CZ}} = e^{2\mathrm{i}\hat{x}_j\hat{x}_k}$[173,176]. Finally, Z measurements are replaced with x_k quadrature measurements.

In the discussion of this approach, I will employ the notation $X(s) = e^{2\mathrm{i}s\hat{p}}$ to denote the operator for a displacement in the $\hat{x}$ quadrature by the amount s, and $Z(s) = e^{-2\mathrm{i}s\hat{x}}$ for a displacement of s in the $\hat{p}$ quadrature. Additionally, I note that the rotation operator $F = \hat{P}(\pi/2)$ (Eqn. 1.38), which maps $\hat{x} \to \hat{p}$, is equivalent to a Fourier transform of the quadratures (Eqn. 1.20).

Similarly to the discrete-variable case, the CZ gate can be used to teleport the state of a qumode. Consider applying a CZ gate to an initial product state consisting of a general state $|\psi\rangle = \int_{-\infty}^{\infty} \mathrm{d}x'_j \, \psi(x'_j) \left|x'_j\right\rangle$ and a qumode in the $|0_{p_k}\rangle$ state,

$$\begin{aligned} &\hat{U}_{\mathrm{CZ}} \, |\psi\rangle \otimes |0_{p_k}\rangle && (7.37) \\ &= e^{2\mathrm{i}\hat{x}_j\hat{x}_k} \, 1/\sqrt{\pi} \int_{-\infty}^{\infty} \int_{-\infty}^{\infty} \mathrm{d}x'_j \mathrm{d}x'_k \, \psi(x'_j) \, |x'_j\rangle \otimes |x'_k\rangle && (7.38) \\ &= 1/\sqrt{\pi} \int_{-\infty}^{\infty} \int_{-\infty}^{\infty} \mathrm{d}x'_j \mathrm{d}x'_k \, e^{2\mathrm{i}x'_j x'_k} \psi(x'_j) \, |x'_j\rangle \otimes |x'_k\rangle \, . && (7.39) \end{aligned}$$

Evaluating the integral over x'_k gives (from the definition of the Fourier transform in Eqn. 1.20)

$$= \int_{-\infty}^{\infty} \mathrm{d}x'_j \, \psi(x'_j) \, |x'_j\rangle \otimes |(p'_k = x'_j)\rangle \, \mathrm{d}x_j \tag{7.40}$$

If one now measures the $\hat{p}_j$ quadrature, finding the result m, this projects the state into

$$= \int_{-\infty}^{\infty} \mathrm{d}x'_j \, \psi(x'_j) e^{-2\mathrm{i}mx'_j} \, |(p'_k = x'_j)\rangle \, . \tag{7.41}$$

This can be rewritten as

$$= X(m) \int_{-\infty}^{\infty} \mathrm{d}p'_k \psi(p'_k) \, |p'_k\rangle \, . \tag{7.42}$$

The initial state $|\psi\rangle$ has therefore been teleported onto the other qumode, modulo a known displacement of m in the $\hat{p}$ quadrature and a Fourier transform. An equivalent circuit representation is

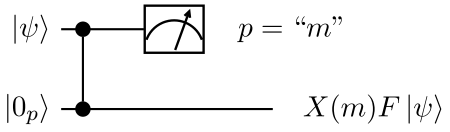

If we act on the state $|\psi\rangle$ before the circuit with any operation $D(\hat{x})$ that is diagonal in the $|x\rangle$ basis, which includes any arbitrary polynomial in $\hat{x}$, this operation will commute with the CZ gate, and so we find that

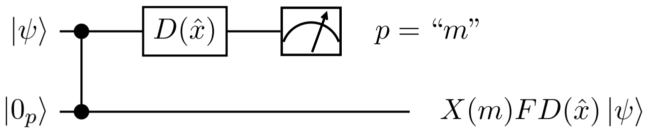

Concatenating this procedure twice allows for the implementation of a further transformation, this time with an arbitrary operator diagonal in the $\hat{p}$ quadrature. This follows from the equivalence[174] of the following two expressions

$$X(m_2)FD_2(\hat{x})X(m_1)FD_1(\hat{x})\,|\psi\rangle \tag{7.43}$$

$$= X(m_2)FX(m_1)FD_2(-\hat{p}+m_1)D_1(\hat{x})\,|\psi\rangle\,. \tag{7.44}$$

The output state is therefore transformed by $D_1(\hat{x})$ and then $D_2(-\hat{p}+m_1)$. The additional transformation $X(m_2)FX(m_1)F$ can be accounted for by simply changing the final measurement basis when the output state is read out. This shows that through a suitable series of measurements on a one-dimensional cluster state, it is possible to implement unitaries in $\hat{x}$ and $\hat{p}$ on the initial qumode.

Of course, in order to be able to implement a given unitary, it is necessary to be able to make the measurement basis transformations given by $D(\hat{x})^T\hat{p}D(\hat{x})$. For displacement operations, the required measurement basis is $\hat{p}+s$, which trivially equates to measuring in $\hat{p}$, and then adding the desired displacement to the measured result. Similarly, implementing a so-called shearing transformation of the form $e^{\mathrm{i}s\hat{x}^2}$ requires measuring in the basis $\hat{p}+s\hat{x}$. This can be achieved by phase shifting the mode, corresponding to a rotation of the quadrature basis in which it is measured. Further, it can be shown that in both of these cases, it is possible to incorporate the effects of the outcomes m after the measurements have already been made[174]. Therefore Gaussian transformations can be implemented without any feed-forward elements in the cluster-state model of continuous-variable quantum computing.

Unsurprisingly, this is not the case for non-Gaussian transformations. These still require the ability to induce a non-Gaussian transformation on the state before measurement. It can be shown, however, that it is possible to induce these gates by inserting appropriate non-Gaussian resource states into the cluster[174]. This then shifts the burden from the active implementation of non-Gaussian operations to the potentially easier off-line preparation of non-Gaussian resource states[161].

As in the discrete-variable case, it is possible to extend this model of continuous-variable cluster-state computing to implement arbitrary multi-mode Gaussian transformations. This requires a two-dimensional cluster resource state of entangled qumodes[18,174]. As discussed here, the addition of the capability to perform a single type of non-Gaussian operation on this 2D cluster state then allows for universal quantum computing[161].

7.4 Conclusions

Here I have provided an outline of some of the most promising currently known techniques for building a linear-optical quantum computer. However, even with these theoretical advances, there are huge practical challenges that must be overcome in order to build a functional universal quantum computer. This will require the combination of advances in non-classical light sources, high efficiency detectors and schemes for the low-loss manipulation of optical quantum information. In the remaining two chapters of this thesis, I consider one small part of this problem, developing novel techniques for the efficient encoding and manipulation of quantum information in the time-frequency degrees of freedom of the electromagnetic mode.

Chapter 8

Linear-optical quantum computing in a single spatial mode

As we have discussed in the previous chapter, in LOQC, logical gates can only be implemented probabilistically. Several techniques have been proposed to circumvent this problem, including the original KLM scheme, and more efficient measurement-based quantum computing schemes using cluster states. However, for all of these schemes, the overhead necessary for near-deterministic quantum computing is still large[9], and this presents one of the most significant challenges to the scalability of these approaches. To date, experimental demonstrations of these schemes have mainly adopted spatial degrees of freedom for the manipulation of quantum states[8,9,177–182]. Using this encoding, implementations of even few-qubit protocols in LOQC will demand many spatial modes and complex routing networks with active switches, necessary to implement feed-forward[51].

A similar need for ever-higher bandwidth encoding of information in optical fields has spurred innovation in modern telecommunication technologies. State of the art wavelengthdivision-multiplexed systems can now provide terabytes per second of capacity in a single fibre by leveraging sophisticated time-frequency (TF) encodings[183]. Adapting this approach for quantum information and communication protocols can naturally provide access to high dimensional Hilbert spaces[184–187] while maintaining a compact device design, and can leverage the existing classical communications technology base. Additionally, time-frequency encodings benefit from a relative insensitivity to inhomogeneities in transmission media[185,188]. These advantages have been recognised in works exploring the preparation of time-frequency entangled states[189–192], including their use in the violation of Bell inequalities[193,194], quantum key distribution[195], teleportation[44], and cluster states[196–200].

Quantum computing based on time-frequency encoding has received comparatively little attention, but has become increasingly feasible with the advent of fast switchable integrated phase controllers [54,201]. This was highlighted by a recent classical simulation of a quantum random walk based on a time-bin encoding and fast polarisation switching[202]. Previous studies have explored unitary operations for time[203,204] and frequency encodings[205], but these implementations have relied on conversion from time-frequency to multiple spatial modes for manipulation.

Here I present a concept for linear-optical quantum computing using time-bin encoded qubits and only a single spatial mode. Time bins provide a practical solution for the manipulation and detection of time-frequency modes with current technology. I outline methods that provide a sufficient set of operations to allow for universal quantum computing with both the KLM scheme and measurement-based quantum computing. In order to illustrate this scheme, we demonstrated experimentally the first implementation of a two-qubit quantum gate in a single spatial mode and showed its high fidelity of operation.

8.1 Encoding quantum information in time bins

Our scheme is based on a string of time-bin encoded qubits in a single spatial mode. The polarisation degree of freedom is used to define a 'register' polarisation, in which qubits are stored and transmitted, and a 'processing' polarisation in which specific time bins are briefly manipulated. After each processing stage, all qubits are returned to the register polarisation to ensure that a high degree of coherence is maintained between the time bins during further transmission.

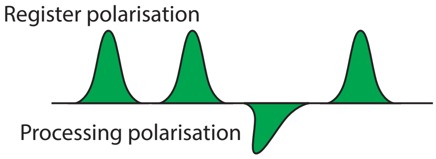

Figure 8.1: Encoding scheme for quantum information processing using time-bin qubits. A register polarisation (vertical) is used to store qubits; these qubits are rotated to the processing polarisation (horizontal) for manipulation.

8.1.1 Manipulating time-bin encoded quantum information

Five basic operations are needed for our implementation, as shown in Fig. 8.1: a polarisation rotation moves a time bin between register and processing polarisations; a displacement operation moves a time bin in the processing polarisation forwards and backwards relative to time bins in the register polarisation; a phase shift adds a specified phase between two polarisations; a polarisation coupling operation is a partial polarisation rotation between two orthogonally polarised time bins; and finally, a read-out operation measures the number of photons in a specified bin. With the exception of read out, each of these operations are equivalent to a relative phase shift between appropriate choices of polarisation axes. However, it is convenient to consider them separately here for clarity.

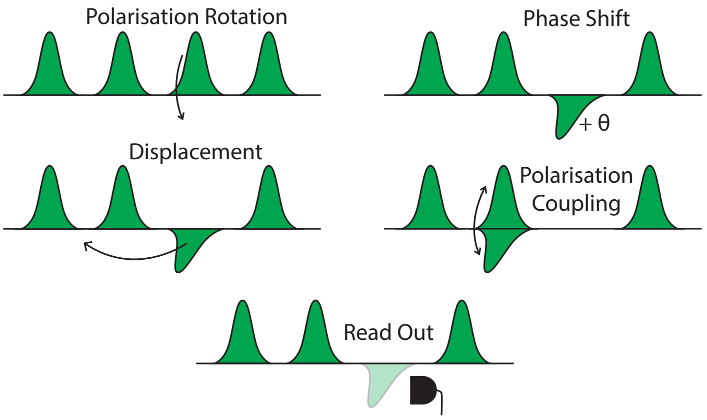

Figure 8.2: The complete set of basic operations necessary for the manipulation of a string of time bins in a single spatial mode.

Time-bin encoded single-qubit operations

Using this set of manipulations, I show in Fig. 8.3 how to perform arbitrary single-qubit operations. The operation uses a polarisation coupling, equivalent to a variable beam-splitter between the two polarisations, and two relative phase shifts applied to one polarisation. As discussed in Section 1.4.1, this is sufficient to implement any single-qubit rotation.

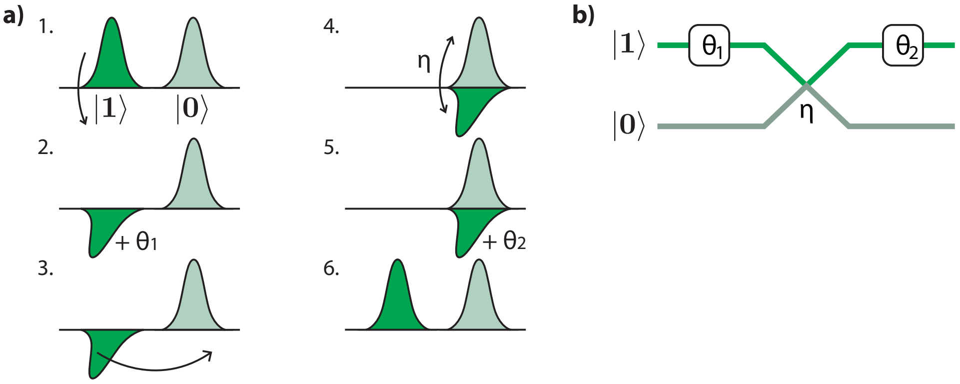

Figure 8.3: a) Operations sufficient for arbitrary time-bin encoded single-qubit operations. For brevity, the final displacement and rotation are implicit in the last line. b) Equivalent spatially encoded single-qubit operation.

The minimal set of processing elements required to perform these arbitrary single-qubit operations is shown in Fig. 8.4. Since all of the time bins in a given spatial mode will pass through these elements, they are sufficient to perform a different single qubit operation on every qubit in the spatial mode.

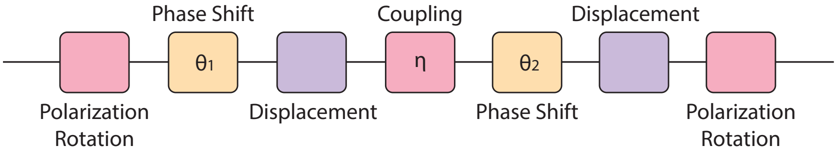

Figure 8.4: The minimal set of elements required to implement time-bin encoded single-qubit operations.

CPhase gate for time-bin encoded qubits

In Fig. 8.5, I provide a sequence of operations to perform a time-bin heralded KLM-CPhase gate[177,206] using two ancilla photons, sufficient to realise the entire KLM scheme in combination with single-qubit operations[154]. This can be trivially combined with local operations to perform a heralded controlled-NOT gate. The proposed scheme could be implemented using four of the sets of the elements in Fig. 8.4. Alternatively, since each stage of the operation returns the qubits to a single mode and polarisation, the string could simply be sent through the same processing elements four times. In this way, the simple set of elements shown could be used to enact arbitrary multi-gate operations.

Time-bin encoded cluster-state fusion gates

Our scheme is equally relevant to cluster state computing[8], as it also allows the implementation of type-I and type-II fusion operations. Although I will not discuss these operations in detail here, I note that these are extensively employed for the efficient construction of graph states, and would therefore allow for the creation of time-bin encoded optical cluster

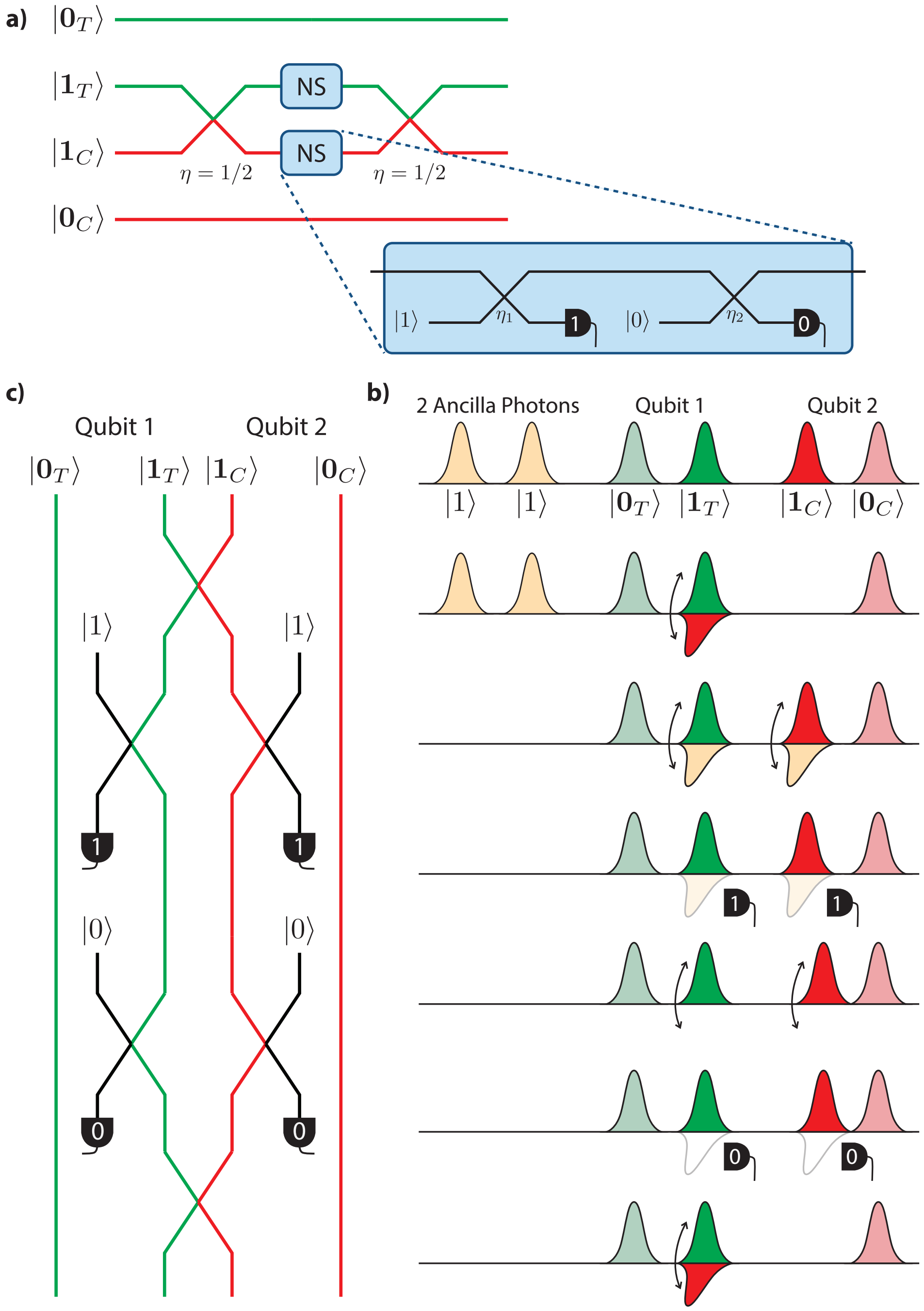

Figure 8.5: a) As discussed in Section 7.2.2, it is possible to construct a CPhase gate using two NS gates. Here we employ a simpler construction for a NS gate than shown in Fig. 7.5, but with an only slightly lower probability of success $P \approx 0.23$. The numbers on detectors represent the number of photons detected in order to herald successful gate operation. b) Explicit dual-rail construction for the CPhase gate in shown in a). c) Equivalent time-bin scheme for a CPhase gate. Displacement and rotation operations are omitted for brevity. This set of operations could be enacted by four sets of the elements shown in Fig. 8.2c, along with appropriate read-out elements.

states[159]. In Fig. 8.6 I provide protocols for these fusion gates.

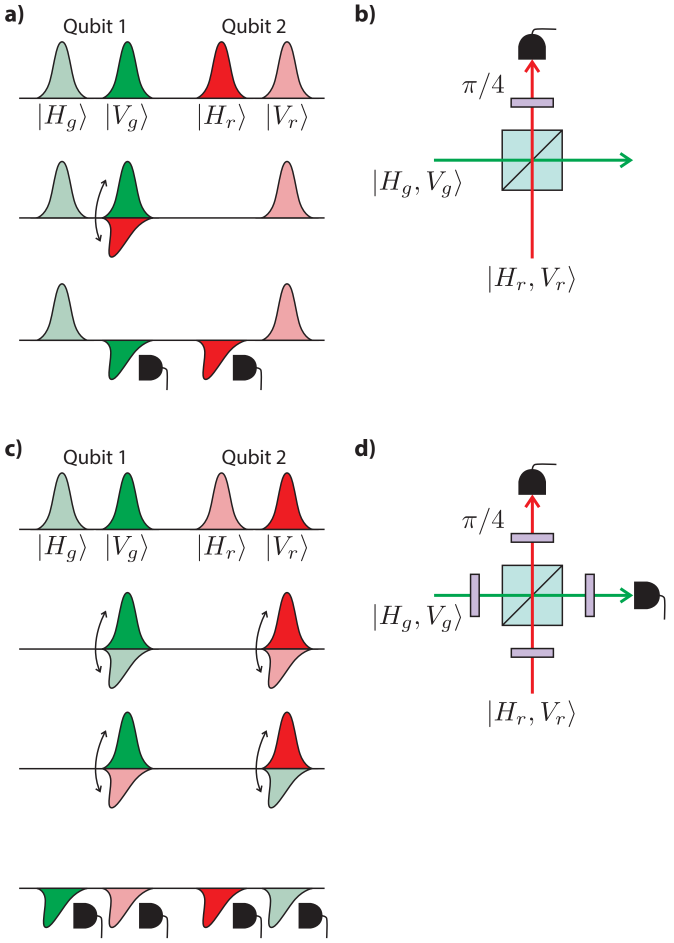

Figure 8.6: a) Protocol for the implementation of a type-I fusion operation. b) The equivalent conventional polarisation encoded circuit is given for comparison. The blue square represents a polarising beam splitter, while the purple optical elements represent $\pi/4$ polarisation rotations. c) Protocol for type-II fusion with d) equivalent polarisation encoded circuit.

8.2 Practical implementation of time-bin operations

Here I elaborate on a specific practical implementation of our scheme and discuss its feasibility within the current state of the art. As mentioned above, the basic logical operations are equivalent to a relative optical path length difference between a suitable choice of polarisation axes. The appropriate experimental approach to generating these path length differences will depend on the specific time-bin structure that is used, as the bandwidth of different photon sources, and thus the time-bin duration, can differ by several orders of magnitude[74]. Here I will consider time bins with sub-ps duration; these are suitable for heralded single photons from spontaneous parametric down-conversion pumped by a pulsed laser. Bin-to-bin delay is set by the pump-pulse repetition period, which has been reduced below 10 ps in a number of systems[207–209].

Polarisation rotation and polarisation coupling operations require a programmable birefringent element that independently manipulates each time bin. The switching time for this element must be less than the delay between consecutive time bins. A suitable integrated optical switch based on cross-phase modulation in a fibre has demonstrated a switching window of 10 ps[201]. As cross-phase modulation is polarisation sensitive, this technique could be adapted to create fast-switched birefringent elements.

The detector time resolution does not constrain the bin-to-bin delay since switching allows arbitrary time-bin components to be moved to the processing polarisation or even to a separate read-out spatial mode for detection. Therefore read out can be achieved with standard photon-number resolving detectors, including spatially[210,211] and temporally-multiplexed[78,212] single-photon detectors as well as transition edge sensors[213,214].

For a displacement operation, a simple approach is to use a birefringent element that effects a polarisation-dependent path length difference equal to integer multiples of the time-bin separation. A few-cm length of calcite would achieve a displacement of 10 ps. Alternatively, a delay loop could be used, coupled to the main mode by a Mach-Zehnder interferometer. A π phase shift created in this interferometer for only one polarisation would couple that polarisation into the delay line. The controllable phase shift could then be set to keep this polarisation in the delay loop for an arbitrary integer number of loops, delaying it with respect to the primary set of time bins. A 3 mm delay line, possibly implemented on an integrated photonic chip, would create a 10 ps displacement. Although the scheme is no longer entirely single spatial modal with the use of a delay line, the arbitrary number of delay steps it allows may be desirable for faster processing. Finally, in the near future, it should be possible to use a quantum memory to reorder time bins arbitrarily, as demonstrated with classical pulses in a warm-vapour gradient echo memory [215]. This could provide a significant reduction in the number of individual operations needed.

8.3 Experimental demonstration of a time-bin encoded CPhase gate

In order to demonstrate the feasibility of our scheme, we have built an entirely single-spatial-mode post-selected CPhase gate for time-encoded qubits. Our gate is equivalent in principle to previous implementations [179,216] that use spatial encoding, often along with a second degree of freedom such as polarisation. Preceding the gate is a polarisation-to-time conversion stage, and following it a time-to-polarisation conversion stage allows for measurement. The experimental layout is shown in Fig. (8.7). At the core of our experiment, a single-spatial-mode two-qubit gate is enacted. In this proof-of-principle experiment, we have replaced birefringent switches with passive beam splitters and a second spatial mode, as this allows us to readily incorporate two-mode analogues of single-spatial-mode single-qubit rotations and displacement operations (Fig. 8.2).

8.3.1 Experimental details

Our experiment uses two spontaneous parametric down-conversion sources for the generation of heralded single photons. An 80MHz Ti:Sapphire oscillator (Mai-Tai, Spectra Physics) producing 100 fs pulses at 830nm (2.6W average power) is up-converted to 700mW of 415nm light via a $700\mu m$ BaB2O4 (BBO) crystal cut for type-I second-harmonic generation. This is split on a 50:50 beam splitter and used to pump two 8mm-long AR-coated Potassium Dihydrogen Phosphate (KDP) crystals phase-matched for degenerate type-II collinear parametric down-conversion. We spend time optimising the collection optics and spatial mode-matching to achieve a coincidence count rate of 160kHz on each crystal with a raw heralding efficiency of 28-30% without any filters. The source is designed to be spectrally factorable[155] so that the heralded photons remain in a pure state (purities of upwards of 95% are achievable from this source without filtering). This is necessary to ensure high quality HOM interference between the photons. Interference filters (Semrock, $\Delta\lambda = 3$nm) are used to further boost this purity with limited impact on the source brightness. With the filters in place we achieve a four photon coincidence rate of 20 Hz when measured directly from the sources.

Two heralded single photons from these sources are initially used to encode qubits in the polarisation state of each photon using $\lambda/2$ and $\lambda/4$ waveplates. To provide a concise mathematical description of the photon states, I will label them the ‘control’ and ‘target’

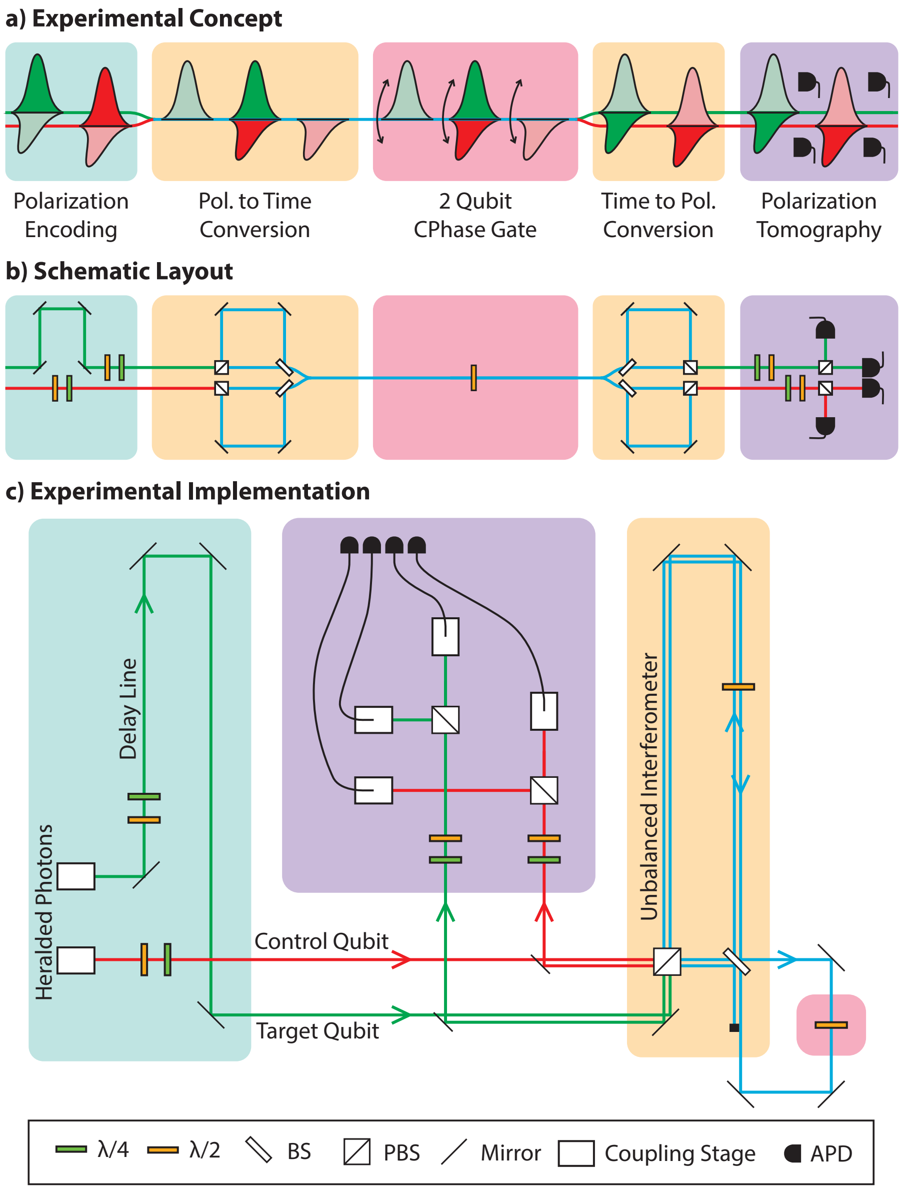

Figure 8.7: a) Concept for a single-spatial-mode CPhase gate with preceding state-preparation and following measurement stages. The photons are spectrally degenerate, and are colour coded here for clarity. b) Schematic of the associated experimental layout. Waveplates are used to encode polarisation states for both the target photon (green) and the control photon (red). The target photon is delayed with respect to the control photon, and both are coupled into unbalanced interferometers for conversion of polarisation encoding to time encoding. The photons are then combined into a single spatial mode in which a two-qubit gate is implemented using a half-wave plate. Conversion back to polarisation-encoding states again uses unbalanced interferometers. Finally, polarisation tomography is carried out using four avalanche-photodiode (APD) detectors. c) Actual experimental implementation. Two SPDC sources provide heralded single photons for the experiment, which proceeds as described above, except that a single unbalanced interferometer is used instead of the four separate unbalanced interferometers for conversion between polarisation-encoding and time-encoding.

photon respectively.

$$\begin{aligned}\text{Control Photon: } |\psi_C\rangle &= \alpha_C |H\rangle + \beta_C |V\rangle \\ \text{Target Photon: } |\psi_T\rangle &= \alpha_T |H\rangle + \beta_T |V\rangle \end{aligned} \tag{8.1}$$

The target photon is delayed with respect to the control photon, and then both are coupled into the same polarising beam splitter (PBS). This is used to send the polarisation components down different arms of a 1.5m unbalanced interferometer. Bringing the two components back together using a balanced beam splitter finishes the polarisation to time-encoding conversion. The final beam splitter can only recombine the time-bin components probabilistically, although the failure modes come out of the wrong port of the beam splitter, and so do not contaminate the rest of the experiment. This could be replaced by an active switching element to deterministically recombine the time bins into a single spatial mode.

After this conversion, the two photons are orthogonally polarised along a common mode, with the target photon delayed so that its first time bin coincides with the second time bin of the control photon. Due to the interferometric technique used for polarisation to time conversion, relative phases are acquired by different qubit components. These are denoted by θ_{C1} and θ_{T1}, where I have used the convention that the phase is applied to the delayed component. The qubits are now in the state

$$\begin{aligned}|\psi_C\rangle &= \alpha_C |1H\rangle + e^{\mathrm{i}\theta_{C1}}\beta_C |2H\rangle \\ |\psi_T\rangle &= e^{\mathrm{i}\theta_{T1}}\alpha_T |3V\rangle + \beta_T |2V\rangle \end{aligned} \tag{8.2}$$

where, for example, $|1H\rangle$ denotes a photon in time-bin 1 and polarisation H, and the time bins are numbered sequentially from earliest to latest. This encoding allows the gate operation to be implemented using a single half waveplate as a variable beam splitter between the two polarisations, creating Hong-Ou-Mandel interference[69] between the two coincident time bins. When the axes of the waveplate are aligned with photon polarisations, the gate operates with identity, while at 27.4 degrees, it implements a CPhase operation. The non-overlapped time bins also couple with ancillary loss modes due to this polarisation beam splitter, analogously to the coupling to spatial ancilla modes in a more conventional CNOT gate. As with other implementations of this scheme, the gate only succeeds with probability 1/9. A successful operation maps

$$\begin{aligned} & \alpha_1 \left|1H\right\rangle \left|3V\right\rangle + \alpha_2 \left|1H\right\rangle \left|2V\right\rangle + \alpha_3 \left|2H\right\rangle \left|3V\right\rangle + \alpha_4 \left|2H\right\rangle \left|2V\right\rangle \\ \rightarrow \quad & \alpha_1 \left|1H\right\rangle \left|3V\right\rangle + \alpha_2 \left|1H\right\rangle \left|2V\right\rangle + \alpha_3 \left|2H\right\rangle \left|3V\right\rangle - \alpha_4 \left|2H\right\rangle \left|2V\right\rangle \qquad (8.3) \\ & \text{where } \alpha_1 = e^{\mathrm{i}\theta_{T1}}\alpha_C\alpha_T,\ \alpha_2 = \alpha_C\beta_T, \alpha_3 = e^{\mathrm{i}(\theta_{T1}+\theta_{C1})}\alpha_T\beta_C,\ \alpha_4 = e^{\mathrm{i}\theta_{C1}}\beta_T\beta_C. \end{aligned}$$

After the gate, the photons are reinjected into the same unbalanced interferometer in the other direction (with the components in the long arm again gaining relative phase terms, this time denoted θ_{C2} and θ_{T2}). This allows the time-bin encoding to be decoded back into polarisation, after which polarisation tomography can be carried out to measure the state of the qubits. This gives the output state

$$\begin{aligned} & e^{\mathrm{i}(\theta_{T1}+\theta_{C2})}\Big(\alpha_C\alpha_T \left|2V\right\rangle \left|3V\right\rangle + e^{\mathrm{i}(\theta_{T2}-\theta_{T1})}\alpha_C\beta_T \left|2V\right\rangle \left|3H\right\rangle + e^{\mathrm{i}(\theta_{C1}-\theta_{C2})}\alpha_T\beta_C \left|2H\right\rangle \left|3V\right\rangle \ldots \\ & - e^{\mathrm{i}(\theta_{T2}-\theta_{T2}+\theta_{C1}-\theta_{C2})}\beta_T\beta_C \left|2H\right\rangle \left|3H\right\rangle \Big), \qquad (8.4) \end{aligned}$$

where the polarisation qubits (in time bins 2 and 3 respectively) have been output in separate modes from the unbalanced interferometer (Fig. 8.7).

The reuse of the initial encoding interferometer creates an intrinsically phase stable encoding and decoding. As can be seen in Eqn. (8.4), if $\theta_{C1} - \theta_{C1}$ and $\theta_{T2} - \theta_{T1}$ are constant, the operation will be unaffected. This removes the need for phase stabilisation, although slow drifts in the alignment of the paths must be corrected for in order to ensure that the encoding is kept the same. Before each basis set measurement, we ensured that input diagonally polarised photons were output in the diagonally polarised basis. This was accomplished by using a $\lambda/4, \lambda/2, \lambda/4$ series of waveplates in the output paths to correct for the relative phase between the horizontal and vertical polarisations. Diagonally-polarised photons were input to the experiment, the $\lambda/2$ half waveplate was then adjusted to maximise the ratio of diagonally-polarised single photon detections to anti-diagonally-polarised single photon detections.

The output photons were detected using an array of four avalanche photodiode (APD) single photon counting modules (PerkinElmer SPCM-AQ4C). Due to the loss modes and non-deterministic decoding of the photons, the specific time bins of the output qubits must be measured separately. Therefore the outputs from the APD modules were each split into four different channels with different temporal delays, and monitored by a home-built coincidence counting program loaded onto a commercially available FPGA development board (Xilinx SP605) operating with a 2.86 ns coincidence window. This splitting was necessary as the coincidence counting electronics did not have the ability to separately process different time bins of the same input signal. The 16 possible combinations of 2-folds of the register photons and two herald signals were recorded by the coincidence counter, allowing the qubit state to be reconstructed.

8.3.2 Results

Single-qubit polarisation-time-polarisation conversion results

In Fig. 8.8 I present data showing the high fidelity of the polarisation to time conversion. For the control and target photons, process tomography for the mapping from input polarisation state to output polarisation state gives a fidelity with the identity of 0.960 ± 0.001 and 0.936 ± 0.001 respectively. This shows that we can reliably create time-bin encoded qubits, and maintain their coherence across the setup. The error in the fidelity is due to the slight deviation of the non-polarising beam splitter away from its ideal reflectivity, and due to differences in coupling and loss between the different time-bins.

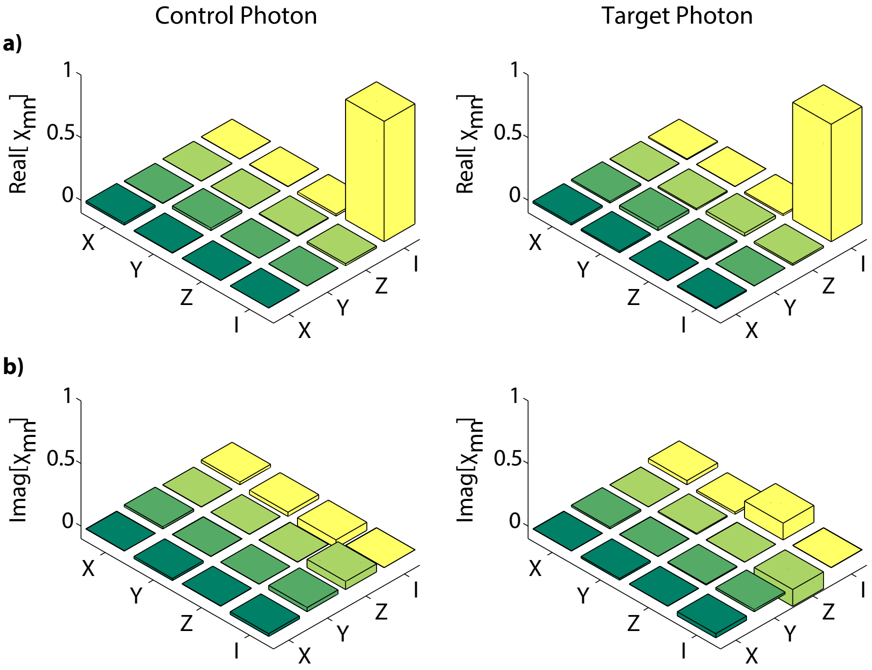

Figure 8.8: Single photon encoding and decoding performance. a) Real and b) imaginary parts of single qubit polarisation state tomography data for the 'control' and 'target' input photons respectively. Each shows a high fidelity with the identity.

Time-bin encoded CPhase gate results

To characterise the two-photon operation of our gate, we initially input a control photon with a horizontal (H) or vertical (V) polarisation and a target photon with an anti-diagonal (A) or diagonal (D) polarisation. For these inputs, the CPhase gate should swap the target photon polarisation between A and D if the control photon is V polarised. The measured gate outcomes are shown in Fig. (8.9), where the control and target photons are measured in the H-V and A-D bases, respectively. For these bases, we define a classical fidelity measure[217]

$$\begin{aligned} F_{HA} = 1/4[&P(HA|HA) + P(HD|HD) \\ &+P(VD|VA) + P(VA|VD)] \end{aligned} \tag{8.5}$$

where, for example, $P(VA|VD)$ represents the conditional probability of measuring outputs V and A given input V and D for the control and target photons respectively. We measure a classical fidelity of $F_{HA} = 0.84 \pm 0.03$. Changing the photon inputs to the control A-D and target H-V bases and also measuring in these bases, equivalent to transforming the bases by a Hadamard operation, allows us to measure a complementary fidelity F_{AH}. For this latter case, we measure a similar fidelity $F_{AH} = 0.84 \pm 0.02$.

Following Ref. [217], we use these fidelity measures to bound the quantum process fidelity. The resulting bound of the gate process fidelity F_{process}

$$F_{AH} + F_{HA} - 1 \leq F_{\text{process}} \leq \text{Min}[F_{AH}, F_{HA}] \tag{8.6}$$

is calculated to be $0.68 \pm 0.04 \leq F_{\text{process}} \leq 0.84 \pm 0.02$, comparable to other optical two-qubit

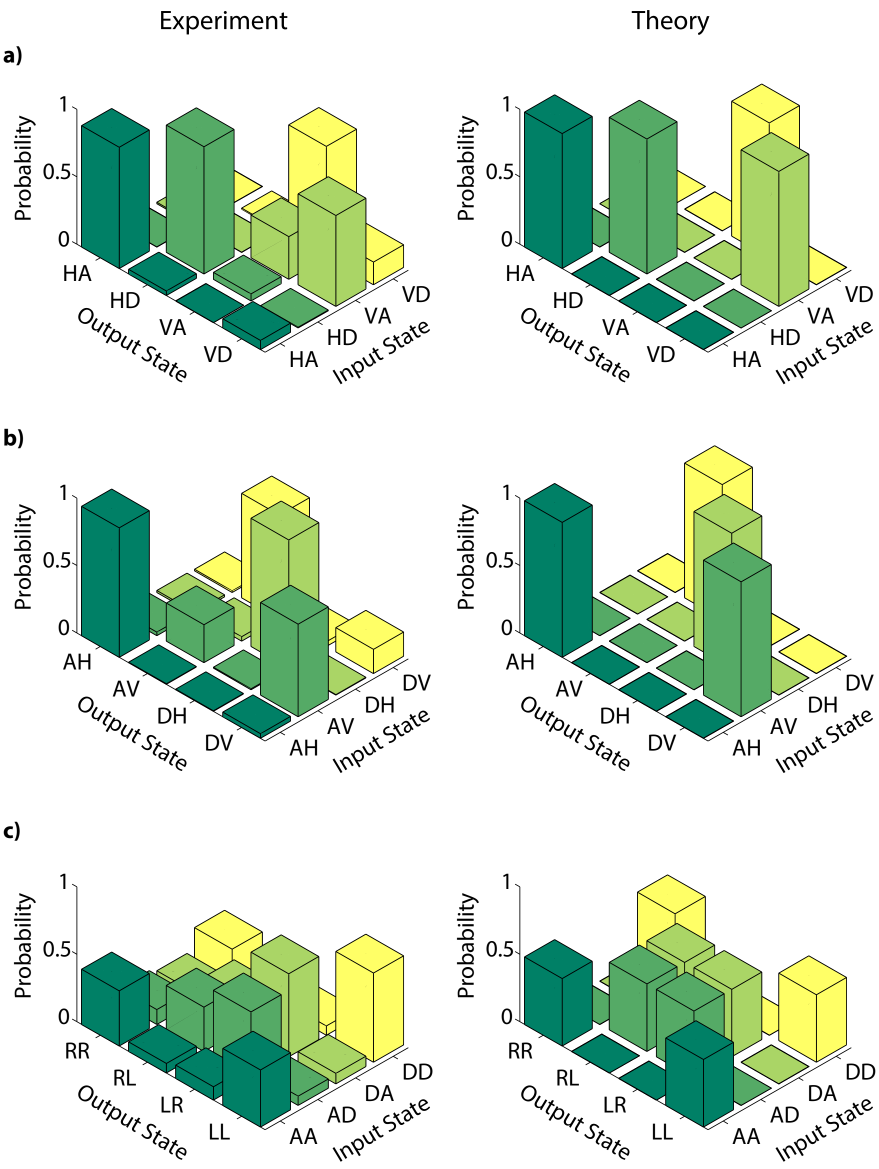

Figure 8.9: Two-qubit output state measurements: a) Input H-V and A-D bases for control and target photons respectively, output H-V and A-D bases. The measured classical fidelity for this operation is $F_{HA} = 0.84 \pm 0.03$. b) Input A-D and H-V bases, output A-D and H-V bases, resulting in $F_{AH} = 0.84 \pm 0.02$. c) Input A-D bases for both photons, output R-L bases for both photons, resulting in $F_{AA} = 0.85 \pm 0.06$. Each row of the experimentally determined output state matrices was determined from approximately 300 coincidence events, measured at a rate of 8 coincidences per minute. Theoretical ideal outputs are shown for comparison.

gate implementations[179,218].

An alternative measure of our gate fidelity demonstrates its non-classical operation. For this, we consider an additional choice of bases with both inputs in the A-D basis, and both outputs in the R-L (right-left) basis. We measure the classical fidelity for this operation to be $F_{AA} = 0.85 \pm 0.06$. As shown in Ref. [219], since this measure, along with F_{HA} and F_{AH}, are all greater than 2/3 the gate operation must be non-classical. Our gate exceeds this criterion with 99.8% confidence.[1]

The gate fidelity is primarily limited by the spatial mode overlap of our photons. Due to the long path length in the time-to-polarisation converter, this overlap is sensitive to the slight changes in alignment caused by temperature variations and vibrations. This path length is necessary to achieve a delay between consecutive time bins that is resolvable by the coincidence counting electronics (2 ns resolution) and detectors; it could be significantly reduced by using time-tagging electronics with few-hundred-ps temporal resolution[220]. We modelled this effect by calculating the ideal gate operation on partially distinguishable input photons in the states $|\psi\rangle$ and $\alpha\,|\psi\rangle + \sqrt{1-\alpha^2}\,|\psi_{\text{disting.}}\rangle$ respectively. We found that $\alpha = 0.91$ minimised the average L_1 distance $\langle L_1\rangle = \frac{1}{k}\sum_{j,k}|p_e(j|k) - p_t(j|k)|$ between the experimentally determined $p_e(j|k)$ and theoretical $p_t(j|k)$ probabilities for outcome j given input k. The minimised $\langle L_1\rangle$ was 0.18, as compared to 0.36 when assuming perfectly indistinguishable photons (the L_1 distance ranges from 0 for identical probability distributions to 1 for completely orthogonal distributions). Other experimental imperfections include higher-order photon number terms and residual photon impurity.

---

[1] The confidences (assuming Gaussian distributed errors) that F_{HA}, F_{AH} and F_{AA} are each greater than 2/3 are $1 - 2\times10^{-18}$, $1 - 4\times10^{-9}$, and 0.998 respectively. Multiplying these gives the overall confidence of 0.998.

8.4 Conclusions

In this chapter, I have presented a scheme for linear-optical quantum computing using time-bin encoded qubits in a single spatial mode. I have shown how to implement arbitrary single-qubit operations and a heralded CPhase gate as required for universal quantum computing in the KLM scheme. In support of this concept, we demonstrated a novel post-selected single-spatial-mode two-qubit CPhase gate. We measured an average classical gate fidelity of 0.84 ± 0.07 across 3 different bases, confirming its non-classical operation.

Our scheme is well suited to exploit the readily accessible high dimensionality and robustness of time-frequency modes to environmental dephasing noise. Fast switchable elements can enact different transformations on multiple time bins in a single pass, potentially allowing a substantial reduction in the required number of physical circuit elements. These advantages suggest that this scheme would naturally complement near-deterministic single photon sources [187,196], for which significant challenges exist in building many identical sources. In this case, a single repetitive source would prepare the computational resource state: a string of otherwise indistinguishable single photons in pure quantum states consisting of multiple time bins of a single spatial mode. Our scheme then circumvents the complexity and spatial requirements involved in converting many temporally encoded photons into a spatial encoding. Further, combining temporal and spatial degrees of freedom may enable a significant increase in information capacity [221].

Although this scheme presents a promising near-term route to significantly increasing the channel capacity of quantum information processing protocols, it does not fully utilise the available space of time-frequency modes, as we only consider modes with the same central frequency. Additionally, our scheme is intrinsically one-dimensional (unless combined with another degree of freedom, such as spatial modes). This may increase the complexity of information processing protocols, since the average distance between modes scales with the total number of modes N. In the following chapter, I will present an alternative approach to time-frequency quantum information processing that better exploits the full space of time-frequency modes. As we will discuss, this approach also has the benefit of creating an intrinsically two-dimensional encoding, in which the average distance between modes therefore scales as $N^{1/2}$.

Chapter 9

Continuous-variable quantum computing using quantum memories

In the last chapter, I introduced a scheme for linear-optical quantum computing that exploits the high dimensionality of time-bin modes. As previously noted, this encoding has also been used for other quantum information schemes[61,197–199,203,215]. Additionally, other works have exploited frequency encodings[222,223], in which information is encoded in different central-frequency modes with the same temporal profile. Irrespective of which method is chosen, both of these encodings can be visualised as a one-dimensional (1D) set of modes in time-frequency (TF) space, as shown in Fig. 9.1a.

These schemes can lead to a significant increase in the information available in an optical channel. However, they still use far fewer modes than the ultimate channel capacity. This can be seen by considering an arbitrary mode in TF space; it is constrained by the Fourier uncertainty principle, which defines a minimum area region occupied by each mode, $\delta t\, \delta\omega \geq 1/2$. Using a two-dimensional (2D) encoding in which these minimal area plaquettes are

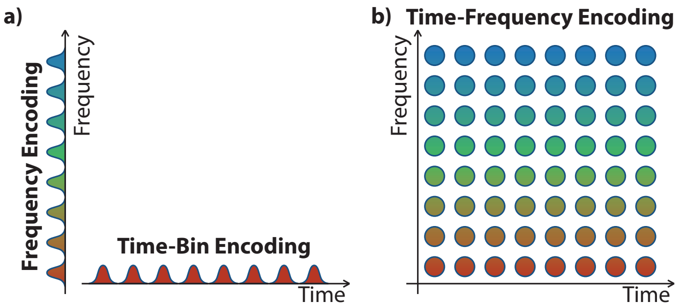

Figure 9.1: Quantum information can be encoded in a) central-frequency modes or time-bin modes. However, the maximum channel capacity can be achieved by b) tiling minimum uncertainty TF modes across the entire available encoding space.

tiled over the total available frequency bandwidth and time duration therefore achieves the maximum channel capacity (Fig. 9.1b).[1]

In order to take full advantage of this large potential encoding space, methods must be developed for the coherent generation, manipulation and measurement of TF encoded information. Here I will introduce such a scheme, discussing a method for continuous-variable (CV) cluster-state computing using TF modes. This focus on CV quantum computing is motivated by the applicability of the tools we develop to this model of quantum computing. In particular, the large Hilbert space allows for the effective encoding of the large resource state of entangled modes necessary for measurement-based quantum computing. However, the methods that we develop should also be widely applicable to many other QIP tasks.

9.0.1 Requirement for time non-stationary elements

Time-frequency (TF) manipulation schemes require an operation that can displace a mode in TF space from (ω_i, t_i) to (ω_j, t_j)[224–226]. This can be decomposed into separate translations

---

[1] In Fig. 9.1, for ease of discussion and illustration, we depict a set of modes with well separated time and central-frequency degrees of freedom. This modal decomposition can be made asymptotically orthogonal, however, it should be noted that it does not achieve the theoretical maximum support in time-frequency space. Modal decompositions such as Hermite-Gaussian modes are compatible with our scheme, and achieve a higher channel capacity.

in frequency and in time. Displacements in time are trivially achieved by, for example, using a delay line. However, time non-stationary interactions are necessary to couple different frequency modes. In the following, I briefly outline an argument demonstrating this.

For a linear interaction with an optical mode, the output field E_{out} is related to the input mode E_{in} by

$$E_{\text{out}}(t) = \int_{-\infty}^{\infty} R(t, t') E_{\text{in}}(t') \mathrm{d}t'. \tag{9.1}$$

If the response function $R(t, t')$ is time-stationary, it can only depend on the time difference $(t - t')$, giving

$$E_{\text{out}}(t) = \int_{-\infty}^{\infty} R(t - t') E_{\text{in}}(t') \mathrm{d}t'. \tag{9.2}$$

This integral has the form of a convolution, and so the Fourier transform gives

$$E_{\text{out}}(\omega) = \chi(\omega) E_{\text{in}}(\omega), \tag{9.3}$$

where the linear susceptibility $\chi(\omega)$ is the Fourier transform of $R(t)$. Therefore this time-stationary response function cannot couple different frequencies.

9.1 Time-frequency manipulation using Raman interactions

Although time non-stationary elements have been demonstrated for purely frequency-encoded quantum information[185,194,205], the dual requirement for both time and frequency sensitive manipulation is more challenging to satisfy[224,225]. Here we propose a method for controllably producing, manipulating and measuring TF encoded quantum states by exploiting the powerful modal selectivity of Raman light-matter interactions. These interactions have been demonstrated in diverse systems including alkali atom quantum memories [215,227–230], bulk diamond [231] and opto-mechanical resonators [232].

We consider an electromagnetic field mode, with a central frequency ω_i, that is temporally localised near local time $\tau_i = t - z/c$, where z represents the position along the direction of propagation (restricting ourselves to one spatial mode) and t is the laboratory time. We define an annihilation operator $\hat{a}_i$ for the mode. This field mode is coupled to a stationary memory mode $\hat{b}$ by an interaction Hamiltonian

$$\hat{H} = K_{ij}\, \hat{b}^\dagger\, \hat{a}_j^\dagger\, \hat{a}_i + K_{ij}^*\, \hat{a}_i^\dagger\, \hat{a}_j\, \hat{b}. \tag{9.4}$$

The coupling is mediated by a control field mode with central frequency ω_j, localised near τ_j, with an associated annihilation operator $\hat{a}_j$. The intrinsic strength of the coupling is determined by K_{ij}, which is a property of the specific system considered. The creation and annihilation operators for the modes obey the standard commutation relations $[\hat{a}_i, \hat{a}_j^\dagger] = \delta_{ij}$, $[\hat{a}_i, \hat{a}_j] = [\hat{a}_i, \hat{b}] = [\hat{a}_i, \hat{b}^\dagger] = 0$, $[\hat{b}, \hat{b}^\dagger] = 1$.

This phenomenological Hamiltonian may be used to describe several useful physical systems, and is the basis of Raman quantum memories, in which an electromagnetic mode is coupled into a stationary mode, stored, and subsequently read out through appropriate application of the control field.

9.1.1 Beam splitter operation

In the case when the control field is a bright coherent state, we can replace $\hat{a}_j$ with a c-number γ_j representing the field amplitude. In this case the effective Hamiltonian between the electromagnetic and stationary modes takes the form of a beam splitter (BS) interaction

$$\hat{H}_{\mathrm{BS}} = \gamma_j K_{ij}\, \hat{b}^\dagger\, \hat{a}_i\, + \gamma_j^* K_{ij}^*\, \hat{a}_i^\dagger\, \hat{b}. \tag{9.5}$$

Crucially, since the coupling, via $\gamma_j(\omega_j, \tau_j)$, is a function of ω_j and τ_j, the control field can be adjusted to coherently couple different TF modes with the stationary memory mode[226,230,233]. This TF dependent beam splitter is exactly the time non-stationary element that is required to carry out TF linear-optical quantum computing. This was recognised in a recent paper on the implementation of linear unitaries between different central-frequency modes using quantum memories[233]. In our scheme, we use this interaction to couple arbitrary TF plaquettes (Fig. 9.1b). With this element, it is therefore possible to implement TF versions of any linear-optical quantum computing scheme.

The Hamiltonian in Eqn 9.5 induces the modal transformation

$$\begin{pmatrix} \hat{a}_i \\ \hat{b} \end{pmatrix} = \begin{pmatrix} 1 & 0 \\ 0 & e^{\mathrm{i}\,\theta} \end{pmatrix} \begin{pmatrix} \cos\phi & \sin\phi \\ -\sin\phi & \cos\phi \end{pmatrix} \begin{pmatrix} 1 & 0 \\ 0 & e^{-\mathrm{i}\,\theta} \end{pmatrix} \begin{pmatrix} \hat{a}_i \\ \hat{b} \end{pmatrix} \tag{9.6}$$

where we have made the substitution $\phi\, e^{\mathrm{i}\theta} = \mathrm{i}\,\gamma_i K_{ij}/\hbar$. Written in this form, it is evident that this Hamiltonian produces a transformation equivalent to the application of a phase shift of $-\theta$ to mode $\hat{b}$, followed by a ‘standard’ (real coefficients) BS operation (as introduced in Section 1.4.1), and a final phase shift of θ to the same mode (Fig 9.3a).

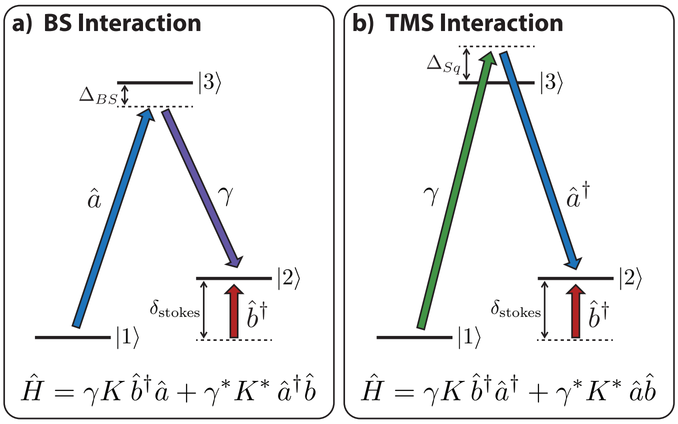

Figure 9.2: An example off-resonant Raman memory scheme based on a three-level system. An electromagnetic mode $\hat{a}$ is coupled to the transition $\hat{b}$ between levels $|1\rangle$ and $|2\rangle$ through a Raman transition to a virtual energy level detuned by Δ from $|3\rangle$. By adjusting the frequency of the control field-mode γ, both a) beam splitter interactions and b) two-mode squeezing interactions can be generated between the modes. The BS operation can realise read in/out from the memory.

9.1.2 Two-mode squeezing operation

For continuous-variable quantum computing, the utility of Raman quantum memories extends beyond linear mode manipulations. If in Eqn. 9.4, the classical limit of the $\hat{a}_i$ field-mode is instead taken (for notational consistency with the BS interaction, we will also swap $\hat{a}_i$ and γ_i), two-mode squeezing (TMS) can be generated between the $\hat{a}_j$ mode and the stationary $\hat{b}$ mode[167,230,234]

$$\hat{H}_{\text{TMS}} = \gamma_i K_{ij}\, \hat{b}^\dagger\, \hat{a}_j^\dagger \; + \gamma_i^* K_{ij}^*\, \hat{a}_j\, \hat{b}. \tag{9.7}$$

In this case, the electromagnetic mode that is coupled to the memory has changed. However, in many physical systems, it is possible to adjust the frequency of the classical field used so that the electromagnetic mode coupled is the same for BS and TMS operations.

In the Heisenberg picture, with the substitution $r\, e^{\mathrm{i}\psi} = -\mathrm{i}\, \gamma_i K_{ij}/\hbar$, this operation induces a mode transformation

$$\begin{pmatrix} \hat{a}'_j \\ \hat{b}' \end{pmatrix} = \begin{pmatrix} 1 & 0 \\ 0 & e^{\mathrm{i}\psi} \end{pmatrix} \begin{pmatrix} \mu & 0 \\ 0 & \mu \end{pmatrix} \begin{pmatrix} 1 & 0 \\ 0 & e^{-\mathrm{i}\psi} \end{pmatrix} \begin{pmatrix} \hat{a}_j \\ \hat{b} \end{pmatrix} + \begin{pmatrix} 1 & 0 \\ 0 & e^{\mathrm{i}\psi} \end{pmatrix} \begin{pmatrix} 0 & \nu \\ \nu & 0 \end{pmatrix} \begin{pmatrix} 1 & 0 \\ 0 & e^{\mathrm{i}\psi} \end{pmatrix} \begin{pmatrix} \hat{a}^\dagger_j \\ \hat{b}^\dagger \end{pmatrix}. \tag{9.8}$$

This Hamiltonian therefore produces a transformation equivalent to the application of a phase shift of $-\psi$ to mode $\hat{b}$, followed by a 'standard' (real coefficients) TMS operation (as introduced in Section 1.4.2), and then a final phase shift of ψ to the same mode (Fig. 9.3b).

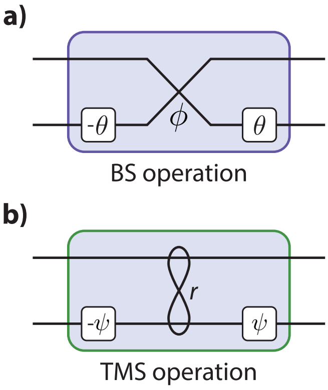

Figure 9.3: a) The Raman memory BS operation can be decomposed into a phase shift of $-\theta$ to mode $\hat{b}$, followed by a standard BS operation parametrised by ϕ, and a final phase shift of θ to the same mode. The coefficients θ and ϕ are determined by the control field applied. b) The TMS operation can be similarly decomposed into a phase shift of $-\psi$ to mode $\hat{b}$, followed by a standard TMS operation parametrised by r, and a final phase shift of ψ to the same mode.

9.1.3 Arbitrary operations

More generally, for arbitrary linear-optical manipulations, it is desirable to be able to implement transformations consisting of the application of an arbitrary phase to each mode, followed by either a standard BS or TMS squeezing operation, as shown in Fig. 9.4a & Fig. 9.4b.

For the BS operation, this transformation corresponds to

$$\begin{pmatrix} \hat{a}'_i \\ \hat{b}' \end{pmatrix} = \begin{pmatrix} \cos\phi & \sin\phi \\ -\sin\phi & \cos\phi \end{pmatrix} \begin{pmatrix} e^{\mathrm{i}\,\theta_1} & 0 \\ 0 & e^{\mathrm{i}\,\theta_2} \end{pmatrix} \begin{pmatrix} \hat{a}_i \\ \hat{b} \end{pmatrix} \tag{9.9}$$

It can be seen that an equivalent transformation is given by

$$\begin{pmatrix} \hat{a}'_i \\ \hat{b}' \end{pmatrix} = \begin{pmatrix} e^{\mathrm{i}\,\theta_1} & 0 \\ 0 & e^{\mathrm{i}\,\theta_2} \end{pmatrix} \begin{pmatrix} \cos\phi & e^{-\mathrm{i}\,(\theta_1-\theta_2)}\sin\phi \\ -e^{\mathrm{i}\,(\theta_1-\theta_2)}\sin\phi & \cos\phi \end{pmatrix} \begin{pmatrix} \hat{a}_i \\ \hat{b} \end{pmatrix} \tag{9.10}$$

Therefore, by adjusting the phase of the control field so that $\theta' = (\theta_1 - \theta_2)$, it is possible to commute the phase shifts through the BS operation.

Similarly, for the TMS squeezing operation, the transformation in Fig. 9.4b corresponds to

$$\begin{pmatrix} \hat{a}'_j \\ \hat{b}' \end{pmatrix} = \begin{pmatrix} \mu & 0 \\ 0 & \mu \end{pmatrix} \begin{pmatrix} e^{\mathrm{i}\,\theta_1} & 0 \\ 0 & e^{\mathrm{i}\,\theta_2} \end{pmatrix} \begin{pmatrix} \hat{a}_j \\ \hat{b} \end{pmatrix} + \begin{pmatrix} 0 & \nu \\ \nu & 0 \end{pmatrix} \begin{pmatrix} e^{-\mathrm{i}\,\theta_1} & 0 \\ 0 & e^{-\mathrm{i}\,\theta_2} \end{pmatrix} \begin{pmatrix} \hat{a}_j^\dagger \\ \hat{b}^\dagger \end{pmatrix} \tag{9.11}$$

An equivalent transformation with the phase shifts moved to after the TMS operation is given by

$$\begin{pmatrix} \hat{a}'_j \\ \hat{b}' \end{pmatrix} = \begin{pmatrix} e^{\mathrm{i}\,\theta_1} & 0 \\ 0 & e^{\mathrm{i}\,\theta_2} \end{pmatrix} \begin{pmatrix} \mu & 0 \\ 0 & \mu \end{pmatrix} \begin{pmatrix} \hat{a}_j \\ \hat{b} \end{pmatrix} + \begin{pmatrix} e^{\mathrm{i}\,\theta_1} & 0 \\ 0 & e^{\mathrm{i}\,\theta_2} \end{pmatrix} \begin{pmatrix} 0 & e^{-\mathrm{i}\,(\theta_2+\theta_1)}\nu \\ e^{-\mathrm{i}\,(\theta_2+\theta_1)}\nu & 0 \end{pmatrix} \begin{pmatrix} \hat{a}_j^\dagger \\ \hat{b}^\dagger \end{pmatrix} \tag{9.12}$$

This can be achieved by adjusting the phase of the control field so that $\psi' = -(\theta_1 + \theta_2)$.

In this way a string of BS operations, TMS operations and phase shifts (Fig. 9.4c) can be implemented between a stationary mode and near-arbitrary TF modes using the Raman memory Hamiltonian. As shown in Fig. 9.4d, this is achieved by moving the desired phases

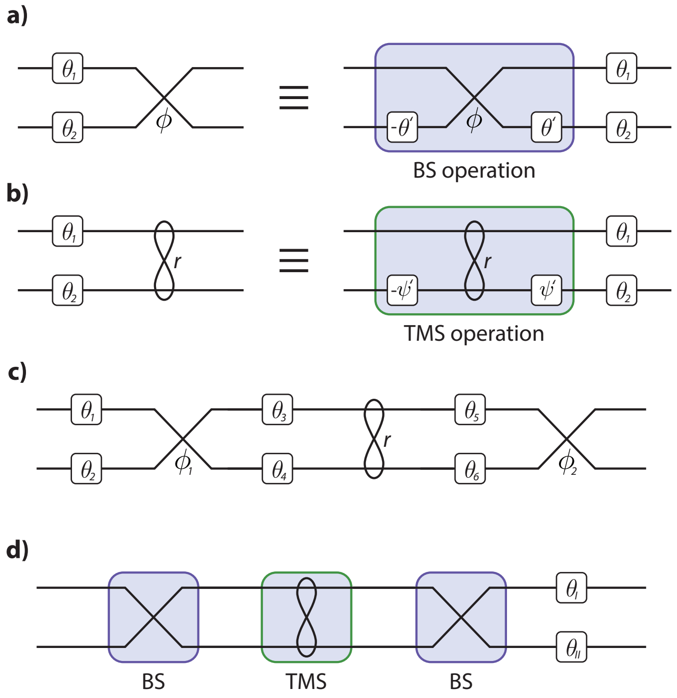

Figure 9.4: a) A general two mode interaction consisting of the application of a phase to each mode, followed by a standard BS transformation can be shown to be equivalent to a suitable Raman BS operation (with $\theta' = (\theta_1 - \theta_2)$) followed by the same phase shifts. b) Similarly, a two mode interaction consisting of the application of a phase to each mode, followed by a standard TMS transformation can be shown to be equivalent to a suitable Raman TMS operation (with $\psi' = -(\theta_1 + \theta_2)$) followed by the same phase shifts. c) Using these equivalences, an arbitrary string of phase shifts, BS and TMS operations can be implemented using Raman memories. A final corrective phase shift for each mode can simply be incorporated into a change of measurement basis when the mode is read out.

through each operation to the end of the chain. The final necessary corrective phases θ_I and θ_{II} can then simply be incorporated into a change of measurement basis when each mode is finally read out. Using this approach, Raman memories can therefore act as universal time non-stationary elements. As I will show below, this enables the full generation and manipulation of TF CV cluster states.

9.2 CV cluster state generation

As introduced in Section 7.3.1, the resource state in the canonical model of CV cluster-state computing is composed of a number of qumodes, each prepared in the $|0_{p_i}\rangle = \int_{-\infty}^{\infty} |x_i\rangle \, dx_i$ eigenstate. These qumodes must be entangled with each other as required to create a given cluster state geometry.

9.2.1 Two-qumode cluster

As a first step towards a full cluster state, we demonstrate how to use the TMS interaction to create two-qumode TF encoded cluster states. These will function as primitives for our full state. To do this, we note[175] that a two-mode canonical cluster state provides the same correlations as a two-mode squeezed state under a rotation of the quadratures of one of the modes, so that $x_i \to p_i$ and $p_i \to -x_i$. Therefore application of the TMS interaction between a vacuum electromagnetic mode and a memory initialised in its ground state will produce a qumode in the memory entangled with a qumode in the field (Fig. 9.5). A subsequent BS interaction can be used to 'read out' the memory qumode by coupling it into another TF plaquette. This produces a two-qumode TF cluster state (equivalent to an EPR state[18]).

9.2.2 Implementing a controlled-Z operation

After creation, these two-qumode clusters must then be linked to create a 2D cluster state. The canonical method for generating these links is to apply a so-called controlled-Z (CZ) gate, which implements the unitary operation $e^{2\,\mathrm{i}\,\hat{x}_i\hat{x}_j}$[173,176]. For this purpose, the TMS operation can not substitute the CZ gate, as the qumodes are not initially in the vacuum. The ability to implement the CZ gate also enables other cluster state computing schemes,

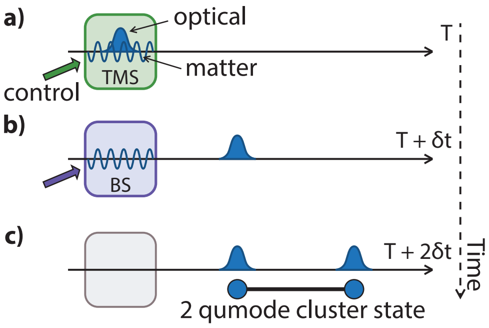

Figure 9.5: a) Initial time-bin two-qumode cluster states can be produced by using a Raman memory to create a TMS interaction between electromagnetic and memory vacuum modes. b) A BS interaction is then used to read out the memory qumode into another TF plaquette, resulting in c) a flying 2-TF mode cluster state.

such as the memory based cluster-state scheme described in[235]. Here I show that this gate can be achieved using three Raman memory interactions between an electromagnetic qumode and a memory qumode.

As I discussed in Section 1.4.3, all Gaussian operations can be decomposed into the combination of a linear interferometer, followed by parallel single-mode squeezing operations, and finally another linear interferometer. This is because, for the Bogoliubov transformation

$$\hat{a}_k \to \sum_j A_{jk}\hat{a}_j + \sum_j B_{jk}\hat{a}_j^\dagger, \tag{9.13}$$

the matrices A and B can be decomposed via the Bloch-Messiah reduction into

$$A = UA_DV^\dagger, \qquad B = UB_DV^T. \tag{9.14}$$

Using this decomposition, the CZ Hamiltonian is given by [2]

$$U = \begin{pmatrix} \sin\phi & -\mathrm{i}\cos\phi \\ \mathrm{i}\cos\phi & -\sin\phi \end{pmatrix}, \quad V = \begin{pmatrix} \cos\phi & -\mathrm{i}\sin\phi \\ \mathrm{i}\sin\phi & -\cos\phi \end{pmatrix},$$
$$A_D = \begin{pmatrix} \frac{\sqrt{5}}{2} & 0 \\ 0 & \frac{\sqrt{5}}{2} \end{pmatrix}, \quad B_D = \begin{pmatrix} \frac{1}{2} & 0 \\ 0 & \frac{1}{2} \end{pmatrix} \tag{9.15}$$

where $\phi = \frac{1}{2}\sin^{-1}(2/\sqrt{5}) \approx 31.72^\circ$.

This cannot be directly implemented using Raman quantum memories, as they can only implement TMS and BS operations. However, since the squeezing is the same for each mode, it is possible to substitute a TMS operation and suitable linear-optical transformations for the single mode squeezing[20]. A standard TMS operation, parametrised by μ and ν (Eqn. 1.67), is given by

$$A_{TMS} = \begin{pmatrix} \mu & 0 \\ 0 & \mu \end{pmatrix}, \quad B_{TMS} = \begin{pmatrix} 0 & \nu \\ \nu & 0 \end{pmatrix}. \tag{9.16}$$

Applying a 50:50 beam splitter operation and $\pi/2$ phase transformation before and after

---

[2] The discrepancy with[35] is due to a slight difference in the definition of the CZ Hamiltonian.

the squeezing operation, we find that

$$\begin{aligned}
A' &= \begin{pmatrix} \frac{1}{\sqrt{2}} & \frac{1}{\sqrt{2}} \\ \frac{\mathrm{i}}{\sqrt{2}} & -\frac{\mathrm{i}}{\sqrt{2}} \end{pmatrix} \begin{pmatrix} \mu & 0 \\ 0 & \mu \end{pmatrix} \begin{pmatrix} \frac{1}{\sqrt{2}} & -\frac{\mathrm{i}}{\sqrt{2}} \\ \frac{1}{\sqrt{2}} & \frac{\mathrm{i}}{\sqrt{2}} \end{pmatrix} \\
&= \begin{pmatrix} \mu & 0 \\ 0 & \mu \end{pmatrix} = A_D \\
B' &= \begin{pmatrix} \frac{1}{\sqrt{2}} & \frac{1}{\sqrt{2}} \\ \frac{\mathrm{i}}{\sqrt{2}} & -\frac{\mathrm{i}}{\sqrt{2}} \end{pmatrix} \begin{pmatrix} 0 & \nu \\ \nu & 0 \end{pmatrix} \begin{pmatrix} \frac{1}{\sqrt{2}} & \frac{\mathrm{i}}{\sqrt{2}} \\ \frac{1}{\sqrt{2}} & -\frac{\mathrm{i}}{\sqrt{2}} \end{pmatrix} \\
&= \begin{pmatrix} \nu & 0 \\ 0 & \nu \end{pmatrix} = B_D.
\end{aligned} \tag{9.17}$$

This is the desired parallel single-mode squeezing operation [20]. Combining this with the CZ Bloch-Messiah reduction (Eqn. 9.15), the CZ operation can therefore be implemented by $A = U' A_{TMS} V'^{\dagger}$, $B = U' B_{TMS} V'^{T}$ where

$$\begin{aligned}
U' &= \begin{pmatrix} \cos\phi' & -\sin\phi' \\ \mathrm{i}\sin\phi' & \mathrm{i}\cos\phi' \end{pmatrix}, \quad V' = \begin{pmatrix} \cos\phi' & \sin\phi' \\ -\mathrm{i}\sin\phi' & \mathrm{i}\cos\phi' \end{pmatrix}, \\
A_{TMS} &= \begin{pmatrix} \frac{\sqrt{5}}{2} & 0 \\ 0 & \frac{\sqrt{5}}{2} \end{pmatrix}, \quad B_{TMS} = \begin{pmatrix} 0 & \frac{1}{2} \\ \frac{1}{2} & 0 \end{pmatrix}
\end{aligned} \tag{9.18}$$

and $\phi' = \frac{\pi}{4} - \phi \approx 13.28°$. This operation is equivalent to the sequence of two-mode transformations shown in Fig. 9.6.

A straightforward protocol for implementing these transformations uses three successive memories (Fig. 9.7). It should be noted that it is also possible to use only BS operations to link qumodes [198,199] although, in this case, corrective displacement operations must be physically implemented on each qumode between measurements. Additionally, an alternative approach to creating cluster states requires only vacuum squeezing followed by linear

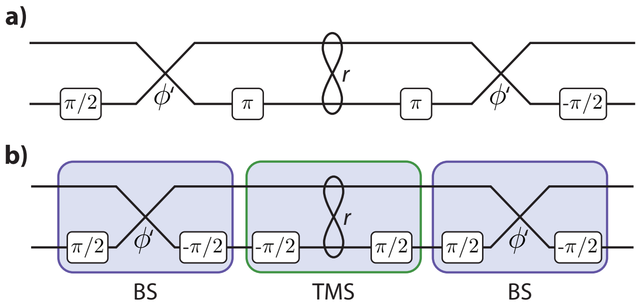

Figure 9.6: a) The sequence of two-mode transformations necessary to implement a CZ operation, with $r = \sinh^{-1}(1/2)$, $\phi' = \frac{\pi}{4} - \frac{1}{2}\sin^{-1}(2/\sqrt{5})$. b) Three Raman memory operations are sufficient to implement this operation.

interactions[175]. However, the number of linear interactions required scales quadratically with the number of qumodes in the cluster.

9.2.3 Building a 2D cluster state

In order to create a full 2D cluster state, we exploit the precise modal selectivity of the Raman memory to controllably address different TF plaquettes. This allows us to implement the CZ operations required to entangle neighbouring initial two-qumode cluster states (Fig. 9.8), creating the desired overall cluster topology. The modes within a time-bin that are not being addressed by a given memory will pass straight through, allowing each link to be created completely independently.

In this way, a linear chain of only $7d - 3$ quantum memories is sufficient to generate 2D cluster states encoded in d different central-frequency modes. The cluster state can be of significant temporal duration, since a given qumode is only stored in a memory for the length of time δt required to implement a BS or TMS operation. This requires that the coherence time of the memory $t_{\mathrm{mem}} \gg \delta t$. However, t_{mem} can be significantly less than the temporal extent of the entire cluster, so that $t_{\mathrm{mem}} \ll n\,\delta t$, where n is the number of time-bin

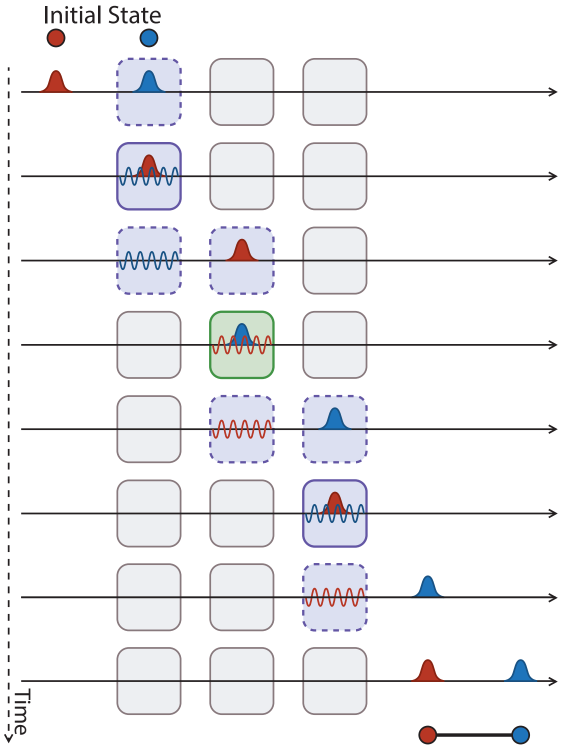

Figure 9.7: Three separate two-qumode operations are required to create a CZ gate, in the sequence BS, TMS, BS. Here we show the full protocol needed to implement such a gate between two qumodes encoded in different time-frequency plaquettes (control fields are omitted for clarity, but colours used to indicate the form of operation, with purple denoting BS operations and green denoting squeezing operations). This can be achieved by using a set of three quantum memories. Only three operations are used to implement the CZ gate (solid outlines), the other BS operations are simply required to maintain the temporal separation of the two qumodes (dashed outlines). The two qumodes are shaded in different colours for clarity, but do not necessarily have different central-frequencies.

modes. For a given δt and therefore $\delta\omega$, the number of different central-frequency modes d is then constrained by the range of frequencies δ_{full} that the memory can access. For example, in memories based on alkali atoms we require $\delta_{\text{full}} \ll \delta_{\text{stokes}}$ (Fig. 9.2) to suppress four-wave-mixing noise[236]. Therefore the maximum d is on the order of $\delta_{\text{full}}/\delta\omega \approx \delta_{\text{full}}\,\delta t$, which is the standard time-bandwidth-product figure of merit for quantum memories. Time-bandwidth-products upwards of 1000 have been demonstrated[228,236].

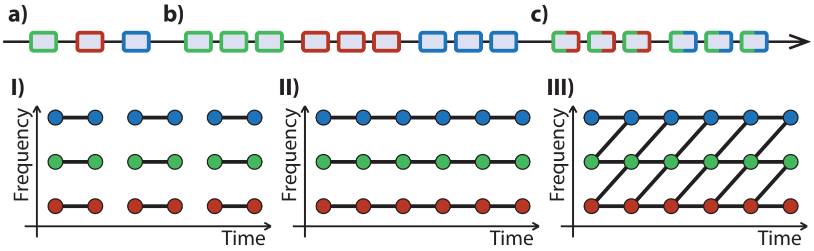

Figure 9.8: A linear chain of $7d-3$ quantum memories can generate 2D cluster states encoded in d different central-frequency modes and a large number of time-bin modes. a) d quantum memories are used to create two-qumode clusters encoded in plaquettes tiled across the available TF space, as shown in I) (colours are used to denote different central-frequency plaquettes, with the colour of the quantum memory corresponding to the central-frequency that it operates upon). b) Entanglement links are generated between two qumode clusters with the same central frequency using CZ interactions, as shown in II). This requires a further $3d$ memories. c) Entanglement is generated between qumodes with different central-frequencies, requiring a final set of $3(d-1)$ memories. This produces the final 2D cluster state shown in III).

9.3 Measurements and non-Gaussian operations

Once the cluster state is successfully constructed, quantum information processing tasks require the measurement of appropriate field quadratures for each qumode in the cluster. Since different central-frequency qumodes are co-propagating in the same time bin, a method of measuring each of these modes separately is needed. For this, we can again exploit the TF selectivity of quantum memories. Consider embedding a memory in one arm of a balanced Mach-Zehnder interferometer, with path lengths adjusted so that the qumodes are mapped back into their original mode (Fig. 9.9a). A BS operation can be applied to one frequency qumode that is sufficiently strong to read it in and then instantaneously read it out of the memory. It can be easily shown that this will create a π phase shift in this mode and therefore swap the output port from which it will exit. Homodyne detection can then be carried out on this qumode without disturbing the others.

In order to carry out universal quantum computation, non-linear operations or non-linear resource states are also needed[157,237] (Section 7.3). Direct implementation of non-

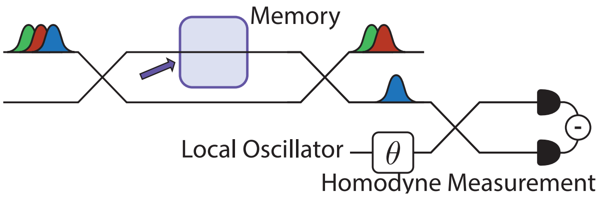

Figure 9.9: Measurement of a frequency qumode by using a quantum memory embedded in a balanced Mach-Zehnder interferometer. A BS operation is used to apply a π phase to the qumode to be measured, changing the output port it exits from. An arbitrary quadrature of the qumode can then be measured by using a local oscillator to carry out homodyne detection. This scheme may be implemented in a signal spatial mode by using appropriate polarisation elements.

linear operations is experimentally challenging[238], therefore most proposed schemes have been based on measurement-induced non-linearities[161,239]. Our method naturally provides a convenient platform for probabilistic non-Gaussian state generation schemes, since the qumodes are already stored in quantum memories at points of the protocol. The interval between storage and read-out therefore provides a period in which multiple attempts can be made at generating suitable non-linear states. The use of quantum memories to increase the success rate of photon subtraction has been studied in recent papers on entanglement distillation[167,234].

9.4 Cluster state generation with imperfect memories

The scheme I have presented has so far assumed ideal memories. Of course, in reality all physical systems will be imperfect at some level. Here I briefly explore the effects of this on our proposal.

The mode coupling BS transformations in the CZ operation (Fig 9.6b) require a beam splitter coupling strength of 5.3%, and the TMS transformation requires 4.2 dB of squeezing. This is compatible with current state-of-the-art Raman memories, which have achieved storage efficiencies of over 80%[240], and are estimated to be able to achieve a squeezing of 9.6 dB[167] (assuming that the modes for each transformation are similarly detuned from resonance).

This current state-of-the-art squeezing is below the levels needed for fault-tolerant quantum computing in the Menicucci scheme[171] (approximately 17-20 dB). However, in principle, an increase of 80% in the mode coupling strength would be sufficient to provide this. With this level of increase, it would also be theoretically possible to transfer modes between electromagnetic field modes and the memory mode with unit efficiency.

In reality, all physical experimental implementations are imperfect at some level. For any real quantum memory, it likely that it is not the coupling strength, but rather the imperfect overlap between the input and output field modes, and other losses associated with field propagation, that are likely to ultimately limit the storage efficiencies achievable. It should be noted that these imperfections are obstacles in all quantum linear-optical schemes, and as such are certainly not confined to memories as optical elements. However, in common with other such schemes, our proposal is sensitive to these deviations from ideal operation. Although a full treatment of the effects of these imperfections is beyond the scope of this thesis, in the following section I present calculations as an initial exploration of their expected impact.

9.4.1 Fidelity of cluster state generation with imperfect memories

We model imperfect two-qumode cluster state generation by applying a non-ideal read-out BS unitary (with a deviation from ideal operation parametrised by $\delta\eta$)

$$\begin{pmatrix} \sqrt{1-\delta\eta} & \sqrt{\delta\eta} \\ \sqrt{\delta\eta} & \sqrt{1-\delta\eta} \end{pmatrix} \tag{9.19}$$

between the memory mode of the initial generated TMS state (Fig. 9.5) and a vacuum electromagnetic field mode. We use the results of Ref. [241] to calculate the fidelity between this state and the ideal state, which we find to be

$$4/\sqrt{\left(\sqrt{1-\delta\eta}-\left(\sqrt{1-\delta\eta}-1\right)\cosh(2r)+1\right)^4} \tag{9.20}$$

where $r=-\frac{1}{2}\log\left(10^{-\frac{dB}{10}}\right)$ and dB is the squeezing in decibels.

The fidelity gives a useful indication of the expected performance of this state for quantum computing as it can be shown to be equal to the minimum overlap of the probability distributions for the outcomes of any general measurement on the respective states[242]. It therefore gives a rough estimate of the probability that a measurement of the state will give an erroneous result.

Fig. 9.10 shows a plot of this fidelity as a function of the desired squeezing level and the deviation from unit efficiency $\delta\eta$ of the read-out operation. As would be expected, the fidelity is increasingly sensitive to $\delta\eta$ as the squeezing increases. As an example, we consider a 17.4 dB squeezed cluster-state resource, sufficient in principle for fault-tolerant cluster-state computing if used with an error code able to tolerate gate error probabilities of 10^{-3}[171]. In order to produce a two-qumode cluster with a corresponding 10^{-3} infidelity to the ideal state, it is necessary to be able to read out the state with $1-7\times10^{-5}$ efficiency.

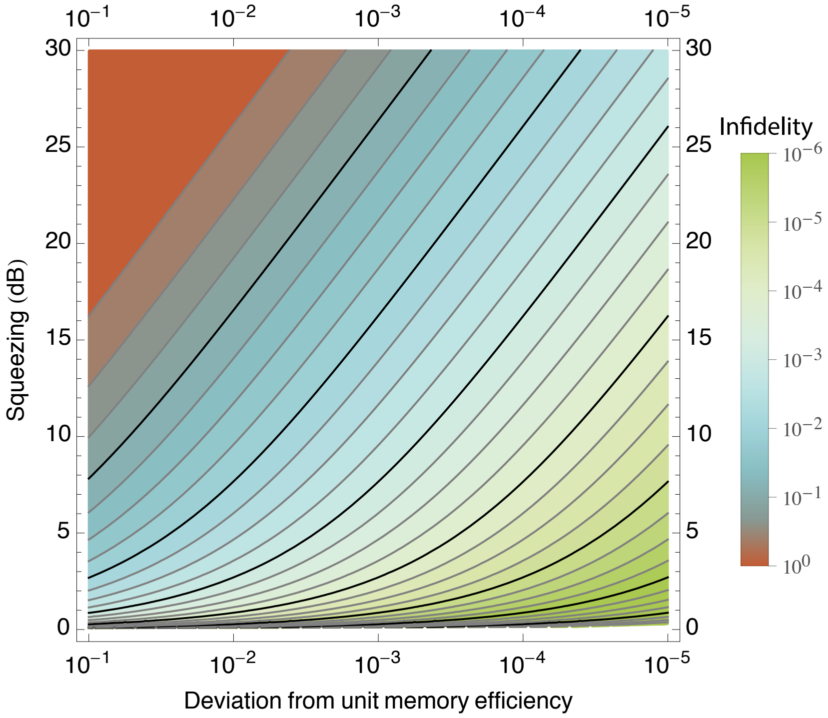

Figure 9.10: The infidelity (1-fidelity) between the state generated by our two-qumode cluster state protocol and an ideal TMS state with the same level of squeezing, as a function of the squeezing desired and the deviation from unit memory efficiency for the read-out operation. Contours are plotted on a logarithmic scale, with solid black lines at each order of magnitude.

This is beyond the current state of the art. However, it is likely that this situation will be improved upon in the near future, both in terms of the requirements for fault tolerance, and in terms of the efficiencies that can be achieved. Specifically considering the case of fault tolerance, it should be noted that Menicucci[171] considers in detail only one specific continuous-variable scheme for encoding qubits[161]. Using this scheme, he estimates the errors induced by finite squeezing and compares these with the error thresholds of contemporary qubit error correction schemes, in order to show that fault tolerance is in principle possible. However, this initial treatment explores only one small part of the parameter space of possible encodings, computational approaches and fault tolerance methods, suggesting that improvements may be possible. This is an important problem to the continuous-variable community and one of active research[243,244].

9.4.2 Fidelity of outputs from an imperfect CZ operation

We additionally calculated the fidelity between the state output by an imperfect CZ operation used to entangle two uncorrelated single mode squeezed states and the equivalent ideal state. This is not the operation that will be carried out in our protocol, as that consists of linking two-qumode cluster state units. However, the additional complexity encountered in dealing with at least four field modes made this full calculation outside of the scope of this work. In our calculation, it is assumed that each of the BS operations that are used to transfer a qumode between a field mode and the spin wave mode in the CZ protocol (Fig. 9.7) deviates from perfect operation as defined in Eqn 9.19. This is equivalent to the set of transformations depicted in Fig. 9.11.

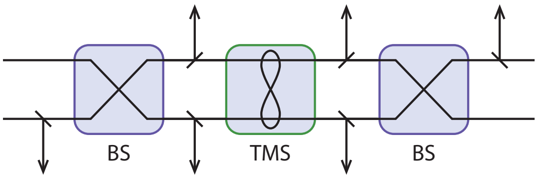

Figure 9.11: Imperfect operation of the CZ operation protocol depicted in Fig. 9.7 is modelled by inserting loss modes (black arrows) at the positions depicted. These loss modes are coupled to the field modes by the BS unitary given in Eqn 9.19.

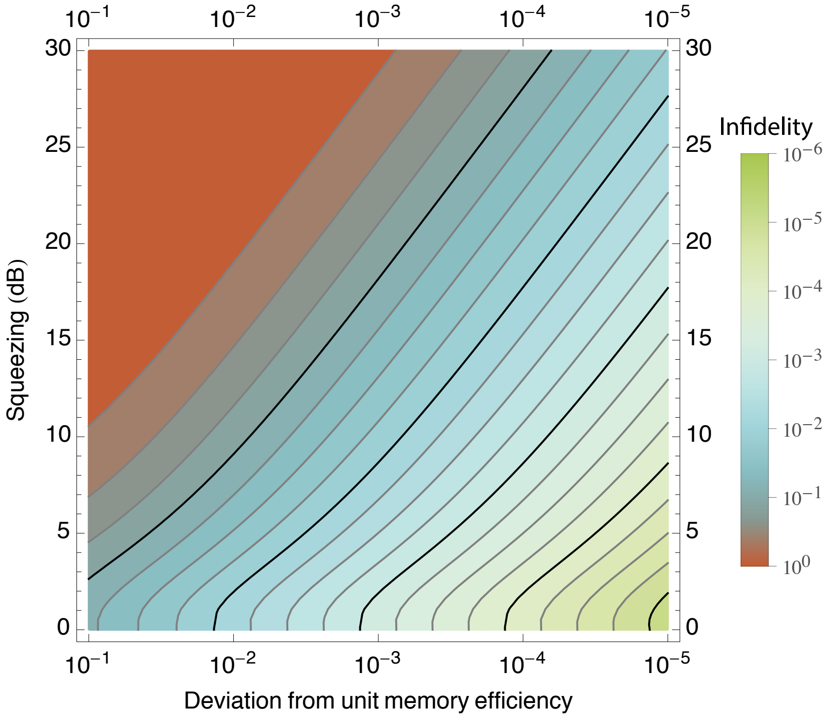

Figure 9.12: The infidelity (1-fidelity) between the state generated by our CZ protocol and an ideal entangled state with the same level of squeezing as a function of the squeezing desired and the deviation from unit memory efficiency for the read-out operation. Contours are plotted on a logarithmic scale, with solid black lines at each order of magnitude.

For this CZ operation, we find a fidelity between the ideal and imperfect states of

$$\begin{aligned}
&4\Big/\bigg(\Big(-(-2(1-\delta\eta)^{3/2}+2(1-\delta\eta)^5+(1-\delta\eta)^3+(1-\delta\eta)^2+2\sqrt{1-\delta\eta}-1)(1-\delta\eta)-(((1-\delta\eta)^2\\
&-6(1-\delta\eta)+2\sqrt{1-\delta\eta}-2)(1-\delta\eta)+1)(1-\delta\eta)\sinh(2r)+(-2(1-\delta\eta)^{5/2}+2(1-\delta\eta)^6\\
&+(1-\delta\eta)^4-\delta\eta+3)\cosh(2r)+3\Big)\Big(-2(1-\delta\eta)^{3/2}+2(1-\delta\eta)^{7/2}-2(1-\delta\eta)^6-(1-\delta\eta)^5\\
&-(1-\delta\eta)^3+(1-\delta\eta)^2+(((1-\delta\eta)^2-2(1-\delta\eta)+2\sqrt{1-\delta\eta}-6)(1-\delta\eta)+1)(1-\delta\eta)^2\sinh(2r)\\
&+(-2(1-\delta\eta)^{7/2}+2(1-\delta\eta)^6+(1-\delta\eta)^5+(1-\delta\eta)^2+2)\cosh(2r)+3)\bigg)^{1/2}. \qquad (9.21)
\end{aligned}$$

Fig. 9.12 shows a plot of this fidelity as a function of the desired squeezing level and the deviation from unit efficiency $\delta\eta$ of the BS operations. We consider again a 17.4 dB squeezed cluster-state resource as an example. In order to entangle two qumodes with a corresponding 10^{-3} infidelity to the ideal state, we require BS operations with an efficiency of $1 - 10^{-5}$.

As can be seen from these calculations, the requirements for high fidelity operation at these squeezing levels are stringent. This presents a strong technical challenge for all experimental implementations of continuous-variable cluster state quantum computing schemes.

9.5 Conclusions

We have proposed novel active elements for TF linear-optical quantum computing based on Raman quantum memories. These elements are able to implement time non-stationary beam splitter and two mode squeezing interactions, providing a versatile toolbox for state generation, manipulation and measurement. Our results suggest a useful route towards maximising the space of encodings available for electromagnetic modes, and could also be combined with other degrees of freedom, including polarisation and spatial encodings, in order to obtain further increases in dimensionality. This may enable innovative approaches to QIP [191,245].

Chapter 10

Conclusions

It is a testament to the vastly unfamiliar landscape of quantum mechanics that, almost a century after its initial conception, vigorous debate still continues on its fundamental underpinnings. It is quite remarkable, for example, that no strong consensus yet exists as to what exactly happens when a quantum system is measured, or even what measuring a quantum system means[246]. Yet somehow, despite these shaky foundations, quantum mechanics continues to remain in almost perfect agreement with all experimental evidence[247,248], no matter how much it conflicts with our intuition[34,249].

In the past few decades, a close link has been formed between the abstract notions of information science and the more physically motivated ideas in quantum theory, in the guise of the new field of quantum information science. This link has pushed forward our understanding of quantum correlations[2,250], stimulated progress on the unification of general relativity and quantum mechanics[251] and may even provide insights into the origin of space-time[252]. On a more practical level, quantum information science has underpinned our understanding of quantum computational complexity[11,25] and has led to the development of novel approaches to manipulating quantum information that have steadily pushed down thresholds for error tolerant quantum computing[160]. There are strong prospects for progress on these and many other theoretical questions as the field of quantum information science continues to grow.

Of course, theory requires experiment, and vice versa, with each stimulating progress in the other. From the very beginnings of experimental investigations into quantum mechanics, optics has played a leading role[5]. Unlike for matter-based systems, optical quantum phenomena can be easily measured at room temperature and atmospheric pressures, and often require little more than a laser light source, non-linear crystals, and sensitive detectors. Optics is by far the dominant approach for the distribution of quantum information, and still proves to be the best platform for many foundational tests. The ubiquity of optical sensors also suggests that optics will continue to play an important part in quantum enhanced metrology experiments, as I have explored in this thesis.

Unfortunately, for quantum information processing tasks, we are now reaching a stage at which many of the most easily achieved experiments have been carried out, and for which further progress will require the high-fidelity control of complex entangled states. Due to the difficulty of generating entanglement between single photons, and the ever-present problem of optical losses, this is a huge challenge for conventional discrete-variable linear optics in the near to mid-term, even with the use of techniques such as those presented in this thesis. This challenge has to be measured against the astonishing progress of matter-based systems in terms of the quality of qubit control, suppression of decoherence, and the number of linked interacting qubits[253,254]. It is therefore unclear whether linear optical quantum computing will prove to be the most effective means of building a universal quantum computer.

This is not to say that optics will not be integral to whichever solution eventually succeeds at this hugely challenging task. Many of the most promising current ideas for matter-based quantum computers employ a hybrid approach, in which matter qubits provide the processing and memory cores, while flying optical qubits are used to link small units of cores into a network suitable for large scale quantum computing[255,256]. In such an approach, it is conceivable that the techniques developed for linear optical quantum computing will prove useful for efficiently distributing entanglement, and perhaps even for some level of initial processing, for example, by employing entanglement distillation protocols[234].

More speculatively, it is possible that a purely optical approach to quantum information processing based on non-linear optics may make large strides forwards in the coming decades. In the last few years, this possibility has moved from being broadly dismissed within the community to a tantalisingly concrete prospect, with multiple experiments demonstrating single-photon level non-linearities[152]. Many challenges remain, particularly with regard to optical loss, but this approach seems to have significant potential. Another possibility stems from the somewhat neglected continuous-variable approach to quantum optics. Unlike for discrete-variable approaches, continuous-variable resource states and entanglement can be generated straightforwardly and on-demand. The significant problem of producing non-Gaussian operations has still not been satisfactorily solved, but it may prove that a hybrid discrete/continuous-variable approach can leverage the best of both worlds[257]. Further work on both the experimental and theoretical aspects of this possibility is needed to better evaluate how promising this approach is.

In conclusion, quantum optics still has much to contribute. More broadly, considering the whole field of quantum mechanics and quantum information science, it remains for me to note that if any lesson can be learnt from our remarkable progress in learning to control quantum systems in the last half-century, it is that unanticipated leaps forward can happen over periods of just a few years, as has been highlighted by the remarkable recent improvement of superconducting qubits[253]. This provides a strong motivation and justification for casting our nets as widely as possible in our continuing exploration of this perplexing, yet always incredibly rich field. I am excited to see what new surprises the next few decades will bring.

Bibliography

[1] M. Arndt and K. Hornberger, "Testing the limits of quantum mechanical superpositions," Nat. Phys. **10**, 271 (2014).

[2] V. Vedral, "Quantum entanglement," Nat. Phys. **10**, 256 (2014).

[3] S. Popescu, "Nonlocality beyond quantum mechanics," Nat. Phys. **10**, 264 (2014).

[4] D. Salart, A. Baas, C. Branciard, N. Gisin, and H. Zbinden, "Testing the speed of 'spooky action at a distance'." Nature **454**, 861 (2008).

[5] P. Shadbolt, J. C. F. Mathews, A. Laing, and J. L. O'Brien, "Testing foundations of quantum mechanics with photons," Nat. Phys. **10**, 278 (2014).

[6] N. Thomas-Peter, B. J. Smith, A. Datta, L. Zhang, U. Dorner, and I. A. Walmsley, "Real-World Quantum Sensors: Evaluating Resources for Precision Measurement," Phys. Rev. Lett. **107**, 113603 (2011).

[7] H. Yonezawa, D. Nakane, T. A. Wheatley, K. Iwasawa, S. Takeda, H. Arao, K. Ohki, K. Tsumura, D. W. Berry, T. C. Ralph, H. M. Wiseman, E. H. Huntington, and A. Furusawa, "Quantum-enhanced optical-phase tracking." Science **337**, 1514 (2012).

[8] P. Kok, W. J. Munro, K. Nemoto, T. C. Ralph, J. P. Dowling, and G. J. Milburn, "Linear optical quantum computing with photonic qubits," Rev. Mod. Phys. **79**, 135 (2007).

[9] T. C. Ralph and G. J. Pryde, "Optical Quantum Computation," in *Prog. Opt.*, Vol. 54, edited by E. Wolf (Elsevier, 2010) Chap. 4, pp. 209–269.

[10] D. Fukuda, G. Fujii, T. Numata, K. Amemiya, A. Yoshizawa, H. Tsuchida, H. Fujino, H. Ishii, T. Itatani, S. Inoue, and T. Zama, "Titanium-based transition-edge photon number resolving detector with 98% detection efficiency with index-matched small-gap fiber coupling." Opt. Express **19**, 870 (2011).

[11] S. Aaronson and A. Arkhipov, "The Computational Complexity of Linear Optics," Proc. forty-third Annu. ACM Symp. theory Comput. , 94 (2010), arXiv:1011.3245 .

[12] J. B. Spring, B. J. Metcalf, P. C. Humphreys, W. S. Kolthammer, X.-M. Jin, M. Barbieri, A. Datta, N. Thomas-Peter, N. K. Langford, D. Kundys, J. C. Gates, B. J. Smith, P. G. R. Smith, and I. A. Walmsley, "Boson sampling on a photonic chip." Science **339**, 798 (2013).

[13] D. Tong, *Quantum F. Theory Lect. Notes, Univ. Cambridge Part III Math. Tripos* (2007).

[14] K. Hammerer, “Lecture Notes: Quantization of the Electromagnetic Field,” .

[15] R. Orús, “A practical introduction to tensor networks: Matrix product states and projected entangled pair states,” Ann. Phys. (N. Y). **349**, 117 (2014).

[16] C. Bennett, F. Bessette, G. Brassard, L. Salvail, and J. Smolin, “Experimental quantum cryptography,” J. Cryptol. **5**, 3 (1992).

[17] V. Giovannetti, S. Lloyd, and L. Maccone, “Advances in quantum metrology,” Nat. Photonics **5**, 222 (2011).

[18] S. L. Braunstein and P. van Loock, “Quantum information with continuous variables,” Rev. Mod. Phys. **77**, 513 (2005).

[19] C. Weedbrook, S. Pirandola, R. García-Patrón, N. J. Cerf, T. C. Ralph, J. H. Shapiro, and S. Lloyd, “Gaussian quantum information,” Rev. Mod. Phys. **84**, 621 (2012).

[20] A. Ferraro, S. Olivares, and M. G. A. Paris, *Gaussian states in continuous variable quantum information* (Bibliopolis, Napoli, 2005).

[21] K. Cahill and R. Glauber, “Ordered Expansions in Boson Amplitude Operators,” Phys. Rev. **177**, 1857 (1969).

[22] K. Banaszek and K. Wódkiewicz, “Direct probing of quantum phase space by photon counting.” Phys. Rev. Lett. **76**, 4344 (1996).

[23] L. Mandel and E. Wolf, *Optical coherence and quantum optics* (Cambridge University Press, 1995).

[24] J. Bertrand and P. Bertrand, “A tomographic approach to Wigner’s function,” Found. Phys. **17**, 397 (1987).

[25] M. A. Nielsen and I. L. Chuang, *Quantum computation and quantum information* (Cambridge University Press, 2010).

[26] A. Peruzzo, A. Laing, A. Politi, T. Rudolph, and J. L. O’Brien, “Multimode quantum interference of photons in multiport integrated devices.” Nat. Commun. **2**, 224 (2011).

[27] M. Reck and A. Zeilinger, “Experimental Realization of Any Discrete Unitary Operator,” Phys. Rev. Lett. **73**, 58 (1994).

[28] B. J. Metcalf, N. Thomas-Peter, J. B. Spring, D. Kundys, M. A. Broome, P. C. Humphreys, X.-M. Jin, M. Barbieri, W. S. Kolthammer, J. C. Gates, B. J. Smith, N. K. Langford, P. G. R. Smith, and I. A. Walmsley, “Multiphoton quantum interference in a multiport integrated photonic device.” Nat. Commun. **4**, 1356 (2013).

[29] E. Shchukin, T. Richter, and W. Vogel, “Nonclassicality criteria in terms of moments,” Phys. Rev. A - At. Mol. Opt. Phys. **71**, 1 (2005).

[30] A. I. Lvovsky, “Squeezed light,” Arxiv (2014), arXiv:1401.4118 .

[31] M. Kim, G. Antesberger, C. Bodendorf, and H. Walther, “Scheme for direct observation of the Wigner characteristic function in cavity QED,” (1998).

[32] M. T. Jaekel and S. Reynaud, “Quantum Limits in Interferometric Measurements,” Europhys. Lett. **13**, 301 (1990).

[33] S. L. Braunstein and H. J. Kimble, "Teleportation of Continuous Quantum Variables," Phys. Rev. Lett. **80**, 869 (1998).

[34] A. Einstein, B. Podolsky, and N. Rosen, "Can Quantum-Mechanical Description of Physical Reality Be Considered Complete?" Phys. Rev. **47**, 777 (1935).

[35] S. L. Braunstein, "Squeezing as an irreducible resource," Phys. Rev. A **71**, 055801 (2005).

[36] M. G. Thompson, A. Politi, J. C. F. Matthews, and J. L. O'Brien, "Integrated waveguide circuits for optical quantum computing," IET Circuits Devices Syst. **5**, 94 (2011).

[37] N. Thomas-Peter, N. K. Langford, A. Datta, L. Zhang, B. J. Smith, J. B. Spring, B. J. Metcalf, H. B. Coldenstrodt-Ronge, M. Hu, J. Nunn, and I. A. Walmsley, "Integrated photonic sensing," New. J. Phys. **13**, 055024 (2011).

[38] A. Crespi, R. Osellame, R. Ramponi, V. Giovannetti, R. Fazio, L. Sansoni, F. De Nicola, F. Sciarrino, and P. Mataloni, "Anderson localization of entangled photons in an integrated quantum walk," Nat. Photonics **7**, 322 (2013).

[39] B. J. Metcalf, J. B. Spring, P. C. Humphreys, N. Thomas-Peter, M. Barbieri, W. S. Kolthammer, X.-M. Jin, N. K. Langford, D. Kundys, J. C. Gates, B. J. Smith, P. G. R. Smith, and I. a. Walmsley, "Quantum teleportation on a photonic chip," Nat. Photonics **8**, 770 (2014).

[40] P. S. Salter, A. Jesacher, J. B. Spring, B. J. Metcalf, N. Thomas-Peter, R. D. Simmonds, N. K. Langford, I. A. Walmsley, and M. J. Booth, "Adaptive slit beam shaping for direct laser written waveguides," Opt. Lett. **37**, 470 (2012).

[41] G. Della Valle, R. Osellame, and P. Laporta, "Micromachining of photonic devices by femtosecond laser pulses," J. Opt. A.-Pure Appl. Op. **11**, 013001 (2009).

[42] J. B. Spring, P. S. Salter, B. J. Metcalf, P. C. Humphreys, M. Moore, N. Thomas-Peter, X.-M. Jin, N. K. Langford, S. W. Kolthammer, M. J. Booth, and I. A. Walmsley, "On-chip low loss heralded source of pure single photons," Opt. Express **21**, 5932 (2013).

[43] M. Fiorentino, P. Voss, J. Sharping, and P. Kumar, "All-fiber photon-pair source for quantum communications," IEEE Photonic Tech. L. **14**, 983 (2002).

[44] I. Marcikic, H. de Riedmatten, W. Tittel, H. Zbinden, and N. Gisin, "Long-distance teleportation of qubits at telecommunication wavelengths," Nature **421**, 509 (2003).

[45] A. Politi, M. J. Cryan, J. G. Rarity, S. Yu, and J. L. O'Brien, "Silica-on-silicon waveguide quantum circuits," Science **320**, 646 (2008).

[46] S. Tanzilli, H. de Riedmatten, W. Tittel, H. Zbinden, P. Baldi, M. de Micheli, D. B. Ostrowsky, and N. Gisin, "Highly efficient photon-pair source using a Periodically Poled Lithium Niobate Waveguide," Electron. Lett. **37**, 8 (2000), arXiv:0012053 [quant-ph] .

[47] A. Eckstein, A. Christ, P. Mosley, and C. Silberhorn, "Highly Efficient Single-Pass Source of Pulsed Single-Mode Twin Beams of Light," Phys. Rev. Lett. **106**, 1 (2011).

[48] X. Zhang, M. Harrison, A. Harker, and A. M. Armani, "Serpentine low loss trapezoidal silica waveguides on silicon," Opt. Express **20**, 22298 (2012).

[49] J. W. Silverstone, D. Bonneau, K. Ohira, N. Suzuki, H. Yoshida, N. Iizuka, M. Ezaki, C. M. Natarajan, M. G. Tanner, R. H. Hadfield, V. Zwiller, G. D. Marshall, J. G. Rarity, J. L. O'Brien, and M. G. Thompson, "On-chip quantum interference between silicon photon-pair sources," Nat. Photonics **8**, 104 (2013).

[50] R. Dekker, N. Usechak, M. Först, and a. Driessen, "Ultrafast nonlinear all-optical processes in silicon-on-insulator waveguides," J. Phys. D. Appl. Phys. **40**, R249 (2007).

[51] X.-S. Ma, S. Zotter, J. Kofler, T. Jennewein, and A. Zeilinger, "Experimental generation of single photons via active multiplexing," Phys. Rev. A **83**, 043814 (2011).

[52] T. Meany, L. A. Ngah, M. J. Collins, A. S. Clark, R. J. Williams, B. J. Eggleton, M. J. Steel, M. J. Withford, O. Alibart, and S. Tanzilli, "Hybrid photonic circuit for multiplexed heralded single photons," Laser Photonics Rev. **8** (2014), 10.1002/lpor.201400027, arXiv:1402.7202 .

[53] A. Christ and C. Silberhorn, "Limits on the deterministic creation of pure single-photon states using parametric down-conversion," Phys. Rev. A **85**, 023829 (2012).

[54] D. Bonneau, M. Lobino, P. Jiang, C. Natarajan, M. Tanner, R. Hadfield, S. Dorenbos, V. Zwiller, M. Thompson, and J. O'Brien, "Fast path and polarization manipulation of telecom wavelength single photons in lithium niobate waveguide devices," Phys. Rev. Lett. **108**, 1 (2012).

[55] O. Alibart, D. B. Ostrowsky, P. Baldi, and S. Tanzilli, "High-performance guided-wave asynchronous heralded single-photon source," Opt. Lett. **30**, 1539 (2005).

[56] R. Alferness, V. Ramaswamy, S. Korotky, M. Divino, and L. Buhl, "Efficient single-mode fiber to titanium diffused lithium niobate waveguide coupling for lambda = l.32 mu m," IEEE Trans. Microw. Theory Tech. **30**, 1795 (1982).

[57] B. J. Smith, D. Kundys, N. Thomas-Peter, P. G. R. Smith, and I. A. Walmsley, "Phase-controlled integrated photonic quantum circuits," Opt. Express **17**, 13516 (2009).

[58] M. Poot and H. X. Tang, "Broadband nanoelectromechanical phase shifting of light on a chip," Appl. Phys. Lett. **104**, 061101 (2014).

[59] S. Donati, L. Barbieri, and G. Martini, "Piezoelectric actuation of silica-on-silicon waveguide devices," IEEE Photonic Tech. L. **10**, 1428 (1998).

[60] K. K. Tsia, S. Fathpour, and B. Jalali, "Electrical tuning of birefringence in silicon waveguides," Appl. Phys. Lett. **92**, 061109 (2008).

[61] P. C. Humphreys, B. J. Metcalf, J. B. Spring, M. Moore, X.-M. Jin, M. Barbieri, W. S. Kolthammer, and I. A. Walmsley, "Linear optical quantum computing in a single spatial mode," Phys. Rev. Lett. **111**, 150501 (2013).

[62] A. Bertholds and R. Dandliker, "Determination of the individual strain-optic coefficients in single-mode optical fibers," J. Light. Technol. **88**, 17 (1988).

[63] J. B. Spring, *Single photon generation and quantum computing with integrated photonics*, Ph.D. thesis, University of Oxford (2014).

[64] M. C. Rechtsman, J. M. Zeuner, A. Tünnermann, S. Nolte, M. Segev, and A. Szameit, "Strain-induced pseudomagnetic field and photonic Landau levels in dielectric structures," Nat. Photon. **7**, 153 (2012).

[65] L. A. Fernandes, J. R. Grenier, P. R. Herman, J. S. Aitchison, and P. V. S. Marques, "Stress induced birefringence tuning in femtosecond laser fabricated waveguides in fused silica," Opt. Express **20**, 24103 (2012).

[66] G. Corrielli, A. Crespi, R. Geremia, R. Ramponi, L. Sansoni, A. Santinelli, P. Mataloni, F. Sciarrino, and R. Osellame, "Rotated waveplates in integrated waveguide optics." Nat. Commun. **5**, 4249 (2014), arXiv:1307.7541 .

[67] E. L. Wooten, K. M. Kissa, A. Yi-Yan, E. J. Murphy, D. A. Lafaw, P. F. Hallemeier, D. Maack, D. V. Attanasio, D. J. Fritz, G. J. McBrien, and D. E. Bossi, "Review of lithium niobate modulators for fiber-optic communications systems," IEEE J. Sel. Top. Quantum Electron. **6**, 69 (2000).

[68] O. P. M.-b. A. S. Witch, "Optical switching technology comparison: optical mems vs. other technologies," IEEE Commun. Mag. **41**, 50 (2003).

[69] C. K. Hong, Z. Y. Ou, and L. Mandel, "Measurement of subpicosecond time intervals between two photons by interference," Phys. Rev. Lett. **59**, 2044 (1987).

[70] R. Ghosh and L. Mandel, "Observation of nonclassical effects in the interference of two photons," Phys. Rev. Lett. **59**, 1903 (1987).

[71] X. D. Wang, P. Basseras, R. J. Dwayne Miller, J. Sweetser, and I. A. Walmsley, "Regenerative pulse amplification in the 10-kHz range," Opt. Lett. **15**, 839 (1990).

[72] T. Bartley, P. Crowley, A. Datta, J. Nunn, L. Zhang, and I. Walmsley, "Strategies for enhancing quantum entanglement by local photon subtraction," Phys. Rev. A **87**, 022313 (2013).

[73] A. E. Lita, A. J. Miller, and S. W. Nam, "Counting near-infrared single-photons with 95% efficiency," Opt. Express **16**, 3032 (2008).

[74] M. D. Eisaman, J. Fan, A. Migdall, and S. V. Polyakov, "Invited review article: Single-photon sources and detectors." Rev. Sci. Instrum. **82**, 071101 (2011).

[75] P. C. Humphreys, M. Barbieri, A. Datta, and I. A. Walmsley, "Quantum Enhanced Multiple Phase Estimation," Phys. Rev. Lett. **111**, 070403 (2013).

[76] A. Datta, L. Zhang, N. Thomas-Peter, U. Dorner, B. J. Smith, and I. A. Walmsley, "Quantum metrology with imperfect states and detectors," Phys. Rev. A **83**, 063836 (2011).

[77] F. Ewert, P. van Loock, and P. V. Loock, "3/4-Efficient Bell Measurement with Passive Linear Optics and Unentangled Ancillae," Phys. Rev. Lett. **113**, 140403 (2014), arXiv:arXiv:1403.4841v1 .

[78] D. Achilles, C. Silberhorn, C. Sliwa, K. Banaszek, and I. A. Walmsley, "Fiber-assisted detection with photon number resolution." Opt. Lett. **28**, 2387 (2003).

[79] A. Avella, G. Brida, I. P. Degiovanni, M. Genovese, M. Gramegna, L. Lolli, E. Monticone, C. Portesi, M. Rajteri, M. L. Rastello, E. Taralli, P. Traina, and M. White, "Self consistent, absolute calibration technique for photon number resolving detectors." Opt. Express **19**, 23249 (2011).

[80] G. Brida, L. Ciavarella, I. P. Degiovanni, M. Genovese, L. Lolli, M. G. Mingolla, F. Piacentini, M. Rajteri, E. Taralli, and M. G. a. Paris, "Quantum characterization of superconducting photon counters," New J. Phys. **14**, 085001 (2012).

[81] Z. H. Levine, T. Gerrits, A. L. Migdall, D. V. Samarov, B. Calkins, A. E. Lita, and S. W. Nam, "Algorithm for finding clusters with a known distribution and its application to photon-number resolution using a superconducting transition-edge sensor," J. Opt. Soc. Am. B **29**, 2066 (2012).

[82] J. S. Lundeen, A. Feito, K. L. Pregnell, C. Silberhorn, T. C. Ralph, J. Eisert, M. B. Plenio, and I. A. Walmsley, "Tomography of quantum detectors," Nat. Phys. **5**, 27 (2008).

[83] L. Zhang, A. Datta, H. B. Coldenstrodt-Ronge, X.-M. Jin, J. Eisert, M. B. Plenio, and I. A. Walmsley, "Recursive quantum detector tomography," New J. Phys. **14**, 115005 (2012).

[84] H. Abdi and L. J. Williams, "Principal component analysis," Wiley Interdiscip. Rev. Comput. Stat. **2**, 433 (2010).

[85] A. J. Miller, *Development of a broadband optical spectrophotometer using superconducting transition-edge sensors*, Ph.D. thesis, Stanford University (2001).

[86] A. J. Miller, A. E. Lita, B. Calkins, I. Vayshenker, S. M. Gruber, and S. W. Nam, "Compact cryogenic self-aligning fiber-to-detector coupling with losses below one percent." Opt. Express **19**, 9102 (2011).

[87] M. Krystek and M. Anton, "A weighted total least-squares algorithm for fitting a straight line," Meas. Sci. Technol. **18**, 3438 (2007).

[88] C. DeCusatis, *Handbook of Fiber Optic Data Communication*, 4th ed. (Academic Press, 2013).

[89] Z. I. Botev, J. F. Grotowski, and D. P. Kroese, "Kernel density estimation via diffusion," Ann. Stat. **38**, 2916 (2010).

[90] M. Cooper, M. Karpiski, and B. J. Smith, "Local mapping of detector response for reliable quantum state estimation." Nat. Commun. **5**, 4332 (2014).

[91] S. Ramelow, A. Mech, M. Giustina, S. Gröblacher, W. Wieczorek, J. Beyer, A. Lita, B. Calkins, T. Gerrits, S. W. Nam, A. Zeilinger, and R. Ursin, "Highly efficient heralding of entangled single photons." Opt. Express **21**, 6707 (2013).

[92] C. M. Bishop, *Pattern Recognition and Machine Learning* (Springer, 2006) p. 738.

[93] T. Lunghi, B. Korzh, B. Sanguinetti, and H. Zbinden, "Absolute calibration of fiber-coupled single-photon detector." Opt. Express **22**, 18078 (2014).

[94] F. Marsili, V. B. Verma, J. A. Stern, S. Harrington, A. E. Lita, T. Gerrits, I. Vayshenker, B. Baek, M. D. Shaw, R. P. Mirin, and S. W. Nam, "Detecting single infrared photons with 93% system efficiency," Nat. Photonics **7**, 210 (2013).

[95] S. L. Braunstein and C. Caves, "Statistical distance and the geometry of quantum states," Phys. Rev. Lett. **72**, 3439 (1994).

[96] M. Hayashi, *Quantum Information* (Springer Berlin Heidelberg, 2006).

[97] A. Fujiwara, "Quantum channel identification problem," Phys. Rev. A **63**, 042304 (2001).

[98] J. Bollinger, W. Itano, D. Wineland, and D. Heinzen, "Optimal frequency measurements with maximally correlated states," Phys. Rev. A **54**, 4649 (1996).

[99] M. Hayashi, "Phase estimation with photon number constraint," Prog. Informatics , 81 (2011).

[100] R. Demkowicz-Dobrzaski, J. Koodyski, and M. Gu, "The elusive Heisenberg limit in quantum-enhanced metrology." Nat. Commun. **3**, 1063 (2012).

[101] M. Holland and K. Burnett, "Interferometric detection of optical phase shifts at the Heisenberg limit," Phys. Rev. Lett. **71**, 1355 (1993).

[102] V. Giovannetti, S. Lloyd, and L. Maccone, “Quantum-enhanced positioning and clock synchronization.” Nature **412**, 417 (2001).

[103] M. W. Mitchell, J. S. Lundeen, and A. M. Steinberg, “Super-resolving phase measurements with a multiphoton entangled state.” Nature **429**, 161 (2004).

[104] T. Nagata, R. Okamoto, J. L. O’brien, K. Sasaki, and S. Takeuchi, “Beating the standard quantum limit with four-entangled photons.” Science **316**, 726 (2007).

[105] I. Afek, O. Ambar, and Y. Silberberg, “High-NOON states by mixing quantum and classical light.” Science **328**, 879 (2010).

[106] A. Vourdas and J. Dunningham, “Fourier multiport devices,” Phys. Rev. A **71**, 013809 (2005).

[107] Aasi *et al.*, “Enhanced sensitivity of the LIGO gravitational wave detector by using squeezed states of light,” Nat. Photonics , 1 (2013).

[108] F. Wolfgramm, C. Vitelli, F. A. Beduini, N. Godbout, and M. W. Mitchell, “Entanglement-enhanced probing of a delicate material system,” Nat. Photonics **7**, 28 (2012).

[109] G. Y. Xiang, B. L. Higgins, D. W. Berry, H. M. Wiseman, and G. J. Pryde, “Entanglement-enhanced measurement of a completely unknown optical phase,” Nat. Photonics **5**, 43 (2010).

[110] Abadie *et al.*, “A gravitational wave observatory operating beyond the quantum shot-noise limit,” Nat. Phys. **7**, 962 (2011).

[111] R. Demkowicz-Dobrzaski, K. Banaszek, and R. Schnabel, “Fundamental quantum interferometry bound for the squeezed-light-enhanced gravitational wave detector GEO 600,” Phys. Rev. A - At. Mol. Opt. Phys. **88**, 1 (2013), arXiv:1305.7268 .

[112] M. A. Taylor, J. Janousek, V. Daria, J. Knittel, B. Hage, H.-A. Bachor, and W. P. Bowen, “Biological measurement beyond the quantum limit,” Nat. Photonics **7**, 229 (2013).

[113] H. Lee, P. Kok, and J. P. Dowling, “A quantum Rosetta stone for interferometry,” J. Mod. Opt. **49**, 2325 (2002).

[114] U. Dorner, R. Demkowicz-Dobrzanski, B. Smith, J. Lundeen, W. Wasilewski, K. Banaszek, and I. Walmsley, “Optimal Quantum Phase Estimation,” Phys. Rev. Lett. **102**, 040403 (2009).

[115] R. Demkowicz-Dobrzanski, U. Dorner, B. Smith, J. Lundeen, W. Wasilewski, K. Banaszek, and I. Walmsley, “Quantum phase estimation with lossy interferometers,” Phys. Rev. A **80**, 1 (2009).

[116] J. Dunningham, K. Burnett, and S. Barnett, “Interferometry below the Standard Quantum Limit with Bose-Einstein Condensates,” Phys. Rev. Lett. **89**, 150401 (2002).

[117] A. Monras, “Phase space formalism for quantum estimation of Gaussian states,” Arxiv (1303.3682) (2013), arXiv:1303.3682 .

[118] J. Sahota, “Quantum correlations in optical metrology: Heisenberg-limited phase estimation without mode entanglement,” Phys. Rev. A **013808**, 1 (2015), arXiv:1404.7110 .

[119] M. D. Lang and C. M. Caves, “Optimal quantum-enhanced interferometry,” Phys. Rev. A **90**, 025802 (2014).

[120] M. Jarzyna and R. Demkowicz-Dobrzaski, “Quantum interferometry with and without an external phase reference,” Phys. Rev. A - At. Mol. Opt. Phys. **85**, 1 (2012), arXiv:1108.3844 .

[121] X.-X. Zhang, Y.-X. Yang, and X.-B. Wang, "Lossy quantum-optical metrology with squeezed states," Phys. Rev. A **88**, 013838 (2013).

[122] P. M. Anisimov, G. M. Raterman, A. Chiruvelli, W. N. Plick, S. D. Huver, H. Lee, and J. P. Dowling, "Quantum Metrology with Two-Mode Squeezed Vacuum: Parity Detection Beats the Heisenberg Limit," Phys. Rev. Lett. **104**, 103602 (2010).

[123] G. Y. Xiang, H. F. Hofmann, and G. J. Pryde, "Optimal multi-photon phase sensing with a single interference fringe." Sci. Rep. **3**, 2684 (2013).

[124] P. J. D. Crowley, A. Datta, M. Barbieri, and I. A. Walmsley, "Tradeoff in simultaneous quantum-limited phase and loss estimation in interferometry," Phys. Rev. A **89**, 023845 (2014).

[125] H. Imai and A. Fujiwara, "Geometry of optimal estimation scheme for SU (D) channels," J. Phys. A Math. Theor. **40**, 4391 (2007).

[126] A. Fujiwara, "Estimation of SU(2) operation and dense coding: An information geometric approach," Phys. Rev. A **65**, 012316 (2001).

[127] M. Ballester, "Estimation of unitary quantum operations," Phys. Rev. A **69**, 022303 (2004).

[128] C. Macchiavello, "Optimal estimation of multiple phases," Phys. Rev. A **67**, 062302 (2003).

[129] M. Ballester, "Entanglement is not very useful for estimating multiple phases," Phys. Rev. A **70**, 032310 (2004).

[130] N. Spagnolo, L. Aparo, C. Vitelli, A. Crespi, R. Ramponi, R. Osellame, P. Mataloni, and F. Sciarrino, "Quantum interferometry with three-dimensional geometry." Sci. Rep. **2**, 862 (2012).

[131] M. D. Vidrighin, G. Donati, M. G. Genoni, X.-M. Jin, W. S. Kolthammer, M. S. Kim, A. Datta, M. Barbieri, and I. a. Walmsley, "Joint estimation of phase and phase diffusion for quantum metrology." Nat. Commun. **5**, 3532 (2014).

[132] V. Giovannetti, S. Lloyd, L. Maccone, and J. Shapiro, "Sub-Rayleigh-diffraction-bound quantum imaging," Phys. Rev. A **79**, 77 (2009).

[133] E. Brainis, "Quantum imaging with N-photon states in position space," Opt. Express **19**, 24228 (2011).

[134] O. Schwartz and D. Oron, "Improved resolution in fluorescence microscopy using quantum correlations," Phys. Rev. A **85**, 033812 (2012).

[135] F. Guerrieri, L. Maccone, F. N. C. Wong, J. H. Shapiro, S. Tisa, and F. Zappa, "Sub-Rayleigh Imaging via N-Photon Detection," Phys. Rev. Lett. **105**, 163602 (2010).

[136] G. Brida, M. Genovese, and I. Ruo Berchera, "Experimental realization of sub-shot-noise quantum imaging," Nat. Photonics **4**, 227 (2010).

[137] M. Tsang, "Quantum Imaging beyond the Diffraction Limit by Optical Centroid Measurements," Phys. Rev. Lett. **102**, 253601 (2009).

[138] H. Shin, K. W. C. Chan, H. J. Chang, and R. W. Boyd, "Quantum Spatial Superresolution by Optical Centroid Measurements," Phys. Rev. Lett. **107**, 083603 (2011).

[139] C. A. Pérez-Delgado, M. E. Pearce, and P. Kok, "Fundamental Limits of Classical and Quantum Imaging," Phys. Rev. Lett. **109**, 123601 (2012).

[140] C. Preza, D. L. Snyder, and J. a. Conchello, "Theoretical development and experimental evaluation of imaging models for differential-interference-contrast microscopy." J. Opt. Soc. Am. A. Opt. Image Sci. Vis. **16**, 2185 (1999).

[141] C. Helstrom, *Quantum Detection and Estimation Theory, Mathematics in Science and Engineering* (Academic Press, 1976).

[142] M. G. A. Paris, "Quantum estimation for quantum technology," Int. J. Quantum Inf. **7**, 125 (2009).

[143] K. Matsumoto, "A new approach to the Cramér-Rao-type bound of the pure-state model," J. Phys. A. Math. Gen. **35**, 3111 (2002).

[144] S. L. Braunstein, C. M. Caves, and G. Milburn, "Generalized Uncertainty Relations: Theory, Examples, and Lorentz Invariance," Ann. Phys. (N. Y). **247**, 135 (1996).

[145] Y. Lim and A. Beige, "Multiphoton entanglement through a Bell-multiport beam splitter," Phys. Rev. A **71**, 062311 (2005).

[146] M. C. Tichy, M. Tiersch, F. Mintert, and A. Buchleitner, "Many-particle interference beyond many-boson and many-fermion statistics," New J. Phys. **14**, 093015 (2012).

[147] T. D. Ladd, F. Jelezko, R. Laflamme, Y. Nakamura, C. Monroe, and J. L. O'Brien, "Quantum computers," Nature **464**, 45 (2010).

[148] D. DiVincenzo, "Two-bit gates are universal for quantum computation," Phys. Rev. A **51**, 1015 (1995).

[149] S. Lloyd, "Almost Any Quantum Logic Gate is Universal," Phys. Rev. Lett. **75**, 346 (1995).

[150] D. P. DiVincenzo, "Topics in Quantum Computers," in *Mesoscopic electron Transp.* (Springer, 1996) pp. 657–677, arXiv:9612126 [cond-mat] .

[151] C. a. Pérez-Delgado and P. Kok, "Quantum computers: Definition and implementations," Phys. Rev. A **83**, 012303 (2011).

[152] D. E. Chang, V. Vuletić, and M. D. Lukin, "Quantum nonlinear optics photon by photon," Nat. Photonics **8**, 685 (2014).

[153] O. Firstenberg, T. Peyronel, Q.-Y. Liang, A. V. Gorshkov, M. D. Lukin, and V. Vuletić, "Attractive photons in a quantum nonlinear medium." Nature **502**, 71 (2013).

[154] E. Knill, R. Laflamme, and G. J. Milburn, "A scheme for efficient quantum computation with linear optics." Nature **409**, 46 (2001).

[155] P. Mosley, J. Lundeen, B. Smith, P. Wasylczyk, A. U'Ren, C. Silberhorn, and I. Walmsley, "Heralded Generation of Ultrafast Single Photons in Pure Quantum States," Phys. Rev. Lett. **100**, 133601 (2008).

[156] T.-M. Zhao, H. Zhang, J. Yang, Z.-R. Sang, X. Jiang, X.-H. Bao, and J.-W. Pan, "Entangling Different-Color Photons via Time-Resolved Measurement and Active Feed Forward," Phys. Rev. Lett. **112**, 103602 (2014).

[157] R. Raussendorf, D. Browne, and H. Briegel, "Measurement-based quantum computation on cluster states," Phys. Rev. A **68**, 022312 (2003).

[158] P. Kok, "Five Lectures on Optical Quantum Computing," Lect. Notes Phys. Lecture Notes in Physics, **787**, 187 (2010).

[159] D. E. Browne and T. Rudolph, "Resource-Efficient Linear Optical Quantum Computation," Phys. Rev. Lett. **95**, 010501 (2005).

[160] R. Raussendorf and J. Harrington, "Fault-Tolerant Quantum Computation with High Threshold in Two Dimensions," Phys. Rev. Lett. **98**, 190504 (2007).

[161] D. Gottesman, A. Kitaev, and J. Preskill, "Encoding a qubit in an oscillator," Phys. Rev. A **64**, 012310 (2001).

[162] D. Deutsch, A. Barenco, and A. Ekert, "Universality in Quantum Computation," Proc. R. Soc. A Math. Phys. Eng. Sci. **449**, 669 (1995).

[163] S. Sefi and P. van Loock, "How to Decompose Arbitrary Continuous-Variable Quantum Operations," Phys. Rev. Lett. **107**, 170501 (2011).

[164] A. Mari and J. Eisert, "Positive wigner functions render classical simulation of quantum computation efficient," Phys. Rev. Lett. **109**, 1 (2012), arXiv:1208.3660 .

[165] M. G. Genoni, M. L. Palma, T. Tufarelli, S. Olivares, M. S. Kim, and M. G. a. Paris, "Detecting quantum non-Gaussianity via the Wigner function," Phys. Rev. A - At. Mol. Opt. Phys. **87**, 1 (2013), arXiv:1304.3340 .

[166] S. Bartlett and B. Sanders, "Universal continuous-variable quantum computation: Requirement of optical nonlinearity for photon counting," Phys. Rev. A **65**, 042304 (2002).

[167] A. Datta, L. Zhang, J. Nunn, N. K. Langford, A. Feito, M. B. Plenio, and I. A. Walmsley, "Compact Continuous-Variable Entanglement Distillation," Phys. Rev. Lett. **108**, 060502 (2012).

[168] M. Yukawa, K. Miyata, H. Yonezawa, P. Marek, R. Filip, and A. Furusawa, "Emulating quantum cubic nonlinearity," Phys. Rev. A **88**, 053816 (2013).

[169] S. L. Braunstein, "Error Correction for Continuous Quantum Variables," Phys. Rev. Lett. **80**, 4084 (1998).

[170] T. C. Ralph, "Quantum error correction of continuous-variable states against Gaussian noise," Phys. Rev. A **84**, 022339 (2011).

[171] N. C. Menicucci, "Fault-Tolerant Measurement-Based Quantum Computing with Continuous-Variable Cluster States," Phys. Rev. Lett. **112**, 120504 (2014).

[172] S. Sefi, V. Vaibhav, and P. van Loock, "Measurement-induced optical Kerr interaction," Phys. Rev. A **88**, 012303 (2013).

[173] N. Menicucci, P. van Loock, M. Gu, C. Weedbrook, T. Ralph, and M. Nielsen, "Universal Quantum Computation with Continuous-Variable Cluster States," Phys. Rev. Lett. **97**, 110501 (2006).

[174] M. Gu, C. Weedbrook, N. Menicucci, T. Ralph, and P. van Loock, "Quantum computing with continuous-variable clusters," Phys. Rev. A **79**, 062318 (2009).

[175] P. van Loock, C. Weedbrook, and M. Gu, "Building Gaussian cluster states by linear optics," Phys. Rev. A **76**, 032321 (2007).

[176] R. Ukai, S. Yokoyama, J.-I. Yoshikawa, P. van Loock, and A. Furusawa, “Demonstration of a Controlled-Phase Gate for Continuous-Variable One-Way Quantum Computation,” Phys. Rev. Lett. **107**, 250501 (2011).

[177] T. Pittman, B. Jacobs, and J. Franson, “Probabilistic quantum logic operations using polarizing beam splitters,” Phys. Rev. A **64**, 062311 (2001).

[178] S. Gasparoni, J.-W. Pan, P. Walther, T. Rudolph, and A. Zeilinger, “Realization of a Photonic Controlled-NOT Gate Sufficient for Quantum Computation,” Phys. Rev. Lett. **93**, 020504 (2004).

[179] J. L. O’Brien, G. J. Pryde, A. G. White, T. C. Ralph, and D. Branning, “Demonstration of an all-optical quantum controlled-NOT gate.” Nature **426**, 264 (2003).

[180] X.-H. Bao, T.-Y. Chen, Q. Zhang, J. Yang, H. Zhang, T. Yang, and J.-W. Pan, “Optical Nondestructive Controlled-NOT Gate without Using Entangled Photons,” Phys. Rev. Lett. **98**, 170502 (2007).

[181] B. P. Lanyon, M. Barbieri, M. P. Almeida, T. Jennewein, T. C. Ralph, K. J. Resch, G. J. Pryde, J. L. OBrien, A. Gilchrist, and A. G. White, “Simplifying quantum logic using higher-dimensional Hilbert spaces,” Nat. Phys. **5**, 134 (2008).

[182] R. Okamoto, J. L. O’Brien, H. F. Hofmann, and S. Takeuchi, “Realization of a Knill-Laflamme-Milburn controlled-NOT photonic quantum circuit combining effective optical nonlinearities.” Proc. Natl. Acad. Sci. U. S. A. **108**, 10067 (2011).

[183] G. E. Keiser, “Tutorial Paper A Review of WDM Technology and Applications,” Opt. Fiber Technol. **5**, 3 (1999).

[184] H. de Riedmatten, I. Marcikic, V. Scarani, W. Tittel, H. Zbinden, and N. Gisin, “Tailoring photonic entanglement in high-dimensional Hilbert spaces,” Phys. Rev. A **69**, 050304 (2004).

[185] A. Hayat, X. Xing, A. Feizpour, and A. M. Steinberg, “Multidimensional quantum information based on single-photon temporal wavepackets,” Opt. Express **20**, 29174 (2012).

[186] J. Nunn, L. Wright, C. Söller, L. Zhang, I. A. Walmsley, and B. J. Smith, “Large-Alphabet Time-Frequency Entangled Quantum Key Distribution by means of Time-to-Frequency Conversion,” Opt. Express **21**, 14 (2013), arXiv:1305.0960 .

[187] P. B. R. Nisbet-Jones, J. Dilley, A. Holleczek, O. Barter, and A. Kuhn, “Photonic qubits, qutrits and ququads accurately prepared and delivered on demand,” New J. Phys. **15**, 053007 (2013).

[188] R. Thew, S. Tanzilli, W. Tittel, H. Zbinden, and N. Gisin, “Experimental investigation of the robustness of partially entangled qubits over 11 km,” Phys. Rev. A **66**, 062304 (2002).

[189] J. Brendel, N. Gisin, W. Tittel, and H. Zbinden, “Pulsed Energy-Time Entangled Twin-Photon Source for Quantum Communication,” Phys. Rev. Lett. **82**, 2594 (1999).

[190] C. Simon and J.-P. Poizat, “Creating Single Time-Bin-Entangled Photon Pairs,” Phys. Rev. Lett. **94**, 030502 (2005).

[191] J. Barreiro, N. Langford, N. Peters, and P. Kwiat, “Generation of Hyperentangled Photon Pairs,” Phys. Rev. Lett. **95**, 260501 (2005).

[192] A. Zavatta, M. D’Angelo, V. Parigi, and M. Bellini, “Remote Preparation of Arbitrary Time-Encoded Single-Photon Ebits,” Phys. Rev. Lett. **96**, 020502 (2006).

[193] J. Franson, “Bell inequality for position and time.” Phys. Rev. Lett. **62**, 2205 (1989).

[194] L. Olislager, J. Cussey, A. T. Nguyen, P. Emplit, S. Massar, J.-M. Merolla, and K. P. Huy, “Frequency-bin entangled photons,” Phys. Rev. A **82**, 013804 (2010).

[195] W. Tittel, J. Brendel, H. Zbinden, and N. Gisin, “Quantum cryptography using entangled photons in energy-time bell states,” Phys. Rev. Lett. **84**, 4737 (2000).

[196] N. Lindner and T. Rudolph, “Proposal for Pulsed On-Demand Sources of Photonic Cluster State Strings,” Phys. Rev. Lett. **103**, 113602 (2009).

[197] N. C. Menicucci, X. Ma, and T. C. Ralph, “Arbitrarily Large Continuous-Variable Cluster States from a Single Quantum Nondemolition Gate,” Phys. Rev. Lett. **104**, 250503 (2010).

[198] N. C. Menicucci, “Temporal-mode continuous-variable cluster states using linear optics,” Phys. Rev. A **83**, 062314 (2011).

[199] S. Yokoyama, R. Ukai, S. C. Armstrong, C. Sornphiphatphong, T. Kaji, S. Suzuki, J.-i. Yoshikawa, H. Yonezawa, N. C. Menicucci, and A. Furusawa, “Ultra-large-scale continuous-variable cluster states multiplexed in the time domain,” Nat. Photonics **7**, 982 (2013).

[200] M. Chen, N. C. Menicucci, and O. Pfister, “Experimental Realization of Multipartite Entanglement of 60 Modes of a Quantum Optical Frequency Comb,” Phys. Rev. Lett. **112**, 120505 (2014).

[201] M. A. Hall, J. B. Altepeter, and P. Kumar, “Ultrafast Switching of Photonic Entanglement,” Phys. Rev. Lett. **106**, 053901 (2011).

[202] A. Schreiber, A. Gábris, P. P. Rohde, K. Laiho, M. **S**tefaák, V. Poto**c**ek, C. Hamilton, I. Jex, and C. Silberhorn, “A 2D quantum walk simulation of two-particle dynamics.” Science **336**, 55 (2012).

[203] Y. Soudagar, F. Bussières, G. Berlín, S. Lacroix, J. M. Fernandez, and N. Godbout, “Cluster-state quantum computing in optical fibers,” J. Opt. Soc. Am. B **24**, 226 (2007).

[204] F. Bussieres, Y. Soudagar, G. Berlin, S. Lacroix, and N. Godbout, “Deterministic unitary operations on time-bin qudits for quantum communication,” Arxiv (0608183) , 4 (2006), arXiv:0608183 [quant-ph] .

[205] E. Huntington and T. Ralph, “Components for optical qubits encoded in sideband modes,” Phys. Rev. A **69**, 042318 (2004).

[206] T. Ralph, A. White, W. Munro, and G. Milburn, “Simple scheme for efficient linear optics quantum gates,” Phys. Rev. A **65**, 012314 (2001).

[207] A. E. H. Oehler, M. C. Stumpf, S. Pekarek, T. Südmeyer, K. J. Weingarten, and U. Keller, “Picosecond diode-pumped 1.5 μm Er,Yb:glass lasers operating at 10100 GHz repetition rate,” Appl. Phys. B **99**, 53 (2010).

[208] B. Dromey, M. Zepf, M. Landreman, K. O’keeffe, T. Robinson, and S. M. Hooker, “Generation of a train of ultrashort pulses from a compact birefringent crystal array.” Appl. Opt. **46**, 5142 (2007).

[209] K. G. Wilcox, A. H. Quarterman, V. Apostolopoulos, H. E. Beere, I. Farrer, D. A. Ritchie, and A. C. Tropper, “175 GHz, 400-fs-pulse harmonically mode-locked surface emitting semiconductor laser.” Opt. Express **20**, 7040 (2012).

[210] S. Jahanmirinejad, G. Frucci, F. Mattioli, D. Sahin, A. Gaggero, R. Leoni, and A. Fiore, "Photon-number resolving detector based on a series array of superconducting nanowires," Appl. Phys. Lett. **101**, 072602 (2012).

[211] A. Divochiy, F. Marsili, D. Bitauld, A. Gaggero, R. Leoni, F. Mattioli, A. Korneev, V. Seleznev, N. Kaurova, O. Minaeva, G. Gol'tsman, K. G. Lagoudakis, M. Benkhaoul, F. Lévy, and A. Fiore, "Superconducting nanowire photon-number-resolving detector at telecommunication wavelengths," Nat. Photonics **2**, 302 (2008).

[212] M. Fitch, B. Jacobs, T. Pittman, and J. Franson, "Photon-number resolution using time-multiplexed single-photon detectors," Phys. Rev. A **68**, 043814 (2003).

[213] T. Gerrits, N. Thomas-Peter, J. Gates, A. Lita, B. Metcalf, B. Calkins, N. Tomlin, A. Fox, A. Linares, J. Spring, N. Langford, R. Mirin, P. G. Smith, I. Walmsley, and S. Nam, "On-chip, photon-number-resolving, telecommunication-band detectors for scalable photonic information processing," Phys. Rev. A **84**, 1 (2011).

[214] A. Lamas-Linares, B. Calkins, N. a. Tomlin, T. Gerrits, A. E. Lita, J. Beyer, R. P. Mirin, and S. Woo Nam, "Nanosecond-scale timing jitter for single photon detection in transition edge sensors," Appl. Phys. Lett. **102**, 231117 (2013).

[215] M. Hosseini, B. M. Sparkes, G. Hétet, J. J. Longdell, P. K. Lam, and B. C. Buchler, "Coherent optical pulse sequencer for quantum applications." Nature **461**, 241 (2009).

[216] T. Ralph, N. Langford, T. Bell, and A. White, "Linear optical controlled-NOT gate in the coincidence basis," Phys. Rev. A **65**, 1 (2002).

[217] H. F. Hofmann, "Complementary Classical Fidelities as an Efficient Criterion for the Evaluation of Experimentally Realized Quantum Operations," Phys. Rev. Lett. **94**, 160504 (2005).

[218] N. Langford, T. Weinhold, R. Prevedel, K. Resch, A. Gilchrist, J. OBrien, G. Pryde, and A. White, "Demonstration of a Simple Entangling Optical Gate and Its Use in Bell-State Analysis," Phys. Rev. Lett. **95**, 210504 (2005).

[219] H. Hofmann, "Quantum parallelism of the controlled-NOT operation: An experimental criterion for the evaluation of device performance," Phys. Rev. A **72**, 022329 (2005).

[220] A. Eckstein, G. Boucher, A. Lemaître, P. Filloux, I. Favero, G. Leo, J. E. Sipe, M. Liscidini, and S. Ducci, "High-resolution spectral characterization of two photon states via classical measurements," Laser & Photonics Rev. **80**, 76 (2014).

[221] J. T. Barreiro, T.-C. Wei, and P. G. Kwiat, "Beating the channel capacity limit for linear photonic superdense coding," Nat. Phys. **4**, 282 (2008).

[222] N. Menicucci, S. Flammia, and O. Pfister, "One-Way Quantum Computing in the Optical Frequency Comb," Phys. Rev. Lett. **101**, 130501 (2008).

[223] J. Roslund, R. M. de Araújo, S. Jiang, C. Fabre, and N. Treps, "Wavelength-multiplexed quantum networks with ultrafast frequency combs," Nat. Photonics **8**, 109 (2013).

[224] B. Brecht, A. Eckstein, R. Ricken, V. Quiring, H. Suche, L. Sansoni, and C. Silberhorn, "Demonstration of coherent time-frequency Schmidt mode selection using dispersion-engineered frequency conversion," Arxiv **030302**, 1 (2014).

[225] D. V. Reddy, M. G. Raymer, and C. J. McKinstrie, "Efficient sorting of quantum-optical wave packets by temporal-mode interferometry," Opt. Lett. **39**, 2924 (2014).

[226] E. Saglamyurek, N. Sinclair, J. A. Slater, K. Heshami, D. Oblak, and W. Tittel, "An integrated processor for photonic quantum states using a broadband light-matter interface," New J. Phys. **16** (2014), 10.1088/1367-2630/16/6/065019, arXiv:1402.0481 .

[227] K. F. Reim, J. Nunn, X.-M. Jin, P. S. Michelberger, T. F. M. Champion, D. G. England, K. C. Lee, W. S. Kolthammer, N. K. Langford, and I. A. Walmsley, "Multipulse Addressing of a Raman Quantum Memory: Configurable Beam Splitting and Efficient Readout," Phys. Rev. Lett. **108**, 263602 (2012).

[228] X.-H. Bao, A. Reingruber, P. Dietrich, J. Rui, A. Dück, T. Strassel, L. Li, N.-L. Liu, B. Zhao, and J.-W. Pan, "Efficient and long-lived quantum memory with cold atoms inside a ring cavity," Nat. Phys. **8**, 517 (2012).

[229] P. J. Bustard, R. Lausten, D. G. England, and B. J. Sussman, "Toward Quantum Processing in Molecules: A THz-Bandwidth Coherent Memory for Light," Phys. Rev. Lett. **111**, 083901 (2013).

[230] K. Hammerer, A. S. Sørensen, and E. S. Polzik, "Quantum interface between light and atomic ensembles," Rev. Mod. Phys. **82**, 1041 (2010), arXiv:0807.3358 .

[231] K. C. Lee, B. J. Sussman, M. R. Sprague, P. Michelberger, K. F. Reim, J. Nunn, N. K. Langford, P. J. Bustard, D. Jaksch, and I. A. Walmsley, "Macroscopic non-classical states and terahertz quantum processing in room-temperature diamond," Nat. Photonics **6**, 41 (2011).

[232] T. A. Palomaki, J. D. Teufel, R. W. Simmonds, and K. W. Lehnert, "Entangling mechanical motion with microwave fields." Science **342**, 710 (2013).

[233] G. T. Campbell, O. Pinel, M. Hosseini, T. C. Ralph, B. C. Buchler, and P. K. Lam, "Configurable unitary transformations and linear logic gates using quantum memories," Phys. Rev. Lett. **113**, 1 (2014), arXiv:arXiv:1311.1889v1 .

[234] L. Chakhmakhchyan, S. Guérin, J. Nunn, and A. Datta, "Compact entanglement distillery using realistic quantum memories," Phys. Rev. A **88**, 042312 (2013).

[235] A. J. Roncaglia, L. Aolita, A. Ferraro, and A. Acín, "Sequential measurement-based quantum computing with memories," Phys. Rev. A **83**, 062332 (2011).

[236] K. F. Reim, P. Michelberger, K. C. Lee, J. Nunn, N. K. Langford, and I. A. Walmsley, "Single-Photon-Level Quantum Memory at Room Temperature," Phys. Rev. Lett. **107**, 053603 (2011).

[237] S. Lloyd and S. L. Braunstein, "Quantum Computation over Continuous Variables," Phys. Rev. Lett. **82**, 1784 (1999).

[238] T. Peyronel, O. Firstenberg, Q.-Y. Liang, S. Hofferberth, A. V. Gorshkov, T. Pohl, M. D. Lukin, and V. Vuletić, "Quantum nonlinear optics with single photons enabled by strongly interacting atoms." Nature **488**, 57 (2012).

[239] J. Wenger, R. Tualle-Brouri, and P. Grangier, "Non-Gaussian Statistics from Individual Pulses of Squeezed Light," Phys. Rev. Lett. **92**, 153601 (2004).

[240] M. Hosseini, B. M. Sparkes, G. Campbell, P. K. Lam, and B. C. Buchler, "High efficiency coherent optical memory with warm rubidium vapour." Nat. Commun. **2**, 174 (2011).

[241] P. Marian and T. A. Marian, "Uhlmann fidelity between two-mode Gaussian states," Phys. Rev. A **86**, 022340 (2012).

[242] H. Barnum, C. Caves, C. Fuchs, R. Jozsa, and B. Schumacher, "Noncommuting mixed states cannot be broadcast." Phys. Rev. Lett. **76**, 2818 (1996).

[243] G. Ferrini, J. Roslund, F. Arzani, Y. Cai, C. Fabre, and N. Treps, "Optimization of networks for measurement-based quantum computation," Phys. Rev. A **91**, 032314 (2015), arXiv:1407.5318 .

[244] K. Kieling, T. Rudolph, and J. Eisert, "Percolation, Renormalization, and Quantum Computing with Nondeterministic Gates," Phys. Rev. Lett. **99**, 130501 (2007).

[245] R. Raussendorf, S. Bravyi, and J. Harrington, "Long-range quantum entanglement in noisy cluster states," Phys. Rev. A **71**, 062313 (2005).

[246] M. Schlosshauer, J. Kofler, and A. Zeilinger, "A snapshot of foundational attitudes toward quantum mechanics," Stud. Hist. Philos. Sci. Part B - Stud. Hist. Philos. Mod. Phys. **44**, 222 (2013), arXiv:1301.1069 .

[247] A. Aspect, J. Dalibard, and G. Roger, "Experimental test of Bell's inequalities using time-varying analyzers," Phys. Rev. Lett. **49**, 1804 (1982).

[248] M. Ringbauer, B. Duffus, C. Branciard, E. G. Cavalcanti, a. G. White, and a. Fedrizzi, "Measurements on the reality of the wavefunction," Nat. Phys. , 1 (2015).

[249] J. S. Bell, "On the Einstein-Podolsky-Rosen paradox." Physics (College. Park. Md). **1.3**, 195 (1967).

[250] M. Howard, J. Wallman, V. Veitch, and J. Emerson, "Contextuality supplies the magic for quantum computation," Nature , 1 (2014).

[251] R. Orus, "Advances on Tensor Network Theory: Symmetries, Fermions, Entanglement, and Holography," Eur. Phys. J. B **87**, 280 (2014), arXiv:1407.6552 .

[252] S. Ryu and T. Takayanagi, "Aspects of Holographic Entanglement Entropy," J. High Energy Phys. **2006**, 45 (2006), arXiv:0605073 [hep-th] .

[253] M. H. Devoret and R. J. Schoelkopf, "Superconducting circuits for quantum information: an outlook." Science **339**, 1169 (2013).

[254] C. Monroe and J. Kim, "Scaling the ion trap quantum processor." Science **339**, 1164 (2013).

[255] C. Monroe, R. Raussendorf, a. Ruthven, K. R. Brown, P. Maunz, L. M. Duan, and J. Kim, "Large-scale modular quantum-computer architecture with atomic memory and photonic interconnects," Phys. Rev. A - At. Mol. Opt. Phys. **89**, 1 (2014), arXiv:1208.0391 .

[256] N. H. Nickerson, Y. Li, and S. C. Benjamin, "Topological quantum computing with a very noisy network and local error rates approaching one percent." Nat. Commun. **4**, 1756 (2013), arXiv:arXiv:1211.2217v3 .

[257] U. L. Andersen, J. S. Neergaard-Nielsen, P. van Loock, and A. Furusawa, "Hybrid quantum information processing," Arxiv , 13 (2014), arXiv:1409.3719 .